

UNIVERSITY OF BOLOGNA

DEPARTMENT OF ELECTRONICS, COMPUTER SCIENCE AND SYSTEMS

XXII PhD. Course in Electronics, Computer Science, and Telecommunications

ING-INF/03

Synchronization and Detection Techniques for Navigation and Communication Systems

by

Claudio Palestini

Coordinator:

Prof. **Paola Mello**

Supervisor:

Prof. **Giovanni Emanuele Corazza**

March 2010

*A connecting principle
Linked to the invisible
Almost imperceptible
Something inexpressible
Science insusceptible
Logic so inflexible
Causally connectible
Nothing is invincible*

The Police - Synchronicity I

Contents

I	Synchronization in Modern Navigation Systems	5
1	System Model	9
1.1	The Galileo System	9
1.2	Binary Offset Carrier Modulation	9
1.3	Galileo Signals in the E1 Band	10
1.3.1	Galileo PRS Signal in the E1 Band: E1-A	12
1.3.2	Galileo OS Signals in the E1 Band: E1-B and E1-C	13
1.3.3	Current modulation for Galileo OS Signals: Composite BOC	15
2	Robust Detection of BOC Modulated Signals	17
2.1	Code Acquisition for BOC Modulated Signals	17
2.1.1	Non Coherent Post Detection Integration for BOC Modulated Signals	19
2.2	The Quadribranch Detector	24
2.2.1	Performance Evaluation	28
2.2.2	Comparison with the ASPeCT Detector	31
2.3	Robust Detection of BOC Modulated Signals: Conclusions	35
3	High-Sensitivity GNSS Receivers	37
3.1	Soft Combining for Improved Sensitivity GNSS Code Acquisition . .	37
3.1.1	Soft Combining with Post Detection Integration	38
3.1.2	NCPDI Analytical Model in a Rice Fading Channel	40
3.1.3	Soft Combining: Performance evaluation	42
3.1.4	Mean Acquisition Time	45
3.1.5	Soft Combining for Improved GNSS Code Acquisition: Con- clusions	47

3.2	Multi-hypothesis Secondary Code Ambiguity Elimination	47
3.2.1	Code Acquisition with Multi-Hypotheses on Secondary Code	48
3.2.2	Performance Evaluation	51
3.2.2.1	Numerical Analysis	54
3.2.3	Multi-hypotheses Secondary Code Ambiguity Elimination: Con- clusions	55
4	Acquisition and Tracking of the E1-A Signal	57
4.1	Signal Distortion of High-Order BOC Modulated Signals	58
4.1.1	Linear Filter and Channel Propagation	59
4.1.2	Effects of Linear Distortion on Received Signals and on De- tection Algorithms	59
4.1.3	Multipath Propagation	60
4.2	Code Acquisition of Distorted Sequences	63
4.2.1	Full Band Acquisition	63
4.2.1.1	Code Doppler Effects	65
4.2.1.2	Numerical Results	66
4.2.2	Dual-Side Band Acquisition	67
4.2.2.1	Numerical Results	69
4.2.3	Combining E1-A with Open Service Signals E1-B and E1-C .	70
4.3	Transition from Acquisition to Tracking	71
4.3.1	Numerical results	76
4.4	Code Tracking	76
4.4.1	Bump Jumping technique	77
4.4.2	BPSK-like technique: Dual Sideband Technique	78
4.4.3	Double Estimation Technique	81
4.4.4	DET Tracking in the Presence of Signal Distortion	82
4.4.5	Translating the Two Delays in a Single Delay	83
4.4.5.1	Rounding Strategy	84
4.4.5.2	Smoothing Strategy	84
4.4.5.3	Averaging Strategy	84
4.4.5.4	Numerical Results	85
4.4.6	Code Tracking Numerical Results	88
4.4.7	Code Tracking in the Presence of Multipath	88
4.5	Acquisition and Tracking of the E1-A Signal: Conclusions	89

5	Integrated NAV-COM Systems: Assisted Code Acquisition and Interference Mitigation	91
5.1	The Presence of Interference in a GNSS System	95
5.1.1	Low-Complexity Interference Mitigation	97
5.1.2	Code Acquisition Strategy	102
5.1.3	NCPDI Performance Analysis in the Presence of Interference	103
5.1.4	NCPDI Performance Analysis in the Absence of Interference	105
5.1.5	NCPDI Performance Analysis with Interference Mitigation .	105
5.1.6	Mean Acquisition Time Analytical Characterization	106
5.2	Performance Evaluation	107
5.3	Integrated NAV-COM Systems: Conclusions	110
5.4	Appendix: Derivation of Signal Statistics After BOC Demodulation and IM Filter	111
II	Synchronization in Wireless and Satellite Communication Systems	115
6	Code Acquisition in the Mobile Broadband Satellite Standard DVB-RCS+M	119
6.1	Introduction	119
6.2	DS Spreading in the Forward Link of DVB-RCS+M	121
6.3	Channel model	122
6.4	Synchronization subsystem	123
6.4.1	Cold start code acquisition	126
6.4.2	Acquisition after short interruptions	129
6.5	Forward link performance results	130
6.5.1	Cold start code acquisition	130
6.5.2	Reacquisition after a short interruption	133
6.6	DS Spreading in the Return Link of DVB-RCS+M SCPC	135
6.7	Return Link Performance results	136
6.8	Code acquisition in DVB-RCS+M Conclusions	138
7	Synchronization in Future OFDM Standards: LTE and WiMAX	141
7.1	System Model	144
7.2	Frame Acquisition in LTE	144
7.3	Frame Acquisition in WiMAX	148

7.4	Synchronization in LTE and WiMAX: Conclusions	153
8	Preamble Insertion in Future Satellite-Terrestrial OFDM Broad-	
	casting Standards	155
8.1	System model	156
8.2	Hybrid channel Description	158
8.3	Preamble Description	158
8.4	Joint Frame Detection / Frequency Estimation scheme	160
	8.4.1 Frame Detection	161
	8.4.2 Frequency Estimation	164
8.5	Numerical Results	165
8.6	Preamble Insertion in Future OFDM Broadcasting Standards: Con-	
	clusions	165
A	Single Frequency Satellite Networks	167
A.1	Introduction	167
A.2	OFDM and Cyclic Delay Diversity	169
A.3	SFN over satellite networks	170
	A.3.1 Multi-beam coverage for SFSN	171
	A.3.2 Spot Beam Radiation Diagram	172
	A.3.3 MBCDD Approximated Transfer Function	173
A.4	SFSN Capacity	174
	A.4.1 Parameter Optimization	176
A.5	Preliminary Proof of Concept	176
A.6	Link Budget Analysis	179
A.7	Numerical Evaluation	180
A.8	Single Frequency Networks over Satellite: Conclusions	181
	Conclusions	183
	Bibliography	185
	Acknowledgments	199

List of Figures

1.1	CASM phase-states for E1 signal	11
1.2	E1-A autocorrelation function	12
1.3	E1-A Power Spectral Density	13
1.4	BOC autocorrelation function	14
1.5	E1-B or E1-C (OS) Power Spectral Density	15
1.6	MBOC Power Spectral Density	16
2.1	BOC autocorrelation function	19
2.2	Uncertainty region discretization in time and frequency domains	20
2.3	NCPDI block diagram	21
2.4	ROC NCPDI(1023,4) Galileo <i>E1</i> signal $C/N_0 = 35\text{dBHz}$	24
2.5	Quadribranch detector Block Diagram	25
2.6	BOC and BOCc waveforms cross-correlation function	26
2.7	Quadribranch Performance with Galileo <i>E1</i> signal	27
2.8	H_1/H_0 signal power ratio ρ for Quadribranch and NCPDI detectors vs. fractional delay δ	29
2.9	Performance Comparison with $\delta = 0$ and $\delta = T_c/4$	30
2.10	Average Performance Comparison	30
2.11	Mean Acquisition Time Comparison	31
2.12	BOC/PRN Block Diagram	32
2.13	Normalized Squared Correlation functions	33
2.14	H_1/H_0 signal power ratio ρ for BOC/PRN, NCPDI, and Quadribranch detectors vs. fractional delay δ	33
2.15	Performance comparison for BOC/PRN, conventional NCPDI, and Quadribranch: mean δ , $\delta = 0$, $\delta = \frac{T_c}{3}$	34
2.16	Average Mean Acquisition Time Comparison	34

3.1	Soft combining technique block diagram	39
3.2	Primary code detector block diagram: (a) NCPDI, (b) DPDI, (c) n-Span DPDI, (d) GPDI	41
3.3	Cross-validation between analytical and simulated performance of the NCPDI detector for different values of (M,L) in AWGN channel with $C/N_0 = 35\text{dBHz}$ and frequency error of 100Hz	43
3.4	Comparison between the NCPDI, DPDI and GPDI detectors in AWGN channel with $C/N_0 = 35\text{dBHz}$ and frequency error of 100Hz	44
3.5	Comparison between the NCPDI, DPDI and GPDI detectors in AWGN channel with $C/N_0 = 25\text{dBHz}$ and frequency error of 100Hz	44
3.6	NCPDI ROC performance with soft combining in the presence of Rice fading channels for $K = 0, 5, 10, 100$, $C/N_0 = 35\text{dBHz}$, $f_e = 100\text{Hz}$, $N = 5$ and $N = 10$, $M = 2046$, and $L = 2$	45
3.7	Mean Acquisition Time for NCPDI with soft combining in the pres- ence of Rice fading channels for $K = 0, 5, 10, 100$, $C/N_0 = 35\text{dBHz}$, $f_e = 100\text{Hz}$, $N = 5$ and $N = 10$, $M = 2046$, and $L = 2$	46
3.8	Classic parallel detector block diagram	49
3.9	Secondary code hypotheses tree for $N_c = 3$	50
3.10	Block diagram of primary code detection with multi-hypotheses sec- ondary code for $N_c = 2$	51
3.11	Low-complexity implementation of primary code detection with multi- hypotheses secondary code for $N_c = 2$	52
3.12	Receiver Operating Characteristics comparison with $C/N_0 = 30 \text{ dBHz}$. Analytical and simulated results are reported for different N_c	55
3.13	Mean acquisition time in seconds vs. false alarm probability with $C/N_0 = 30 \text{ dBHz}$	56
4.1	E1-A autocorrelation function: effect of a 6 taps Butterworth filter for different bandwidths	58
4.2	40MHz Butterworth 6-taps filter	60
4.3	2D Correlation Output	61
4.4	2D Correlation Output: the maximum is in the diagonal	61
4.5	2D Correlation Output: filtered	62
4.6	2D Correlation Output: the effect of the filter is that the maximum is shifted away from the diagonal	62
4.7	Multipath Error Envelope SMR= 3dB Phase= 0	63

4.8	Multipath effect on the 2D autocorrelation	64
4.9	Multipath effects on the Code Delay and on the Subcode Delay . . .	64
4.10	Parallel Code Phase Search block diagram	65
4.11	Effect of Doppler in the code	66
4.12	Probability of detection vs. signal to noise ratio (ideal case): Sampling Frequency= 122MHz - 1000 Iterations	67
4.13	Probability of detection vs. signal to noise ratio in the presence of signal distortion: Sampling Frequency= 122MHz - 1000 Iterations . .	68
4.14	Dual-Side Band with Parallel Code Phase Search block diagram . . .	68
4.15	Dual-Side Band Correlation Function	69
4.16	Probability of detection vs. signal to noise ratio for the Dual-band acquisition technique: Sampling Frequency= 122MHz - 1000 Iterations	69
4.17	Probability of detection vs. signal delay for $C/N_0 = 35\text{dBHz}$	70
4.18	E1-A and E1-C non-coherent combining	71
4.19	E1-A and E1-C non-coherent combining in the presence of signal distortion	72
4.20	Probability of detection vs. total signal to noise ratio: E1-A E1-B coherent combining (ideal case)	72
4.21	Probability of detection vs. total signal to noise ratio: E1-A E1-B coherent combining (in the presence of signal distortion)	73
4.22	Transition to Tracking block diagram	73
4.23	Transition to Tracking: Three hypotheses in parallel	75
4.24	Transition to Tracking: Frequency Estimation Performance (Sampling Frequency= 122MHz - 1000 Iterations)	76
4.25	Transition to Tracking: Phase Estimation Performance (Sampling Frequency= 122MHz - 1000 Iterations)	77
4.26	Bump Jumping false lock example	78
4.27	Delay Estimate: Full Band Tracking with Bump Jumping. AWGN $C/N_0 = 35\text{dBHz}$	79
4.28	Dual Sideband Concept	80
4.29	Delay Estimate: Dual Sideband Tracking. AWGN $C/N_0 = 35\text{dBHz}$.	80
4.30	Double Estimation Technique block diagram	81
4.31	Double Estimation Technique. AWGN $C/N_0 = 42\text{dBHz}$	82
4.32	Double Estimation Technique in the presence of signal distortion. AWGN $C/N_0 = 30\text{dBHz}$	83

4.33	Combining of the two delays: unfiltered case	85
4.34	Combining of the two delays: filtered case	86
4.35	Combining of the two delays: filtered case, very low SNR	86
4.36	Standard Deviation and Mean of the tracking error: unfiltered case	87
4.37	Standard Deviation and Mean of the tracking error: filtered case	87
4.38	Code Tracking: standard deviation	88
4.39	Multipath Error Envelope for different tracking algorithms	89
5.1	Receiver logical block diagram	92
5.2	Integrated navigation-communication system architecture for A-GNSS with interference mitigation	94
5.3	Amplitude frequency response of the 5 taps notch filter vs. frequency and interference IF normalized to T_{sc}	98
5.4	SINR at the filter output vs.interference IF normalized to T_c , $E_s/N_0 = -25$ dB, $M = 4092$	101
5.5	NCPDI block diagram	102
5.6	Autonomous GNSS - ROC performance for NCPDI with $M = 341$, $L = 12$, $C/N_0 = 35$ dBHz, $\nu_I = 0.4$	107
5.7	A-GNSS - ROC performance for NCPDI with $M = 2046$, $L = 2$ $C/N_0 = 35$ dBHz, $\nu_I = 0.4$	108
5.8	Mean acquisition time vs. false alarm probability for Autonomous (dashed) and A-GNSS (solid) with $\nu_I = 0.4$, $C/N_0 = 35$ dBHz	109
5.9	A-GNSS - ROC performance for NCPDI with $M = 2046$, $L = 2$ $C/N_0 = 35$ dBHz, $\nu_I = 0.8$	109
5.10	Mean acquisition time vs. false alarm probability for Autonomous (dashed) and Assisted GNSS (solid) with $\nu_I = 0.8$, $C/N_0 = 35$ dBHz	110
6.1	DVB-S2 Physical Layer Frame (PLFRAME) structure	121
6.2	Forward link spectrum spreading	122
6.3	Code/frame acquisition finite state machine	124
6.4	Detectors block diagrams for Non Coherent PDI (NCPDI), Differential PDI (DPDI), Generalized PDI (GPDI), and Differential GPDI (D-GPDI)	127
6.5	Cold start acquisition procedure flow-graph	128
6.6	Cold start acquisition - Receiver Operating Characteristics	131
6.7	Cold start acquisition - Mean acquisition time vs. false alarm probability	132

6.8	Re-acquisition after short interruptions with constant modulation - Mean acquisition time vs. false alarm probability	134
6.9	Re-acquisition after short interruptions with variable modulation - Mean acquisition time vs. false alarm probability	135
6.10	Simulated ROC performance at $E_s/N_0 = 0.7\text{dB}$, with non ideal sam- pling ($\delta = 0.25$) considering spreading factors $\eta = 1, 2, 3, 4, 8, 16$. . .	136
6.11	Simulated ROC performance at $E_s/N_0 = -1\text{dB}$, with non ideal sam- pling ($\delta = 0.25$) considering spreading factors $\eta = 1, 2, 3, 4, 8, 16$. . .	137
6.12	Mean Acquisition Time performance in AWGN at $E_s/N_0 = 0.7\text{dB}$, with non ideal sampling ($\delta = 0.25$) considering spreading factors $\eta = 1, 2, 3, 4, 8, 16$	138
6.13	Mean Acquisition Time performance in AWGN at $E_s/N_0 = -1\text{dB}$, with non ideal sampling ($\delta = 0.25$) considering spreading factors $\eta = 1, 2, 3, 4, 8, 16$	138
7.1	LTE Frame Structure	145
7.2	Receiver Block Diagram	146
7.3	Non Coherent Post Detection Integration (NCPDI)	147
7.4	Performance of the LTE PSCH Acquisition: AWGN $E_s/N_0 = 0\text{dB}$	147
7.5	Performance of the LTE PSCH Acquisition in a Rice fading channel: $E_s/N_0 = 0\text{dB}$ and Rice factor of 7dB	148
7.6	WiMAX Frame Structure	148
7.7	Structure of the active carriers in the WiMAX preamble	149
7.8	Structure of the WiMAX preamble in the time domain	149
7.9	Sliding Window Correlation Scheme	150
7.10	Moving Sum: a practical example	150
7.11	Sliding Window approach for WiMAX Preamble Detection	151
7.12	WiMAX Frame: Autocorrelation Function	151
7.13	Performance of WiMAX Preamble Detection	152
8.1	P1 Structure in time domain	159
8.2	Detector block diagram optimized for P1 preamble (Adaptive Corre- lator Scheme)	161
8.3	Autocorrelation function and argument with the Adaptive Correla- tion Scheme considering AWGN with $E_s/N_0 = 20\text{dB}$	162
8.4	Detection in the presence of fractional timing error	163

8.5	Simulation scheme for P1 performance evaluation	164
8.6	Fractional frequency estimation (MSE) in AWGN and HYB channel at 3 km/h	165
8.7	Comparison between P1 and Guard Interval Based (1/8) approaches (MSE) in AWGN and HYB channel at 3 km/h	166
A.1	CDD OFDM transmitter	170
A.2	Broadcasting over Europe: single beam, linguistic beams, local beams	171
A.3	Spot beam radiation and mask for $T = 20\text{dB}$ and $p = 2$	173
A.4	Overall transfer function for three beams and $N = 1, 2, 3, 20$ paths each beam as a function carrier index	174
A.5	Effective transfer function without MBCDD. Three overlapping beams.	174
A.6	Capacity comparison in the three scenarios: single beam, two over- lapping beams, three overlapping beams.	175
A.7	Parameter optimization	177
A.8	Capacity obtained in an area covered with six beams.	178
A.9	Snapshot of capacity	178
A.10	Capacity comparison: SFSN vs. Single Beam Single Carrier	181

List of Tables

5.1	Scenario definition for autonomous and assisted GNSS	95
6.1	Orthogonal Variable Spreading Factor (OVSF) sequences	122
6.2	Phase noise mask	123
6.3	Acquisition performance at the optimal operating point, i.e., minimum mean acquisition time, for D-GPDI and GPDI with different spreading factors, $\eta = 2$ and $\eta = 4$. Cold Start.	132
6.4	Acquisition performance at the optimal operating point, i.e., minimum mean acquisition time, for D-GPDI, GPDI, and NCPDI with different spreading factors, $\eta = 2$ and $\eta = 4$. Re-acquisition after a short interruption, constant QPKS modulation mode	134
6.5	Acquisition performance at the optimal operating point, i.e., minimum mean acquisition time, for D-GPDI, GPDI, and NCPDI with different spreading factors, $\eta = 2$ and $\eta = 4$. Re-acquisition after a short interruption, variable modulation mode	135
6.6	Minimum MAT in AWGN at $E_s/N_0 = 0.7$ and -1 dB, with non ideal sampling ($\delta = 0.25$) considering spreading factors $\eta = 1, 2, 3, 4, 8, 16$.	139
7.1	Parameters of LTE and WiMAX Air Interfaces	145
7.2	Number of the Active Carriers on the WiMAX Preamble	149
8.1	Hybrid Channel power delay profile	159
8.2	P1 Detection Probability - $P_{fa} = 0.001$	163
8.3	P1 Detection Probability - $P_{fa} = 0.001$	163
A.1	Link budget for Single Beam and SFSN systems	179

List of acronyms

3G Third Generation

3.5G Third Generation transitional

4G Fourth Generation

ACF Auto-Correlation Function

ADC Analog to Digital Converter

AGC Automatic Gain Control

A-GNSS Assisted-GNSS

AWGN Additive White Gaussian Noise

B3G Beyond Third Generation

BOC Binary Offset Carrier

BOC_c Binary Offset Carrier Cosine

BPSK Binary Phase Shift Keying

CASM Coherent Adaptive Subcarrier Modulation

CBOC Composite Binary Offset Carrier

CDD Cyclic Delay Diversity

CDMA Code Division Multiple Access

CFO Carrier Frequency Offset

CFT Channel Transfer Function

- CHILD** CoHerent Integration Length Dimensioning
- CP** Cyclic Prefix
- CPF** Central Processing Facility
- CRB** Cramer-Rao Bound
- CTE** Coarse Timing Estimation
- CW** Continuous Wave
- CWI** Continuous Wave Interferer
- DET** Double Estimator Technique
- D-GPDI** Differential Generalized Post Detection Integration
- DLL** Delay Locked Loop
- DPDI** Differential Post Detection Integration
- DS-SS** Direct Sequence Spread Spectrum
- DVB** Digital Video Broadcasting
- DVB-NGH** Digital Video Broadcasting - Next Generation Handheld
- DVB-H** Digital Video Broadcasting - Handheld
- DVB-RCS** Digital Video Broadcasting - Return Channel Satellite
- DVB-RCS+M** Digital Video Broadcasting - Return Channel Satellite Mobile extension
- DVB-S2** Digital Video Broadcasting - Satellite second generation
- DVB-SH** Digital Video Broadcasting - Satellite services to Handhelds
- DVB-T2** Digital Video Broadcasting - Terrestrial second generation
- DVB-TM** Digital Video Broadcasting - Technical Module
- EGNOS** European Geostationary Navigation Overlay Service
- EIRP** Effective Isotropic Radiated Power

FFE Fractional Frequency Estimation

FFT Fast Fourier Transform

FIR Finite Impulse Response

FL Forward Link

FSM Finite State Machine

FTE Fine Timing Estimation

GEO Geostationary

GI Guard Interval

GIOVE Galileo In-Orbit Validation Element

GLONASS Global Orbiting Navigation Satellite System

GNSS Global Navigation Satellite System

GPDI Generalized Post Detection Integration

GPS Global Positioning System

GSA GNSS Supervisory Authority

HDTV High Definition Television

HPA High Power Amplifier

ICC Interference Control Center

ICD Interface Control Document

ICI Inter Carrier Interference

IDFT Inverse Discrete Fourier Transform

IF Instantaneous Frequency

IFE Integer Frequency Estimation

IFFT Inverse Fast Fourier Transform

IIR Infinite Impulse Response

IM Interference Mitigation

INS Inertial Navigation System

IOS Interference Observation Sensors

IP Internet Protocol

ISI Inter Symbol Interference

LoS Line-of-Sight

LTE Long Term Evolution

MAT Mean Acquisition Time

MBCDD Multi-Beam Cyclic Delay Diversity

MBOC Multiplexed Binary Offset Carrier

MF Matched Filter

MIMO Multiple-Input Multiple-Output

ML Maximum Likelihood

MSE Mean Squared Error

NAV-COM Navigation-Communication

NCPDI Non Coherent Post Detection Integration

NLOS Non-Line-Of-Sight

OFDM Orthogonal Frequency Division Multiplex

OS Open Service

OVSF Orthogonal Variable Spreading Factor

pdf Probability Density Function

PDI Post Detection Integration

PHY Physical Layer

PLFRAME Physical Layer Frame

PLL	Phase Locked Loop
PLS	Physical Layer Signalling
PRS	Public Regulated Service
PSD	Power Spectral Density
PSK	Phase Shift Keying
QoS	Quality of Service
QPSK	Quadrature Phase Shift Keying
RF	Radio Frequency
RFI	Radio Frequency Interference
RL	Return Link
ROC	Receiver Operating Characteristic
SCPC	Single Channel Per Carrier
SDR	Software Defined Radio
SDTV	Standard Definition Television
SFN	Single Frequency Network
SFSN	Single Frequency Satellite Network
SINR	Signal-to-Interference-plus-Noise Ratio
SIS	Signal In Space
SLL	Sub-carrier Locked Loop
SMR	Signal to Multipath Ratio
SNR	Signal to Noise Ratio
SOF	Start Of Frame
SoL	Safety-of-Life
SS	Spread Spectrum

SSB Single Side Band

TC Threshold Crossing

TFD Time-Frequency Distribution

TMBOC Time-Multiplexed Binary Offset Carrier

TTI Transmit Time Interval

UMTS Universal Mobile Telecommunications System

UW Unique Word

VCC Voltage Control Clock

WiMAX Worldwide interoperability for Microwave Access

WLAN Wireless Local Area Network

Introduction

Motivation and Goals

This thesis is the outcome of the work performed within my Ph.D. research activities. The central research topic of this thesis is synchronization for navigation and telecommunication systems.

First of all, what is synchronization? From an encyclopedic point of view, synchronization is the process of aligning the time scales between two or more processes that occur at spatially separated points. From a more practical point of view, it is a necessary convention for the aggregation and the timing agreement of human behaviors. Thus, it is worthwhile noting that, during the years, synchronization has been a key element for the evolution of human beings.

In the modern world, the necessity of a finer synchronization has grown together with the increased possibilities and potentialities enabled by modern technologies. In particular, telecommunication systems have allowed effectual and powerful applications, but have required more stringent synchronization capabilities. Furthermore, the concept of localization has given birth to a vast area of killer applications, but, at the same time, it has called for an increasingly more precise time alignment.

On the other hand, the individualization of the needs has caused the concept of synchronization to rapidly change, straining from a powerful concept to a critical and potentially harmful design issue: broadcasting has been rapidly juxtaposed with broadband services, i.e. personal services with no relation in time with the others; time division has been substituted by code division multiple access, which guarantees the use of the same band simultaneously to many users; flexible and adaptive infrastructures have allowed triple-play services, etc.

Even though it has been a well-investigated topic for many years [17], synchronization has seen a renewed interest from the scientific community recently, because of the development of new Global Navigation Satellite Systems (GNSS) and the

modernization of the existent ones in the field of navigation, and of the introduction of novel concepts in the communication area. In fact, synchronization plays an important role in communication, since it represents the necessary pre-requisite for proper data demodulation and decoding, but it becomes fundamental in the navigation systems, that rely entirely on the estimation of the time delay of the signals coming from the satellites for the computation of the position estimate.

Novel modulations, as Binary Offset Carrier (BOC) in navigation and Orthogonal Frequency Division Multiplexing (OFDM) in communication, innovative synchronization techniques, and new powerful concepts, as peer-to-peer cooperation, Inertial Navigation System (INS) aiding or Assisted GNSS, have raised challenging and exciting problems to be dealt with, and during my PhD I successfully faced up with these problems, proposing solutions and novel ideas which have contributed to the assessment of viable solutions in the field of communication and navigation. The proposal and adoption of these design solution in the framework of several projects in the National and International arena [18][19][20][21][22][23][24] have provided the proof of their applicability as well as the identification of the trade-offs related to the practical constraints of realistic systems.

What will become of synchronization in the next decade? It is always hard to make predictions, but some trends can be already forecasted. From the engineering point of view, integration between communication and navigation will see an ever increasing role, and joint synchronization techniques will be explored. Robust techniques should be able to tackle with any challenging scenarios, thanks to iterative approaches and a very strict combining between equalization and synchronization. The concept of aiding will be exploited in novel paradigms, and software radio and cognitive radio concepts will bring about receivers able to synchronize in every bandwidth and with any possible standard. Finally, from the social perspective, synchronization will come back to be the main aspect for the definition of national or international identities, more than languages, television, money, or information. In fact, since future technological innovations will push the limits of globalization, synchronization will become the effective common point for human collaboration and cooperation. A little revenge against the social deconstructionism and individualism that have marked the last decade.

Thesis Outline

This thesis is organized in two parts that tackle the problem of synchronization in recent GNSS systems and communication systems respectively.

Part I deals with synchronization strategies for the novel GNSS signals, characterized by new modulations and new signal structures. The aim is to obtain a viable synchronization scheme able to provide robust and reliable detection everywhere and at anytime. Moreover, new concepts of aiding, like Assisted GNSS and its extension to Interference Mitigation (IM) strategies are analyzed, based both on theory and application.

Part II considers the problem of synchronization in several communication systems, like Digital Video Broadcasting - Return Channel via Satellite Mobile extension (DVB-RCS+M), 3GPP Long Term Evolution (LTE), and Worldwide Interoperability for Microwave Access (WiMAX). The design of effective synchronization solutions and their performance assessment has been conducted in many challenging scenarios.

Finally, in Appendix A, a novel concept identified as Single Frequency Satellite Network (SFSN), reminiscent of the Single Frequency Network of terrestrial broadcasting systems, is applied over multi-beams satellites with hundreds of beams, allowing to achieve extreme flexibility in satellite broadcasting systems.

Original Contributions

This thesis presents original contributions in different fields. Regarding GNSS systems, the main contributions are summarized in the following:

- Introduction of a novel detector for BOC modulated signals, with the aim of minimizing the fluctuations due to the BOC autocorrelation function.
- Exploitation of known communication concepts in the field of navigation in order to improve the sensitivity of GNSS receivers, especially in very harsh scenario, like indoor and urban canyons.
- Exploitation of a multi-hypotheses tree for secondary code ambiguity elimination in high-sensitivity Galileo receivers.
- Introduction of a theoretical framework for the two dimensional correlation of BOC modulated signals in the presence of signal distortion and multipath.

- Introduction of a possible extension of the classical approach of Assisted GNSS, with the assistance network capability of estimating both the presence and the parameters of the interferers and broadcasting this information to the users; an analytical evaluation in terms of false alarm probability, missed detection probability, and mean acquisition time has been carried out.

Regarding the wireless and satellite communication systems, the main contributions are:

- Performance evaluation of the DVB-RCS+M synchronization subsystem and support in the DVB-RCS Guidelines preparation.
- Design of novel detectors for WiMAX and LTE, and comparison in terms of synchronization capabilities of the future 4G standards.
- Introduction of a terrestrial standard-like preamble for future satellite OFDM broadcasting systems and its performance analysis.
- Design of a novel joint frame synchronization / frequency estimation scheme for a preamble-based OFDM system.
- Design of the synthetic multipath profile and of the on-board antenna in a SFSN network for the optimization of the coverage region in a broadcasting system.

Part I

Synchronization in Modern
Navigation Systems

Global Navigation Satellite System (GNSS) is an exciting technology with the potential to play an ever increasing role in modern, mobile societies. The advent of Galileo, the European satellite navigation system, and the modernization of the Global Positioning System (GPS) will have a deep impact in the quality of services supplied to users, and consequently into diffusion and development of mass market devices [25] [26].

The basic operation for every positioning system is the pseudo-range estimation, i.e. the measurement of the distance between the satellite and the receiver. This is achieved by synchronizing a locally generated code sequence with the received signal in order to determine the transmission delay. This operation, referred to as code synchronization, is crucial because it drives the overall system performance.

Code synchronization is usually achieved through two steps in cascade: acquisition and tracking. Code acquisition is in charge of exploring the entire code epoch domain (uncertainty region) in order to get a first rough estimate, while code tracking is asked to eventually detect erroneous synchronization events and to refine the estimate to a higher precision [27].

Code acquisition is typically the most critical phase because the uncertainty region is large, up to the entire code duration, and, being GNSS typically based on Spread Spectrum (SS), the signal to noise ratio before despreading is extremely low, so that no carrier estimation is practically feasible. In order to reduce complexity, the uncertainty region is usually discretized in one or more hypotheses per chip, so transforming the epoch estimation problem in a detection problem, where the correct hypothesis H_1 has to be selected among many wrong hypotheses H_0 .

The signal tracking process covers a carrier tracking and a code tracking, and both of them must be performed for correct receiver function [28]. The code tracking process is necessary for pseudorange estimation. The feedback system for code tracking is represented by Delay Lock Loop (DLL). The carrier tracking process is capable to synchronize the frequency or phase of the carrier wave, for correct Doppler offset removal due to satellite and user movement, and in some cases, can be also used for precise pseudorange estimation (phase measurement).

In the following the problem of code acquisition, and code tracking will be tackled for the novel GNSS signals.

1

System Model

1.1 The Galileo System

Galileo is intended to provide high quality navigation services, consisting of ten different navigation signals on three frequency bands: 1164-1215 MHz (E5a and E5b), 1260-1300 MHz (E6), and 1559-1592 MHz (E1) [29]. In particular, the Galileo E1 band, which is overlapped with the GPS L1 band, represents the most promising application case for interoperable GNSS receivers.

The E1 signal contains three channels (denoted as A, B and C) that are transmitted at the same carrier frequency (1575.42MHz). The A signal is designed to be used for the Public Regulated Services (PRS), while B and C for the Open Service (OS).

1.2 Binary Offset Carrier Modulation

The introduction of the Binary Offset Carrier (BOC) modulation represents the main innovation in the signals of the Galileo and of the modernized GPS systems.

A BOC modulated signal is obtained through the spreading of the input signal with a square wave subcarrier that has a frequency multiple of the chip rate [30].

It is denoted as $\text{BOC}(f_s, f_c)$, where f_s and f_c are the subcarrier frequency and the chip rate, respectively, related by the equation $f_c = \frac{1}{T_c} = \frac{2}{n}f_s = \frac{1}{nT_{sc}}$, where n is the number of subcarrier half periods T_{sc} , in a chip period T_c ($T_c = nT_{sc}$). In the GNSS context, the BOC modulated signal is often indicated as $\text{BOC}(\alpha, \beta)$, where $\alpha = f_s/1.023$ MHz and $\beta = f_c/1.023$ MHz.

The waveform can be expressed as

$$p_{\text{BOC}}(t) = \text{rect}_{T_c}(t) \text{sign}[\sin(2\pi f_s t)] \quad (1.1)$$

Analogously, a BOC_c (Binary Offset Carrier Cosine) can be described by the following waveform

$$p_{\text{BOC}_c}(t) = \text{rect}_{T_c}(t) \text{sign}[\cos(2\pi f_s t)] \quad (1.2)$$

The main characteristic of BOC modulation is that it shifts the signal power from the band center, reducing the interference with coexisting systems.

1.3 Galileo Signals in the E1 Band

The E1 signal contains three channels that are transmitted at the same carrier frequency (1575.42 MHz). The A channel contains encrypted data for PRS, while the B and C channels contain navigation data and the pilot code for the OS, respectively.

These channels are modulated through BOC modulation, in particular B and C are described by the Composite BOC (CBOC) modulation [31], which will be described in 1.3.3, while A is characterized by the $\text{BOC}_c(15,2.5)$, i.e. $n = 12$. Nevertheless in this thesis, the $\text{BOC}(1,1)$ modulation, i.e. $n = 2$, has been considered for E1-B and E1-C instead of CBOC for the following reason:

- up until 2007 the baseline for E1-B and E1-C was the $\text{BOC}(1,1)$ modulation, and political discussions were underway to define a shared spectrum between GPS and Galileo [32];
- although CBOC offers exploitable characteristics, this happens at the cost of receiver re-design; the use of a lower complexity receiver matched to the $\text{BOC}(1,1)$ leads to a performance loss in the code acquisition of fractions of dB [33];
- the scope of this thesis is not the optimization of a CBOC receiver, and thus for the sake of simplicity the less complex mathematical analysis of a $\text{BOC}(1,1)$ has been preferred.

Multiplexing between A, B and C channels is achieved through the Coherent Adaptive Subcarrier Modulation (CASM) modulation, which enables to achieve a constant envelope signal. Accordingly, the Galileo signal on the E1 band, if the BOC(1,1) modulation is considered, is a hexaphase complex signal, which can be expressed as

$$s_{E1}(t) = s_{E1,I}(t) + js_{E1,Q}(t) \quad (1.3)$$

with in-phase and quadrature components respectively given by

$$s_{E1,I}(t) = \frac{\sqrt{2}}{3}[s_{E1-B}(t) - s_{E1-C}(t)] \quad (1.4)$$

$$s_{E1,Q}(t) = \frac{1}{3}[2s_{E1-A}(t) + s_{E1-A}(t)s_{E1-B}(t)s_{E1-C}(t)] \quad (1.5)$$

Note that s_{E1-A} , s_{E1-B} , s_{E1-C} represent the A, B and C channels respectively that will be thoroughly described in the next pages.

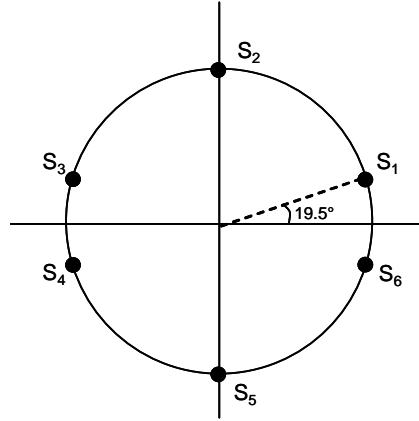


Figure 1.1: CASM phase-states for E1 signal

By mapping the three input bits respectively from A, B, and C channels, CASM yields to a constellation with only 6 symbols as shown in Figure 1.1, i.e. two couples of bit triplets are mapped onto the same transmitted symbols. But, despite of this inherent ambiguity, by processing separately the PRS signal and the OS signals, the code despreading is not affected by this ambiguity.

Notably, if CBOC is considered for E1-B and E1-C, a modified version of CASM, known as Interplex modulation or Modified Hexaphase modulation leads to a eight-points constellation.

1.3.1 Galileo PRS Signal in the E1 Band: E1-A

The E1-A signal is described by the BOCc(15,2.5) modulation, i.e. $n = 12$, which represents the highest ratio of subcarrier frequency to chip rate of any GPS and Galileo signals.

The signal can be expressed as

$$s_{E1-A}(t) = \sum_{i=-\infty}^{+\infty} c_i d_{[i]_N} \text{rect}_{T_c}(t - iT_c) \text{sign}[\cos(2\pi f_s t)] \quad (1.6)$$

$$= \sum_{i=-\infty}^{+\infty} c_i d_{[i]_N} p\text{BOCc}(t - iT_c) \quad (1.7)$$

where $[a]_b$ indicates the integer part of a/b , c_i are the i th chip of the spreading code, d_i are the data symbols to transmit the navigation message, N is the duration in chips of the navigation bit, T_c is the chip period, and $\text{rect}_T(t)$ is the rectangular pulse shape function over the time period T .

In the fully operational service, the signal E1-A will be transmitted encrypted, with an aperiodic spreading sequence. In the current experimental mode, the E1-A signals transmitted by the two satellites, GIOVE-A and GIOVE-B, are characterized by a fixed full code period equal to 10ms: a primary code length N of 25575 (10ms) in GIOVE-A without any secondary code, and a primary code length N of 5115 (2ms) in GIOVE-B with a secondary code of length equal to 5 [34].

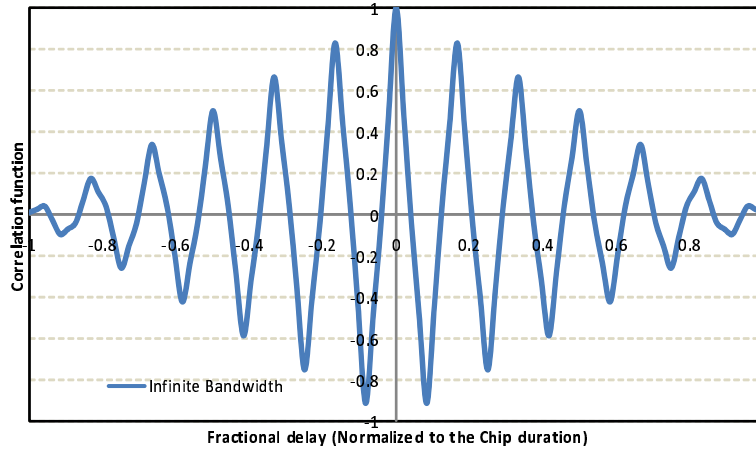


Figure 1.2: E1-A autocorrelation function

The autocorrelation function of the BOCc(15,2.5) (Figure 1.2) is very critical.

It is characterized by the presence of a very narrow main peak, but, on the other hand presents $2 \cdot n = 24$ secondary peaks, as well as $2 \cdot n = 24$ nulls. Moreover, the ratio between the strongest secondary peak and the first peak is only 0.9 in the ideal case, making the detection algorithms very challenging.

The Power Spectral Density (PSD) of the BOCc(15,2.5) is shown in Figure 1.3. It is worthwhile noting that the two main lobes are shifted from the carrier frequency by the amount equal to the subcarrier frequency, i.e. 15.345MHz.

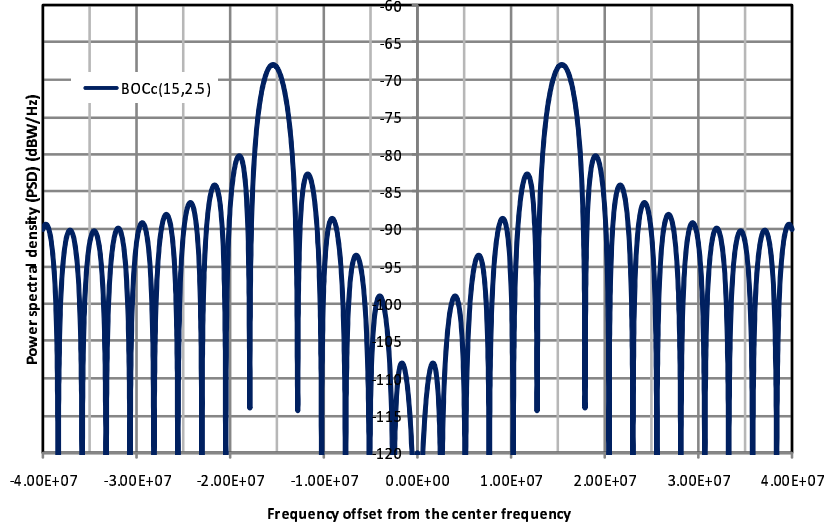


Figure 1.3: E1-A Power Spectral Density

1.3.2 Galileo OS Signals in the E1 Band: E1-B and E1-C

The B and C signals are described by the BOC(1,1) modulation, i.e. $n = 2$, and can be written as

$$s_{E1-B}(t) = \sum_{i=-\infty}^{+\infty} c_{B,|i|_N} d_{|i|_N} \text{rect}_{T_c}(t - iT_c) \text{sign}[\sin(2\pi f_s t)] \quad (1.8)$$

$$s_{E1-C}(t) = \sum_{i=-\infty}^{+\infty} c_{C,|i|_N} \text{rect}_{T_c}(t - iT_c) \text{sign}[\sin(2\pi f_s t)] \quad (1.9)$$

where $[a]_b$ indicates the integer part of a/b , $|a|_b$ is the a module b operation, $c_{B,i}$ and $c_{C,i}$ are the i th chip of the spreading code of channel B and C, respectively, d_i are the data symbols to transmit the navigation message, N is the spreading factor equal to the code length, T_c is the chip period of both B and C signals, and $\text{rect}_T(t)$ is the rectangular pulse shape function over the time period T [35].

The B channel contains navigation data and the C channel is the pilot code to perform code synchronization. In particular, the C signal is composed by a secondary code of 25 symbols that is spread by a 4092 chip long primary code, so forming an overall sequence of 102300 chips that is continuously repeated.

Note that the hierarchical structure of the signals in E1 band can be fruitfully exploited in order to reduce the synchronization complexity. In particular, the synchronization with the overall code length, for example 102300 for E1-B, can be split into the synchronization with the primary code only, followed by the synchronization with the secondary code. This allows for reducing the number of hypotheses in the uncertainty region from 102300 to 4092+25. The synchronization with the secondary code is somehow less critical because it can be completed after frequency estimation and timing recovery, so the problem of primary code acquisition only is considered in the following.

The autocorrelation function of BOC(1,1) modulation is shown in Figure 1.4. It can be seen that the attenuation introduced on the useful signal can be high also in the presence of limited timing misalignment, up to a null corresponding to $\frac{T_c}{3}$. On the other hand, it can be noted that the presence of a secondary peak in $\frac{T_c}{2}$ may cause problems of false locks in the tracking stage.

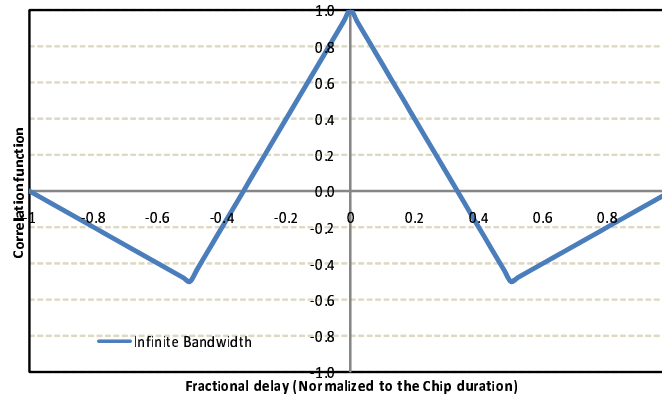


Figure 1.4: BOC autocorrelation function

BOC(1,1) PSD is shown in Figure 1.5. Note that, as for the BOCc(15,2.5), also in this case the signal power is shifted from the band center, in order to reduce the interference with the existing GNSS systems.

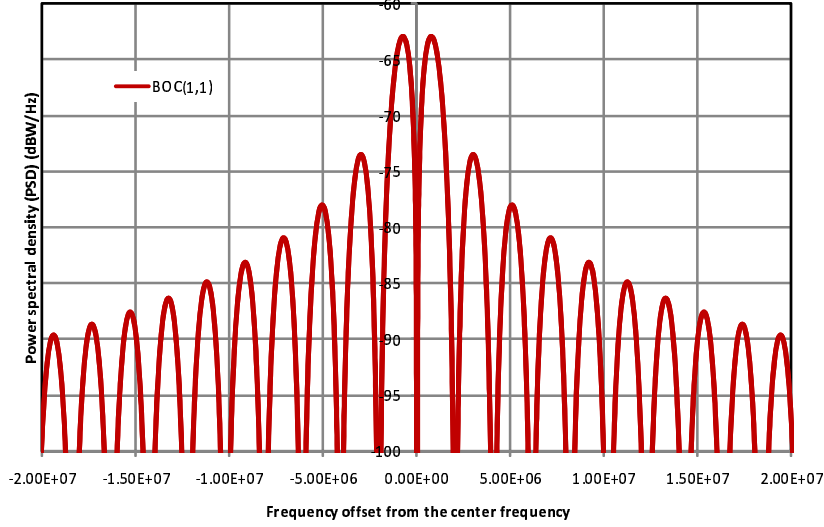


Figure 1.5: E1-B or E1-C (OS) Power Spectral Density

1.3.3 Current modulation for Galileo OS Signals: Composite BOC

Nevertheless the BOC(1,1) modulation has been considered in this thesis for the B and C signals of Galileo OS, the analysis of the CBOC modulation is herein reported. This slightly different modulation has been adopted in 2007 in order to guarantee a common power spectral density both for the future GPS L1C and the Galileo OS civil signals in E1 band. The agreed power spectral density (PSD) known as multiplexed binary offset carrier (MBOC) [36][37][38] is shown in Figure 1.6, and is expressed as:

$$G_{MBOC}(f) = \frac{10}{11}G_{BOC(1,1)}(f) + \frac{1}{11}G_{BOC(6,1)}(f) \quad (1.10)$$

Since the MBOC has been defined only in the frequency domain, different implementations in the time domain can be considered, in particular the following two versions have been considered: the CBOC(6,1,1/11) (Composite BOC) modulation, which has been adopted by the European system Galileo, and the Time-Multiplexed BOC (TMBOC), designed for the modernized GPS. TMBOC multiplexes in the time domain BOC(1,1) and BOC(6,1) subcarriers, while CBOC linearly combines BOC(1,1) and BOC(6,1) subcarriers as the weighted sum of two squared-wave subcarriers (i.e. both components being present at all times) for the data channel, and the weighted difference for the pilot [39].

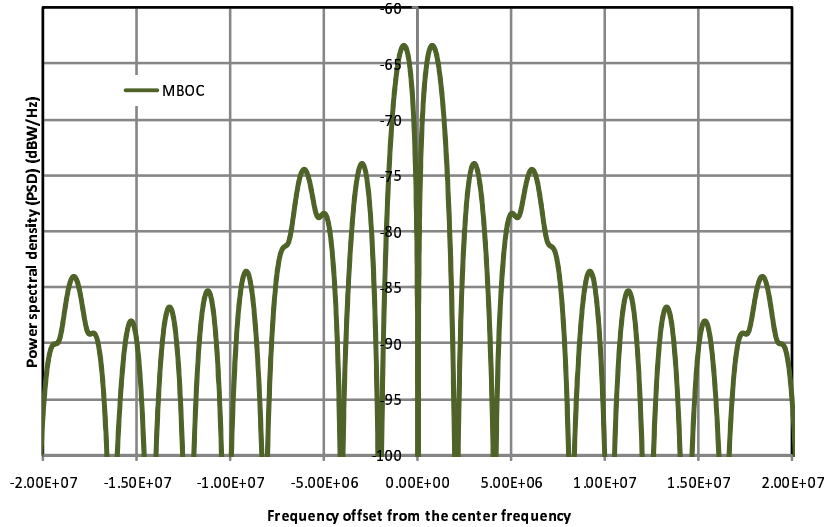


Figure 1.6: MBOC Power Spectral Density

Obviously, the optimum detector should be able to locally generate the CBOC or TMBOC if a filter matched to the transmitted waveform it is desired to be used, but, as also mentioned in the previous section, it has been shown that the use of a lower complexity locally generated BOC(1,1) leads to a very limited performance loss in the code acquisition [33]. In the following, the analysis of the classical BOC(1,1) has been conducted. Extension to the CBOC or TMBOC can be obtained straightforwardly, substituting the BOC(1,1) autocorrelation function with the CBOC or TMBOC ones. In order to optimize the receiver and exploit the characteristics of CBOC or TMBOC, a deeper analysis on the receiver re-design should be performed. However, this topic is out of the scope of this thesis.

2

Robust Detection of BOC Modulated Signals

In this section the analysis of code acquisition of BOC modulated signals is conducted, with particular attention on the Galileo OS signals, and a novel solution to guarantee robustness without increasing complexity is proposed. Note that these results have been partially reported in [1] and [2]. My contribution to this topic lies in the design of a novel detector, and the analytical performance evaluation of all the detection schemes described in the following.

2.1 Code Acquisition for BOC Modulated Signals

Considering the Galileo signal described in the previous section, the received signal can be written as

$$r(t) = e^{j2\pi f_e t + \phi} s_{E1}(t) + n(t) \quad (2.1)$$

where $n(t)$ is the AWGN with two-sided power spectral density equal to N_0 , f_e is the frequency error, and ϕ is the unknown phase. In the following, the analysis will be conducted for the Galileo OS signals, in particular for the pilot code present in

the E1-C channel. As in all digital systems, the first operations to be performed are: Automatic Gain Control (AGC), Analog-to-Digital Converter (ADC), filtering and sampling. In the following, for the sake of simplicity, the effects of the AGC and the ADC have been neglected. It is worthwhile noting that these blocks have an important consequences on the acquisition results, but this problem is not the focus of the study. Thus, considering the signal model of (1.8)-(1.9), two filtering options are available. The first foresees filtering matched to $\text{rect}_{T_c}(\cdot)$ followed by conventional BOC demodulation, the second jointly performs the two operations by employing a filter matched to $p_{\text{BOC}}(\cdot)$. Notably, because only linear processing is involved, this two approaches are equivalent, although the second leads to a simpler analytical model, and will be considered in the following. Accordingly, sampling at $t_h = (h + \Delta)T_c + \delta$, being $h \in \mathbb{Z}$, Δ the integer timing misalignment between the transmitted signal and the locally generated replica ($\Delta \in \mathbb{Z}$), and δ the fractional timing error ($\delta \in [-T_c/2, T_c/2]$), the h -th sample can be expressed as

$$r_h = \sqrt{\frac{E_s}{2}} e^{j[2\pi f_e(hT_c + \delta) + \varphi]} \cdot \left(\sum_{i=-\infty}^{+\infty} c_{B,|i|_N} d_{[i]_N} R_{\text{BOC}}((h - i + \Delta)T_c + \delta) - \sum_{i=-\infty}^{+\infty} c_{C,|i|_N} R_{\text{BOC}}((h - i + \Delta)T_c + \delta) \right) + \eta_h \quad (2.2)$$

where R_{BOC} is the autocorrelation function of the BOC waveform, $\varphi = \phi + 2\pi f_e \Delta$, and $\eta_h = \eta_h^p + j\eta_h^q$ is the noise component at the output of the matched filter, where η^p and η^q results to be two zero-mean Gaussian random variables (r.v.'s) with the same variance $\sigma_n^2 = \frac{N_0}{2}$.

The integer displacement Δ discriminates the correct alignment hypothesis H_1 , (corresponding to the condition $\Delta = 0$) from the out-of-sync hypothesis H_0 ($\Delta \neq 0$). Differently, the presence of the fractional timing displacement δ results in an attenuation of the useful energy and in the introduction of an additional disturbance component given by the inter-symbol interference (ISI). In particular, the attenuation introduced on the useful signal can be dramatic also in the presence of limited values of δ . In fact, the autocorrelation of the BOC pulse waveform function, $R_{\text{BOC}}(\delta)$, shown in Figure 1.4 here reported for the sake of simplicity, decreases rapidly and becomes equal to zero for $|\delta| = T_c/3$. On the other hand, observing the autocorrelation function, it can be noted that the presence of a secondary peak in $\frac{T_c}{2}$ may cause serious problems both in the acquisition both in the tracking stage. In fact

the tracking block can lock onto the secondary peak instead of the main peak [30]. For this reason, in the last few years, many detectors have been proposed in order to achieve an unambiguous tracking, for example the ASPeCT detector [40] [41].

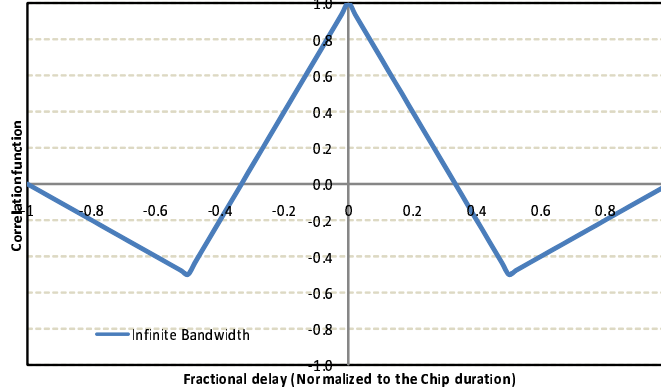


Figure 2.1: BOC autocorrelation function

By noting that $R_{\text{BOC}}(\tau) = 0$ for $|\tau| \geq T_c$, Equation (2.2) can be simplified as:

$$\begin{aligned}
 r_h = & \sqrt{\frac{E_s}{2}} e^{j[2\pi f_s((h+\Delta)T_c+\delta)+\varphi]} \\
 & [(c_{B,|h+\Delta|_N} d_{|h+\Delta|_N} - c_{C,|h+\Delta|_N}) R_{\text{BOC}}(\delta) + \\
 & (c_{B,|h+\Delta+1|_N} d_{|h+\Delta+1|_N} - c_{C,|h+\Delta+1|_N}) R_{\text{BOC}}(\delta - T_c)] + \eta_h \quad (2.3)
 \end{aligned}$$

The impact of the very particular shape of $R_{\text{BOC}}(\delta)$ on detection performance is detailed in the following sections.

2.1.1 Non Coherent Post Detection Integration for BOC Modulated Signals

The purpose of acquisition is to identify all satellites visible to a certain user. If a satellite is visible, the acquisition must determine the corresponding frequency and code phase, which represents the time alignment of the code in the block of data under evaluation. The frequency of the signal from a specific satellite can differ from its nominal value, since the signals are affected by the relative motion between the satellite and the user, causing a Doppler effect, and from the oscillators mismatch.

Thus, for each satellite, considering a discretization of the timing uncertainty domain in time slots, and of the frequency uncertainty domain in frequency bins, the acquisition search space can be seen as a two dimensional matrix which has

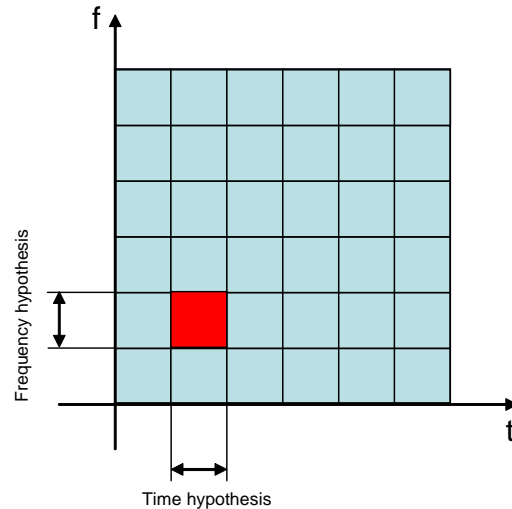


Figure 2.2: Uncertainty region discretization in time and frequency domains

to be scanned in order to perform acquisition tests, as shown in Figure 2.2. A test "cell" is defined as the combination of a frequency bin and a time slot. The serial search strategy consists of consecutive acquisition tests performed by a single correlation scheme. The parallel acquisition scheme simultaneously tests all possible code phases, enabling a significant reduction of the acquisition time at the cost of increased complexity.

A very efficient approach to perform the acquisition scanning all the code phases in parallel is based on the principle that the circular convolution of two signals in the time domain can be seen, in frequency, as the product of the Fourier transforms of those signals [42]. Although this algorithm has been widely used thanks to its very good performance-complexity trade-off, in this section, a serial search approach is considered, in order to maintain low the code acquisition complexity.

As detailed before, the hierarchical structure of the pilot channel in E1 band is exploited in order to reduce the code acquisition complexity, splitting the overall code acquisition into the synchronization with the primary code only, followed by the synchronization with the secondary code, and allowing for reducing the number of hypotheses in the uncertainty region from 102300 to $4092 + 25$.

Thus, the samples r_h at the output of the p_{BOC} matched filter are processed by the Non-Coherent Post Detection Integration (NCPDI) detector, depicted in Figure 5.5. In order to mitigate the effects of the phase rotation, the basic idea of PDI detectors is to perform coherent accumulation over a sequence segment of length

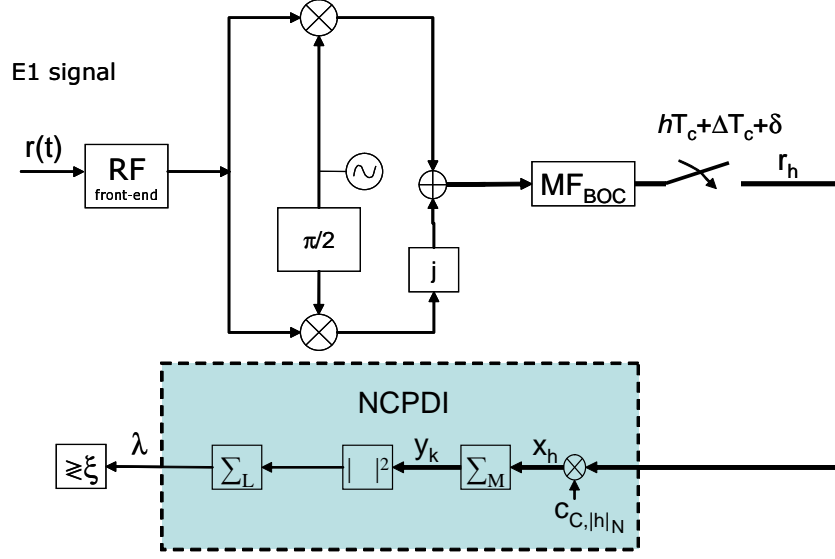


Figure 2.3: NCPDI block diagram

$M \leq N$, followed by a second integration phase over L samples after a non linear processing. The coherent integration M and the PDI length L have to be optimized depending on the maximum frequency error f_e affecting the received signal under the constraint $M \cdot L \leq N$. Different PDI options have been proposed in the literature [43][44][45] and in the following chapters will be analyzed more in details. In this chapter, NCPDI has been selected because it provides a good performance/complexity trade-off in the scenario under evaluation and is analytically treatable.

By multiplying r_h for the locally generated code sequence chips $c_{C,|h|_N}$, five terms can be identified in the resulting symbol x_h :

$$x_h = \sqrt{\frac{E_s}{2}} e^{j[2\pi f_e(hT_c + \delta) + \varphi]}.$$

$$[c_{C,|h|_N} c_{B,|h+\Delta|_N} d_{[h+\Delta]_N} R_{\text{BOC}}(\delta) + \quad (2.4a)$$

$$- c_{C,|h|_N} c_{C,|h+\Delta|_N} R_{\text{BOC}}(\delta) + \quad (2.4b)$$

$$+ c_{C,|h|_N} c_{B,|h+\Delta+1|_N} d_{[h+\Delta+1]_N} R_{\text{BOC}}(\delta - T_c) + \quad (2.4c)$$

$$- c_{C,|h|_N} c_{C,|h+\Delta+1|_N} R_{\text{BOC}}(\delta - T_c)] + \quad (2.4d)$$

$$+ \eta_h c_{C,|h|_N} \quad (2.4e)$$

Under the H_1 hypothesis ($\Delta = 0$), the sample x_h is composed by a useful deterministic part (2.4b), three i.i.d. binary ± 1 valued random variables, (2.4a), (2.4c)

and (2.4d), and the noise component, (2.4e), which is still a Gaussian random variable. As a consequence, it is difficult to express the p.d.f. of x_h in a tractable form. However, for sufficiently large values of the coherent accumulation M , it is possible to invoke the central limit theorem to model the resulting symbols $y_k = \sum_{h=kM}^{(k+1)M-1} x_h$ as Gaussian random variables with mean and variance given by

$$\mu_{y|H_1} = \sqrt{\frac{E_s}{2}} M R_{\text{BOC}}(\delta) \cdot \text{sinc}(\Delta_f M) \quad (2.5)$$

$$\sigma_{y|H_1}^2 = M\sigma_n^2 + \frac{ME_s}{2} R_{\text{BOC}}^2(\delta) \text{sinc}^2(\Delta_f M) + ME_s R_{\text{BOC}}^2(\delta - T_c) \text{sinc}^2(\Delta_f M) \quad (2.6)$$

where $\Delta_f = f_e T_c$ is the the frequency offset normalized to the chip rate.

On the other hand, under H_0 ($\Delta \neq 0$), there are no deterministic components in the sample x_h , so that the symbols y_k have a Gaussian distribution with zero mean and variance

$$\sigma_{y|H_0}^2 = M\sigma_n^2 + ME_s R_{\text{BOC}}^2(\delta) \text{sinc}^2(\Delta_f M) + ME_s R_{\text{BOC}}^2(\delta - T_c) \text{sinc}^2(\Delta_f M) \quad (2.7)$$

Finally, the decision variable λ is obtained as

$$\lambda = \sum_{k=0}^{L-1} |y_k|^2 \quad (2.8)$$

and results to be a χ^2 random variable with $2L$ degrees of freedom, which is non-central under H_1 and central under H_0 as

$$\lambda \sim \begin{cases} \chi_{2L}^2(0, \sigma_{y|H_0}^2) & \text{under } H_0 \\ \chi_{2L}^2(s_{\text{BOC}}^2, \sigma_{y|H_1}^2) & \text{under } H_1 \end{cases} \quad (2.9)$$

where it is intended that the variance indicated in the equation above is referred to the composing Gaussian variables, and

$$s_{\text{BOC}}^2 = \frac{E_s}{2} LM^2 R_{\text{BOC}}^2(\delta) \cdot \text{sinc}^2(\Delta_f M) \quad (2.10)$$

Thus, the *missed detection probability* (P_{md}) and the *false alarm probability* (P_{fa}) can be expressed as [43][46]:

$$P_{md}^{\text{NCPDI}} = 1 - Q_L \left(\frac{s_{\text{BOC}}}{\sigma_{y|H_1}}, \frac{\sqrt{\gamma}}{\sigma_{y|H_1}} \right) \quad (2.11)$$

$$P_{fa}^{\text{NCPDI}} = e^{-\frac{\gamma}{2\sigma_{y|H_0}^2}} \sum_{k=0}^{L-1} \frac{1}{k!} \left(\frac{\gamma}{2\sigma_{y|H_0}^2} \right)^k \quad (2.12)$$

where γ is the decision threshold, to be normalized according to the CFAR (Constant False Alarm Rate) criterion [47], and $Q_n(\alpha, \beta)$ is the generalized Marcum Q-function, defined as

$$Q_n(\alpha, \beta) = \frac{1}{\alpha^{n-1}} \int_{\beta}^{\infty} x^n \exp -(x^2 + \alpha^2)/2I_{n-1}(\alpha x) dx \quad (2.13)$$

where $I_m(x)$ is a modified Bessel function of the first kind. Note that these probabilities refer to the single cell test, and they are not valid for the whole frequency-code delay search space.

While $\sigma_{y|H_1}^2$ and $\sigma_{y|H_0}^2$ are practically independent of δ as usual in Spread Spectrum scenarios, where the noise component is dominant, the non-centrality parameter s_{BOC}^2 strongly depends on δ , directly affecting P_{md}^{NCPDI} . In order to evaluate the effects of non-ideal sampling on NCPDI performance, a set of Receiver Operating Characteristics (ROCs), i.e. P_{md} vs. P_{fa} , is reported in Figure 2.4 for $\delta \in [0, T_c/2]$. A typical scenario for outdoor positioning in the Galileo system has been considered, with $C/N_0 = 35\text{dBHz}$, corresponding to an energy per chip versus noise power density $E_c/N_0 = -25\text{dB}$ for a chip rate equal to 1.023MHz , where E_c is the energy per chip. Note a fixed frequency error $f_e = 100\text{Hz}$ is considered. This frequency error can be seen as the resulting frequency error affecting the acquisition if a certain parallelism in the frequency is adopted. It is worthwhile noting that for a rather limited frequency error, as in the case under consideration, a large value of the coherent integration length provides the best performance, so that $M = 1023$ and $L = 4$ has been selected. Note that analytical and simulated curves are reported in the figure, with a perfect overlapping that validates the analytical model presented above: the Monte Carlo simulation has been performed with a number of iterations equal to 10^4 , and an infinite bandwidth filter.

As expected, performance follows the pattern of the BOC autocorrelation function, gradually getting worse by increasing δ in the interval $[0, \frac{T_c}{3}]$, then going better for $\delta \in [\frac{T_c}{3}, \frac{T_c}{2}]$, and, at last, holding out to the worst performance.

Therefore, the presence of BOC modulation makes the traditional code acquisition approach ineffective in the presence of non-ideal sampling, if no countermeasures are taken. Two possible alternatives can be adopted. Firstly, a higher oversampling can be applied in order to limit the autocorrelation function of the BOC waveform in an interval without zero values. Although this approach is widely used in the GNSS context, since they are based on the time alignment of the received signal and the local replica, it results in a very large complexity increase. Thus, in some peculiar situations, like SDR (Software Defined Radio) architectures, in order to limit com-

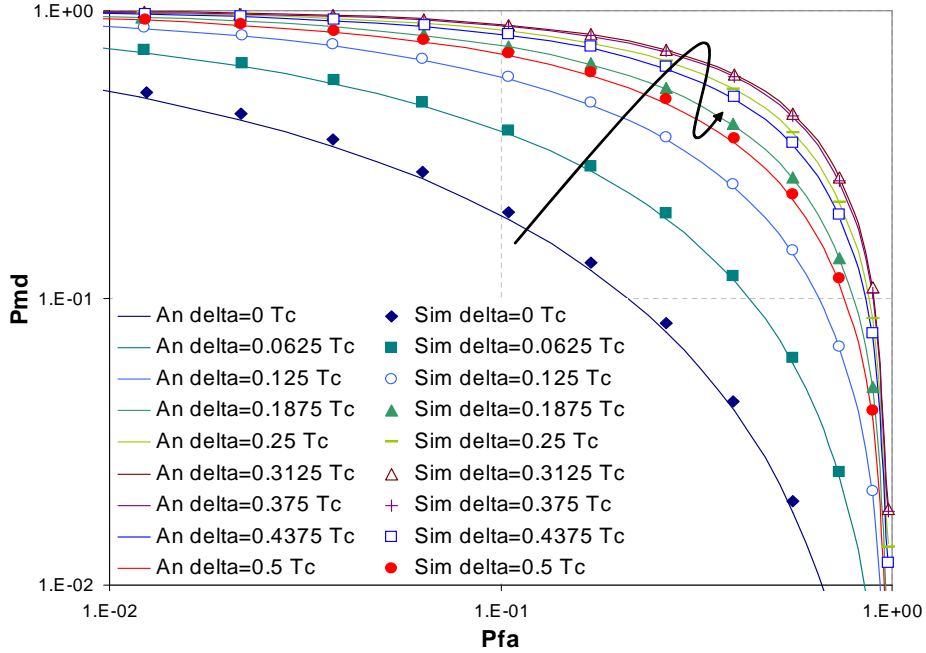


Figure 2.4: ROC NCPDI(1023,4) Galileo $E1$ signal $C/N_0 = 35\text{dBHz}$

plexity, another countermeasure can be adopted: an ad-hoc scheme on purposely designed to cope with the BOC autocorrelation. This is the main motivation of Quadribranch detector, illustrated in the next section.

2.2 The Quadribranch Detector

The two main impairments that have to be considered for a robust design of a code synchronization scheme are frequency errors, due to oscillator mismatches and Doppler effects, and non-ideal sampling, which introduces useful energy degradation and inter-chip interference when discretizing the uncertainty region. The presence of frequency errors can be fruitfully counteracted by adopting a detector based on partial correlations, like described before, and upon Post Detection Integration (PDI) [43][47][48]. Differently, the effects of non ideal sampling are typically counteracted by considering two or more hypotheses per symbol (oversampling). This is usually a good solution because it allows for reducing the maximum sampling fractional misalignment at the cost of an increased complexity, due to the fact that the uncertainty region is explored with smaller steps and a large number of tests has to be computed. Unfortunately, the BOC (Binary Offset Carrier) modulation can lead

to unacceptable performance still with low oversampling. Exactly to overcome this problem, a possible countermeasure to cope with degradation due to timing error is to shape the pulse autocorrelation function in order to minimize its fluctuations due to the timing misalignment. In this section a novel approach, identified as Quadribranch detector, is proposed. The main idea is to exploit in the receiver both BOC and BOCc (BOC cosine) pulse waveforms. In this way, it is possible to extract larger useful signal energy in the presence of fractional timing misalignments, at the cost of a performance worsening when sampling in the ideal instant. Analytical and numerical results show that this approach allows for considering a single hypothesis per chip, limiting complexity and improving average performance.

The resulting Quadribranch block diagram is shown in Figure 2.5, where two parallel complex branches project the received signal over p_{BOC} and p_{BOCc} , respectively. Note that, after the two different matched filtering and sampling operations, the detection block diagram in each branch is a conventional NCPDI as described above. It is worthwhile noting that BOC and BOCc waveforms are orthogonal

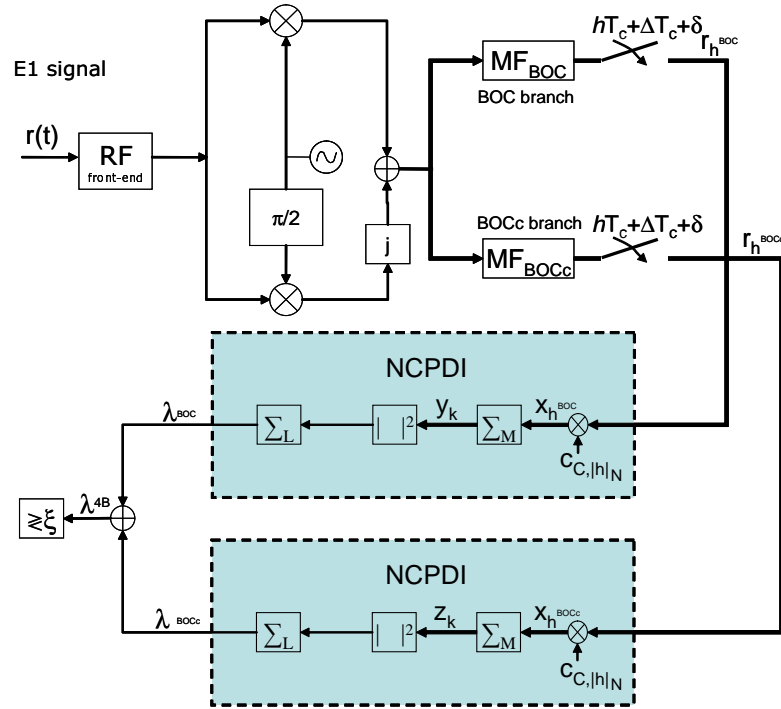


Figure 2.5: Quadribranch detector Block Diagram

when they are perfectly aligned, while they present a residual correlation otherwise, as shown in Figure 2.6, where the cross correlation R_{BOCc} between p_{BOC} and

$p_{\text{BOC}c}$ is reported. The fact that $R_{\text{BOC}c}(0) = 0$ ensures that the BOC and BOCc branches are uncorrelated and so the Gaussian random variables processed by the two Quadribranch NCPDI detectors are independent. At the same time, in the presence of timing misalignments in the received signal, the BOCc branch is able to collect useful energy mitigating the degradation experienced by the BOC branch.

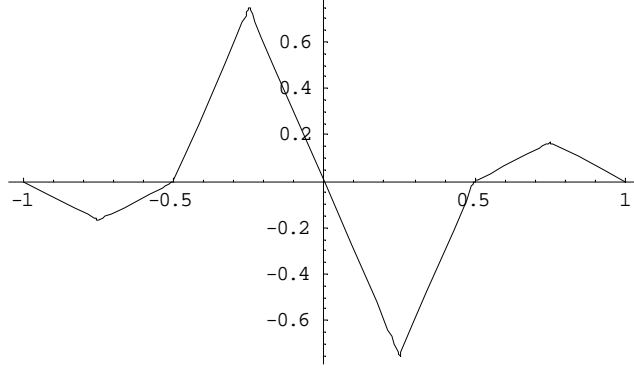


Figure 2.6: BOC and BOCc waveforms cross-correlation function

Starting from the analytical model presented in the previous section, it is possible to achieve closed form Quadribranch performance modeling each branch as a stand-alone NCPDI detector. In particular, the decision variable λ^{BOC} of the BOC branch is again described by Equation (5.22), while, $\lambda^{\text{BOC}c}$ of the BOCc branch is distributed as

$$\lambda^{\text{BOC}c} \sim \begin{cases} \chi_{2L}^2(0, \sigma_{z|H_0}^2) & \text{under } H_0 \\ \chi_{2L}^2(s_{\text{BOC}c}^2, \sigma_{z|H_1}^2) & \text{under } H_1 \end{cases} \quad (2.14)$$

where

$$\sigma_{z|H_0}^2 = M\sigma_n^2 + ME_s R_{\text{BOC}c}^2(\delta) \text{sinc}^2(\Delta_f M) + ME_s R_{\text{BOC}c}^2(\delta - T_c) \text{sinc}^2(\Delta_f M) \quad (2.15)$$

$$\sigma_{z|H_1}^2 = M\sigma_n^2 + M \frac{E_s}{2} R_{\text{BOC}c}^2(\delta) \text{sinc}^2(\Delta_f M) + ME_s R_{\text{BOC}c}^2(\delta - T_c) \text{sinc}^2(\Delta_f M) \quad (2.16)$$

$$s_{\text{BOC}c}^2 = \frac{E_s}{2} LM^2 R_{\text{BOC}c}^2(\delta) \cdot \text{sinc}^2(\Delta_f M) \quad (2.17)$$

Formally, $\sigma_{y|H_1}^2 \neq \sigma_{z|H_1}^2$ and $\sigma_{y|H_0}^2 \neq \sigma_{z|H_0}^2$, thus the decision variable λ^{4B} for the Quadribranch detector, given by

$$\lambda^{4B} = \lambda^{\text{BOC}} + \lambda^{\text{BOC}c} \quad (2.18)$$

has a distribution that can be found by adopting the formula described at page 46 of [49]. However, in the typical SNR scenarios of the Galileo system, $\sigma_{y|H_0}^2 \simeq$

$\sigma_{z|H_0}^2$ and $\sigma_{y|H_1}^2 \simeq \sigma_{z|H_1}^2$, because they are dominated by the noise component. Consequently, the decision variable λ^{4B} of the Quadribranch in the H_1 hypothesis, can be approximated by a χ^2 random variable with $4L$ degrees of freedom, as

$$\lambda^{4B} \sim \begin{cases} \chi_{4L}^2(0, \sigma_{4B|H_0}^2) & \text{under } H_0 \\ \chi_{4L}^2(s_{4B}^2, \sigma_{4B|H_1}^2) & \text{under } H_1 \end{cases} \quad (2.19)$$

where $\sigma_{4B|H_0}^2 = \sigma_{y|H_0}^2$, $\sigma_{4B|H_1}^2 = \sigma_{y|H_1}^2$, and

$$s_{4B}^2 = \frac{E_s}{2} LM^2 (R_{\text{BOC}}^2(\delta) + R_{\text{BOCc}}^2(\delta)) \cdot \text{sinc}^2(\Delta_f M) \quad (2.20)$$

Accordingly, the Quadribranch detection probabilities can be expressed as

$$P_{md}^{AB} = 1 - Q_L \left(\frac{s_{4B}}{\sigma_{4B|H_1}}, \frac{\sqrt{\gamma}}{\sigma_{4B|H_1}} \right) \quad (2.21)$$

$$P_{fa}^{AB} = e^{-\frac{\gamma}{2\sigma_{4B|H_0}^2}} \sum_{k=0}^{2L-1} \frac{1}{k!} \left(\frac{\gamma}{2\sigma_{4B|H_0}^2} \right)^k \quad (2.22)$$

The model of Equation (2.21) and Equation (2.22) is validated in Figure 2.7, where analytical and simulated ROC are reported for $E_s/N_0 = -25\text{dB}$, a fixed frequency error $f_e = 100\text{Hz}$, $\delta \in [-T_c/2, T_c/2]$, $M = 1023$, $L = 4$. Observing

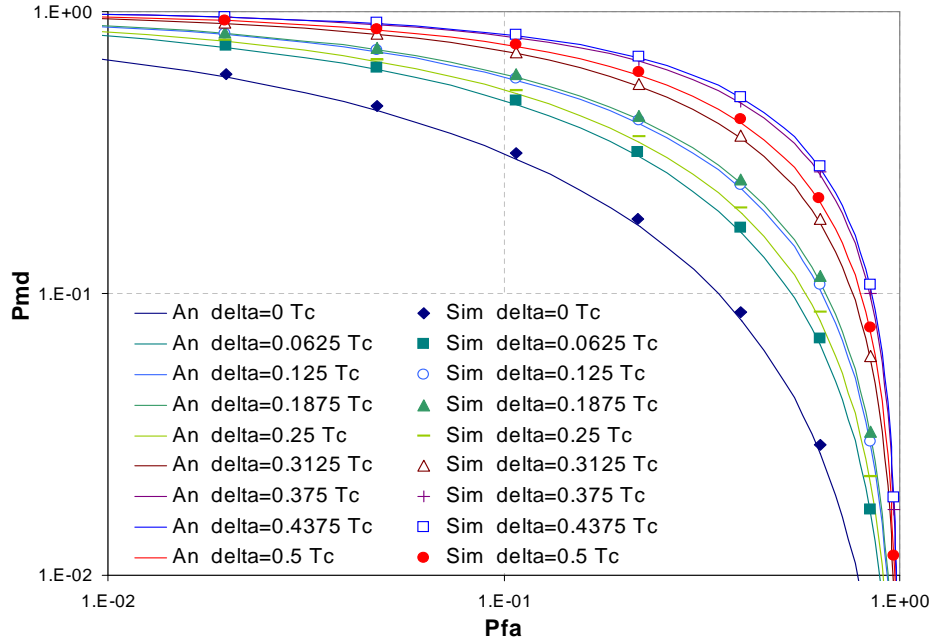


Figure 2.7: Quadribranch Performance with Galileo $E1$ signal

the figure, besides confirming the good match between simulations and analysis, it is possible to see that Quadribranch performance is still affected by non ideal sampling, but the negative effects of BOC autocorrelation are mitigated by the presence of the second branch. As for the model discussed before, also in this case, the Monte Carlo simulation has been performed with a number of iterations equal to 10^4 , and an infinite bandwidth filter. A detailed performance comparison with the classic NCPDI approach is detailed in the following.

2.2.1 Performance Evaluation

To provide a clear and immediate comparison between the classic NCPDI detector and Quadribranch, it is useful to define the ratio ρ between the decision variable power under H_1 and under H_0 . Being both NCPDI and Quadribranch decision variables distributed as χ^2 r.v.'s, it holds

$$\rho = \frac{E[\lambda^2 | H_1]}{E[\lambda^2 | H_0]} = 1 + \frac{s^2}{n\sigma_{H_0}^2} \left(2 + \frac{s^2}{(2+n)\sigma_{H_0}^2} \right) \quad (2.23)$$

where n is the number of degrees of freedom, s^2 the non-centrality parameter, and $\sigma_{H_1}^2 \simeq \sigma_{H_0}^2$ has been assumed for simplicity being true in typical SNR scenarios for the Galileo system. Notably, ρ can be seen as a signal to noise ratio measure for the decision variable λ . Applying Equation (2.23) to NCPDI and Quadribranch, it follows

$$\rho^{NCPDI} = 1 + \frac{E_s M^2 R_{\text{BOC}}^2(\delta) \cdot \text{sinc}^2(\Delta_f M)}{4\sigma_{y|H_0}^2} \left(2 + \frac{E_s M^2 R_{\text{BOC}}^2(\delta) L \cdot \text{sinc}^2(\Delta_f M)}{2(2L+2)\sigma_{y|H_0}^2} \right) \quad (2.24)$$

$$\rho^{4B} = 1 + \frac{E_s M^2 (R_{\text{BOC}}^2(\delta) + R_{\text{BOCc}}^2(\delta)) \cdot \text{sinc}^2(\Delta_f M)}{8\sigma_{4B|H_0}^2} \left(\frac{E_s M^2 (R_{\text{BOC}}^2(\delta) + R_{\text{BOCc}}^2(\delta)) L \cdot \text{sinc}^2(\Delta_f M)}{2(4L+2)\sigma_{4B|H_0}^2} \right) \quad (2.25)$$

Figure 2.14 shows the comparison between ρ^{NCPDI} and ρ^{4B} for $\delta \in [-T_c, T_c]$, $E_s/N_0 = -25\text{dB}$, $f_e = 100\text{Hz}$, $M = 1023$ and $L = 4$. Note that there are interesting trade-offs between NCPDI and Quadribranch. When $\delta \approx 0$, NCPDI outperforms Quadribranch, while the opposite behavior is present for larger δ . In particular, in the interval around $\delta = T_c/3$, where $R_{\text{BOC}} \approx 0$, it results $\rho^{NCPDI} = 1$ (equal signal power under both H_0 and H_1 with very poor detection performance), while ρ^{4B} is still acceptable. Note that $|\delta| > T_c/2$ refers to H_0 hypotheses and are out of interest.

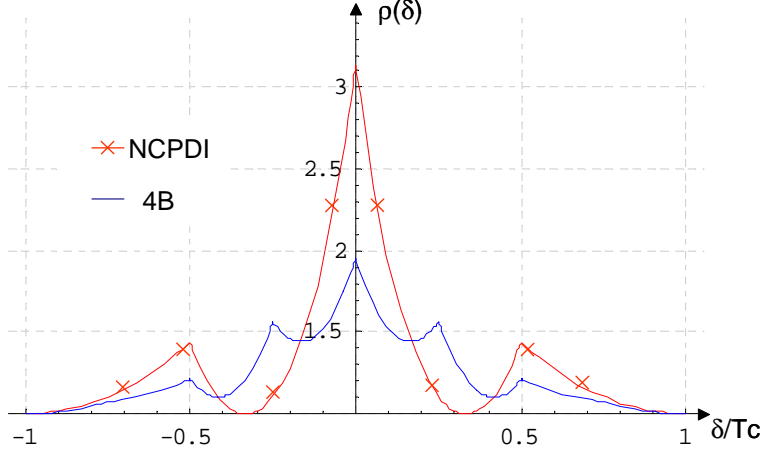


Figure 2.8: H_1/H_0 signal power ratio ρ for Quadribranch and NCPDI detectors vs. fractional delay δ

The same conclusions drawn observing the shape of $\rho(\delta)$ can be found also by observing the detection performance. Considering the simulation parameters used above, Figure 2.9 shows that NCPDI is the best solution in the ideal case $\delta = 0$, because the BOCc branch of the Quadribranch collects noise only in this condition. Differently, with $\delta = T_c/4$ Quadribranch is able to provide a considerable performance improvement because R_{BOCc} assumes the largest value in this case. Note that $\delta = T_c/4$ is the worst case scenario for NCPDI with oversampling factor equal to 2. The average detection performance considering δ as a uniform random variable in $[-T_c/2, T_c/2]$ is shown in Figure 2.10. It can be seen that Quadribranch outperforms the classical NCPDI solution, because the losses introduced in the ideal sampling case is largely compensated by the gain introduced when $\delta \approx T_c/3$.

The performance improvement in terms of detection probabilities directly translate in improvement in terms of mean acquisition time. For example, considering the single dwell procedure (1TC) [50], the mean acquisition time (MAT) \overline{T}_A can be expressed as

$$\overline{T}_A = \frac{1}{P_D} \left\{ \frac{T_s}{2} \left[1 + \frac{Q}{2}(2 - P_D) \right] + T_p \frac{Q}{2} P_{fa}(2 - P_D) \right\} \quad (2.26)$$

where P_D is the overall correct detection probability, T_s the sample time, Q the number of H_0 cells and T_p the penalty time, assumed equal to 0.8 milliseconds. The resulting MAT, calculated semi-analytically, is reported in Figure 3.7 for NCPDI and Quadribranch with oversampling $l = 1$, and for NCPDI with $l = 2$. The ideal case $\delta = 0$ is reported for the sake of completeness, and, obviously, it can be seen that

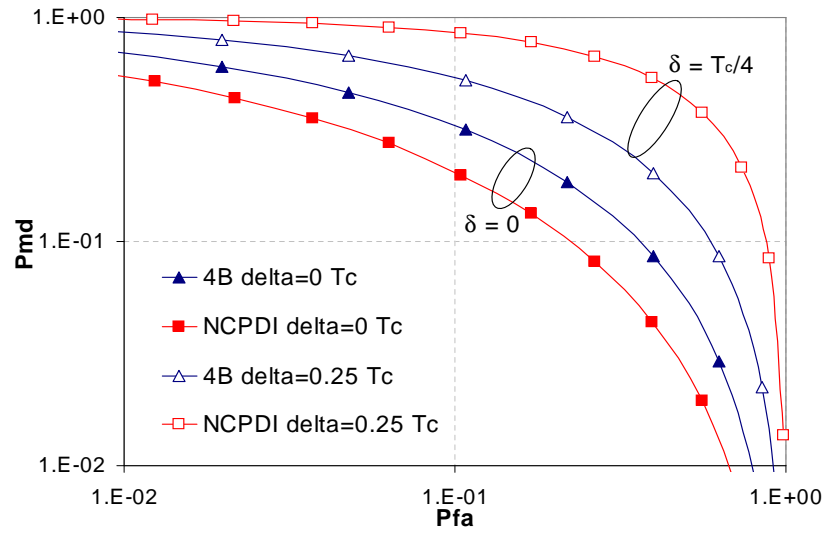


Figure 2.9: Performance Comparison with $\delta = 0$ and $\delta = T_c/4$

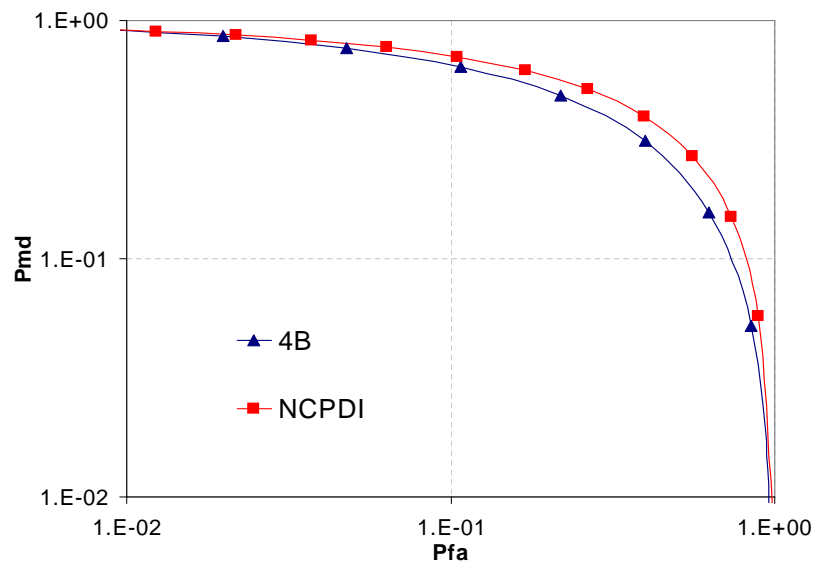


Figure 2.10: Average Performance Comparison

NCPDI with $l = 1$ guarantees the minimum mean acquisition time. Differently, the comparison of the worst case, that drives the code acquisition block design, clearly shows that Quadribranch, with $\text{MAT} = 11.56$ s, provides optimal performance, even with respect to NCPDI with $l = 2$, which provides $\text{MAT} = 14.69$ s.

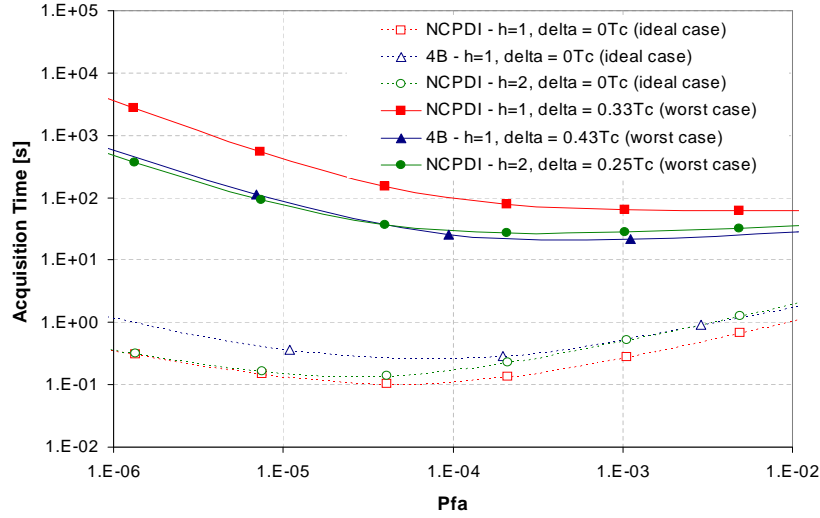


Figure 2.11: Mean Acquisition Time Comparison

2.2.2 Comparison with the ASPeCT Detector

In this section, the Quadribranch detector is compared with another state-of-the-art solution, identified as ASPeCT [41], which has been proposed in order to eliminate the effect of the secondary peaks of the BOC autocorrelation function.

The ASPeCT detector was previously identified with the name of BOC/PRN [40] since, in order to guarantee an unambiguous tracking of the BOC modulated signals, it tries to shape the autocorrelation function and to eliminate the secondary peaks thanks to a new correlation function, obtained combining the correlation with the BOC waveform and the correlation with a rectangular shape filter (PRN), and subtracting the partial outputs. Note that the resulting function presents only one peak.

As shown in Figure 2.12, the decision variable $\lambda^{BOC/PRN}$ is obtained

$$\lambda^{BOC/PRN} = \lambda^{BOC} - \lambda^{PRN} = \sum_{k=0}^{L-1} (|y_k|^2 - |z_k|^2) \quad (2.27)$$

where λ^{BOC} is the decision variable calculated in (3.3), and λ^{PRN} represents the

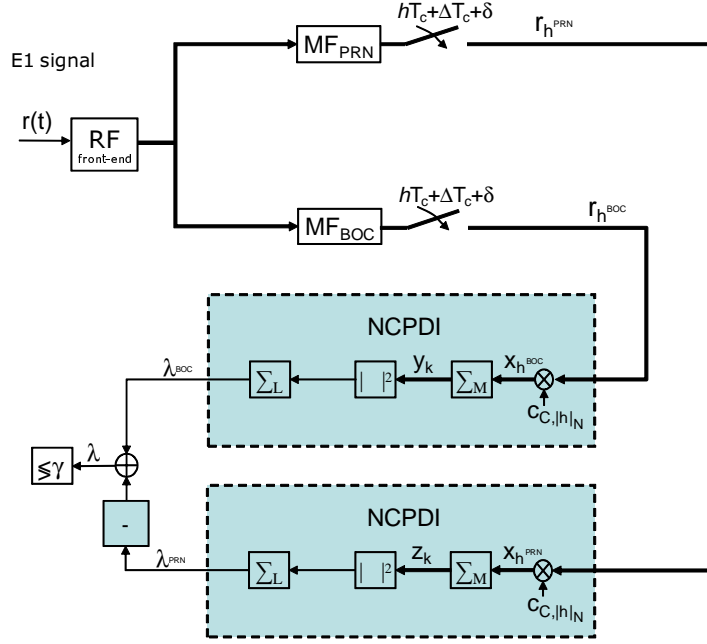


Figure 2.12: BOC/PRN Block Diagram

decision variable obtained by the NCPDI with the correlation obtained with the rectangular shape filter. Note that also λ^{PRN} can be modeled as a χ^2 random variable with $2L$ degrees of freedom, which is non-central under H_1 and central under H_0 . Under the H_0 hypotheses, the resulting decision variable $\lambda^{BOC/PRN}$ is a difference between two central and independent chi square r.v. Being $\sigma_{y|H_0} \approx \sigma_{y^{PRN}|H_0}$, according to [49], the resulting c.d.f. can be expressed in closed form as:

$$P_{fa}^{BOC/PRN} = e^{-\frac{\gamma}{2\sigma_{y|H_0}^2}} \frac{1}{2^{L(L-1)!}} \cdot \sum_{i=0}^{L-1} \sum_{l=0}^i \frac{(2(L-1)-i)!}{(i-l)!(L-1-i)!} \left(\frac{1}{2}\right)^{L-i-l} \left(\frac{\gamma}{2\sigma_{y|H_0}^2}\right)^{i-l} \quad (2.28)$$

Under the H_1 hypothesis, the difference between two independent non-central chi square can not be calculated in an equally tractable form. In the following, for the evaluation of the performance, the analytical expression of the $P_{fa}^{BOC/PRN}$, which has been validated through numerical results, has been used to reduce the computational effort, while the P_{md} has been calculated through simulations. Figure 2.13 also shows the normalized squared correlation obtained by the BOC/PRN detector, in comparison with the conventional NCPDI and the Quadribranch detector.

This detector, proposed with an Early-Minus-Late Power (EMLP) matched to

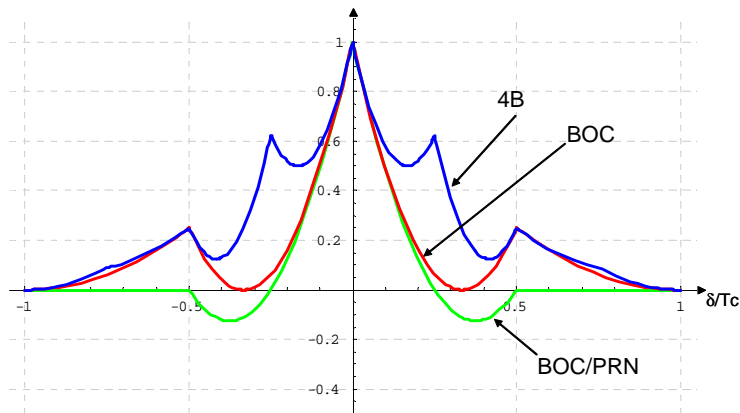


Figure 2.13: Normalized Squared Correlation functions

the new correlation function, is efficient for code tracking, but at the same time presents in the acquisition stage a performance similar, and in some cases worse, than the classical NCPDI.

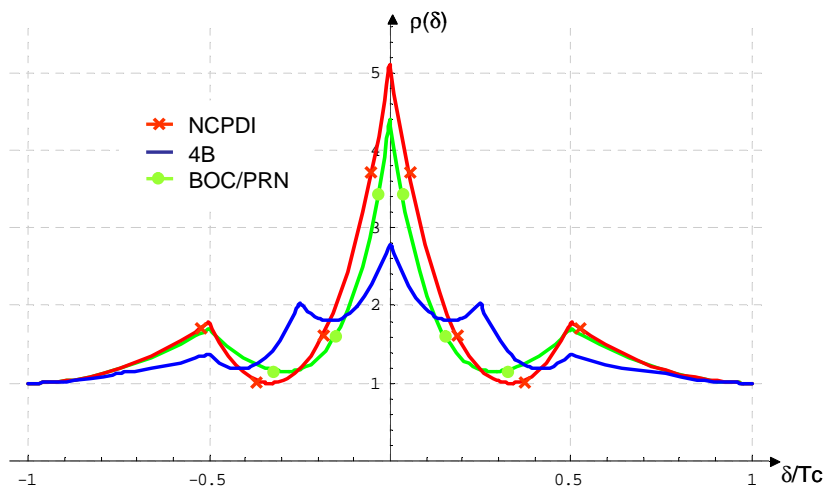
Figure 2.14: H_1/H_0 signal power ratio ρ for BOC/PRN, NCPDI, and Quadribranch detectors vs. fractional delay δ

Figure 2.14 shows that the signal to noise ratio affected by the decision variable in the BOC/PRN detector, $\rho^{BOC/PRN}$, presents a behavior similar to ρ^{NCPDI} , with equal signal power under both H_0 and H_1 in the interval around $\delta = T_c/3$.

The same behavior can be noted by observing Figures 2.15 and 2.16. Figure 2.15 shows the comparison between the three detectors with $C/N_0 = 35\text{dBHz}$ and a frequency error $f_e = 100\text{Hz}$, $M = 2046$ and $L = 2$, considering the average detection performance with δ expressed as a uniform random variable in $[-T_c/2, T_c/2]$, and

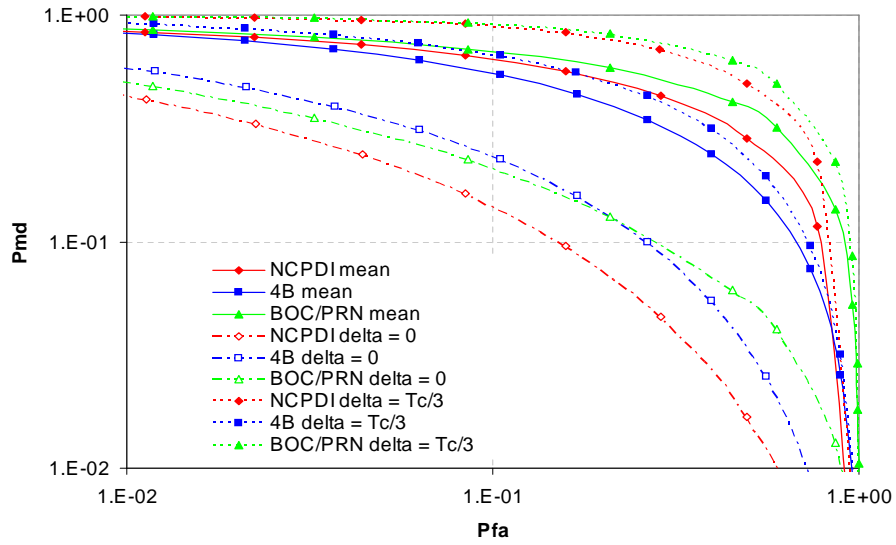


Figure 2.15: Performance comparison for BOC/PRN, conventional NCPDI, and Quadribranch: mean δ , $\delta = 0$, $\delta = \frac{T_c}{3}$

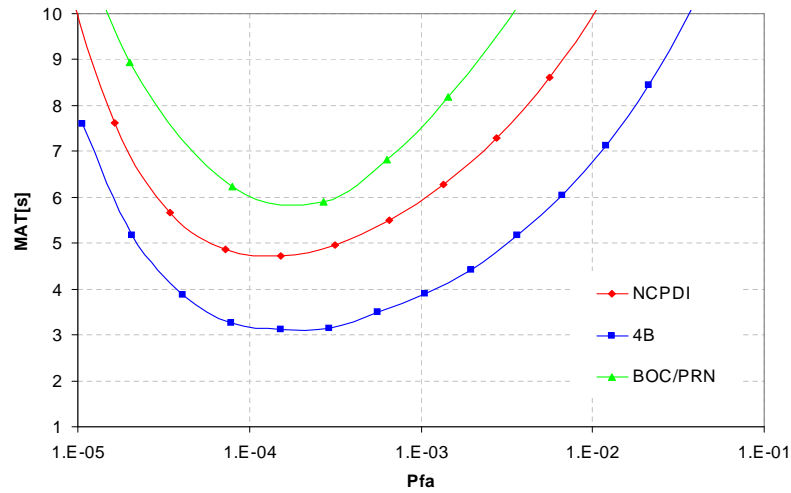


Figure 2.16: Average Mean Acquisition Time Comparison

also in two representative scenarios, of the ideal case $\delta = 0$, and with $\delta = \frac{T_c}{3}$, which is the worst case for both NCPDI and BOC/PRN detectors.

From the comparison of the mean performance, it can be seen that Quadribranch outperforms both the classical approach and the BOC/PRN, because the loss suffered for $\delta = 0$ is more than compensated by the gain introduced when $\delta \approx T_c/3$.

Finally, the performance improvement in terms of detection probabilities directly translates into improvements in terms of mean acquisition time, considering in this case the penalty time equal to 16ms for all the detectors.

Figure 2.16 shows the comparison between the three detectors according to the average MAT, calculated considering δ as a uniform random variable in $[-T_c/2, T_c/2]$. Note that the Quadribranch detector guarantees the minimum MAT, with a gain of about 33% with respect of the NCPDI, and 47% with respect of the BOC/PRN.

Note that a receiver, in order to guarantee the best performance both in acquisition and tracking, should be able to adaptively reconfigure the receiver as a Quadribranch for code acquisition and a BOC/PRN detector for tracking.

2.3 Robust Detection of BOC Modulated Signals: Conclusions

In this chapter, the analysis of code acquisition for BOC modulated signals is reported. An approach based on the combining of the correlation with the BOC and the BOCc modulated sequence has been proposed in order to counteract the effects of non ideal sampling with Galileo signals. Analytical and simulated results show that the proposed detection scheme, referred to as the Quadribranch detector, is able to provide a considerable performance improvement in the presence of fractional misalignment at the cost of a slight performance worsening in the ideal condition. On average, it is possible to obtain a better performance with a single sample per chip, so reducing the mean acquisition time and the overall complexity.

3

High-Sensitivity GNSS Receivers

3.1 Soft Combining for Improved Sensitivity GNSS Code Acquisition

In order to efficiently respond to mobility demands, an ambitious aim will be to guarantee continuous outdoor and indoor location service availability. To this purpose, the main challenging problem for indoor localization is to find a technical solution able to operate at the low signal to noise ratios characteristic of these scenarios with a limited complexity, as required by mass market terminals. In this context, the most critical operation is represented by code synchronization because it becomes very harsh to distinguish the useful autocorrelation peaks from the background noise. The typical approach adopted to overcome this problem and enhance the receiver sensitivity is to integrate the received signal over a longer time period, so improving the mitigation effect against noise. This strategy can be very effective for both code acquisition and code tracking, although it requires a careful design optimization for the application to actual systems where non idealities, such as frequency errors and data transitions, have to be taken into account. In fact, long coherent integration length limits the possible dynamics of the receiver, thus managing moving indoor

receivers represent a critical issue to deal with. Moreover, another critical issue to consider derives from multipath: the problem occurs when the direct signal is weaker than the reflected ones, since the direct signal and the multipath could suffer different attenuations. Finally, the presence of a secondary code in the Galileo standard should be considered since a bit transition between two primary codes can make coherent integration ineffective.

In this following, code acquisition for the Galileo pilot signal in E1 band [29] is considered. As already mentioned in the system model, this is a hierarchical code of 102300 chips, constituted by a repetition of a 4092 chips primary code, modulated by a long duration secondary code of 25 chips. Generally, the integration over a single primary code of 4092 chips is not enough to cope with the very low SNRs, when performing the primary code synchronization. On the other hand, integration over the whole code of 102300 chips is not a viable solution, because of the large associated complexity. To overcome this problem, the adoption of a detector matched to the primary code, followed by non-coherent soft combining of a number N of its outputs is proposed in order to improve performance by enlarging the observation window and removing at the same time the secondary code uncertainty. This approach has been proved to provide good performance/complexity trade-offs for the frame synchronization in the field of communication, with respect to the acquisition of the whole concatenated sequence [51] [52].

In addition, the application of soft combining to the Galileo system is particularly interesting because it allows to exploit the hierarchical structure of the pilot sequence for code synchronization. The following results have been partially published in [3]. My contribution to this topic is the adaptation of known communication techniques to the field of navigation.

3.1.1 Soft Combining with Post Detection Integration

As discussed in the previous section, to increase the receiver sensitivity it is necessary to consider an observation window longer than 4092 chips and equal to a number N of primary codes, where N has to be optimized to meet the desired performance requirements. Considering the acquisition of the primary code only, the presence of the secondary code introduces a further uncertainty that has to be smartly counteracted.

To this aim, a non coherent soft combining strategy, as depicted in Figure 3.1, can be fruitfully introduced. The proposed detector implementation foresees the

adoption of a passive realization of the single primary code detector, able to perform a test every primary code chip duration, so minimizing the processing time. As detailed in the following, this detector performs non-coherent processing to cope with actual operating conditions. Then, a buffer of length $(N-1)4092$ is introduced before the combining summation of the N soft values and the final threshold comparator. Note that, in this case the synchronization with the secondary code is left for a second acquisition phase, reducing the overall complexity.

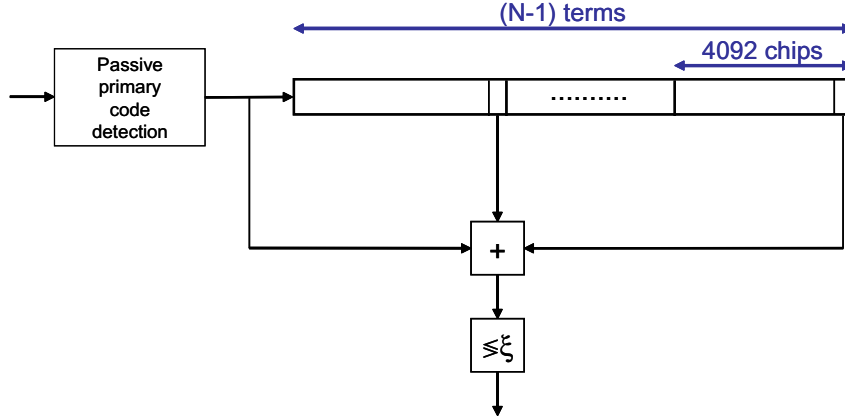


Figure 3.1: Soft combining technique block diagram

The design of the primary code detector has to be carefully optimized because the very low SNRs characteristic of all spread spectrum systems (and of indoor scenarios in particular) makes it typically unfeasible to achieve carrier recovery before code synchronization. Thus, code acquisition must be achieved taking into account the unavoidable phase and frequency uncertainty affecting the received signal. In particular, the frequency offset introduces an energy degradation, which does not allow to perform coherent correlation over the entire code period. This energy degradation can be quantified as $M\text{sinc}^2(Mf_eT_c)$ [43], being M the coherent correlation length and f_e the absolute frequency offset. Thus, for a maximum f_e affecting the system, this degradation can be alleviated by introducing a windowing technique, limiting coherent correlation over an appropriately dimensioned sub-sequence, and introducing Post Detection Integration (PDI) on the collected partial outputs to exploit the entire sequence. In the following, three different PDI detectors are considered: NCPDI (Non Coherent PDI), which pragmatically extends the energy detector solution, and whose performance have been evaluated in the previous chapter; DPDI (Differential PDI), which reduces the noise enhancement with respect to NCPDI;

and GPDI (Generalized PDI), which combines NCPDI, DPDI, and other differential terms, denoted as n -Span DPDI to improve performance at the cost of increased complexity [44][45]. The block diagrams of NCPDI, DPDI, and GPDI are reported in Figure 3.2. NCPDI, which is the simplest algorithm, can be analytically characterized, as reported in the previous section, and herein extended in a Rice fading channel.

3.1.2 NCPDI Analytical Model in a Rice Fading Channel

Considering the Galileo signal described in the previous section, the received signal in the presence of a Rice channel can be written as

$$r(t) = \rho E1(t) + n(t) \quad (3.1)$$

where $n(t)$ is the AWGN with two-sided power spectral density (PSD) equal to N_0 and ρ is the Rice fading envelope, which is assumed to be quasi-stationary and distributed according to

$$p_\rho(\rho) = 2\rho(K+1)e^{-(K+1)\rho^2-K} I_0(2\rho\sqrt{K(K+1)}) \quad (3.2)$$

where K is the Rice factor [53].

Being y_k the output of the coherent correlation block, the decision variable λ^{BOC} is

$$\lambda^{BOC} = \sum_{k=0}^{L-1} |y_k|^2 = \sum_{k=0}^{L-1} \left| \sum_{h=kM}^{(k+1)M-1} c_{C,h} r_h \right|^2 \quad (3.3)$$

Considering the Central Limit Theorem, it can be modeled as a χ^2 random variable with $2L$ degrees of freedom, which is non-central under H_1 and central under H_0 :

$$\lambda^{BOC} \sim \begin{cases} \chi_{2L}^2(0, \sigma_{y|H_0}^2) & \text{under } H_0 \\ \chi_{2L}^2(s_{BOC}^2, \sigma_{y|H_1}^2) & \text{under } H_1 \end{cases} \quad (3.4)$$

where $\sigma_{y|H_0}^2$ and $\sigma_{y|H_1}^2$ represent the variances of y_k under H_0 and H_1 , constituted by a predominant noise component and inter chip interference, neglected hereafter, and s_{BOC}^2 is defined as:

$$s_{BOC|\rho}^2 = \frac{E_s \rho^2}{2} LM^2 R_{BOC}^2(\delta) \cdot \text{sinc}^2(\Delta_f M) \quad (3.5)$$

where Δ_f is the frequency offset normalized to the chip rate ($\Delta_f = f_e T_c$), and R_{BOC} represents the BOC autocorrelation function.

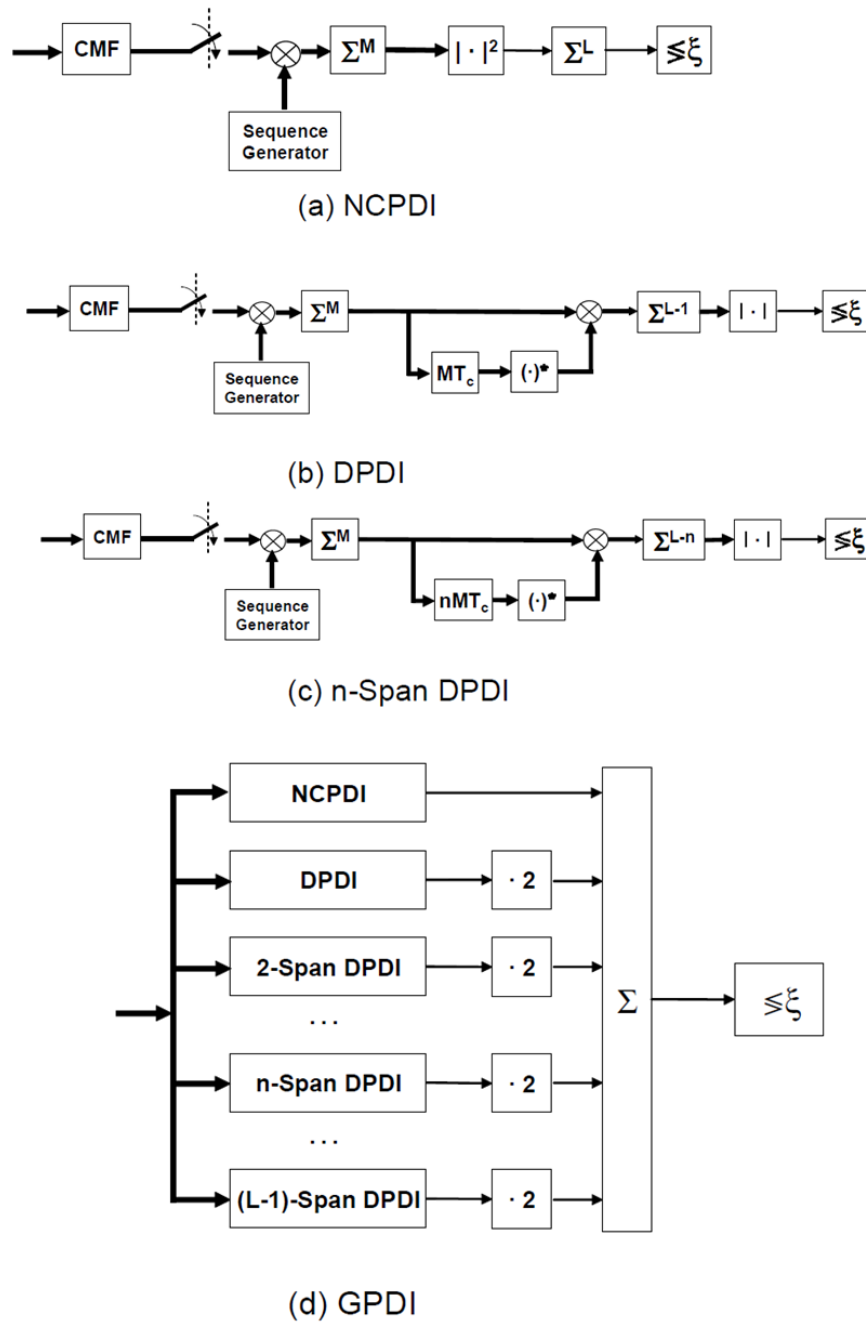


Figure 3.2: Primary code detector block diagram: (a) NCPDI, (b) DPDI, (c) n-Span DPDI, (d) GPDI

Thus, considering the number of repetitions N introduced by the soft combining technique, the *missed detection probability* and the *false alarm probability* conditioned on ρ , $P_{md|\rho}$ and $P_{fa|\rho}$, can be expressed, respectively, as [43][46]

$$P_{md|\rho}^{NCPDI} = 1 - Q_{NL} \left(\frac{s_{BOC|\rho} \cdot N}{\sigma_{y|H1}}, \frac{\sqrt{\gamma}}{\sigma_{y|H1}} \right) \quad (3.6)$$

$$P_{fa|\rho}^{NCPDI} = e^{-\frac{\gamma}{2\sigma_{y|H0}^2}} \sum_{k=0}^{LN-1} \frac{1}{k!} \left(\frac{\gamma}{2\sigma_{y|H0}^2} \right)^k \quad (3.7)$$

where γ is the decision threshold to be normalized according to the CFAR (Constant False Alarm Rate) criterion [44], and $Q_n(\cdot, \cdot)$ is the generalized Marcum Q-function.

Because the channel is assumed to be quasi-stationary, it is possible to remove the conditioning on ρ as

$$P_{md}^{NCPDI} = \int_0^{+\infty} P_{md|\rho}^{NCPDI} p_\rho(\rho) d\rho \quad (3.8)$$

$$P_{fa}^{NCPDI} = \int_0^{+\infty} P_{fa|\rho}^{NCPDI} p_\rho(\rho) d\rho \quad (3.9)$$

In the next section, ideal sampling has been considered for simplicity, in order to evaluate the performance of each detector without the loss due to timing offsets. The obtained results can be extended to the general case of non-ideal sampling by accounting for a further loss.

3.1.3 Soft Combining: Performance evaluation

Soft combining detection performance is reported in terms of Receiver Operating Characteristics (ROCs), i.e. P_{md} vs. P_{fa} to allow an immediate comparison for different values of N combinations. Because the performance evaluation with simulations is very time consuming in the presence of Rice fading channels, the comparison between NCPDI, DPDI, and GDPI has been evaluated in AWGN, leaving to the analysis reported in the previous section the assessment of NCPDI performance in Rice fading channels. In Figure 3.3, analytical and simulated results are reported for $E_c/N_0 = -25\text{dB}$ (corresponding to a carrier power over noise PSD equal to $C/N_0 = 35\text{dBHz}$ considering $R_c = 1/T_c = 1.023\text{MHz}$) and frequency error $\Delta f = 100\text{Hz}$, for three couples (M,L), (2046,2), (1023,4) and (511,8) in order to find the optimal solution. Note that these values are selected starting from the Coherent Integration Length Dimensioning (CHILD) rule [50], which indicates (2046,2) as the best solution in the selected scenario. Observing the Figure 3.3, it can be seen

that soft combining guarantees a considerable improvement, at the cost of memory increase.

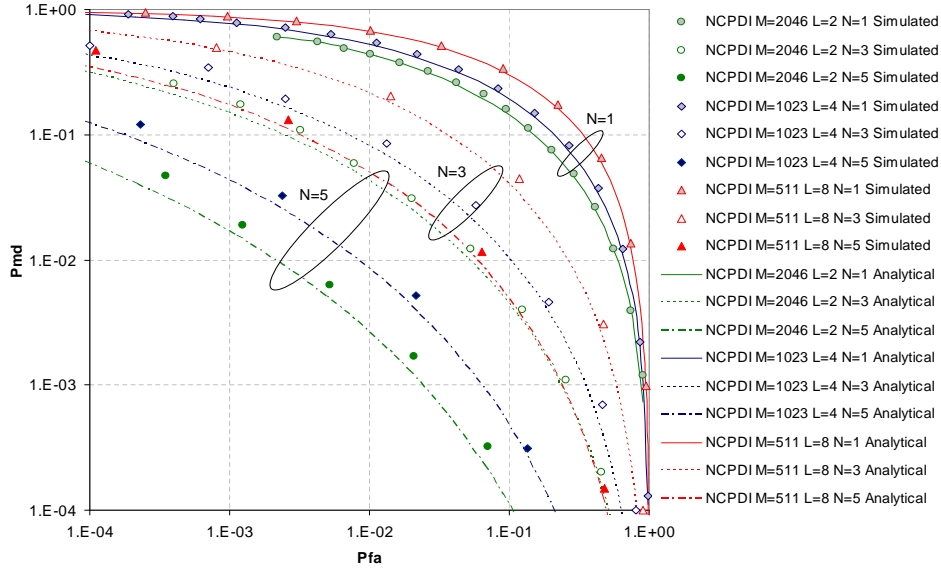


Figure 3.3: Cross-validation between analytical and simulated performance of the NCPDI detector for different values of (M,L) in AWGN channel with $C/N_0 = 35\text{dBHz}$ and frequency error of 100Hz

In Figures 3.4, 3.5, different PDI detectors are compared in AWGN with fixed frequency error $\Delta f = 100\text{Hz}$, for two typical values of signal to noise ratio: $E_c/N_0 = -25\text{dB}$ ($C/N_0 = 35\text{dBHz}$), that is the worst case in outdoor conditions, and $E_c/N_0 = -35\text{dB}$ ($C/N_0 = 25\text{dBHz}$), the worst case for indoor scenarios. Interestingly, two different conclusions can be drawn. For outdoor positioning, the GPDI detector provides the best performance. Differently, in the harsh indoor scenario, the use of GPDI does not introduce relevant performance improvement with respect to NCPDI, which seems to be the best solution, having a limited complexity. This is an interesting result because it is in apparent contradiction with known results of the GPDI detector when applied in a communication system [45]. A justification can be found in the fact that the main impairment to face is not here represented by the frequency error degradation, but by the heavy noise disturbance. In this case, GPDI, which introduces a large number of non-linearities, is not able to outperform the simpler NCPDI technique, saving complexity at the same time.

Finally, starting from the NCPDI analytical evaluation shown in the previous section, the detection performance is reported in Figure 3.6 for different values of the

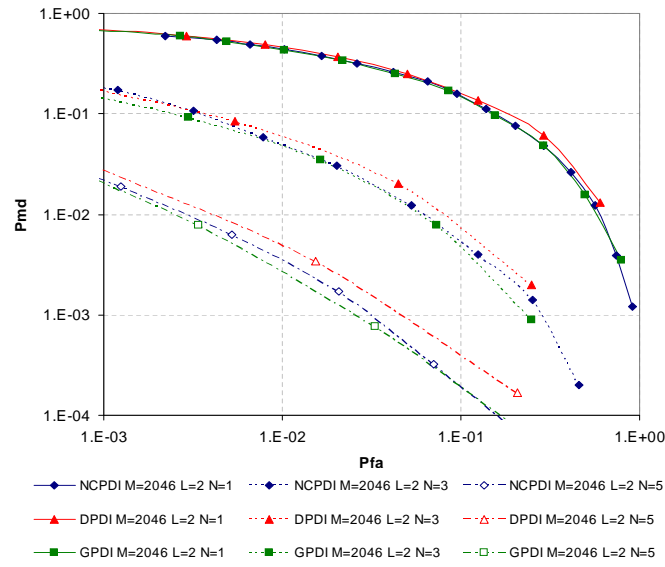


Figure 3.4: Comparison between the NCPDI, DPDI and GPDI detectors in AWGN channel with $C/N_0 = 35\text{dBHz}$ and frequency error of 100Hz

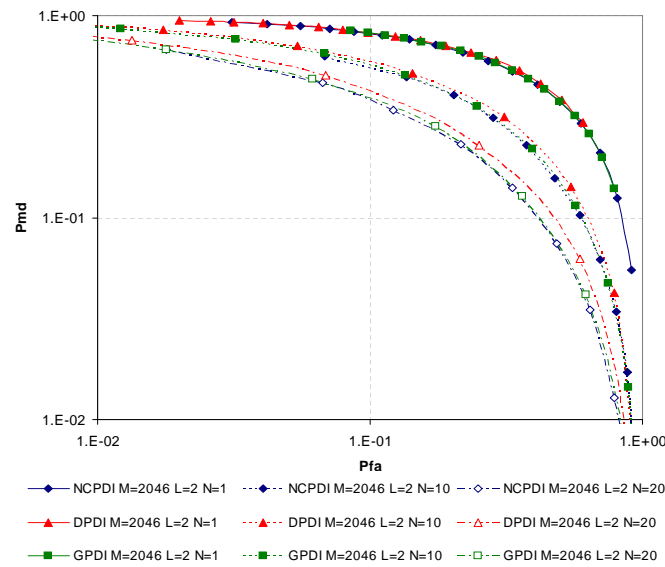


Figure 3.5: Comparison between the NCPDI, DPDI and GPDI detectors in AWGN channel with $C/N_0 = 25\text{dBHz}$ and frequency error of 100Hz

Rice factor, $K = 0, 5, 10, 100$. Note that the Rayleigh fading ($K = 0$) and AWGN ($K = 100$) are obtained as particular cases. The performance has been considered for $C/N_0 = 35\text{dBHz}$ and a Rice distribution truncated at 98% in order to eliminate the most penalizing cases (outage probability of 2%). The decision threshold has been normalized according to a CFAR criterion. Note that the integration time is assumed to be lower than the channel coherence time, i.e. the threshold does not consider the fading effects. As expected, the presence of a Rayleigh fading channel introduces a considerable performance degradation.

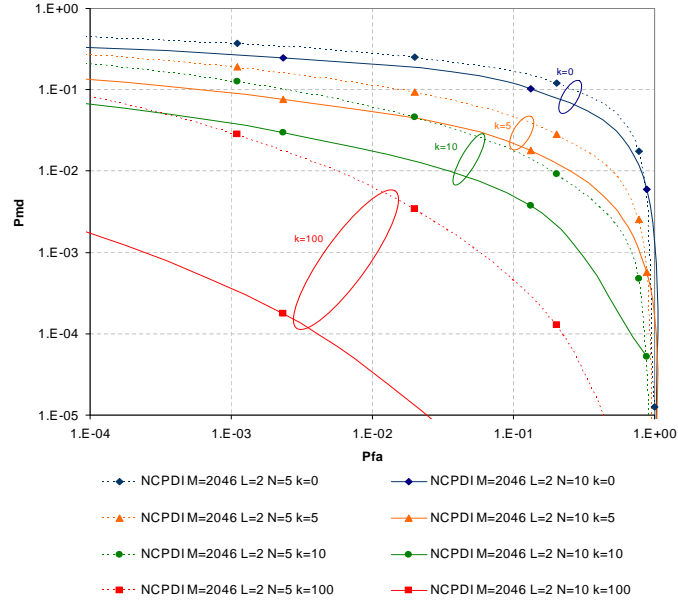


Figure 3.6: NCPDI ROC performance with soft combining in the presence of Rice fading channels for $K = 0, 5, 10, 100$, $C/N_0 = 35\text{dBHz}$, $f_e = 100\text{Hz}$, $N = 5$ and $N = 10$, $M = 2046$, and $L = 2$

3.1.4 Mean Acquisition Time

The achievable gain in terms of mean acquisition time is reported in Figure 3.7, for different numbers of repetitions N , and a penalty time equal to two primary codes duration, i.e. 8ms. Note that this performance has been obtained in a semi-analytical way, calculating by simulation the ROCs, and then analytically the MATs.

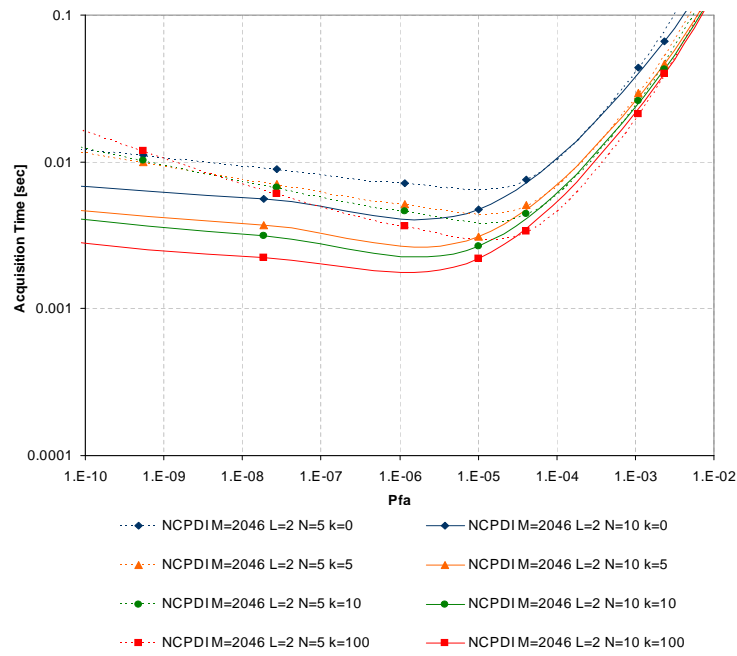


Figure 3.7: Mean Acquisition Time for NCPDI with soft combining in the presence of Rice fading channels for $K = 0, 5, 10, 100$, $C/N_0 = 35\text{dBHz}$, $f_e = 100\text{Hz}$, $N = 5$ and $N = 10$, $M = 2046$, and $L = 2$

3.1.5 Soft Combining for Improved GNSS Code Acquisition: Conclusions

Non coherent soft combining with PDI detection has been considered to improve the receiver sensitivity and counteract the effect of secondary code data transitions and frequency error degradation. It has been shown that the proposed approach is able to meet a suitable performance/complexity trade-off for future mass-market terminals.

3.2 Multi-hypothesis Secondary Code Ambiguity Elimination

In the previous section a non-coherent soft combining of the coherent correlation outputs has been analyzed in order to cope with critical SNR conditions.

Another countermeasure to achieve high sensitivity code acquisition consists in integrating coherently the received signal over an extended observation window with respect to the single code length, in order to increase the processing gain. The simple and direct application of this strategy to the Galileo E1 scenario corresponds to detecting the combination of the primary and the secondary code as a whole (i.e., of the overall pilot code of length $N_p \cdot N_s$, where N_p is the primary code length and N_s is the secondary code length, i.e. $4092 \cdot 25 = 102300$ chips), without taking advantage of the hierarchical structure of the code sequence, and at the cost of a considerable computational effort that often cannot be acceptable for mass market receivers.

To overcome this problem, this chapter investigates a novel technique to improve the receiver sensitivity for primary code acquisition. The idea consists in integrating the received signal over an observation window that is larger than a single primary code, but reduced with respect to the entire hierarchical code. Thus, unknown sign transitions of the secondary code sequence can occur within the considered observation window, and this ambiguity must be handled by the designer to avoid that overall correlation is spoiled. With respect to the non-coherent soft combining, in this case a larger gain is achieved by exploiting coherent combining between different primary codes.

In particular, the proposed solution foresees to adopt a detector adapted to a single primary code, and to coherently combine the soft outputs corresponding to the processing of a generic number N_c of consecutive primary codes, stored in a memory bank. The uncertainty due to the overlaying secondary code is handled by considering all possible combinations of the N_c consecutive secondary code chips, which lead

to a series of decision variables. This corresponds to tracing the *evolutionary tree of depth N_c for the secondary code*, which ends in several different possible leaves. The decision variable for the current test is finally obtained by selecting the maximum accumulated square module value between all these computed variables, and by further comparing it to a threshold in order to discriminate between the different primary code hypotheses. This smart combining approach allows to combine the performance advantages of the exploitation of a larger observation window with the complexity gain offered by the adoption of the two step primary/secondary code acquisition.

A further complexity reduction is achieved by introducing an optimized detector design, which replaces soft values with binary variables that are then processed by simple logical operations, with no performance loss. Note that the following results have been partially published in [4].

3.2.1 Code Acquisition with Multi-Hypotheses on Secondary Code

The multi-hypotheses secondary code acquisition exploits the increased coherent correlation length to achieve high-sensitivity in very low SNR scenarios, but increasing the coherent length M also increases the sensitivity to frequency errors.

Thus, to face frequency uncertainty, the conventional approach consists in jointly exploring the time and frequency domains, testing in parallel P different frequency hypotheses for each hypothesis in the time domain, allowing to achieve very good performance at the cost of complexity increase [54], [55].

In this way, by adopting a sufficiently accurate discretization of the frequency uncertainty domain, the residual frequency offset affecting the correct hypothesis results to be small enough to allow primary code detection exploiting coherent correlation over the entire code length followed by a module operation to eliminate phase uncertainty. The corresponding block diagram is depicted in Figure 3.8, where the local generated replica of the primary code is de-rotated on each branch by a quantity equal to each frequency hypothesis before coherent correlation, i.e. by the quantity $\Delta f_i = -\Delta f_{max} + (i - 1)f_{step}$ on the i th branch ($i = 1, \dots, P$), where $f_{step} = 2\Delta f_{max}/P$.

The proposed solution foresees to adopt a detector adapted to a single primary code and to process N_c consecutive outputs to be coherently combined exploiting a memory bank to store the transient values.

Because primary code acquisition is performed before having acquired the sec-

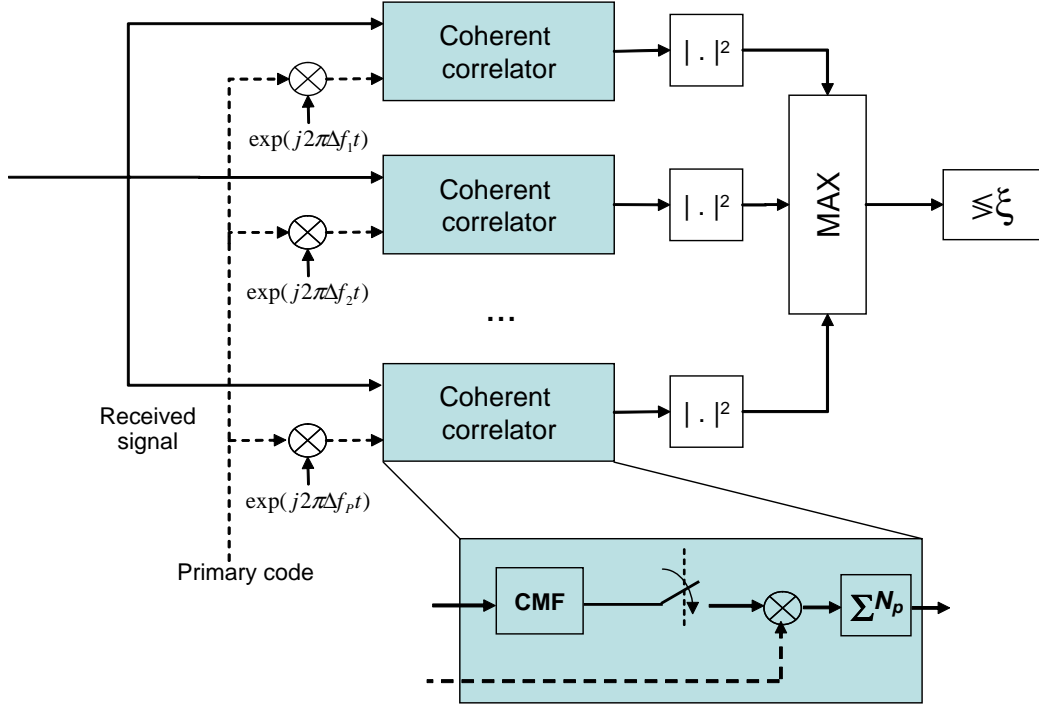


Figure 3.8: Classic parallel detector block diagram

secondary code alignment, the series of N_c primary codes is mapped onto an unknown portion of N_c secondary chips. Thus, to enable effective coherent combining, the secondary code ambiguity is handled by considering all possible combinations of the N_c consecutive secondary code chips, which lead to N_l different decision variables. This corresponds to tracing the evolutionary tree of depth N_c for the secondary code, which ends in N_l different possible leaves, before performing actual soft combining at the receiver. To be rigorous, the number of leaves N_l should be computed taking into consideration the deterministic pattern of the secondary code. However, for small to medium values of N_c , the consideration of all possible combinations of N_c secondary code chips irrespectively of the actual code pattern is a good approach that would lead to a value $N_l = 2^{N_c}$. This can be further cut in a half as shown in the following. Note that the construction of the secondary code evolutionary tree corresponds to enumerating all possible sign combinations of the successive overlaying secondary code chips. The evolutionary tree for $N_c = 3$ is reported in Figure 3.9 as an example.

The decision for the current test is finally obtained by selecting the maximum value from the square module of the computed N_l variables, and by further compar-

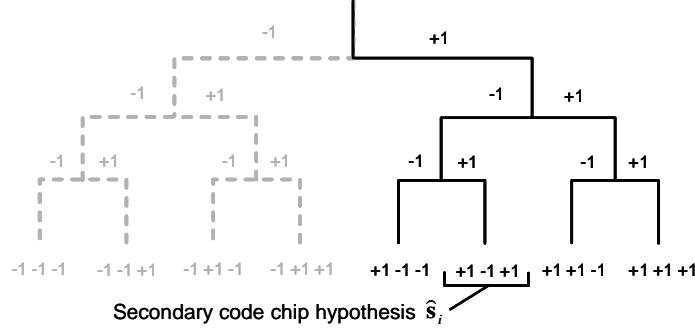


Figure 3.9: Secondary code hypotheses tree for $N_c = 3$

ing it to a threshold in order to detect the primary code correct alignment hypothesis. Note that the squared module operation foreseen after soft combining allows to prune half of the total number of branches in the secondary code evolutionary tree, as shown by the gray branches in Figure 3.9, actually limiting to $N_l = 2^{N_c-1}$ the number of leaves that has to be examined.

In the simplest case of $N_c = 2$ the number of possible secondary code hypotheses reduces to 2, corresponding to the case of 2 successive secondary code chips of the same sign or with opposite sign. The resulting primary code detector block diagram is depicted in Figure 3.10, where a passive coherent detector matched to the primary code [56] is followed by the combining logic, composed by a memory buffer of length $(N_c - 1)N_p = N_p$ chips, where the soft accumulated value collected by the previous primary code is stored, followed by the sum and the difference between the two soft values to account for the secondary code chips hypotheses.

By defining the matrix \mathbf{S} collecting all secondary code hypotheses as

$$\mathbf{S} = \{\hat{\mathbf{s}}_i^T\}_{i=0}^{N_l-1} \quad (3.10)$$

where $\hat{\mathbf{s}}_i = \{\hat{s}_{i,k}\}_{k=0}^{N_c-1}$ is the i th secondary code hypothesis, as shown in Figure 3.10, the decision variable Λ can be written as

$$\Lambda = \max_{\hat{\mathbf{s}}_i \in \mathbf{S}} \{\lambda(\hat{\mathbf{s}}_i)\} \quad (3.11)$$

where $\lambda(\hat{\mathbf{s}}_i)$ is the detector output of each secondary code hypothesis

$$\lambda(\hat{\mathbf{s}}_i) = \left| \sum_{j=0}^{N_c-1} \hat{s}_{i,j} y_j \right|^2 \quad (3.12)$$

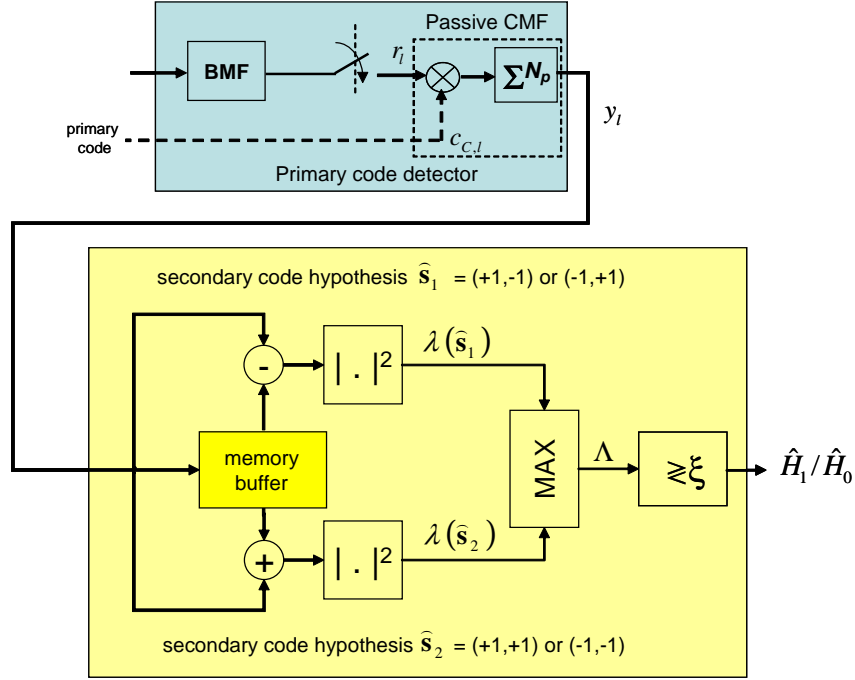


Figure 3.10: Block diagram of primary code detection with multi-hypotheses secondary code for $N_c = 2$.

being y_j the value accumulated on each primary code segment obtained processing the samples r_l taken at the output of the BOC matched filter as

$$y_j = \sum_{l=jN_p}^{(j+1)N_p-1} r_l c_{C,l} \quad (3.13)$$

An alternative implementation of this detector is described by the block diagram in Figure 3.11, where the MAX operation is replaced by a logical OR taking place after the comparison with the detection threshold ξ . Note that the two different implementations provide exactly the same performance, although the second is characterized by lower complexity and is more easy to be analytically treated.

3.2.2 Performance Evaluation

The detection performance can be characterized in terms of missed detection probability P_{md} and false alarm probability P_{fa} , defined as

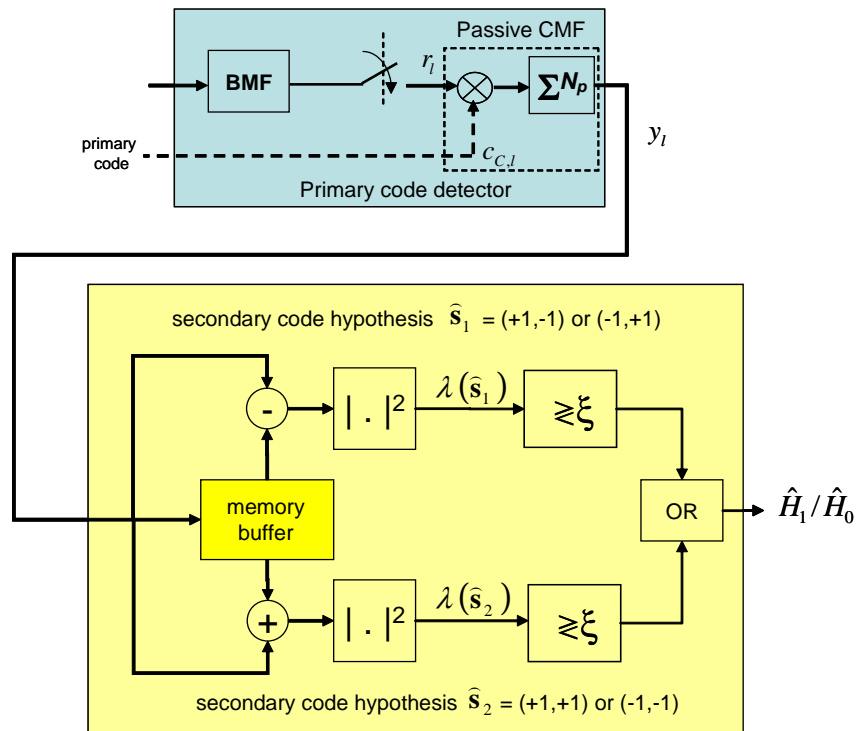


Figure 3.11: Low-complexity implementation of primary code detection with multi-hypotheses secondary code for $N_c = 2$.

$$P_{md} = \int_0^\xi p_{\Lambda|H_1}(\Lambda|H_1)d\Lambda \quad (3.14)$$

$$P_{fa} = \int_\xi^{+\infty} p_{\Lambda|H_0}(\Lambda|H_0)d\Lambda \quad (3.15)$$

By observing Equation (3.12), under H_1 the term $\lambda(\hat{s}_C)$ corresponding to the correct secondary code hypothesis results to be a non-central χ^2 random variable with two degrees of freedom characterized by non centrality parameter s^2 and variance of the composing variables σ_1^2 given by

$$s^2 = N_p^2 N_c^2 \frac{E_s}{2} \quad (3.16)$$

$$\sigma_1^2 = N_p N_c \left(\frac{N_0}{2} + \frac{E_s}{4} \right) \quad (3.17)$$

where σ_1^2 is composed by the AWGN component plus a term due to unknown B-channel data interference, modeled as a Gaussian random variable by invoking the central limit theorem.

The decision variable Λ is then obtained by selecting the largest value among many correlated χ^2 rv's coming from the different secondary code hypotheses branches. The exact characterization of Λ is then a very challenging task, which does not admit, to the best of the author's knowledge, a closed form solution. However, an upper bound can be obtained by neglecting the presence of the branches different from the correct secondary code hypothesis \hat{s}_C , leading to

$$P_{md} \leq Q \left(\frac{\sqrt{\delta}}{\sigma_1}, \frac{\sqrt{\xi}}{\sigma_1} \right) \quad (3.18)$$

where $Q(\cdot, \cdot)$ is the first order generalized Marcum Q function [46]. In fact, considering the correct detection event E_d as the union of all the correct detection events in any possible branch, it results

$$E_d = \bigcup_{i \in N_l} E_{d|i} \geq E_{d|\hat{s}_C} \quad (3.19)$$

Under H_0 , all secondary code hypotheses branches lead to a central χ^2 rv with two degrees of freedom¹, with variance of the composing Gaussian rv σ_0^2 given by

¹Centrality depends on the out-of-phase autocorrelation properties of the primary code, which are nearly ideal for practical purposes.

$$\sigma_0^2 = N_p N_c \frac{N_0 + E_s}{2} \quad (3.20)$$

Also for the exact evaluation of P_{fa} the correlation between all different branches has to be taken into account. The exact formula for $N_c = 2$ can be found in [49], which however leads to a form to be numerically evaluated and cannot be generalized to the case of $N_c > 2$. To overcome this problem, a good approximation is to consider all branches to be statistically independent in the evaluation of the false alarm probability². In particular, referring to the block diagram of Figure 3.11, the probability of correct rejection $P_{cr} = 1 - P_{fa}$ is given by the probability that all branches are jointly below the decision threshold. Accordingly, P_{fa} results to be

$$P_{fa} \simeq 1 - \left(1 - \tilde{P}_{fa}\right)^{N_l} \quad (3.21)$$

where \tilde{P}_{fa} is the per-branch probability of false alarm given by [46]

$$\tilde{P}_{fa} = \exp(-\xi/2\sigma_0^2) \quad (3.22)$$

3.2.2.1 Numerical Analysis

In order to evaluate the effectiveness of the proposed technique, a set of Receiver Operating Characteristics (ROCs), i.e. P_{md} vs. P_{fa} , is reported in Figure 3.12. A typical scenario for indoor or dense urban positioning in the Galileo system has been considered, with $C/N_0 = 30\text{dBHz}$, corresponding to $E_c/N_0 = -30\text{dB}$ at a chip rate of 1.023Mcps . This figure shows the performance for different values of $N_c = 1, 2, 3$. Note that the performance corresponding to $N_c = 1$ represents the classical approach without the multi hypotheses secondary code technique, which is notably outperformed by increasing N_c . The approximated analytical P_{fa} and P_{md} are also reported for cross validation, showing a very good agreement with simulated results, especially for $P_{fa} < 10^{-2}$, which is the most relevant operating region. A less accurate approximation is provided for high P_{fa} with $N_c = 3$ because in this case low values of P_{md} are achieved and the upper bound Equation (3.18) becomes looser.

The benefits of the proposed solution are definitely shown by considering the Mean Acquisition Time (MAT) performance, with a penalty time due to false alarm, assumed constant and equal to $4N_p T_c = 16$ ms.

²Considering N_l as a power of two, the secondary code tree in figure becomes a Walsh-Hadamard code tree, and Equation (3.21) results to be exact.

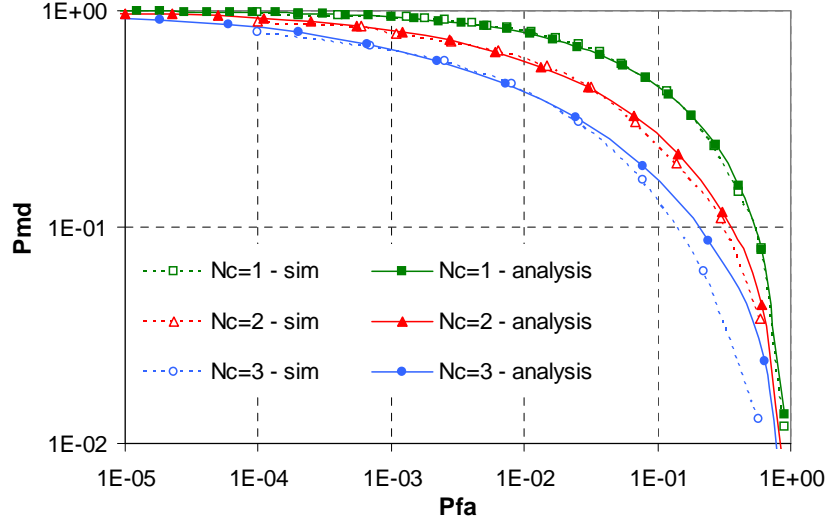


Figure 3.12: Receiver Operating Characteristics comparison with $C/N_0 = 30$ dBHz. Analytical and simulated results are reported for different N_c .

Performance in terms of MAT vs. P_{fa} is reported in Figure 3.13. It is interesting to observe that the performance improvement with increasing N_c already noticed with ROCs is further amplified when the MAT is considered. In particular, the minimum MAT, equal to 0.6s at $N_c = 1$, is strongly reduced to 0.12s and 0.05s, respectively for $N_c = 2$ and 3.

3.2.3 Multi-hypotheses Secondary Code Ambiguity Elimination: Conclusions

The problem of sensitivity improvement for Galileo primary code acquisition has been addressed in the section, proposing a novel technique to increase the observation window, solving the ambiguity of the overlaying secondary code. This uncertainty is handled through the construction of the multi-hypotheses secondary code tree with all possible combinations and exploiting a parallel detection scheme. Interestingly, the resulting detector is characterized by limited complexity increase, requiring larger memory, but with no significant impact in terms of number of multiplications.

The proposed approach is validated through analytical and numerical results, showing that an interesting performance improvement can be introduced by increasing the parallelism order, meeting the required design performance/complexity

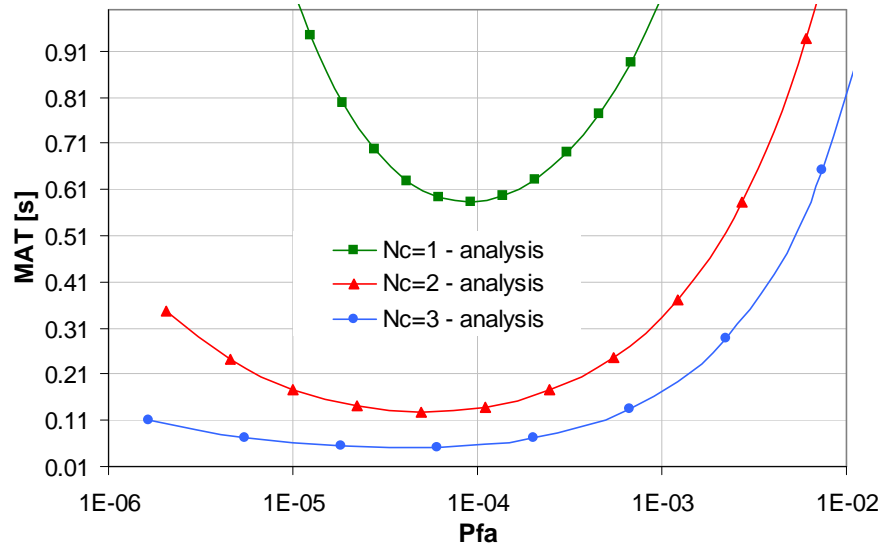


Figure 3.13: Mean acquisition time in seconds vs. false alarm probability with $C/N_0 = 30$ dBHz

trade-off.

4

Acquisition and Tracking of the E1-A Signal

As detailed in Section 1.3.1, the E1-A signal of Galileo is designed to be used for the Public Regulated Services (PRS). Thus, it should provide position and timing to the users with high continuity of service, high accuracy and availability. For this reason, it is necessary to consider all possible impairments that might affect the compliance with the stringent accuracy expectations resulting from the high Gabor bandwidth. In the following the problem of code acquisition, transition to tracking, and code tracking of the E1-A signal in the presence of signal distortion is tackled. Note that all these considerations involve any high-order BOC modulated signals, including BOC(10,5) used in the Galileo E6 and in the GPS M-code.

This activity has been performed within the European Space Agency - European Space Research and Technology Centre (ESA ESTEC) facilities, and its results have been partially reported in [57]. My work has been focused on the evaluation of state-of-the-art acquisition and tracking techniques, my original contributions consist in the definition of a novel combination approach of E1-A with the OS signals in E1, in the theoretical framework for the two-dimensional correlation, and in the innovative

ways of combining the two delays coming from the two-dimensional correlation.

4.1 Signal Distortion of High-Order BOC Modulated Signals

As already discussed, the E1-A signal, which is BOCc(15,2.5) modulated, presents the highest ratio of subcarrier frequency to chip rate of any GPS and Galileo signals, resulting in an autocorrelation function as the one shown in Figure 1.2.

Moreover, in practical situations, the signals coming to the receiver can be affected from non-idealities, resulting in signal distortion. These non-idealities can be due to the signal filtering in the payload, hard propagation environments, onboard non-idealities, receiver filter bandwidth, etc. The main result of this distortion is the tracking performance loss: increase of the ratio between the first false peak and the correct peak (about 0.9 in the ideal case, about 0.96 using a 40MHz Butterworth 6-taps filter if a full band correlation of E1-A is considered), rounded effect on the peaks, as shown in Figure 4.1, and consequently, an harmful bias in the position estimate. In the following a model for the distortion is discussed.

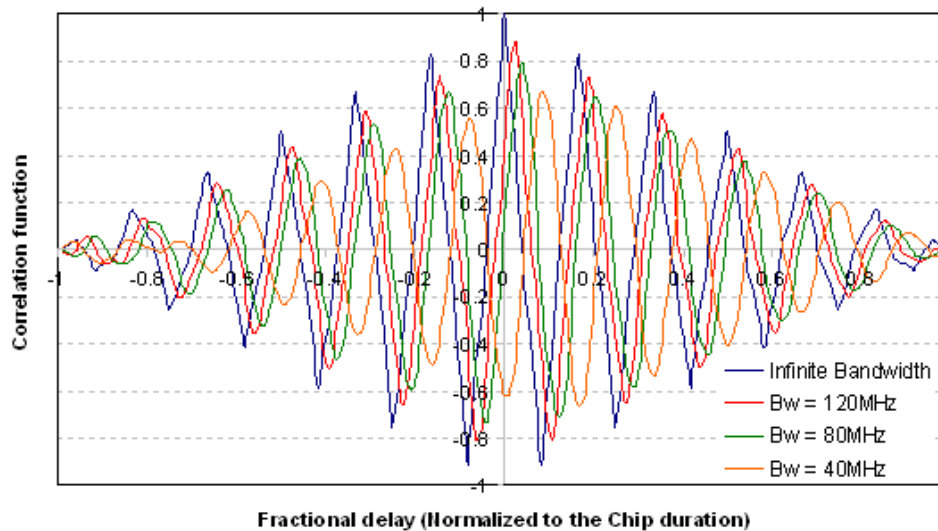


Figure 4.1: E1-A autocorrelation function: effect of a 6 taps Butterworth filter for different bandwidths

4.1.1 Linear Filter and Channel Propagation

The objective of this study is to identify how the frequency characteristics of a filter can affect the performance of the receiver algorithms. There are two types of filter: linear phase filter and non-linear phase filter. A linear phase filter is characterized by the phase response which is a linear function of frequency, excluding the possibility of wraps at $\pm\pi$, and, consequently a non linear phase filter leads to a non linear function of the phase response.

Let $H(\omega)$ be the transfer function of a filter, and $\phi(\omega) = \arg H(\omega)$ be the phase shift. Introducing the two concepts, the group delay and the phase delay, as detailed in the following equations

$$\tau_g = -\frac{d\phi(\omega)}{d\omega} \quad (4.1)$$

$$\tau_\phi = -\frac{\phi(\omega)}{\omega} \quad (4.2)$$

it can be shown that, for a linear phase filter, they are equal to the same constant delay. On the other hand, a non-linear phase filter has a group delay that varies with frequency, resulting in phase distortion. The phase delay gives the time delay experienced by each sinusoidal component of the input signal, while the group delay may be interpreted as the time delay of the amplitude envelope of a sinusoid at a certain frequency. Thus, since for linear phase response filters, the group delay and the phase delay are identical, they may be interpreted as time delay. Non-linear phase filters affect in a different way the carrier and the code. In particular, the carrier is delayed by the phase delay, while the amplitude-envelope frequency-component is delayed by the group delay. In the following all the impairments have been modeled in a 40MHz Butterworth 6-taps filter, which is a simplified model for the otherwise rather complicated non-idealities described above, being nevertheless already sufficient to create degradation. Note that since the minimum receiver bandwidth required to receive the E1 signals for GIOVE-A and GIOVE-B is 32.736MHz according to [34], a 40MHz filter represents a reasonable choice.

4.1.2 Effects of Linear Distortion on Received Signals and on Detection Algorithms

Before entering in the details of the receiver algorithms, a preliminary analysis on the effects of signal distortion on the correlation function can be addressed. Let $s(\tau_s, \tau_c)$ be the local replica, generated considering two different delays, τ_c the delay

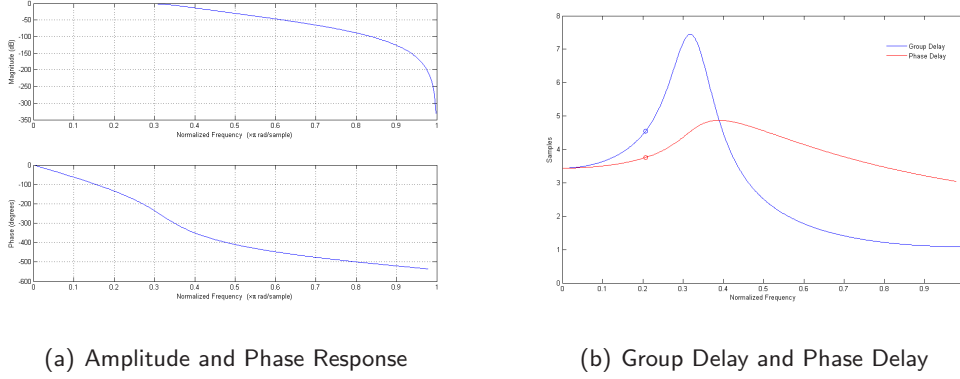


Figure 4.2: 40MHz Butterworth 6-taps filter

for the code, and τ_s the delay for the sub-code, as detailed in the following:

$$s_{local}(\tau_s, \tau_c) = \sum_{i=-\infty}^{+\infty} c_{|i|_N} c(t - \tau_c - iT_c) s(t - \tau_s - iT_c) = \quad (4.3)$$

$$= \sum_{i=-\infty}^{+\infty} c_{|i|_N} \text{rect}_{T_c}(t - \tau_c - iT_c) \text{sign}[\cos(2\pi f_s(t - \tau_s))] \quad (4.4)$$

Thus, taking inspiration from [58], a two dimensional correlation can be performed, considering all the $s(\tau_s, \tau_c)$ possible combinations (Figure 4.3). Note that, according to the $\text{BOCc}(15,2.5)$ waveform, there is a single peak every T_c in the τ_c -axis, while there are multiple peaks per T_c in the τ_s -axis, in particular one peak (alternate positive and negative) every T_{sc} . The classical one-dimensional correlation can be obtained from this considering the diagonal $\tau_c = \tau_s$. The unfiltered case shows that no delay is foreseen in any dimension, and that the maximum of the correlation function is in one of the point of the diagonal (Figure 4.4).

On the other hand the filtered case shows that a shift of (τ_ϕ, τ_g) in the τ_s, τ_c space is obtained (Figure 4.5). More precisely, for a 40MHz Butterworth filter the maximum of the correlation function is in the point (4, 5), which is the rounded value of the (τ_ϕ, τ_g) shown in Figure 4.2(b).

4.1.3 Multipath Propagation

In order to provide a simple evaluation, the easiest multipath profile has been considered in this work: the classical two-taps delay line with static coefficients. According to the multipath error envelope shown in Figures 4.7(a)-4.7(b), the modulation $\text{BOCc}(15,2.5)$ should be more robust to multipath with respect to the other modu-

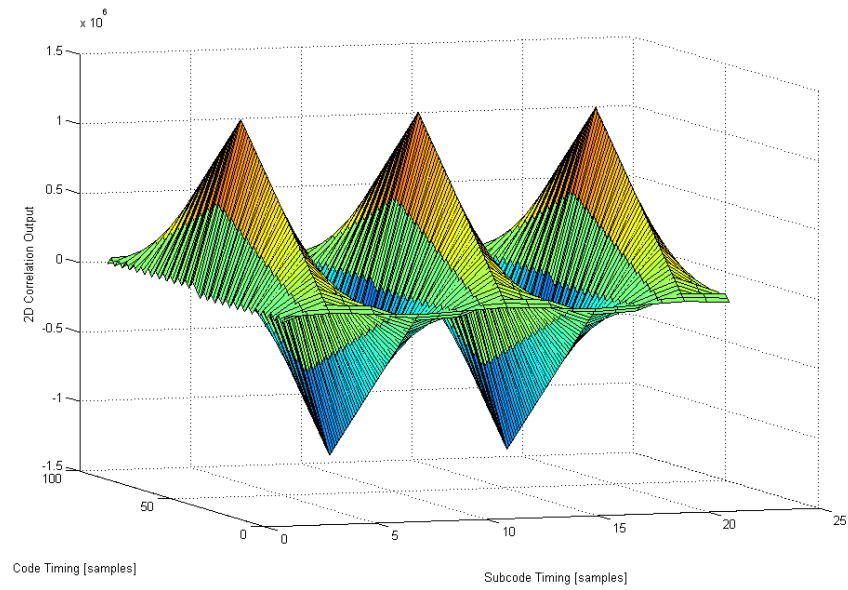


Figure 4.3: 2D Correlation Output

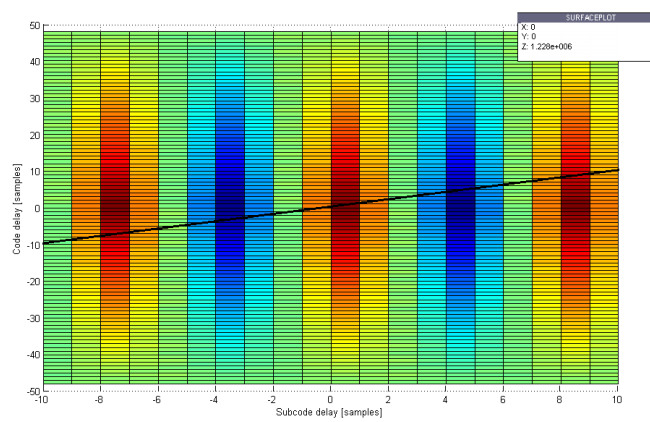


Figure 4.4: 2D Correlation Output: the maximum is in the diagonal

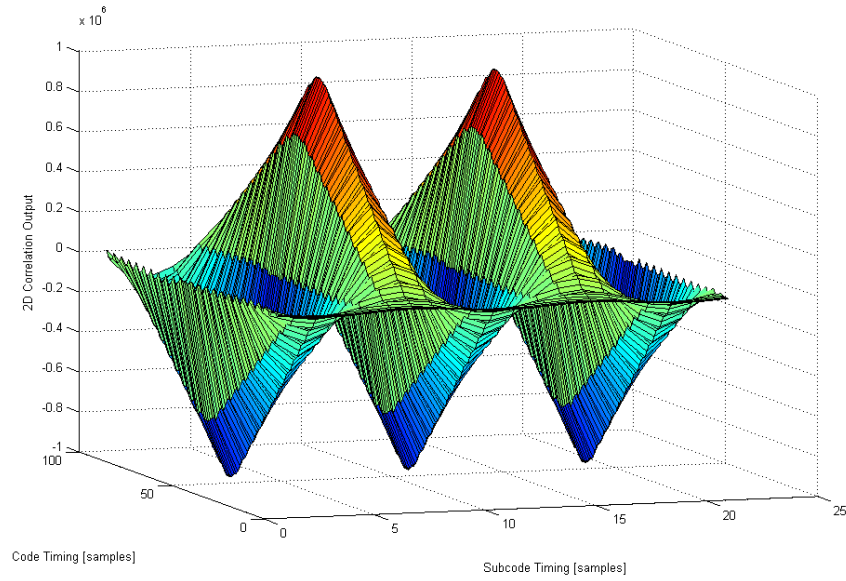


Figure 4.5: 2D Correlation Output: filtered

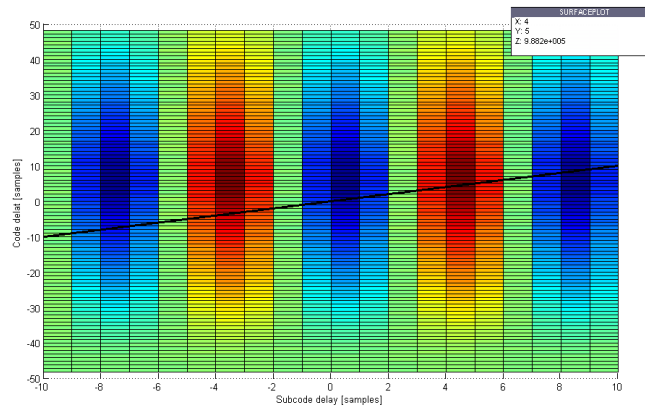


Figure 4.6: 2D Correlation Output: the effect of the filter is that the maximum is shifted away from the diagonal

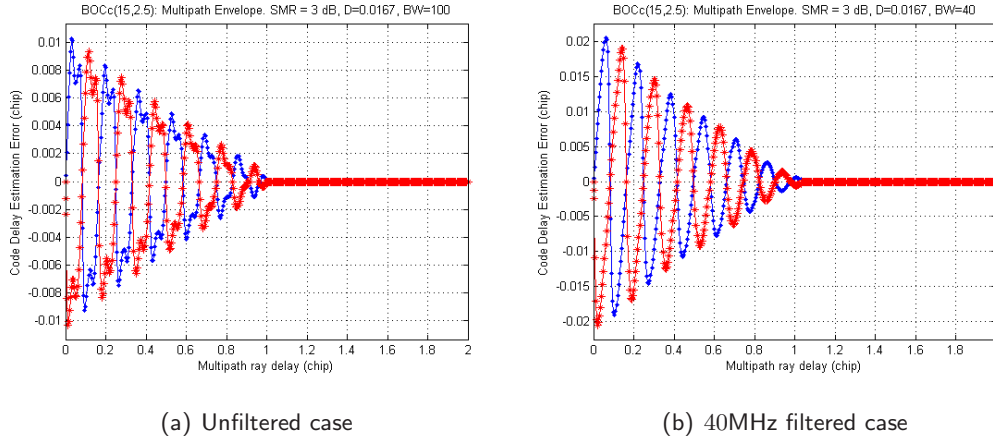


Figure 4.7: Multipath Error Envelope SMR= 3dB Phase= 0

lations. Anyway, as shown in the following section, in a real scenario tracking can be very challenging.

Figure 4.8 and 4.9 show the effect of a multipath with Signal-to-Multipath Ratio (SMR) equal to 3dB and phase equal to 0 on the two dimensional correlation function. Note that, also in the case of multipath, the effects on the code delay and on the subcode delay are different.

4.2 Code Acquisition of Distorted Sequences

4.2.1 Full Band Acquisition

The classical acquisition method for E1-A signal consists in the one dimensional correlation of the received signal with a BOCc(15,2.5) local replica. The classical approach to perform the acquisition scanning all the code phases in parallel is based on the principle that the circular convolution of two signals in the time domain can be seen, in frequency, as the product of the Fourier transforms of those signals [42], according to the block diagram shown in Figure 4.10. Note that, due to the E1-A signal structure and to the presence of a secondary code, the coherent correlation over two primary code periods is needed, since only inside a block of two secondary bits it is possible to find a whole primary code [59]. In this way, the peak can be identified both in the *odd* case, when there is a bit transition inside the correlation length, and the *even* case when there is no such transition. Moreover, for each Doppler cell, the local replica has to be modulated with the correct frequency shift.

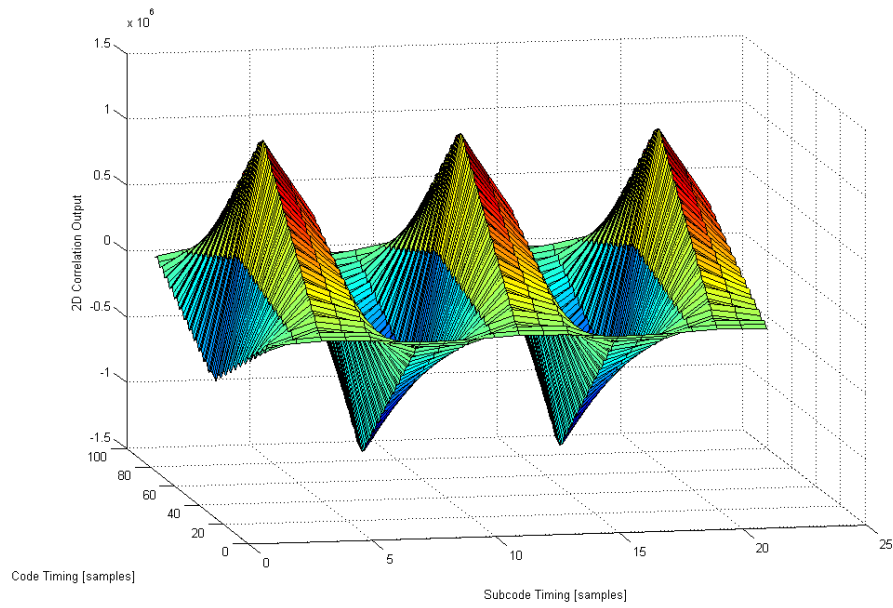


Figure 4.8: Multipath effect on the 2D autocorrelation

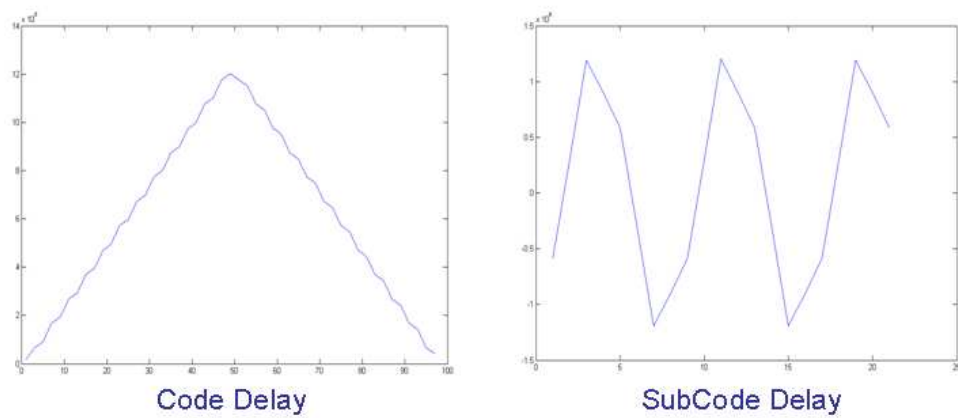


Figure 4.9: Multipath effects on the Code Delay and on the Subcode Delay

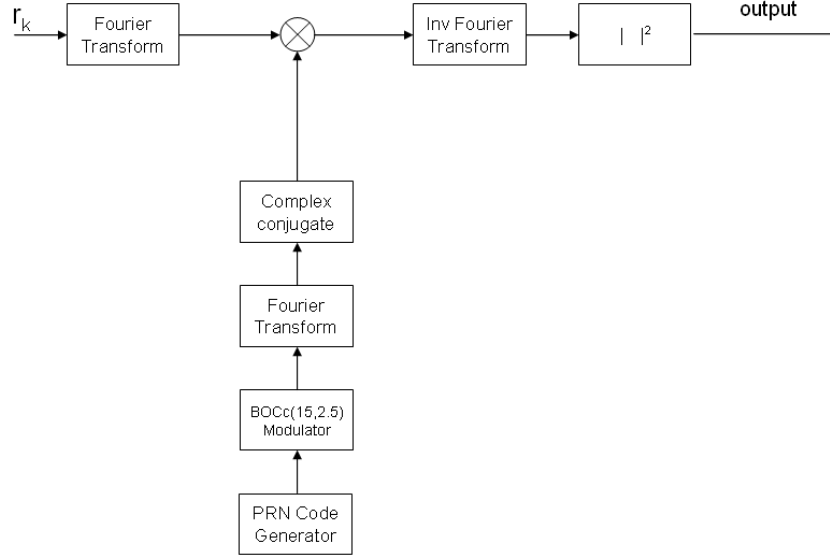


Figure 4.10: Parallel Code Phase Search block diagram

This can be obtained directly applying a circular delay to the frequency samples, avoiding the computation of the FFT of the replica for each Doppler cell. Note that, in this way, only a fixed frequency discretization Δf is foreseen:

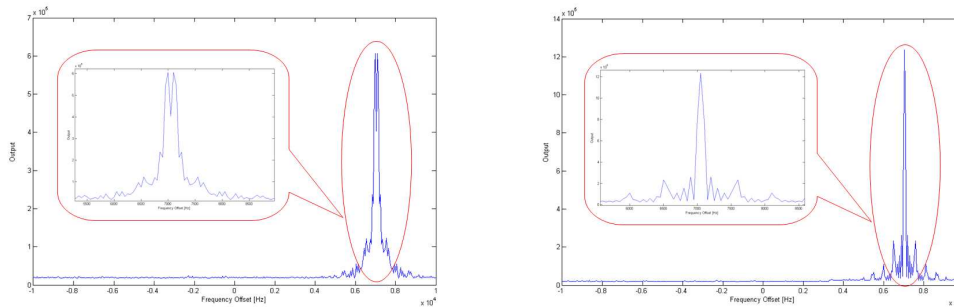
$$\Delta f = \frac{1}{T_{coh}} = \frac{1}{2 \cdot NT_c} \quad (4.5)$$

For GIOVE-A signal, Δf corresponds to 50Hz, while for GIOVE-B signal, Δf is equal to 250Hz.

In this work, a MAX/TC criterion has been used [60]. Thus, the maximum of the two dimensional matrix is selected and the absolute value is compared with a threshold. If a threshold crossing event is detected the combination (τ_i, f_i) is considered as acquired. The threshold is usually designed through the Constant False Alarm Rate (CFAR) criterion. The CFAR threshold allows to have a constant false alarm probability, P_{fa} , by varying the signal to noise ratio. This is an important feature because it enables an optimized detector design, independently of the SNR.

4.2.1.1 Code Doppler Effects

Applying the frequency shift correspondent to the Doppler cell under search to the FFT of the input signal, only the Doppler in the carrier is accounted, leaving on the signal the effects of the Doppler in the code. Since the signal E1-A can be very long, as in the GIOVE-A configuration, it can be seen that the coherent



(a) Effect of Doppler in the code in the Full Band Code Acquisition

(b) Doppler in the code: mitigation

Figure 4.11: Effect of Doppler in the code

correlation performed in the code acquisition can be affected by this phenomenon. Figure 4.11(a) shows the effects of the Doppler in the code for a noiseless scenario with a frequency offset equal to 7050Hz. Note that the maximum at the output of the acquisition corresponds to the Doppler cell 7000Hz. In the scenario at hand, two ears can be obtained instead of one single lobe, leading to an uncorrect detection of the frequency bin.

Thus, in this work, the possibility of completely regenerate the local replica has been considered, accounting for both the Doppler in the carrier and in the code, avoiding performance losses. The same scenario shows that with three regenerations in the Doppler Range ($-5\text{KHz}, 0\text{Hz}, 5\text{KHz}$), the correct acquisition is guaranteed (Figure 4.11(b)) at the cost of complexity increase.

4.2.1.2 Numerical Results

Figures 4.12 and 4.13 show the acquisition performance for different SNRs in the ideal case and in the presence of signal distortion. Note that figures show, for a given C/N_0 , the probability of detection for the correct peak and for the secondary false peaks, considering GIOVE-A E1-A signals. Thus, it can be seen that also in ideal conditions, for a C/N_0 equal to 35dBHz, almost the 10% of the cases one of the secondary peaks is detected as the maximum. In the presence of signal distortion, notably, acquisition becomes even more challenging, with a probability of detection of the first peak less than 0.5, and of one of the secondary peaks almost 0.4 for a C/N_0 equal to 35dBHz. Note that the remaining probability accounts for the non-correct cases. It is worthwhile noting that even in the case of detection of a

secondary peak, the correct detection can be declared, since it is inside the correct H_1 cell, but the tracking loop should be able to correct this bias in order to have the right estimate.

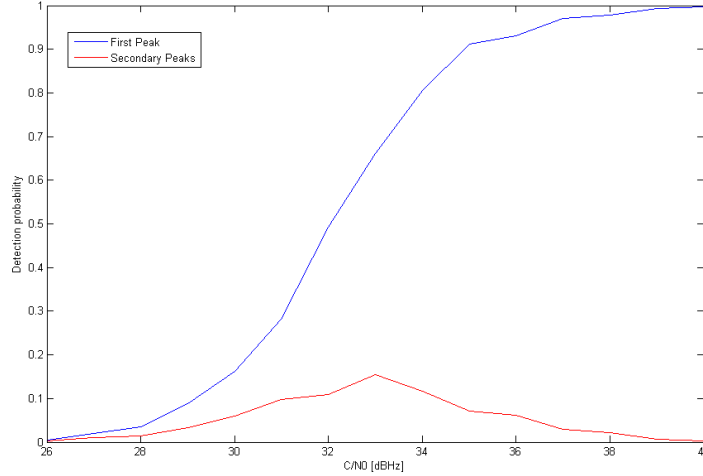


Figure 4.12: Probability of detection vs. signal to noise ratio (ideal case): Sampling Frequency= 122MHz - 1000 Iterations

4.2.2 Dual-Side Band Acquisition

This technique, originally proposed in [61] for the generic BOC modulation, consists in considering the received $\text{BOC}_c(15,2.5)$ signal as the sum of two BPSK signals with carrier frequency symmetrically positioned on each side of the BOC carrier frequency. Thus, each lobe is processed separately as a BPSK signal (Figures 4.15(a) and 4.15(b)). Indeed, each lobe is correlated with a local BPSK reference consisting only of the code, centered respectively in $(F_{carrier} + f_{sc})$ and $(F_{carrier} - f_{sc})$ where $F_{carrier}$ is the carrier frequency and f_{sc} is the subcarrier frequency, i.e. $f_{sc} = n \cdot 1.023\text{MHz} = 15.345\text{MHz}$. Thus, the receiver has to account two correlation channels, one for the upper filtered sideband and one for the lower filtered sideband. Each correlation channel results in an unambiguous correlation function and then the two channels are then combined. In this case non coherent combining has been considered.

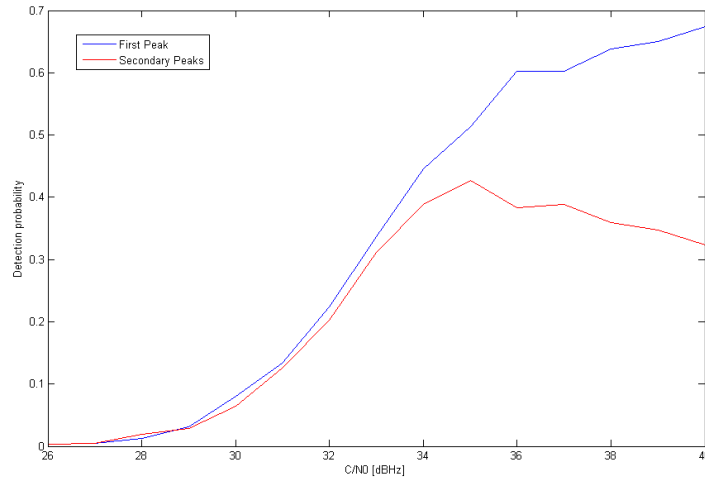


Figure 4.13: Probability of detection vs. signal to noise ratio in the presence of signal distortion: Sampling Frequency= 122MHz - 1000 Iterations

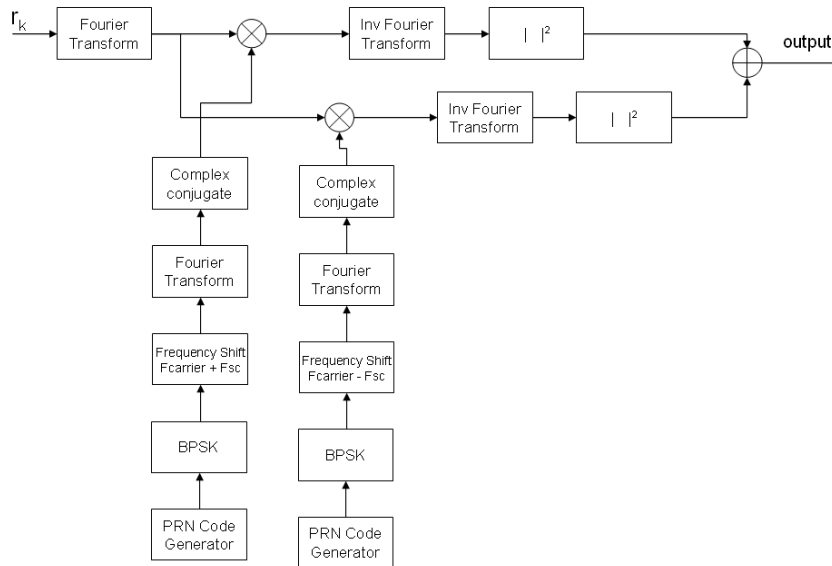


Figure 4.14: Dual-Side Band with Parallel Code Phase Search block diagram

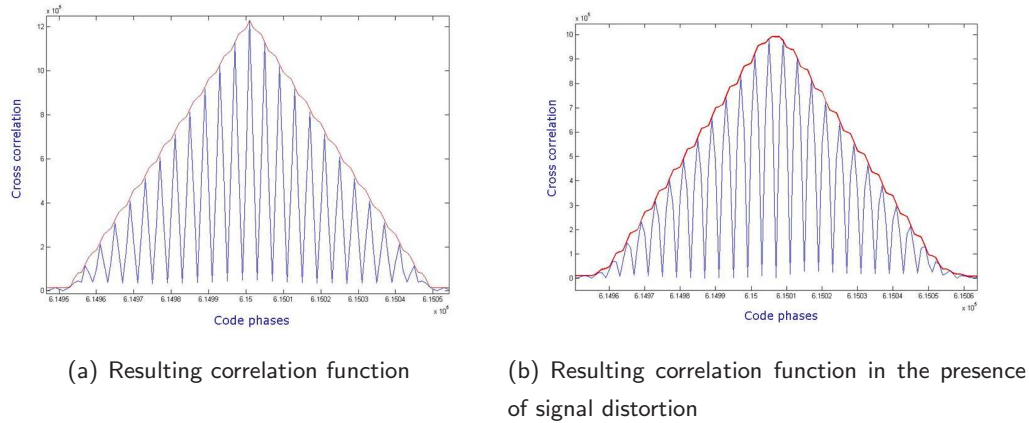


Figure 4.15: Dual-Side Band Correlation Function

4.2.2.1 Numerical Results

Figures 4.16 and 4.17 show the performance of the Dual-Side Band Acquisition technique. Note that the problem of the multiple peak has been fixed, but the accuracy and the sensitivity of the acquisition are lower with respect to the classical full band technique, as can be noted by Figure 4.16 with a loss of about 1.5dB with respect of the full band technique. Note that Figure 4.17 reports the histogram of the detection, showing that the secondary peaks are not present.

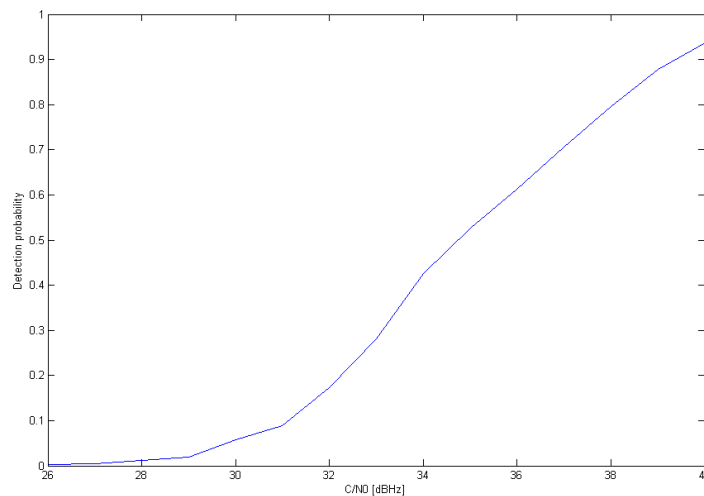


Figure 4.16: Probability of detection vs. signal to noise ratio for the Dual-band acquisition technique: Sampling Frequency= 122MHz - 1000 Iterations

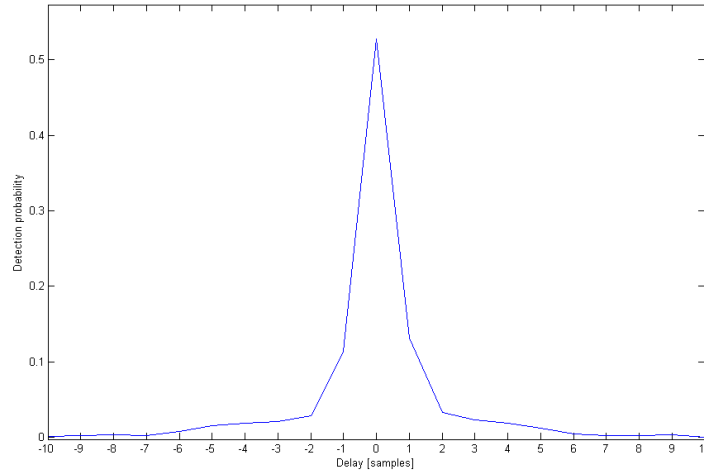
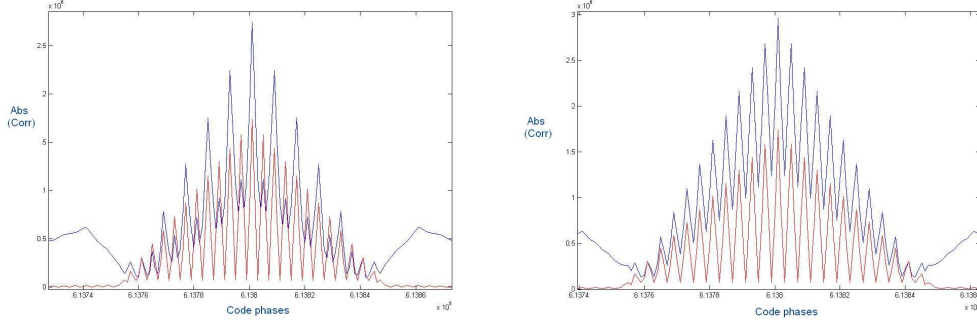


Figure 4.17: Probability of detection vs. signal delay for $C/N_0 = 35\text{dBHz}$

4.2.3 Combining E1-A with Open Service Signals E1-B and E1-C

The problem of false peak detection can be mitigated considering the possibility of combining in the receiver the correlation function of the BOCc(15,2.5) coming from the E1-A signal and the correlation function of the BOC(1,1) of the Open Service signals E1-B and E1-C. Before entering in the details, pros and cons of this approach are discussed. The main drawback of this technique is the fact that the presence of the Open Service signals is needed, which is not consistent with the PRS purpose of being available and robust also in very critical scenarios. Anyway, in normal conditions all these signals are available in the same bandwidth, and the effects of the combining can be very useful in the code acquisition phase. Another drawback is the fact that E1-A and the Open Service E1-B and E1-C have different code periods, resulting in higher processing capability required to the receiver in order to enable the combining. In fact, the receiver should be able to calculate the relative delay between the two different Start of Frames and to align the two autocorrelation function. However, this operation can be addressed to a professional segment, where the processing capabilities are not a limiting factor for the receiver.

The combining, which is performed at the physical layer, can be coherent or non-coherent. Note that E1-C is a pilot signal, while E1-A and E1-B contain data. Thus, the possibility of coherently combining the correlation functions implies a sort of parallelism in order to account all the possible bits combination. The synthesized



(a) E1-A and E1-C coherent combining: resulting correlation function
 (b) E1-A and E1-C non-coherent combining: resulting correlation function

Figure 4.18: E1-A and E1-C non-coherent combining

correlation function can be evaluated in Figures 4.18(a) and 4.18(b) for coherent and non coherent combining. A preliminary analysis shows that the overall received signal energy can improve signal acquisition, if the combining is properly done. In fact, the difference between the first peak and the secondary peaks is increased, resulting in better acquisition performance.

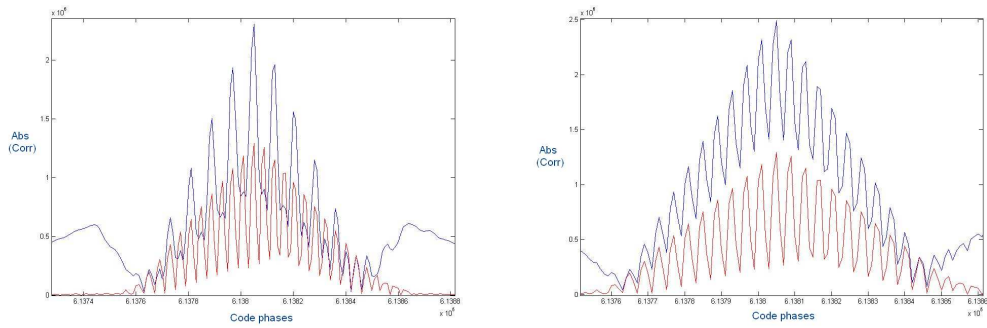
Moreover, in the presence of signal distortion the effects of the combining can be even more useful (Figures 4.19(a)-4.19(b)).

The gain in the autocorrelation function directly translates in benefits in the detection probability. Figures 4.20 and 4.21 show the effect of the coherent combining in the acquisition performance, considering an AWGN scenario and with a signal to noise ratio C/N_0 which takes into account both the signals.

4.3 Transition from Acquisition to Tracking

After the acquisition process, an intermediate step before the tracking loop has been considered. The code delay and the Doppler estimation (τ_i, f_i) are in fact not accurate enough to be given as an input to the tracking loops, especially for a BOCc(15,2.5) modulated signal. In this work, a joint carrier frequency estimation and code acquisition has been considered, as detailed in Figure 4.22. This scheme is inspired on the differential correlator [62], which has been opportunely modified to be matched to the Galileo waveform.

Note that the local replica is generated taking into account the timing and frequency reference from the code acquisition stage. The received symbols r_k are thus



(a) E1-A and E1-C coherent combining: resulting correlation function in the presence of signal distortion
 (b) E1-A and E1-C non-coherent combining: resulting correlation function in the presence of signal distortion

Figure 4.19: E1-A and E1-C non-coherent combining in the presence of signal distortion

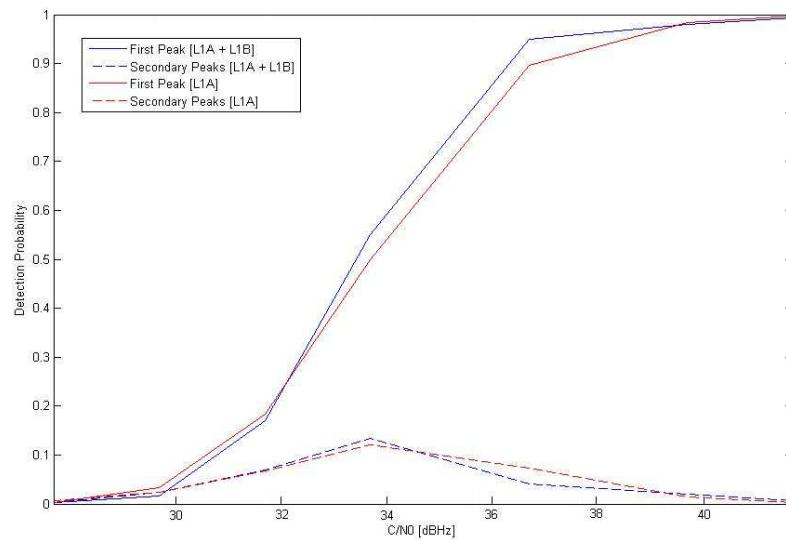


Figure 4.20: Probability of detection vs. total signal to noise ratio: E1-A E1-B coherent combining (ideal case)

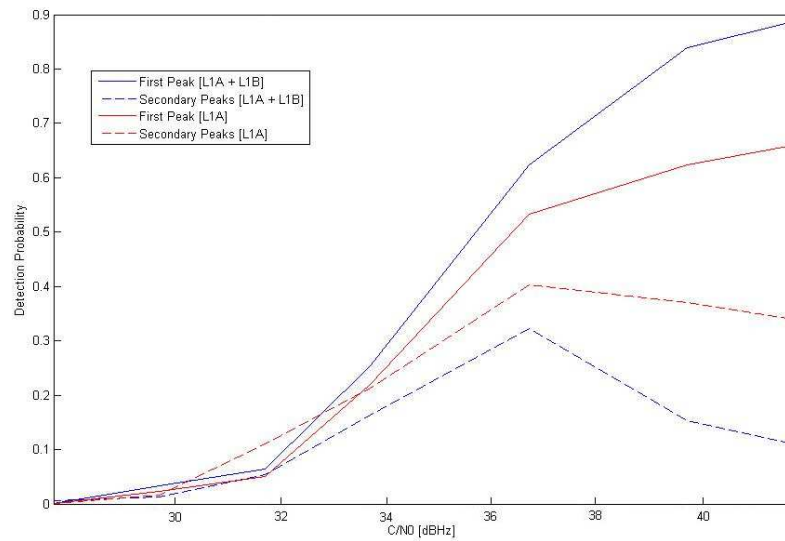


Figure 4.21: Probability of detection vs. total signal to noise ratio: E1-A E1-B coherent combining (in the presence of signal distortion)

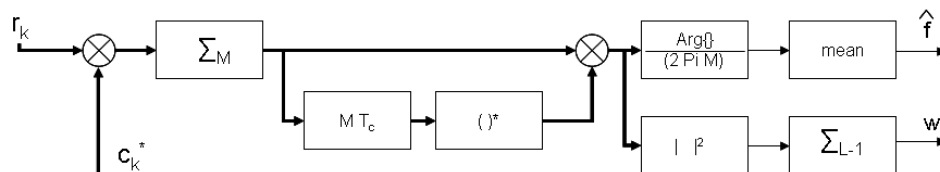


Figure 4.22: Transition to Tracking block diagram

processed by a coherent correlator, producing

$$x_k = \sum_{m=Mk}^{(M+1)k-1} r_m c_m^* = \mu_k + n_k \quad k = 0, \dots, L-1 \quad (4.6)$$

where M is the coherent integration length, L is the Post Detection Integration (PDI) length, n_k is the filtered noise term which is complex Gaussian distributed with zero mean and variance $\sigma^2 = 2M\sigma_n^2$, and μ_k is the useful component in the form

$$\mu_k = Ae^{\Theta+2\pi k\nu M} \quad (4.7)$$

where $A = M\sqrt{E_s}\text{sinc}(M\nu)$, ν is the normalized frequency error, i.e. $\nu = \Delta f T_s$, and $\Theta = \pi\nu(M-1)$. After the coherent integration a Differential PDI (DPDI) scheme has been considered:

$$z_k = x_k x_{k-1}^* \quad (4.8)$$

The useful signal component in Equation 4.8 is given by $\zeta_k = \mu_k \mu_{k-1}^*$, resulting to be a complex variable with module and phase given by

$$|\zeta_k| = M^2 E_s \text{sinc}(M\nu)^2 = A^2 \quad (4.9)$$

$$\text{arg}\{\zeta_k\} = 2\pi M\nu \pm \frac{\pi}{2} \quad (4.10)$$

where the ambiguity of $\pm\frac{\pi}{2}$ depends from the data. If a bit transition is present in the k -th instant, a rotation of π is present. Thus, beside the ambiguity of $\pm\frac{\pi}{2}$, the angular rotation after PDI is directly related to the unknown normalized frequency error ν , thus suggesting the possibility of an accurate frequency estimation.

The frequency error estimate $\hat{\nu}$ can be achieved as

$$\hat{\nu} = \frac{1}{L} \sum_{k=1}^L \frac{\text{arg}(z_k)}{2\pi M} \quad (4.11)$$

where arg is referred to the two quadrant inverse tangent, in order to solve the $\pm\frac{\pi}{2}$ ambiguity and to be insensitive to the phase shifts due to the navigation bit transitions.

Starting from the estimation of the frequency, also the phase can be estimated, according to:

$$\hat{\varphi} = \left| \arctan\left(\frac{\text{Im}(z_k)}{\text{Re}(z_k)}\right) - 2\pi\hat{\nu}ML \right|_{\pi} \quad (4.12)$$

Moreover, introducing a energy detection (absolute value operation) before the PDI integration, the decision variable w can be used to verify the acquisition output.

Note that the choice of M and L is a very important design aspect. First of all, according to the Cramer Rao Bound (CRB) for the frequency estimation [63], the optimal variance results to be

$$Var\{\varepsilon_\nu\} = \left[\frac{3}{2\pi^2(N_{obs})^3} \left(\frac{E_s}{N_0} \right)^{-1} \right] \quad (4.13)$$

where N_{obs} is the length of the observation window, and E_s is the symbol energy. Thus, increasing M and L , a better estimation can be obtained. On the other hand, the coherent length M should be optimized in order to account the maximum frequency offset affecting the system. In fact the pull-in range of the frequency estimation scheme, according to Equation 4.11 and the fact that the inverse tangent refers to two quadrants, is:

$$\nu \in \left[-\frac{1}{4M}, +\frac{1}{4M} \right] \quad (4.14)$$

If M is set to be equal to the primary code length N , it results that $\nu \in [-25, 25]$ Hz for GIOVE-A, and $\nu \in [-125, 125]$ Hz for GIOVE-B. Thus, in GIOVE-A, in order to make the pull-in range of the Transition to Tracking consistent with the output granularity of the Code Acquisition, two possible solutions can be exploited: to select a lower M , or to provide three estimation blocks in parallel. The second solution should overcome the performance of the first one at the cost of complexity. For GIOVE-A, for example, three blocks are considered, one with the local replica at f_i frequency, one $f_i + 25$ Hz and the last one at $f_i - 25$ Hz in order to cover the interval $[-50, 50]$ Hz coming from the acquisition (Figure 4.23). At the end the output is select choosing the block with the maximum accumulated variable. Now, the design of L is fundamental to determine the sensitivity of the estimation block. The discussion on this parameter is the focus of the next section.

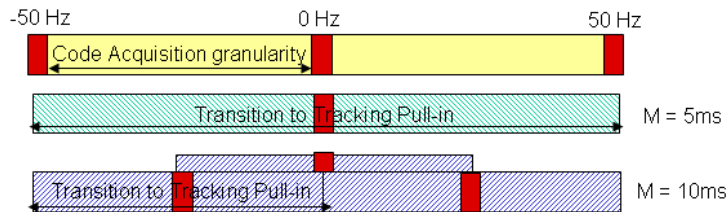


Figure 4.23: Transition to Tracking: Three hypotheses in parallel

4.3.1 Numerical results

In the following, the results for the Transition to Tracking block are reported. Note that if the error variance is calculated considering no errors in the choice of the the maximum accumulated variable, the choice of the three blocks and the exploitation of the maximum M represent the best solution. But, the exploitation of the three blocks, in very hard conditions, can bring to a wrong result. This is because a wrong choice of the maximum leads to a frequency estimate which is not correct and corresponds to a PLL stable point. On the other hand, the solution with $M = 5\text{ms}$, is sub-optimum for high SNRs, but represents the best solution for C/N_0 below approximately 32dBHz. Thus, if the solution of the three blocks is provided, a larger L should be accounted, since the crossing between the two lines depends from L .

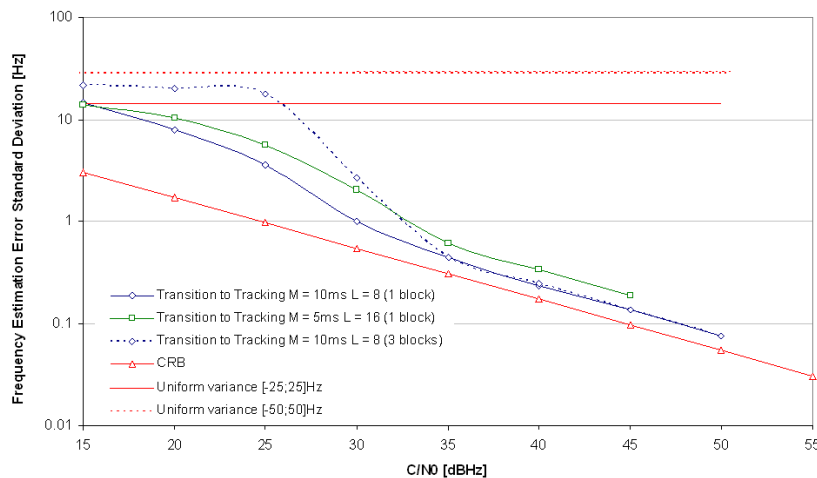


Figure 4.24: Transition to Tracking: Frequency Estimation Performance (Sampling Frequency= 122MHz - 1000 Iterations)

4.4 Code Tracking

Conventional GNSS receivers exploit exclusively the time-of-arrival ranging concept for user receiver position determination. The position is calculated from the distances between the user receiver and a set of satellites. To perform a continuous signal measurement (and thus continual pseudorange estimation) the feedback structure is generally used. The signal tracking process covers a carrier tracking and a

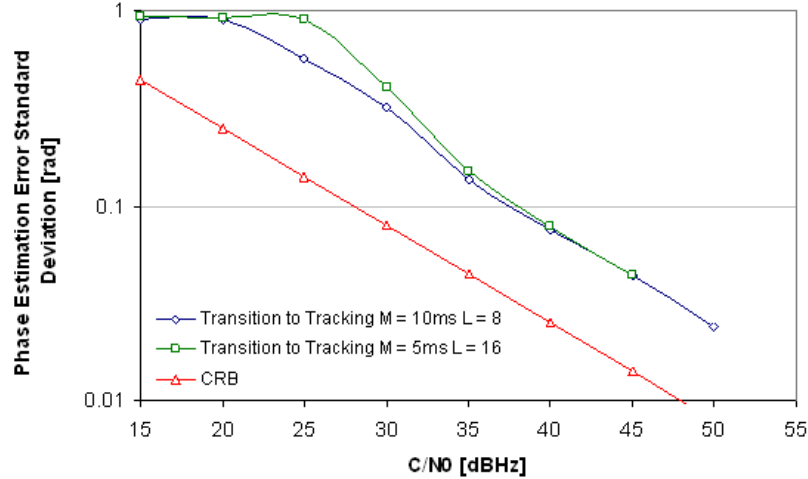


Figure 4.25: Transition to Tracking: Phase Estimation Performance (Sampling Frequency= 122MHz - 1000 Iterations)

code tracking, and both of them must be performed for correct receiver function. The code tracking process is necessary for pseudorange estimation. The feedback system for code tracking is represented by Delay Lock Loop (DLL) [64].

As detailed in the previous sections, for the E1-A signal the autocorrelation function presents several secondary peaks that can be detected instead of the correct one. For this reason, the main objective of the code tracking for high-order BOC modulated signals is to distinguish the correct peak in order to avoid biases in the positioning. In the following the state-of-the-art techniques are discussed, and a novel approach is introduced.

4.4.1 Bump Jumping technique

The fundamental scheme to perform the code tracking is the well known Early-Late gate. It consists of two correlations, one between the received code and an early replica, one between the received code and a late replica, in order to generate an error signal that drives a VCC (Voltage Control Clock) in a feedback loop. In the following the non coherent discriminator has been considered to generate the error signal. One pragmatic approach to overcome the problem of the false locks in high order BOC modulation is the Bump Jumping technique [65], that provides the classical Early-Late gate with two additional gates, Very Early (VE) and Very Late

(VL), intended to check the amplitude of adjacent peaks with respect to the Prompt (P) gate. For this reason, the algorithm foresees three counters, each associated with the VE, VL, and P. After every integration period, the absolute values of VE, P, and VL outputs are compared. The comparison with the amplitude of the Prompt gate indicates that a higher amplitude on VE or VL with respect to P is detected. If either the VE or VL sample is the largest, then the appropriate counter is incremented and the other one is decremented. If the P sample is the largest, then both the VE and VL counter are decremented. Neither counter is decremented below zero; and when either counter reaches a particular threshold, Th , the tracker is jumped to the new peak, and the counters are reset to zero.

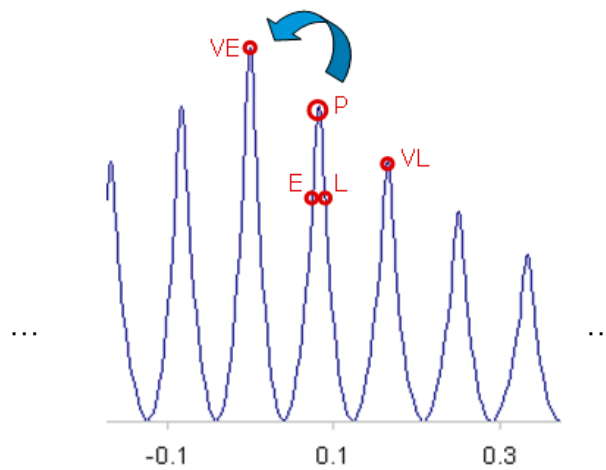


Figure 4.26: Bump Jumping false lock example

An example of the behavior of this technique is shown in Figure 4.27, considering AWGN and with a signal to noise ratio $C/N_0 = 35\text{dBHz}$. The main drawback of this method is that the receiver is essentially blind. It must be in a false lock condition before it knows that it is in this condition. Further, it can only move one sub-chip step at a time, and evaluation of relative amplitudes takes time. Moreover, in the presence of signal distortion, only a single delay is estimated (τ_c), leaving to the counters a kind of estimation of the other delay τ_s .

4.4.2 BPSK-like technique: Dual Sideband Technique

This technique, originally proposed in [61] for the generic BOC modulation, consists in considering the received $\text{BOCc}(15,2.5)$ signal as the sum of two BPSK signals

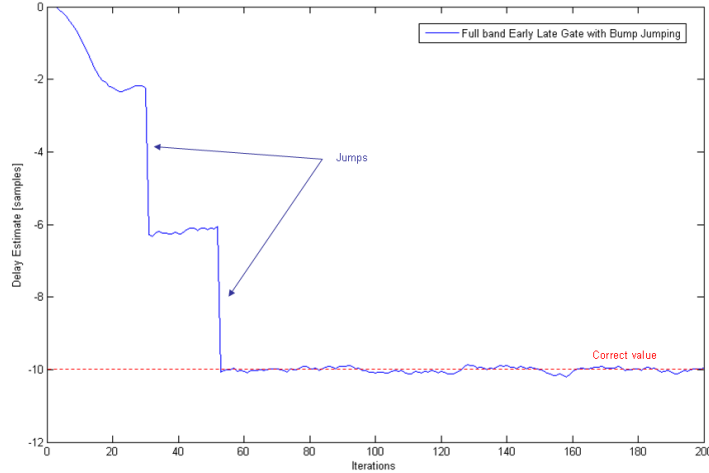


Figure 4.27: Delay Estimate: Full Band Tracking with Bump Jumping. AWGN $C/N_0 = 35\text{dBHz}$

with carrier frequency symmetrically positioned on each side of the BOC carrier frequency. Thus, each lobe is processed separately as a BPSK signal. Indeed, each lobe is correlated with a local BPSK reference consisting only of the code, centered respectively in $(F_{carrier} + f_{sc})$ and $(F_{carrier} - f_{sc})$ where $F_{carrier}$ is the carrier frequency and f_{sc} is the subcarrier frequency. Thus, the receiver has to account two correlation channels, one for the upper filtered sideband and one for the lower filtered sideband. Each correlation channel results in an unambiguous correlation function and then the two channels are then combined. The shape of the two autocorrelation functions (on the upper and lower sideband) and the resulting one can be approximated by the magnitude squared autocorrelation function of the BPSK signal.

Anyway, although the resulting correlation function is unambiguous, the advantages in terms of tracking performance are vanished if a BPSK-like technique is used, as can be seen in the preliminary result shown in Figure 4.29 in AWGN with $C/N_0 = 35\text{dBHz}$. The problem of false peaks is solved but the variance of the estimation error is not as good as the other techniques, since this technique results in a wider peak with respect to the classical $\text{BOC}(15,2.5)$.

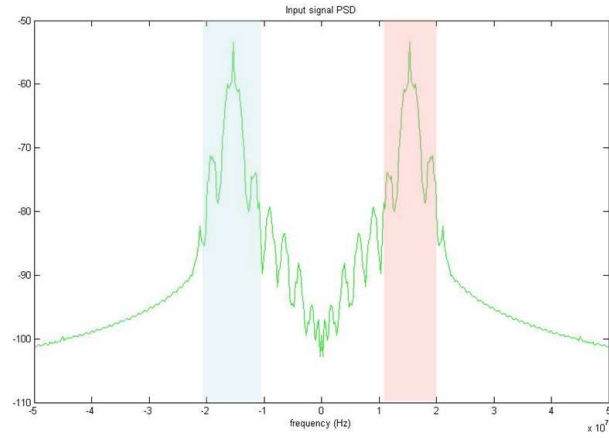
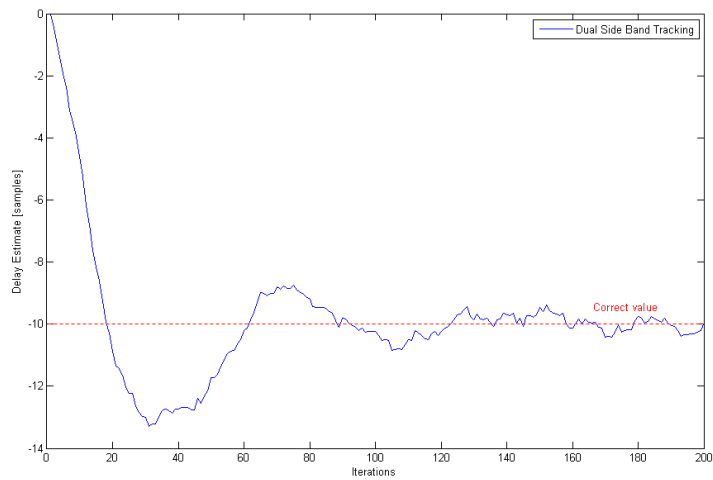


Figure 4.28: Dual Sideband Concept

Figure 4.29: Delay Estimate: Dual Sideband Tracking. AWGN $C/N_0 = 35\text{dBHz}$

4.4.3 Double Estimation Technique

The Double Estimation Technique has been proposed in [58]. It consists of three tracking loops as shown in Figure: a PLL to track the carrier, a DLL for the code tracking, and a sub-carrier locked loop (SLL) to track the sub-code component. The conventional principle of providing early and late gate correlations continues to be employed but is now generalized across two dimensions. The DLL and SLL separately generate the independent estimates as theory requires. Convergence of any one loop depends on convergence of the other two. All three loops run interactively and cooperatively. The following integrators are considered:

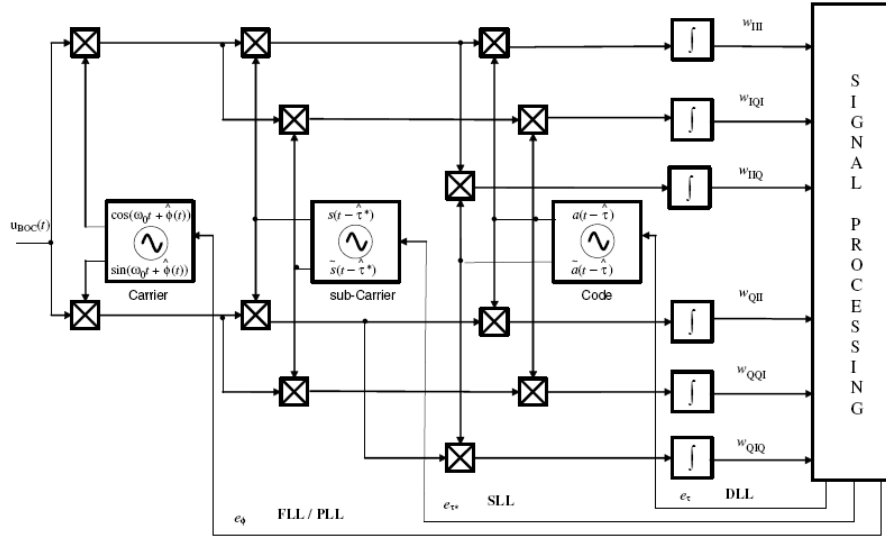


Figure 4.30: Double Estimation Technique block diagram

$$v_{III}(t) = v_I(t) \times s(t - \hat{\tau}_s) \times a(t - \hat{\tau}_c) \quad (4.15)$$

$$v_{IEI}(t) = v_I(t) \times s(t - \hat{\tau}_s + T_{DS}/2) \times a(t - \hat{\tau}_c) \quad (4.16)$$

$$v_{ILI}(t) = v_I(t) \times s(t - \hat{\tau}_s - T_{DS}/2) \times a(t - \hat{\tau}_c) \quad (4.17)$$

$$v_{IIE}(t) = v_I(t) \times s(t - \hat{\tau}_s) \times a(t - \hat{\tau}_c + T_{DC}/2) \quad (4.18)$$

$$v_{IIL}(t) = v_I(t) \times s(t - \hat{\tau}_s) \times a(t - \hat{\tau}_c - T_{DC}/2) \quad (4.19)$$

$$v_{QII}(t) = v_Q(t) \times s(t - \hat{\tau}_s) \times a(t - \hat{\tau}_c) \quad (4.20)$$

where $v_I(t)$ and $v_Q(t)$ represent the I and Q component of the baseband signal after the mixer and the filter, $a(t)$ is the BPSK local replica consisting only of the code, $s(t)$ is the local reference consisting only by the BOCc(15,2.5) subcode, $\hat{\tau}_s$

and $\hat{\tau}_c$ are the subcode and the code trial delays, T_{DS} and T_{DC} are the early late spacing, respectively, for the SLL and for the DLL. The outputs of the integrators are sampled, resulting in six correlations: $w_{III}^{(k)}$, $w_{IEI}^{(k)}$, $w_{ILI}^{(k)}$, $w_{IIE}^{(k)}$, $w_{IIL}^{(k)}$, $w_{QII}^{(k)}$.

Thus, computing the difference between early and late correlations the error functions for the code and for the subcode are calculated. At the end, beside the phase and the frequency estimates, two different delays τ_s and τ_c are obtained. In order to combine the two delays and to find the best representation in a single delay estimate, the following formula can be used:

$$\hat{\tau}_{final} = \tau_s + \text{round}\left(\frac{\tau_c - \tau_s}{T_{sc}}\right) \times T_{sc} \quad (4.21)$$

The resulting delay can be seen as the delay of the subcode nearest to the estimated

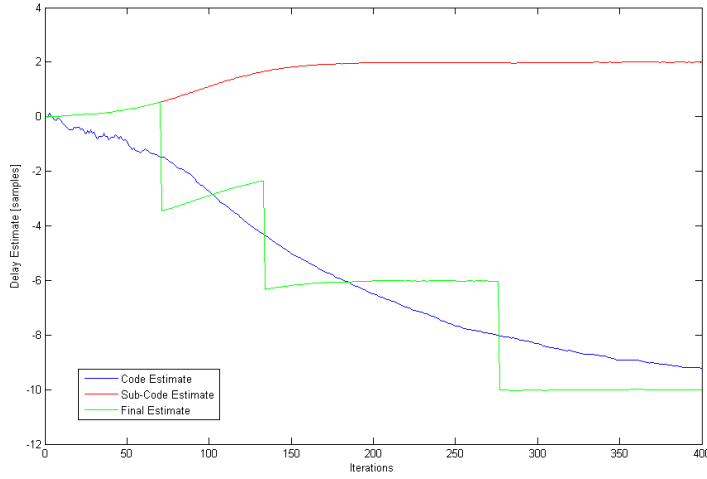


Figure 4.31: Double Estimation Technique. AWGN $C/N_0 = 42\text{dBHz}$

code delay, as shown in Figure 4.31. This expression represents the best solution when the two delays are the same or at least very similar, but it can bring to an erroneous estimation when the two delays are very far, because of signal distortion. In the following a deeper analysis of this combining is addressed.

4.4.4 DET Tracking in the Presence of Signal Distortion

As detailed in the previous sections, in the presence of signal distortion or multipath, the code delay and the subcode delay can be different. But the Double Estimator Technique seems to be designed considering the two delays equal to the same value.

This can be a problem in very hard condition, as shown in Figure 4.32 for a filtered case with a signal to noise ratio $C/N_0 = 30\text{dBHz}$.

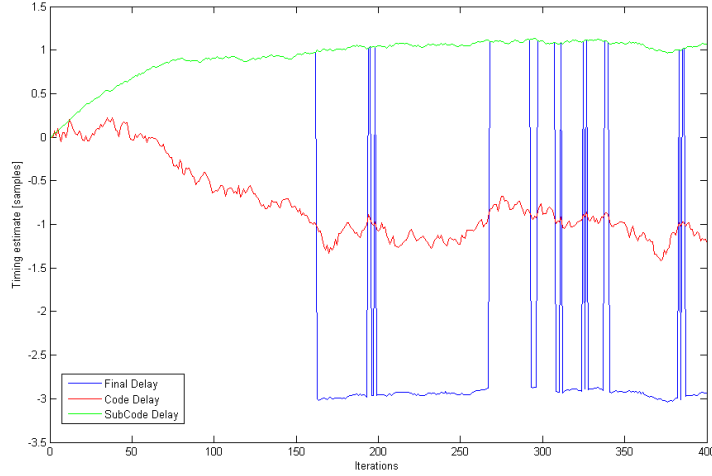


Figure 4.32: Double Estimation Technique in the presence of signal distortion. AWGN $C/N_0 = 30\text{dBHz}$

Note that continuous jumps between the peaks are present, since the code delay estimate, which is more noisy, can be easily above the threshold for the jump. This problem brings to unacceptable performance in terms of timing standard deviation, as it will be shown later.

4.4.5 Translating the Two Delays in a Single Delay

DET tracking is based on the powerful concept of the two dimensional correlation. On the other hand, in order to compute the PVT (Position Velocity and Time) a single delay for each satellite should be extracted. In the absence of signal distortion or multipath, the two delays are identical apart from some integer T_{sc} if a secondary peak is detected. On the other hand, in the presence of signal distortion, also if the first peak is detected, the resulting delays can be different. The correct delay of the signal is τ_c but it more noisy with respect to τ_s . On the other hand, τ_s is biased, but the variance of the estimate is lower with respect to the other.

4.4.5.1 Rounding Strategy

In [58], the formula of Equation 4.24 has been proposed. Here it is reported for the sake of simplicity:

$$\hat{\tau}_{final}^{(k)} = \tau_s^{(k)} + \text{round} \left(\frac{\tau_c^{(k)} - \tau_s^{(k)}}{T_{sc}} \right) \times T_{sc} \quad (4.22)$$

The idea behind this equation is to compute the delay estimate considering the delay of the subcode nearest to the estimated code delay. In fact, the delay of the subcode suffer the problem of ambiguity but is less noisy with respect of the delay of the code. This represent the best solution when the only problem is to distinguish the first peak with respect to the secondary ones. In this case, in fact, in absence of signal distortion or multipath, the two delays are identical apart from some integer T_{sc} . In the presence of signal distortion, since the resulting delays can be different, this expression can lead to bad performance.

4.4.5.2 Smoothing Strategy

A new approach is introduced in order to have an unbiased estimation, but with the variance driven by the τ_s estimate. The basic idea is to combine the two delays according the following equation:

$$\hat{\tau}_{final}^{(k)} = \frac{\tau_c^{(k)} - \tau_c^{(k-1)}}{M} + (\tau_s^{(k)} - \tau_s^{(k-1)}) \frac{M-1}{M} + \overline{\tau_c}^{(j-1)} \quad (4.23)$$

where M is the factor which drives the different weights for the two delays, and $\overline{\tau_c}^{(j-1)}$ is the average of the previous block $\tau_c^{(i)}$ with $i = i-L, \dots, i-1$. The smoothing has been inspired from the theory of the carrier smoothing, and can be seen as a Kalman filter output in steady state, where each estimate is smoothed according its accuracy. Note that this expression can be seen as a smoothing per blocks between the two estimates. Every block of length L the smoothing is provided, but at the end of a block the average value of τ_c in that block is forwarded to the next block. This way of combining the delays avoids jumps between peaks, but depending on M and L the final estimate tries to have the mean of τ_c and the variance of τ_s .

4.4.5.3 Averaging Strategy

The last proposal consists in a modification of the Round strategy. Being the code delay estimation more noisy with respect to the subcode delay, the following modi-

fication can be exploited:

$$\hat{\tau}_{final}^{(k)} = \tau_s^{(k)} + \text{round} \left(\frac{\frac{1}{M} \sum_{j=k-M}^k \tau_c^{(j)} - \tau_s^{(k)}}{T_{sc}} \right) \times T_{sc} \quad (4.24)$$

4.4.5.4 Numerical Results

Figures 4.33, 4.34, and 4.35 show the different approaches working in practical situations. In particular, Figure 4.33 shows the unfiltered case: in this case the two delays have a tendency to the same point and the rounding and the averaging strategies guarantee the best solution.

Figure 4.34 on the other hand shows a first important result: the rounding and the averaging strategies are influenced by the subcode delay instead of the code delay; the smoothing strategy, depending on M and L tries to have the mean of τ_c and the variance of τ_s . Last figure shows the behavior of the three approaches when the signal to noise ratio is very low ($C/N_0 = 30\text{dBHz}$), showing that jumps between the peaks are obtaining if the rounded approach is used; with the averaging the jumps are mitigated but they are still present, while the smoothing algorithm seems to be the best solution.

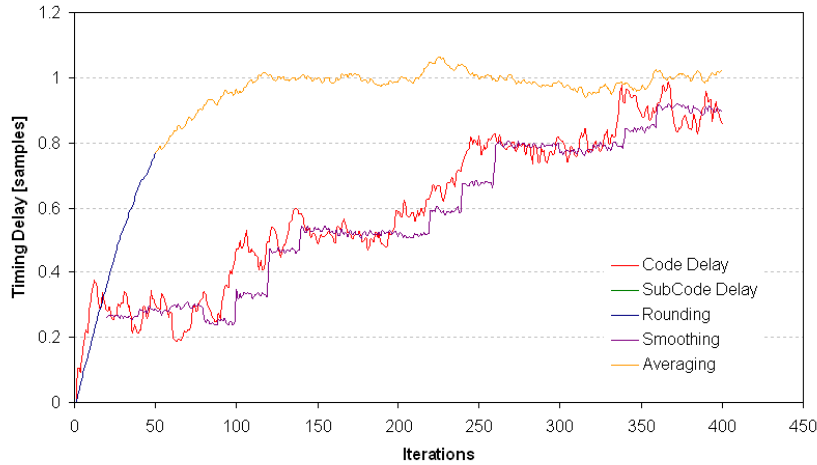


Figure 4.33: Combining of the two delays: unfiltered case

A better evaluation can be seen if the mean and the standard deviation of the tracking error are reported for the three approaches. Note that in the unfiltered case (Figure 4.36) the rounding and the averaging approaches guarantee the best

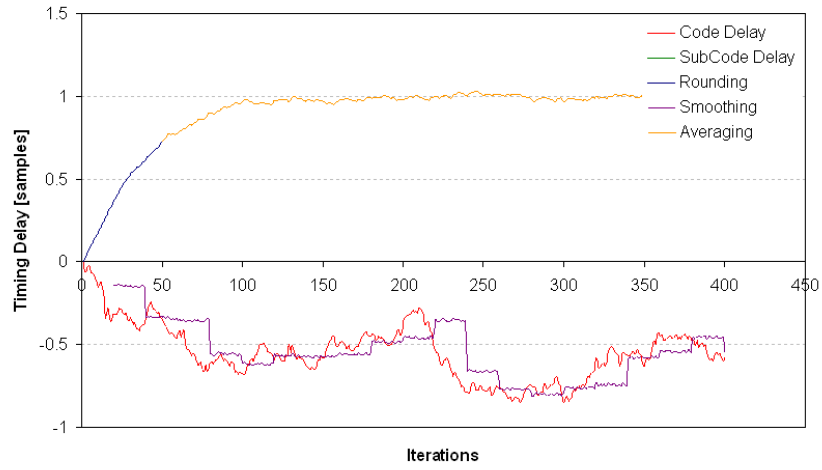


Figure 4.34: Combining of the two delays: filtered case

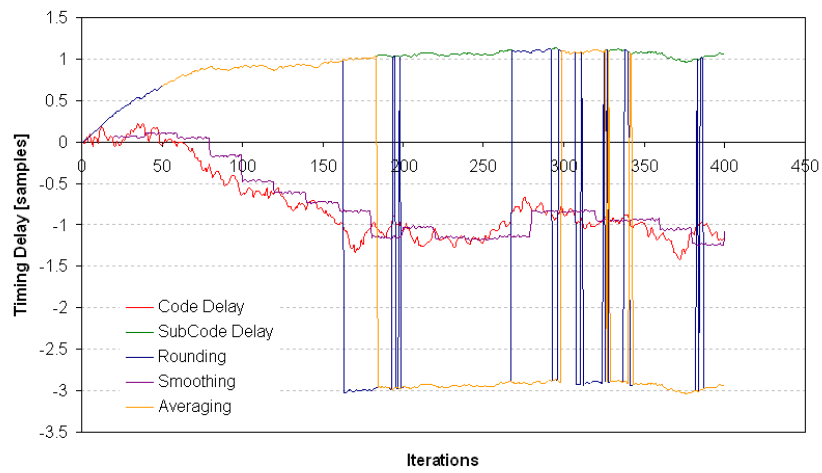


Figure 4.35: Combining of the two delays: filtered case, very low SNR

performance. The smoothing strategy presents a higher standard deviation, and a mean which is more sensitive to the fluctuations of τ_c .

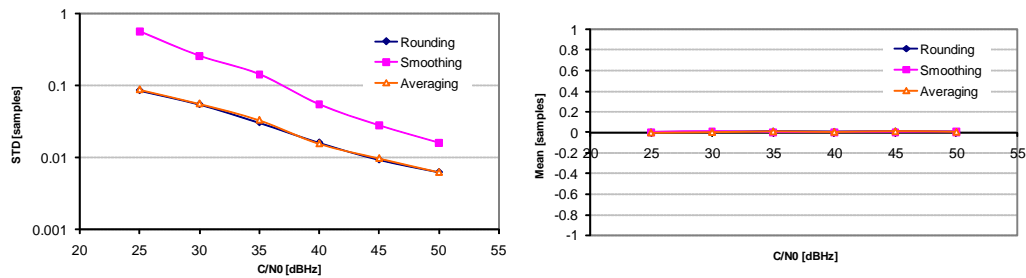


Figure 4.36: Standard Deviation and Mean of the tracking error: unfiltered case

On the other hand, Figure 4.37 shows the standard deviation and the mean of the tracking error in the presence of distortion. In this case, the mean of the error of the smoothing approach is approximately zero, while the rounding and the averaging strategies, following the behavior of τ_s , present a biased estimate. Moreover, the standard deviation of the rounding strategy is always below of the one calculated with the smoothing approach, except for very low SNRs where the jumps between peaks bring to worse performance. Note that, the averaging strategy can solve the problem of the jumps, bringing to the best, but biased, estimate. For these reasons, the most robust approach results to be the smoothing strategy.

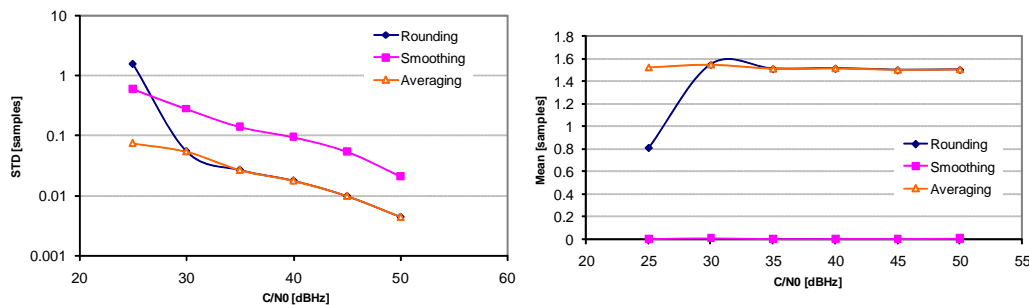


Figure 4.37: Standard Deviation and Mean of the tracking error: filtered case

4.4.6 Code Tracking Numerical Results

Figure 4.38 shows the standard deviation of the code tracking loops for the filtered case. Note that for very low SNR the DET tracking (here reported with the original rounding strategy and with a wider spacing for the DLL with respect of the previous figures) shows a very bad behavior due to the unexpected jumps, while the DSB tracking is less accurate with respect to the others. The full band tracking is a very good approach but in this case the starting point coming from the acquisition corresponds to the first peak, avoiding the problem of the false locks, which, on the other hand, can lead to harmful biases. In conclusion, it can be observed that all these detectors have been designed for ideal scenarios and they are not robust in the presence of linear distortion.

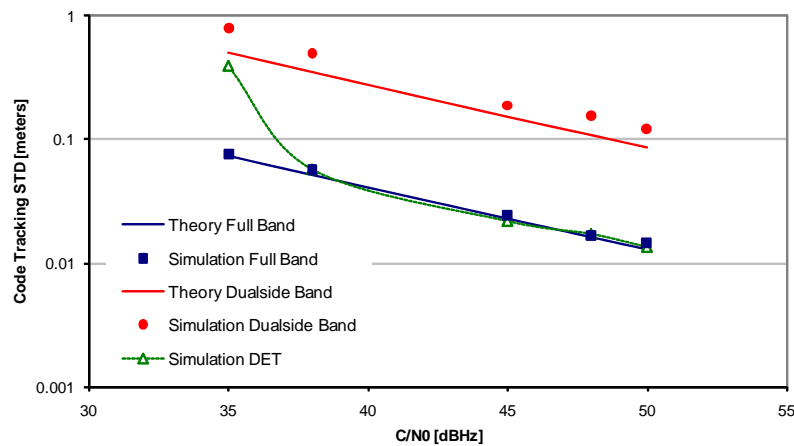


Figure 4.38: Code Tracking: standard deviation

4.4.7 Code Tracking in the Presence of Multipath

Multipath is one of the most important source of ranging error in GNSS. As seen in Section 4.1.3, BOCc(15,2.5) should be more robust with respect to other modulations against multipath, but in realistic scenario tracking can be very challenging. Figure 4.39 shows the Multipath Error Envelope for the different tracking algorithms. Note that the classical full band technique and DET present the same behavior, apart for the point corresponding to the delay T_{sc} , in which the DET technique shows a jump in the other peak with consequently increase in the error variance.

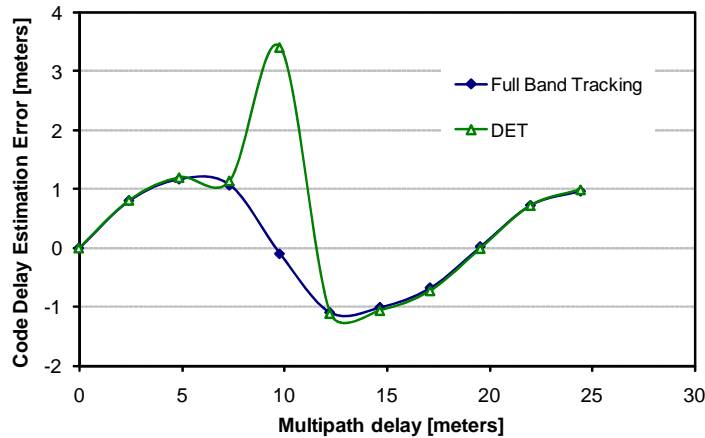


Figure 4.39: Multipath Error Envelope for different tracking algorithms

4.5 Acquisition and Tracking of the E1-A Signal: Conclusions

This chapter showed that all the state-of-the-art techniques (Full correlation with Bump Jumping, Dual Side Band Tracking, and also Double Estimator Technique) have been designed for ideal scenarios and they are not robust in the presence of linear distortion, leading to unsatisfactory performance in terms of code tracking Mean Square Error (MSE). The DET strategy, in particular, is based on the powerful concept of the two-dimensional correlation, but seems to prefer as the final output the subcarrier delay. This is less noisy, but it can be biased since it is affected from the phase delay, with respect to the noisy but unbiased code delay. For this reason a new way to combine the different estimates has been proposed, identified as Smoothing Strategy, which, trying to obtain a final estimate with the mean of τ_c and the variance of τ_s , guarantees better performance.

5

Integrated NAV-COM Systems: Assisted Code Acquisition and Interference Mitigation

Assisted GNSS (A-GNSS) is a technology that supports GNSS devices and enables faster and more reliable position determination in a receiver than could be achieved using the broadcast GNSS satellite data only. It is based on the presence of a communication network able to provide assistance data and significantly simplify the positioning procedure, improving code synchronization performance at the same time.

These assistance data include, among other things: navigation models for ephemerides and clock corrections, reference location, ionosphere models, Doppler and time reference corrections, and optionally differential corrections for high-accuracy positioning and data bit assistance for high sensitivity.

In the following, the A-GNSS concept is recalled and extended to comprise also precise interference characteristics, such as interference frequency, direction of arrival, power. This is achieved by foreseeing in the overall network architecture the presence of a local infrastructure able to estimate and characterize the interference,

augmenting the GNSS system with essential local components specifically designed to ease the system integrity signal and quality of service (QoS).

Thus, a receiver able to fruitfully exploit the assistance data in order to compute Interference Mitigation (IM) jointly with the classical code synchronization should be realized as depicted in Figure 5.1. Note that the IM filter can be activated or deactivated depending on the interference characteristics, as discussed in detail in the following.

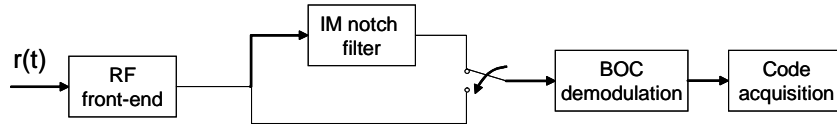


Figure 5.1: Receiver logical block diagram

The evaluation of the impact of the interference in the code acquisition and the design of efficient rejection techniques have been conducted in [66] for a classical spread spectrum system. Herein, a study on code acquisition aided by interference mitigation has been carried out for the Galileo system in E1 band Open Service signals, which presents a BOC modulation scheme.

Note that the classical implementation of A-GNSS to facilitate navigation and positioning requires limited modifications to the ground network architecture, calling for one or a few assistance servers that are in general sufficient to cover an entire region. Each server is a centralized entity which, by exploiting the knowledge of the ephemeris of the GNSS constellation, is able to precisely estimate the Doppler and time reference corrections to be broadcast to each cell in the cellular communication network.

Differently, assistance data for interference mitigation has in general a strong impact on the ground network architecture because interference sources are usually located in specific areas with limited electromagnetic visibility, requiring the adoption of a widespread ancillary network to estimate their characteristics. For this reason, critical areas (e.g. airports or military zones) are usually served by Interference Observation Sensors (IOSs) in order to provide secure islands with guaranteed positioning QoS. The IOSs are devices able to detect the presence of interfering signals and to provide estimates of their frequency, bandwidth, sweep rate, and direction of arrival [67]. Fixed IOSs are in general the preferred solution when accurate interference localization is needed, and accordingly these stations are equipped with phased array antennas. Data coming from all IOSs pertaining to a specific

area are then processed by an Interference Control Center (ICC) that extrapolates the necessary information to be broadcast. Inspired by what is currently under design in the Galileo context [18], this new interference management system extends the GNSS local component, already in charge of local augmentation (e.g. through broadcasting of differential corrections) and local integrity monitoring, by limiting their vulnerability against interference. Besides the fixed IOSs, also mobile IOSs are here envisaged in order to adaptively and dynamically assist also different areas, for example in case of emergency; this choice is in line with the fact that the proposed IM applied at the receiver does not exploit the spatial degree of freedom, to limit mass market terminals complexity. In essence, mobile IOSs are enhanced GNSS terminals with relaxed constraints in terms of battery consumption, since they incorporate all the processing needed for detecting/classifying the interference, beside their normal communication capabilities.

The corresponding navigation-communication (NAV-COM) architecture is depicted in Figure 5.2. Here, the information fused by the ICCs is conveyed to the relevant A-GNSS server that delivers to the user the interference mitigation message along with the navigation assistance data through the cellular network.

To provide an idea of the quantitative gains offered by the assistance GNSS concept, Table 8.1 compares a typical scenario of A-GNSS with the autonomous GNSS counterpart, presenting the main characteristic parameters that are considered in Section 5.2 for numerical performance analysis. Here, the autonomous case is assumed to operate with a detector that tackles the frequency uncertainty by testing different frequency hypotheses in parallel, so that in each branch a residual frequency offset $f_e = 1\text{kHz}$ can be considered. Note that for cold start code acquisition, where it is reasonable to quantify an overall carrier frequency uncertainty up to $\pm 20\text{kHz}$ in the E1 band due to oscillator instability (in the order of 10ppm) plus uncompensated Doppler [19], this choice corresponds to adopt a degree of parallelism equal to 20 in the code synchronization subsystem, increasing the resulting complexity with respect to what is achievable in the assisted case. When assistance is implemented in the network, the available a-priori information allows to reduce the frequency error, and A-GNSS can consequently gain from longer coherent integration time windows, with considerable benefits in terms of code acquisition performance. In fact, it is reasonable to assume that the assisted receiver is locked onto the communication network base station, which is usually characterized by good quality oscillators, and thus it is able to reduce the carrier frequency offset within a small residual uncertainty that

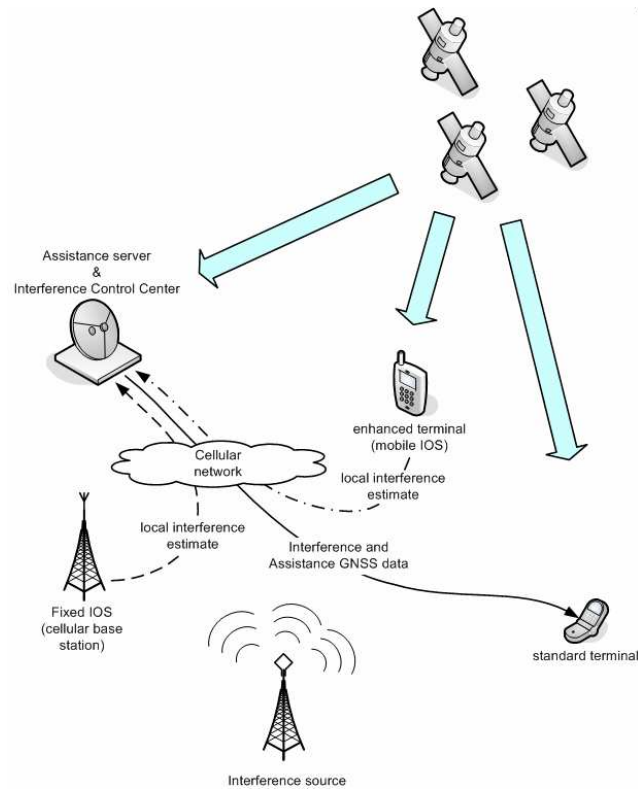


Figure 5.2: Integrated navigation-communication system architecture for A-GNSS with interference mitigation

for mass market terminals can be quantified in the order of 200Hz (0.1ppm). Then, the assistance network broadcasts a further carrier correction accounting for Doppler shifts, yielding to an additional residual offset, which also is in general in the order of 100-200Hz. Therefore, exploiting a modest parallelism in the frequency domain, e.g. testing 4 frequency hypotheses, the assisted detector can operate with a small overall frequency error, here assumed equal to 100Hz, with conspicuous complexity reduction. Note that the autonomous receiver should extend its parallelism up to the very large value of 200 to reach the same reduced uncertainty as the A-GNSS case.

Besides the a-priori information on carrier frequency uncertainty, the assistance network provides indications about the code phase search window. This implies that, while code acquisition in the autonomous case must cope with the maximum time uncertainty equal to 4092 chips for the Galileo *E1* signal as discussed in the following, the assisted code acquisition procedure can limit the search procedure onto a reduced time window, which is here assumed equal to 2046 and 1023 chips.

Finally, the assistance network delivers to the receiver the necessary side information to put in place useful interference mitigation techniques, which may further improve code acquisition performance with respect to the autonomous case, especially when large power interferers affect the reception.

	Autonomous GNSS	Assisted GNSS
Residual frequency error	1kHz	100Hz
Code epoch uncertainty region	4092	2046, 1023
Interference estimate	not available	available

Table 5.1: Scenario definition for autonomous and assisted GNSS

The impact of the proposed assistance network on positioning and interference performance is evaluated herein considering autonomous positioning as a reference, with and without interference mitigation, in outdoor environment. Note that some of the results shown in the following have been already published in [5] and [6], and my original contribution lies in the analytical evaluation of the code acquisition of BOC modulated signals in the presence of interference, and in the presence of the interference mitigation filter.

5.1 The Presence of Interference in a GNSS System

The specific GNSS signals addressed in the paper for quantitative investigation are the Galileo Open Service signals in E1.

Notably, the spread spectrum nature of the Galileo signal already provides an inherent robustness against interference that is one-to-one related with the exploited spreading factor N . Moreover, the presence of BOC, with its spectrum nulls in correspondence of the Galileo central frequency, introduces an additional degree of robustness against narrow band interferers that present the same frequency as the useful carrier. However, the joint exploitation of these advantages is often not sufficient, especially in order to combat high power interference with variable central frequency [68].

Considering transmission in Additive White Gaussian Noise (AWGN), the low-pass equivalent of the received signal is in the form

$$r(t) = s_{E_1}(t)e^{j[2\pi f_e t + \zeta]} + i(t) + n(t) \quad (5.1)$$

where f_e is the carrier frequency error, ζ is the unknown phase of the useful signal, which is assumed to be uniform in $[0, 2\pi[$, $n(t)$ is the complex AWGN noise random

process with two-sided power spectral density N_0 , and

$$i(t) = \sqrt{I}e^{j[2\pi f_i(t)t+\phi]} \quad (5.2)$$

is the continuous wave (CW) interference component modeled as a tone interference with power I , with variable instantaneous frequency (e.g. according to a sweep) as $f_i = f_i(t)$, and random phase ϕ uniformly distributed in $[0, 2\pi[$. Note that, in the assisted case, f_i differs from the estimate \hat{f}_i provided by the assistance network of a quantity f_e , which is small and can be neglected if an IM technique sufficiently robust against limited Instantaneous Frequency (IF) variations is put in place at the receiver. Indeed, this is the case for the notch filtering approach discussed in Section 5.1.1.

The received signal of Equation (5.1) undergoes matched filtering followed by sampling at the time instants $t_k = kT_{sc} + (\Delta + \delta)T_c$, where $\Delta \in \mathbb{Z}$ and $\delta \in [-1/2, 1/2]$. Notably, δ accounts for practical non ideal chip sampling instants, while Δ distinguishes between the H_1 and H_0 code acquisition hypotheses, i.e. $\Delta = 0$ denotes the synchronous case of H_1 and $\Delta \neq 0$ indicates all misaligned H_0 cases. The presence of a residual timing offset $\delta \neq 0$ is particularly critical with BOC modulation, calling for the adoption of specific countermeasures such as large oversampling, e.g. 4 hypotheses per symbol exploited by the code acquisition procedure, or the introduction of detectors robust against timing errors, as explained in [1], [7] and [8]. In the following, the assumption of ideal sampling, i.e. $\delta = 0$, is introduced to focus the attention on the interference impact, leaving to the interested reader the straightforward generalization to the case of non ideal sampling instants. Accordingly, the received samples can be written as

$$\begin{aligned} r_k = & \sqrt{\frac{E_s}{2}} e^{j(2\pi f_e k T_{sc} + \zeta')} (-1)^k \left(c_{B, \lfloor |k|_2 + \Delta \rfloor_N} d_{\lfloor |k+2\Delta|_{2N}} - c_{C, \lfloor |k|_2 + \Delta \rfloor_N} \right) \\ & + A_I e^{j(\pi \nu_I k + \phi')} + n_k = \rho_k + i_k \end{aligned} \quad (5.3)$$

where ν_I is the instantaneous interferer baseband equivalent frequency normalized to the chip rate, i.e. $\nu_I = f_i T_c$, $A_I = \sqrt{I} \text{sinc}(\nu_I/2)$ is the equivalent amplitude of the interference component after matched filtering, n_k are the AWGN samples that are complex zero-mean Gaussian random variables with in-phase and quadrature variance $\sigma_n^2 = N_0/2$, and $\zeta' = \zeta + 4\pi f_e T_c \Delta$ and $\phi' = \phi + 2\pi \nu_I \Delta$ are respectively the resulting unknown phases for the useful and the interfering terms, which are independent and uniformly distributed in $[0, 2\pi[$. Finally, ρ_k is the term comprising the desired signal plus AWGN, while $i_k = A_I e^{j(\pi \nu_I k + \phi')}$ indicates the interference component, the excision of which is described in the next section.

5.1.1 Low-Complexity Interference Mitigation

Several examples of IM applied to GNSS can be found in the literature, operating in either time, frequency, or space domains [69], [67], [70], [71], which however are suitable only against interference with slow dynamics. To combat interferers that are concurrently variable in more than one domain with faster dynamics, joint domain IM [72], [73] is effective to mitigate interference with limited distortion on the useful signal. In this framework, the space domain is often exploited through the introduction of antenna arrays in the receiver [74] [75], [76], [77]. This provides effective countermeasures against narrowband and wideband interference, at the cost of increased terminal complexity. To provide a more economic solution generally applicable to the mass market scenario, a low complexity IM solution, which jointly exploits time and frequency domains, minimizing the impact on the terminal cost [73] [78] is herein investigated. This IM technique is able to fully excise a narrowband CW interference, such as the one modeled in Equation (5.1), by exploiting a finite impulse response (FIR) filter that creates an infinite notch continuously adapted to the interference IF. Of course, the price is paid in terms of distortion induced over the useful signal, so that it can be convenient to switch IM off when the impact of the unexcised interference on the desired signal is limited with respect to inter-symbol interference (ISI) caused by IM itself. This interesting trade-off between the potential benefits of IM and its induced distortion is deeply investigated in the following by evaluating the impact on code acquisition performance. The selection of a FIR filter instead of an Infinite Impulse Response (IIR) has been driven by the need for a faster adaptation capability, at the cost of a less defined notch in frequency, which however results to be useful in terms of robustness against non ideal IF estimates. Accordingly, the FIR filter with 5 taps proposed in [78] is considered. Notch filtering is applied in the receiver after frequency down conversion and before BOC demodulation, i.e. by processing directly the samples described in Equation (5.3); notably, this approach has been demonstrated in [78] to outperform the alternative of acting after BOC demodulation for a wide range of interference IF values. The filter digital impulse response at the time instant k can be written as

$$h_k = \frac{1}{K} \sum_{j=-2}^2 a_j \delta(k - j) \quad (5.4)$$

where $\delta(\cdot)$ is the Kronecker delta function and the filter coefficients are given by

$$\begin{aligned} a_{-2} &= a_2 = 1 \\ a_{-1} &= a_1 = -4 \cos(\pi\nu_I) \\ a_0 &= 2 + 4 \cos^2(\pi\nu_I) \end{aligned} \quad (5.5)$$

where K is the normalization constant selected so that the filter response is normalized in energy, i.e.

$$K = \sqrt{2 [8 \cos^4(\pi\nu_I) + 24 \cos^2(\pi\nu_I) + 3]} \quad (5.6)$$

Notably, the filter introduces a constant delay in the received sample flow, which is compensated by neglecting its first two output samples.

The corresponding amplitude frequency response is depicted in Figure 5.3, where the dependence on the interference IF is highlighted by the three dimensional plot, showing that the notch moves to track IF modifications.

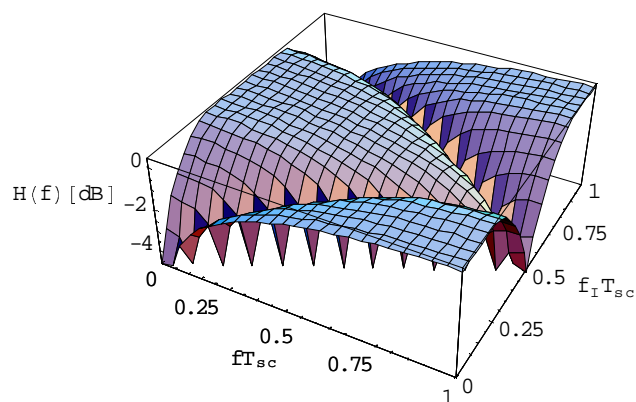


Figure 5.3: Amplitude frequency response of the 5 taps notch filter vs. frequency and interference IF normalized to T_{sc} .

The adoption of real coefficients for the filter taps translates into a symmetric frequency response, which introduces a null also in correspondence of negative frequencies. This causes unwanted additional degradation when an ideal complex exponential tone interference affects the reception. However, a complex filter would have double complexity and longer transients in adaptive tracking mode. For these reasons, in the following only FIR filters with real coefficients have been investigated.

The presence of the notch filter in the receive chain allows to fully excise the tone interference, irrespectively of the actual interference power, under the assumption that precise information about its IF is provided to the receiver by the assistance network. In particular, the mobile or fixed IOS components implement accurate estimation algorithms, e.g. based on Time-Frequency Distribution (TFD) [79], able to provide sufficiently precise interference IF estimates that are promptly signaled to the other user equipments to efficiently adapt their IM filter.

It is important to highlight that there exists a limit in the maximum tolerable dynamics that can be handled by the mitigation circuit. First of all, the 5-taps structure is only able to handle interferers that are practically invariant over a time window equal to the FIR tapped delay line duration, equal to $5T_{sc}$ in this case. Secondly, because interference information is signalled through the assistance network, there is a propagation delay issue to be tackled. To this aim, a system synchronization signal must be distributed throughout the network. Accordingly, considering for example a linear chirp interference, the IOS transmits the interference initial frequency and slope, which are corrected by the terminal compensating for the delay. This compensation strategy results in an imperfect IF knowledge, which however is partly balanced by the fact that the filter notch has a practical width that makes the strategy robust against residual interference jitters. Of course, this strategy fails when very rapid interference dynamics are experienced, calling for local interference detection and estimation as a more effective countermeasure. Alternatively, the filter coefficients can be updated run-time by using an adaptive algorithm, like least-mean-square (LMS) [69][67], so requiring a less frequent estimation and delivery from the IOS components.

The performance of the proposed IM technique can be analytically characterized in terms of Signal-to-Interference-plus-Noise Ratio (SINR), so providing an interesting instrument for fast evaluations of the inter-chip interference (ICI) impact and of the possible interference residual over the desired signal. Following an approach similar to [78], the SINR characterization is here carried out by considering the effects of BOC.

Considering ideal interference excision, i.e. perfect interference excision and absence of residual interference, the samples y_ℓ at the output of the notch filter can be written as

$$y_\ell = \frac{1}{K} \sum_{j=-2}^2 \rho_{\ell-j} h_j \quad (5.7)$$

i.e. only the desired signal plus AWGN (ρ_k component of Equation (5.3)) contribute in forming the output signal. The SINR evaluation is done after BOC demodulation and partial correlation over M chips, which is one-to-one with code acquisition ROC performance.

By substituting Equation (5.5) into Equation (5.7), the output of BOC demodulation and partial coherent correlation is a Gaussian random variable with mean value equal to

$$\mu_m = \frac{2\sqrt{E_s}\text{sinc}(f_e MT_c)}{K} \{M [1 + 2 \cos(\pi\nu_I) + 2 \cos^2(\pi\nu_I)] + R_m(1) [1 + 2 \cos(\pi\nu_I)]\} \quad (5.8)$$

and variance given by

$$\sigma^2 = \frac{M}{K^2} \sigma_n^2 \left\{ [1 + 4 \cos(\pi\nu_I)]^2 + [2 + 4 \cos^2(\pi\nu_I) + 4 \cos(\pi\nu_I)]^2 + 1 \right\} \quad (5.9)$$

where the deterministic term

$$R_m(1) = \sum_{h=mM}^{(m+1)M-1} c_{C,|h|_N} c_{C,|h+1|_N} \quad (5.10)$$

is the partial autocorrelation function of the primary code sequence computed in correspondence of a delay equal to one chip starting from the (mM) -th chip. The derivation of Equations (5.8) and (5.9) has been provided in Appendix 5.4, neglecting the presence of data, and without considering the interference of the B channel, which has been accounted for in the following.

Note that the Galileo E1 primary code are constructed so that $R_m(1) \simeq 0$ when computed with $M = N = 4092$, i.e. the full out-of-phase autocorrelation function is very low. This property is not strictly verified when only partial coherent accumulation is performed, i.e. with $M < N$. However, exhaustive numerical evaluations have demonstrated that in this case $R_m(1)$ results to be invariant with m for all practical purposes and it can be safely neglected without loss in generality. Accordingly, the corresponding SINR can be evaluated as

$$\text{SINR} = \frac{\mu_m^2}{\sigma^2} = \gamma \frac{4M \text{sinc}^2(f_e MT_c) \{ [1 + 2 \cos(\pi\nu_I) + 2 \cos^2(\pi\nu_I)] \}^2}{[1 + 4 \cos(\pi\nu_I)]^2 + [2 + 4 \cos^2(\pi\nu_I) + 4 \cos(\pi\nu_I)]^2 + 1} \quad (5.11)$$

where γ is the equivalent signal-to-noise ratio (SNR) characterizing the chip of the pilot C code, which is given by

$$\gamma = \frac{E_s/N_0}{2 + E_s/N_0} \quad (5.12)$$

where E_s/N_0 is the SNR associated to the chip of the C signal if no signal B were transmitted, the additional term in the denominator takes into account the interference due to the presence of the B channel.

An example of the dependence of SINR on the interference IF ν_I is given in Figure 5.4 considering $M = 4092$ and $E_s/N_0 = -25\text{dB}$ (equivalent to $C/N_0 = 35\text{dBHz}$, typical of outdoor scenarios), corresponding to a SNR of 11.12dB on each primary code period (NT_c). Note that the $1/\sqrt{2}$ normalization in Equation (5.3) along with

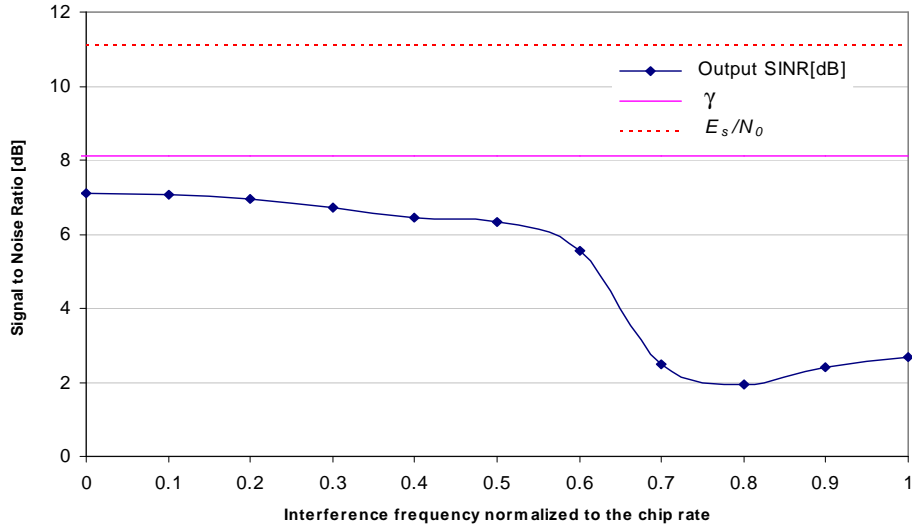


Figure 5.4: SINR at the filter output vs. interference IF normalized to T_c , $E_s/N_0 = -25\text{ dB}$, $M = 4092$.

the interference induced by the presence of the B channel causes a degradation of about 3dB , so that the effective input γ is 8.12dB , which is also reported in the figure as a reference. Interestingly, the filter effect on the resulting SINR after coherent correlation is strongly dependent on the interference IF, presenting the worst behavior for $\nu_I = 0.8$, where a degradation of 6.19dB is introduced, and the best performance for $\nu_I = 0$, with a SNR decrease of 1dB . This behavior demonstrates that the well known dependence of the receiver SINR on the actual interference central frequency [80] is still present also when interference mitigation is applied through notching confirming the results presented in [81], because in this case a different amount of distortion is introduced according to the jammer IF in order to nullify the interference component.

5.1.2 Code Acquisition Strategy

Considering the specific case of Galileo E1 band, the hierarchical code structure of the pilot channel can be fruitfully exploited at the receiver to perform low complexity code acquisition, by splitting the overall synchronization into two steps: first, the alignment with the primary code is recovered exploring an uncertainty region equal to the primary code length (4092 chips) in the autonomous case. Then, secondary code synchronization is achieved, and this is in general a less critical task because it can be completed after frequency estimation and timing recovery. Thus, this chapter focuses on the most challenging problem of primary code acquisition.

The hybrid approach of testing different frequency hypotheses in parallel jointly with PDI techniques is used, since it represents a good performance/complexity trade-off. This approach, applied to mass market receivers, with limited parallelism, allows to optimize the code detection scheme for the operation with a frequency error in the range of 1kHz in the autonomous case. In the scenario at hand, NCPDI, depicted in Figure 5.5, turns out to be the most convenient solution, providing a satisfactory performance with limited complexity along with fully analytical characterization [43]. In fact, due to the very low SNR, the other PDI detectors do not manage to introduce significant improvements. In the following, the performance assessment is done considering the correct frequency hypothesis only in the parallel detector structure, in order to simplify the analytical treatment. The extension to the parallel frequency testing case results in a slight performance degradation as shown in [82].

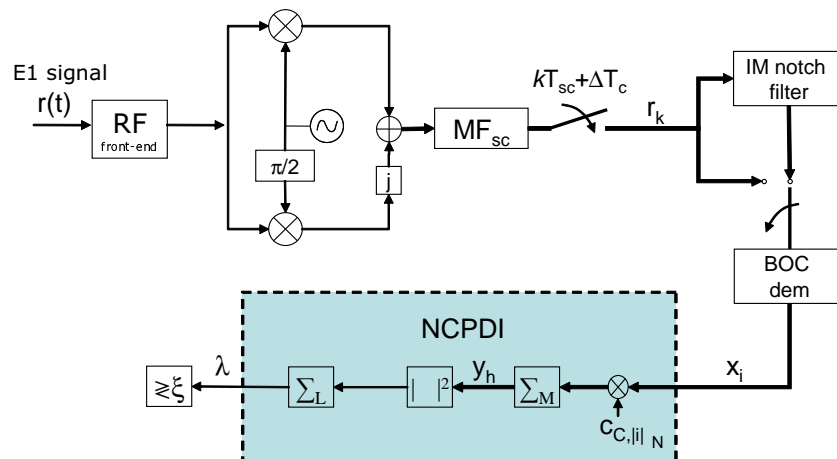


Figure 5.5: NCPDI block diagram

5.1.3 NCPDI Performance Analysis in the Presence of Interference

The signal at the output of the rectangular matched filter represented in Equation (5.3) is processed by the BOC demodulator, which can be considered as a despreading block with spreading sequence equal to $(1/\sqrt{2}, -1/\sqrt{2})$, yielding

$$\begin{aligned}
 x_i &= \frac{1}{\sqrt{2}} \sum_{k=0}^1 (-1)^k r_{k+2i+2\Delta} = \\
 &= \sum_{k=0}^1 \frac{\sqrt{E_s}}{2} e^{j(2\pi f_e(k+2i+2\Delta)T_{sc}+\zeta')} (c_{B,|k+2i+2\Delta|_{2N}} d_{[k+2i+2\Delta]_{2N}} - c_{C,|k+2i+2\Delta|_{2N}}) \\
 &+ \sum_{k=0}^1 (-1)^k \left(\frac{A_I}{\sqrt{2}} e^{j(\pi\nu_I(k+2i+2\Delta)+\phi')} + n_{k+2i+2\Delta} \right) \quad (5.13)
 \end{aligned}$$

Algebraic manipulation of Equation (5.13) yields

$$x_i = \sqrt{E_s} e^{j(2\pi f_e i T_c + \theta)} (c_{B,|i+\Delta|_N} d_{[i+\Delta]_N} - c_{C,|i+\Delta|_N}) + \sqrt{2} A_I \sin\left(\frac{\pi\nu_I}{2}\right) e^{j\varphi} e^{j2\pi\nu_I i} + \eta_i \quad (5.14)$$

being θ the resulting useful signal phase, which is still uniformly distributed in $[0, 2\pi]$, $\varphi = \phi' + 2\pi\nu_I\Delta + \pi\nu_I + 3\pi/2$, η_i the AWGN noise samples after BOC demodulation.

Then, the x_i samples are coherently correlated with the locally generated sequence $c_{C,|i|_N}$

$$\begin{aligned}
 y_h &= \sum_{i=hM}^{(h+1)M-1} \sqrt{E_s} (c_{B,|i+\Delta|_N} d_{[i+\Delta]_N} c_{C,|i|_N} - c_{C,|i+\Delta|_N} c_{C,|i|_N}) e^{j(2\pi f_e i T_c + \theta)} \\
 &+ \sqrt{2} A_I \sin\left(\frac{\pi\nu_I}{2}\right) e^{j\varphi} \sum_{i=hM}^{(h+1)M-1} e^{j2\pi\nu_I i} c_{C,|i|_N} + \sum_{i=hM}^{(h+1)M-1} \eta_i c_{C,|i|_N} \quad (5.15)
 \end{aligned}$$

According to Equation (5.15), under the H_1 hypothesis ($\Delta = 0$), the sample y_h is composed by the useful deterministic part, the term related to the unknown data bits of the B channel that are i.i.d. (independent identically distributed) binary ± 1 valued random variables (rv's), the interference component, and the AWGN term. As a consequence, it is difficult to express the probability density function of y_h in a tractable form. Notably, thanks to the auto-correlation properties of the Galileo C sequence, it is possible to neglect the self-noise of the pilot code, while the cross interference caused by the B channel has been conservatively taken into account by assuming $d_{[i+\Delta]_N} = +1$. Thus, y_h results to be complex Gaussian distributed as

$$y_h \sim \tilde{\mathcal{N}}(\mu_h + I_h, 2\sigma_{H_1}^2) \quad \text{under } H_1 \quad (5.16)$$

$$y_h \sim \tilde{\mathcal{N}}(I_h, 2\sigma_{H_0}^2) \quad \text{under } H_0 \quad (5.17)$$

where $\sigma_{H_1}^2 = M\sigma_n^2$ and $\sigma_{H_0}^2 = M\sigma_n^2 + ME_s/4$ by invoking the central limit theorem to model the self-noise due to the B channel. Finally,

$$\mu_h = \sqrt{E_s} \text{sinc}(Mf_e T_c) \left(\sum_{i=hM}^{(h+1)M-1} c_{B,|i|_N} c_{C,|i|_N} - M \right) \quad (5.18)$$

$$I_h = \sqrt{2} A_I \sin\left(\frac{\pi\nu_I}{2}\right) e^{j\vartheta} \sum_{i=hM}^{(h+1)M-1} e^{j2\pi\nu_I i} c_{C,|i|_N} \quad (5.19)$$

where $\vartheta = \varphi - \theta$, uniformly distributed in $[0, 2\pi[$, and a constant phase term has been neglected without loss in generality. Note that the relative phase between μ_h and I_h is very important because the two components are summed coherently in the received signal under H_1 . This quantity is fully represented by $\arg\{I_h\}$, which is given by

$$\arg\{I_h\} = \vartheta + \arg\left\{ \sum_{i=hM}^{(h+1)M-1} e^{j2\pi\nu_I i} c_{C,|i|_N} \right\} \quad (5.20)$$

Thus, the NCPDI decision variable λ is obtained as

$$\lambda = \sum_{h=0}^{L-1} |y_h|^2 \quad (5.21)$$

and results to be a χ^2 random variable with $2L$ degrees of freedom, which is non-central under both H_1 and H_0 , according to

$$\lambda \sim \begin{cases} \chi_{2L}^2(s_{H_0}^2, \sigma_{H_0}^2) = p_{\lambda|H_0}(\lambda|H_0) & \text{under } H_0 \\ \chi_{2L}^2(s_{H_1}^2(\vartheta), \sigma_{H_1}^2) = p_{\lambda|H_1, \vartheta}(\lambda|H_1, \vartheta) & \text{under } H_1 \end{cases} \quad (5.22)$$

where it is intended that the variance indicated in the equation above is referred to the constituent real-valued Gaussian variables, and

$$s_{H_1}^2(\vartheta) = \sum_{h=0}^{L-1} |\mu_h + I_h|^2 \quad (5.23)$$

$$s_{H_0}^2 = \sum_{h=0}^{L-1} |I_h|^2 \quad (5.24)$$

where

$$\begin{aligned} |\mu_h + I_h|^2 &= [\mu_h + |I_h| \cos(\arg\{I_h\})]^2 + |I_h|^2 \sin^2(\arg\{I_h\}) \\ &= \mu_h^2 + |I_h|^2 + 2\mu_h |I_h| \cos(\arg\{I_h\}) \end{aligned} \quad (5.25)$$

From Equation (5.23) it is important to note that the decision variable depends on the phase ϑ under the H_1 hypothesis. This dependence can be resolved by averaging the conditional missed detection probability ($P_{md|\vartheta}(\vartheta)$) as

$$\begin{aligned} P_{md} &= \frac{1}{2\pi} \int_0^{2\pi} P_{md|\vartheta}(\vartheta) d\vartheta = \frac{1}{2\pi} \int_0^{2\pi} \left(\int_0^\xi p_{\lambda|H_1, \vartheta}(\lambda|H_1, \vartheta) d\lambda \right) d\vartheta \\ &= \frac{1}{2\pi} \int_0^{2\pi} \left[1 - Q_L \left(\frac{s_{H_1}(\vartheta)}{\sigma_{H_1}}, \frac{\sqrt{\xi}}{\sigma_{H_1}} \right) \right] d\vartheta \end{aligned} \quad (5.26)$$

while, being independent of ϑ , the false alarm probability, P_{fa} , can be directly expressed as

$$P_{fa} = 1 - Q_L \left(\frac{s_{H_0}}{\sigma_{H_0}}, \frac{\sqrt{\xi}}{\sigma_{H_0}} \right) \quad (5.27)$$

where ξ is the decision threshold and $Q_L(\cdot, \cdot)$ is the generalized Marcum Q-function of order L .

5.1.4 NCPDI Performance Analysis in the Absence of Interference

The reference performance with no interference has been analyzed in Section and reported here for completeness. In this case, the decision variable λ results to be a χ^2 rv with $2L$ degrees of freedom, which is non-central under H_1 and central under H_0 . The corresponding missed detection probability, $P_{md}^{\text{no int}}$, and false alarm probability, $P_{fa}^{\text{no int}}$, can be expressed as

$$P_{md}^{\text{no int}} = 1 - Q_L \left(\frac{s}{\sigma_{H_1}}, \frac{\sqrt{\xi}}{\sigma_{H_1}} \right) \quad (5.28)$$

$$P_{fa}^{\text{no int}} = e^{-\frac{\xi}{2\sigma_{H_0}^2}} \sum_{k=0}^{L-1} \frac{1}{k!} \left(\frac{\xi}{2\sigma_{H_0}^2} \right)^k \quad (5.29)$$

where

$$s^2 = \frac{E_s}{2} LM^2 \text{sinc}^2(Mf_e T_c) \quad (5.30)$$

5.1.5 NCPDI Performance Analysis with Interference Mitigation

As previously discussed, the presence of the notch filter before BOC demodulation allows to fully excise the interference component, at the cost of a distortion on the useful signal. The impact of IM on detection performance can be analytically evaluated by combining the results in terms of SINR after filtering given by Equation (5.11) with the code acquisition performance in the absence of interference

expressed by Equation (5.28) and Equation (5.29). Accordingly, it holds

$$P_{md}^{\text{IM}} = 1 - Q_L\left(\frac{s}{\sigma_{\text{IM}}}, \frac{\sqrt{\xi}}{\sigma_{\text{IM}}}\right) \quad (5.31)$$

$$P_{fa}^{\text{IM}} = e^{-\frac{\xi}{2\sigma_{\text{IM}}^2}} \sum_{k=0}^{L-1} \frac{1}{k!} \left(\frac{\xi}{2\sigma_{\text{IM}}^2}\right)^k \quad (5.32)$$

where

$$\sigma_{\text{IM}}^2 = \frac{E_s}{\text{SINR}} \quad (5.33)$$

The accuracy of the proposed model is shown in Section 5.2.

5.1.6 Mean Acquisition Time Analytical Characterization

In the following the single dwell acquisition procedure with serial scan of the uncertainty region and application of the Threshold Crossing (TC) criterion [83] has been considered. In the autonomous GNSS case, where the uncertainty region spans the entire primary code sequence of length N , the mean acquisition time can be expressed as the classical expression shown in Section 2.2.1, here reported for the sake of simplicity:

$$\bar{T}_A = \frac{1}{P_d} \left\{ T_c \left[1 + \frac{N-1}{2}(2-P_d) \right] + T_p \frac{N-1}{2}(2-P_d)P_{fa} \right\} \quad (5.34)$$

where $P_d = 1 - P_{md}$ is the correct detection probability and T_p is the penalty time, assumed constant and equal to $4NT_c = 16$ ms.

When considering the A-GNSS case, the reduction of the uncertainty region enabled by the coarse timing reference determines that the serial search procedure has to explore time intervals that are not continuous in time, because a large number of H_0 hypotheses can be a-priori discarded. In particular, the time uncertainty is reduced to a number $U_R < N$ chips, which has been selected equal to 2046 and 1023 according to Table 8.1 for numerical evaluations. Accordingly, a very satisfactory approximation of the mean acquisition time can be obtained following a procedure similar to [83] and introducing different dwell time periods for the H_0 and H_1 hypotheses. In particular, conservatively assuming that the H_1 hypothesis is located in the last position of the uncertainty region, the time delay associated with a missed detection is equal to $T_c(N - U_R)$, and the mean acquisition time results in

$$\bar{T}_A^{\text{A-GNSS}} = \frac{1}{P_d} \left\{ T_c P_d + T_c(N - U_R)(1 - P_d) + T_c \frac{U_R}{2}(2 - P_d) + T_p \frac{U_R - 1}{2}(2 - P_d)P_{fa} \right\} \quad (5.35)$$

5.2 Performance Evaluation

In the following, the parameters summarized in Table 8.1 are considered to evaluate the impact of the assistance network on joint code acquisition and interference mitigation performance.

Figures 5.6 and 5.7 show the performance in terms of ROC, i.e. P_{md} vs. P_{fa} , for autonomous and assisted operation, respectively. In the autonomous case, the performance with IM refers to user terminals with interference estimation and mitigation capabilities (mobile IOSs). A typical outdoor signal-to-noise ratio $C/N_0 =$

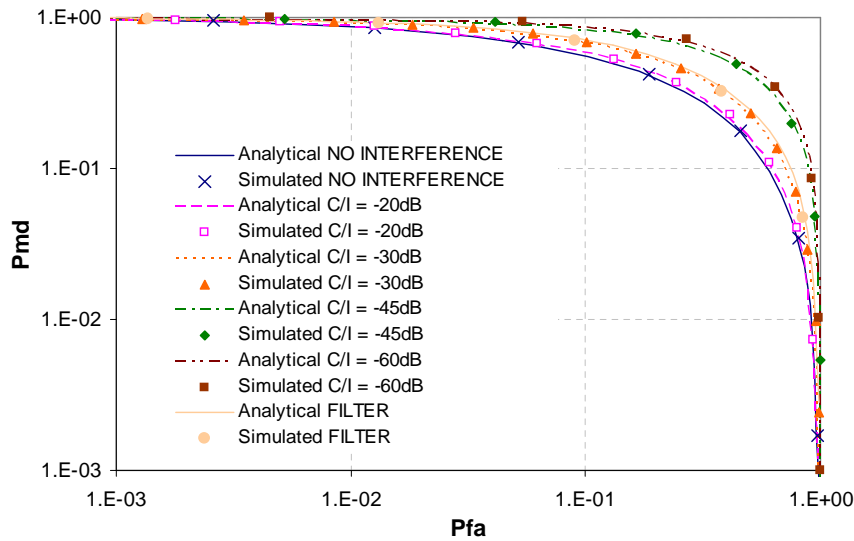


Figure 5.6: Autonomous GNSS - ROC performance for NCPDI with $M = 341$, $L = 12$, $C/N_0 = 35$ dBHz, $\nu_I = 0.4$

35dBHz is assumed, corresponding to $E_c/N_0 = -25$ dB for the Galileo E1-C chip rate. The presence of a constant tone interference with IF equal to $\nu_I = 0.4$, which is an intermediate case with limited impact on the output SINR, with different values of the useful-to-interference power ratio C/I . The figures validate the proposed analytical models, showing a perfect match between analytical curves and simulated points. Interestingly, for low power interference ($C/I = -20$ and -30 dB), the inherent robustness of the Galileo spreading codes is already sufficient to combat the interference effect, resulting in improved performance with respect to code acquisition with IM. When high power interference is considered, IM can considerably improve performance because the useful signal distortion is largely compensated by

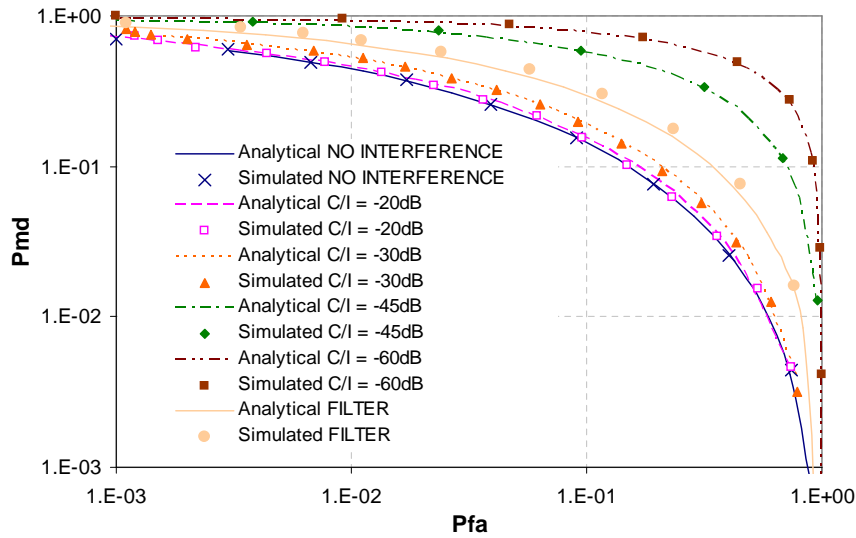


Figure 5.7: A-GNSS - ROC performance for NCPDI with $M = 2046$, $L = 2$, $C/N_0 = 35$ dBHz, $\nu_I = 0.4$

the gain introduced by the interference excision. Note that high power interference is a typical case for intentional jamming or interference sources located close to the receiver, or with spurious harmonics of high power transmitters (e.g. radar, amateur, or TV broadcasting).

The gain introduced by the A-GNSS network and by the adopted IM technique is even more evident in Figure 5.8, where the mean acquisition time is reported against P_{fa} . The large MAT reduction is a confirmation of the fact that the presence of the assistance network allows a twofold performance improvement: it enables IM for all terminals through the signaling of the IF estimates through the network, allowing at the same time the reduction of the time-frequency uncertainty region for code acquisition.

Different conclusions can be inferred by considering a different value of the interference IF. In particular, the worst case operation is for $\nu_I = 0.8$ corresponding to the minimum SINR at the filter output, as reported in Figure 5.4. The corresponding ROC performance in the A-GNSS case is reported as an example in Figure 5.9, where $M = 2046$, $L = 2$, and $C/N_0 = 35$ dBHz. Notably, the direct comparison with the corresponding curves in Figure 5.7 shows an evident performance degradation both in the presence of interference and after interference cancellation. The corresponding mean acquisition time is summarized in Figure 5.10, where the most

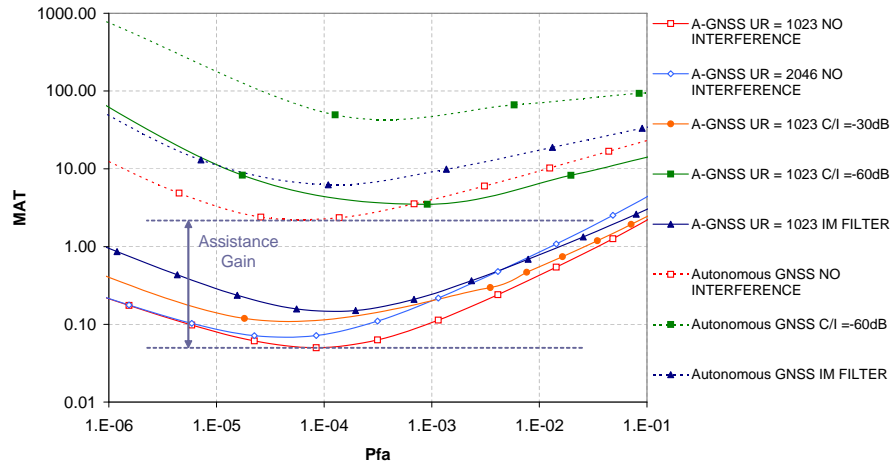


Figure 5.8: Mean acquisition time vs. false alarm probability for Autonomous (dashed) and A-GNSS (solid) with $\nu_I = 0.4$, $C/N_0 = 35$ dBHz

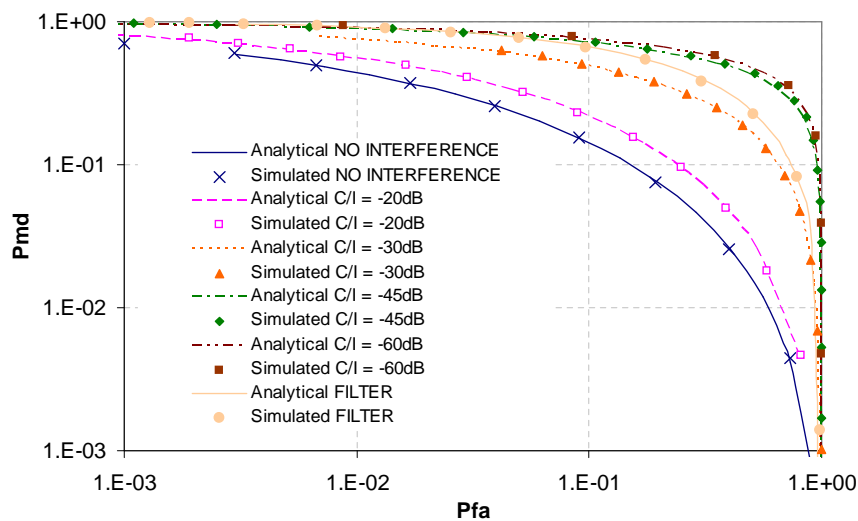


Figure 5.9: A-GNSS - ROC performance for NCPDI with $M = 2046$, $L = 2$ $C/N_0 = 35$ dBHz, $\nu_I = 0.8$

significant region is for small values of P_{fa} . Notably, in this case, the possibility of fully excise the interferer does not always compensate for the large distortion introduced by the IM filter. For low power interference ($C/I = -20$ and -30 dB), the inherent robustness of the Galileo spreading codes is already sufficient to combat the interference effect, resulting in improved performance with respect to code acquisition with IM. This fact is still valid for high power interference in the autonomous

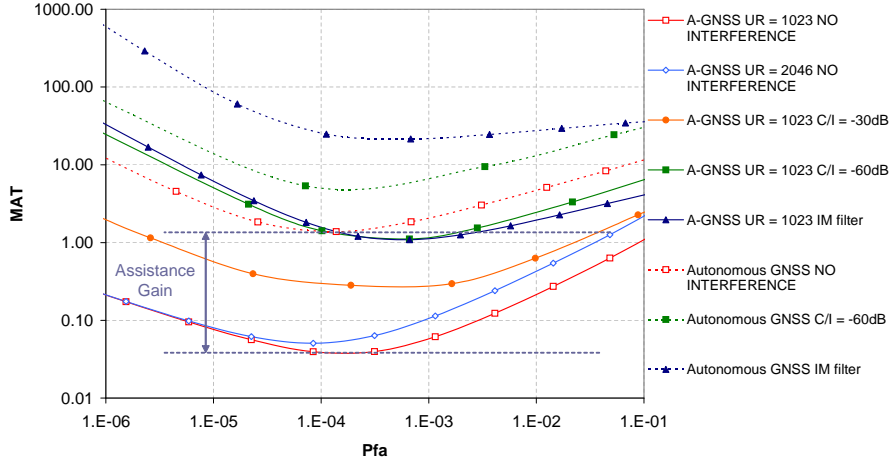


Figure 5.10: Mean acquisition time vs. false alarm probability for Autonomous (dashed) and Assisted GNSS (solid) with $\nu_I = 0.8$, $C/N_0 = 35$ dBHz

case, where the short coherent correlation length is not able to counteract the distortion introduced by the IM notch filter. When considering the A-GNSS case, a different conclusion can be drawn. In fact, the minimum MAT is the same for both IM and no-IM, at the considered T_p .

Note that, even if IM is not convenient in this very critical scenario, the presence of assistance data to aid code acquisition still has an indubitable positive impact on performance, strongly improving the minimum mean acquisition time with respect to the autonomous case, thanks to the reduced frequency and time uncertainty.

This different behavior of code acquisition with IM as a function of the interference IF underlines once again the benefit of the assistance network, which becomes essential to guide the terminal in the selection of the most appropriate countermeasure to be taken against the interference. In particular, for the low-complexity IM notch filter described herein, this signaling is fundamental for adaptive programming of the filter coefficients in order to track interference IF variations, or switching it off for particular values of IF. Note that this switch off operation simply corresponds to filter coefficients equal to $a_0 = 1$ and $a_i = 0$ for $i = -2, -1, 1, 2$ in Equation (5.5).

5.3 Integrated NAV-COM Systems: Conclusions

In this chapter the effect of the interference in a Galileo receiver has been evaluated, proposing a low cost interference mitigation filter which can guarantee a significant

performance gain in most conditions. Emphasis has been placed in the performance of the code acquisition strategy, which is a critical operation for a GNSS system. Since the excision of the interference needs the estimation of parameters like instantaneous frequency and sweep rate, a practical implementation of an assistance network has been introduced. The proposed integrated navigation-communication (NAV-COM) concept for efficient code acquisition applied to GNSS is based on the adoption of an assistance network able to provide receivers with time and frequency references, along with the characterization of possible interference affecting the received signal. The proposed system architecture presents a modular structure, with distributed terminals that collect data on interference and feedback them to a centralized assistance server, which is in charge of broadcasting this information through the communication network. Analytical and simulated results show that the presence of the assistance network makes the code acquisition more efficient, especially in very critical scenarios, reducing at the same time the terminal complexity.

5.4 Appendix: Derivation of Signal Statistics After BOC Demodulation and IM Filter

The output of the notch filter expressed in (5.7) is here manipulated to derive (5.8) and (5.9).

By separating the useful part from the noise component, it is possible to rewrite $\rho_k = s_k + n_k$, being

$$s_k = \sqrt{\frac{E_s}{2}} e^{j(2\pi f_e k T_{sc} + \zeta')} (-1)^k \left(c_{B,|[k]_2+\Delta|_N} d_{[k+2\Delta]_{2N}} - c_{C,|[k]_2+\Delta|_N} \right) \quad (5.36)$$

and the useful component of (5.7) can be expressed as

$$y_l^{(u)} = \frac{1}{K} \sum_{j=-2}^2 s_{l-j} h_j = \frac{1}{K} \{ s_{l+2} - 4 \cos(\pi \nu_I) s_{l+1} + [2 + 4 \cos^2(\pi \nu_I)] s_l - 4 \cos(\pi \nu_I) s_{l-1} + s_{l-2} \} \quad (5.37)$$

These samples are then processed by BOC demodulation and partial coherent correlation. Accordingly, the deterministic useful component of the h -th correlation

output is given by

$$\begin{aligned}
U_h^{(u)} = & \frac{1}{\sqrt{2K}} \sum_{m=hM}^{(h+1)M-1} \sum_{n=0}^1 \left[s_{n+2m+2} (-1)^n c_{C,|[2m+n]_2|_N} + \right. \\
& - s_{n+2m+1} 4 \cos(\pi\nu_I) (-1)^n c_{C,|[2m+n]_2|_N} \\
& + (2 + 4 \cos^2(\pi\nu_I)) s_{n+2m} (-1)^n c_{C,|[2m+n]_2|_N} + \\
& \left. - s_{n+2m-1} 4 \cos(\pi\nu_I) (-1)^n c_{C,|[2m+n]_2|_N} + s_{n+2m-2} (-1)^n c_{C,|[2m+n]_2|_N} \right]
\end{aligned} \tag{5.38}$$

where the sum on h represents coherent accumulation, while the sum on n , along with the $1/\sqrt{2}$ coefficient, derives from BOC demodulation. By substituting (5.36) into (5.38), and neglecting the presence of the B channel for simplicity¹, it follows

$$\begin{aligned}
U_h^{(u)} = & \frac{\sqrt{E_s}}{2K} \sum_{m=hM}^{(h+1)M-1} \left[(e^{j(2\pi f_e(2m+2)T_{sc}+\zeta')} c_{C,|[2m]_2|_N} c_{C,|[2m+2]_2|_N} \right. \\
& + e^{j(2\pi f_e(2m+3)T_{sc}+\zeta')} c_{C,|[2m+1]_2|_N} c_{C,|[2m+3]_2|_N}) + 4 \cos(\pi\nu_I) \cdot \\
& (e^{j(2\pi f_e(2m+1)T_{sc}+\zeta')} c_{C,|[2m]_2|_N} c_{C,|[2m+1]_2|_N} + e^{j(2\pi f_e(2m+2)T_{sc}+\zeta')} c_{C,|[2m+1]_2|_N} c_{C,|[2m+2]_2|_N}) \\
& + (2+4 \cos^2(\pi\nu_I)) (e^{j(2\pi f_e 2m T_{sc}+\zeta')} c_{C,|[2m]_2|_N} c_{C,|[2m]_2|_N} + e^{j(2\pi f_e(2m+1)T_{sc}+\zeta')} c_{C,|[2m+1]_2|_N} c_{C,|[2m+1]_2|_N}) \\
& + 4 \cos(\pi\nu_I) (e^{j(2\pi f_e(2m-1)T_{sc}+\zeta')} c_{C,|[2m]_2|_N} c_{C,|[2m-1]_2|_N} + e^{j(2\pi f_e(2m)T_{sc}+\zeta')} c_{C,|[2m+1]_2|_N} c_{C,|[2m]_2|_N}) \\
& \left. + e^{j(2\pi f_e(2m-2)T_{sc}+\zeta')} c_{C,|[2m]_2|_N} c_{C,|[2m-2]_2|_N} + e^{j(2\pi f_e(2m-1)T_{sc}+\zeta')} c_{C,|[2m+1]_2|_N} c_{C,|[2m-1]_2|_N} \right]
\end{aligned} \tag{5.39}$$

Strictly speaking, in the equation above all the exponential terms are characterized by a different angle rotation. However, considering for example the sum of the first two terms in the equation, it is possible to rearrange it according to

$$\begin{aligned}
& e^{j(2\pi f_e(2m+2)T_{sc}+\zeta')} c_{C,|[2m]_2|_N} c_{C,|[2m+2]_2|_N} + e^{j(2\pi f_e(2m+3)T_{sc}+\zeta')} c_{C,|[2m+1]_2|_N} c_{C,|[2m+3]_2|_N} = \\
& = 2c_{C,|[2m+2]_2|_N} c_{C,|[2m]_2|_N} e^{j(2\pi f_e(2m+2)T_{sc}+\zeta')} e^{j\frac{2\pi f_e T_{sc}+\zeta'}{2}} \cos\left(\frac{2\pi f_e T_{sc}+\zeta'}{2}\right) \simeq \\
& \simeq 2c_{C,|[2m+2]_2|_N} c_{C,|[2m]_2|_N} e^{j(2\pi f_e(2m+2)T_{sc}+\zeta')}
\end{aligned}$$

under the hypothesis of a small frequency error with respect to the subcarrier rate. Extending this approximation to all pairs of exponential terms in (5.39), it results

$$\begin{aligned}
U_h^{(u)} \simeq & \frac{\sqrt{E_s}}{2K} e^{j(2\pi f_e M T_c + \zeta')} \text{sinc}(f_e M T_c) \cdot \\
& [2R_m(1) + 4 \cos(\pi\nu_I)(2R_m(1) + M) + 2M(2 + 4 \cos^2(\pi\nu_I)) + 4 \cos(\pi\nu_I)(2R_m(-1) + M) + 2R_m(-1)] = \\
& = \frac{\sqrt{E_s}}{2K} e^{j(2\pi f_e M T_c + \zeta')} \text{sinc}(f_e M T_c) [4M(1 + 2 \cos(\pi\nu_I) + 2 \cos^2(\pi\nu_I)) + 4R_m(1)(1 + 2 \cos(\pi\nu_I))]
\end{aligned}$$

¹The generalization of the final result to account also for the B channel presence is straightforward and presented in Section 5.1.1, invoking central limit theorem arguments.

Considering now the noise component of (5.7), it can be expressed as

$$\begin{aligned} y_l^{(n)} &= \frac{1}{K} \sum_{j=-2}^2 n_{l-j} h_j = \\ &= \frac{1}{K} (n_{l+2} - 4 \cos(\pi\nu_I) n_{l+1} + (2 + 4 \cos^2(\pi\nu_I)) n_l - 4 \cos(\pi\nu_I) n_{l-1} + n_{l-2}) \end{aligned}$$

where n_k are zero mean complex Gaussian random variables with variance σ_n^2 on the in-phase and quadrature branches.

After BOC demodulation and partial coherent correlation, the h -th output can be obtained as

$$\begin{aligned} U_h^{(n)} &= \frac{1}{\sqrt{2K}} \sum_{m=hM}^{(h+1)M-1} \sum_{n=0}^1 \left[n_{n+2m+2} (-1)^n c_{C, \lfloor 2m+n \rfloor_{2|N}} + \right. \\ &- n_{n+2m+1} 4 \cos(\pi\nu_I) (-1)^n c_{C, \lfloor 2m+n \rfloor_{2|N}} + (2 + 4 \cos^2(\pi\nu_I)) n_{n+2m} (-1)^n c_{C, \lfloor 2m+n \rfloor_{2|N}} \\ &\left. - n_{n+2m-1} 4 \cos(\pi\nu_I) (-1)^n c_{C, \lfloor 2m+n \rfloor_{2|N}} + n_{n+2m-2} (-1)^n c_{C, \lfloor 2m+n \rfloor_{2|N}} \right] \\ &= \frac{1}{2K} \sum_{m=hM}^{(h+1)M-1} \left[(n_{2m+2} c_{C, \lfloor 2m \rfloor_{2|N}} - n_{2m+3} c_{C, \lfloor 2m+1 \rfloor_{2|N}}) \right. \\ &- 4 \cos(\pi\nu_I) (n_{2m+1} c_{C, \lfloor 2m \rfloor_{2|N}} - n_{2m+2} c_{C, \lfloor 2m+1 \rfloor_{2|N}}) \\ &+ (2 + 4 \cos^2(\pi\nu_I)) (n_{2m} c_{C, \lfloor 2m \rfloor_{2|N}} - n_{2m+1} c_{C, \lfloor 2m+1 \rfloor_{2|N}}) \\ &- 4 \cos(\pi\nu_I) (n_{2m-1} c_{C, \lfloor 2m \rfloor_{2|N}} - n_{2m} c_{C, \lfloor 2m+1 \rfloor_{2|N}}) \\ &\left. + n_{2m-2} c_{C, \lfloor 2m \rfloor_{2|N}} - n_{2m-1} c_{C, \lfloor 2m+1 \rfloor_{2|N}} \right] \end{aligned} \quad (5.40)$$

which can be further manipulated yielding

$$\begin{aligned} U_h^{(n)} &= \frac{1}{2K} \left[(1 + 4 \cos(\pi\nu_I)) \sum_{m=hM}^{(h+1)M-1} (n_{2m+2} c_{C, \lfloor 2m \rfloor_{2|N}} - n_{2m-1} c_{C, \lfloor 2m+1 \rfloor_{2|N}}) \right. \\ &+ (2 + 4 \cos^2(\pi\nu_I) + 4 \cos(\pi\nu_I)) \sum_{m=hM}^{(h+1)M-1} (n_{2m} c_{C, \lfloor 2m \rfloor_{2|N}} - n_{2m+1} c_{C, \lfloor 2m \rfloor_{2|N}}) \\ &\left. + \sum_{m=hM}^{(h+1)M-1} (n_{2m-2} c_{C, \lfloor 2m \rfloor_{2|N}} - n_{2m+3} c_{C, \lfloor 2m+1 \rfloor_{2|N}}) \right] \end{aligned} \quad (5.41)$$

Since

$$\text{Var} \left\{ \sum_{m=hM}^{(h+1)M-1} n_{2m+2} c_{C, \lfloor 2m \rfloor_{2|N}} \right\} = M \sigma_n^2 \quad (5.42)$$

as for all of the other summations in (5.41), it results

$$\begin{aligned} E\{U_h^{(n)}\} &= 0 \\ \text{Var}\{U_h^{(n)}\} &= \frac{M \sigma_n^2}{K^2} [(1 + 4 \cos(\pi\nu_I))^2 + (2 + 4 \cos^2(\pi\nu_I) + 4 \cos(\pi\nu_I))^2 + 1] \end{aligned}$$

Finally, the overall output of coherent accumulation $U_h = U_h^{(u)} + U_h^{(n)}$ results to be a Gaussian random variable with mean value $E\{U_h^{(n)}\} + U_h^{(u)}$ given by Equation (5.8) and variance equal to $\text{Var}\{U_h^{(n)}\}$, as reported in (5.9).

Part II

**Synchronization in Wireless and
Satellite Communication
Systems**

Even if satellite communications have evolved over the years establishing their significant role in achieving global communications, novel problems and challenges have to be solved in order to define their future role in the wireless world of next decade. First of all, it is reasonable to believe that future systems will be built upon a hierarchy of systems, in order to achieve the demand for ubiquity and pervasiveness. Thus, satellites will be asked to provide global coverage as the overlay for a multitude of regional, national, local, and personal area covering systems [84].

Fourth generation (4G) broadband standards will exploit an hybrid terrestrial-satellite network, based on Orthogonal Frequency-Division Multiplexing (OFDM), and strongly influenced by innovative trends, like Multiple Input Multiple Output (MIMO), innovative coding schemes, etc. While OFDM is a powerful technology able to guarantee high spectral efficiency, and robustness against multipath and harsh channel conditions, it is also particularly sensitive to synchronization non-idealities. Thus, synchronization represents one of the most important issue in the scenario at hand.

At the same time, the satellite operated Digital Video Broadcasting (DVB) is extending the capabilities of the DVB-S2 (Satellite second generation) standard, with DVB-RCS+M (Return Channel via Satellite Mobile extension) capabilities in order to support broadband access to mobile collective terminals in aeronautical, maritime, and railway land mobile scenarios. In the railway environment, besides the expected mobile channel issues, the most peculiar and critical aspect to be addressed is the presence of the periodic fade events caused by power-supply arches [85]. In this case, synchronization block should be designed in order to rapidly reacquire the signal and to relock the tracking circuits.

In this framework, synchronization represents one of the most critical issues [86]. In the following the problem of designing effective synchronization schemes is tackled for the most promising future communication standards.

6

Code Acquisition in the Mobile Broadband Satellite Standard DVB-RCS+M

6.1 Introduction

In 2006 the Digital Video Broadcasting - Technical Module (DVB-TM) approved a new study mission aimed at extending the capabilities of the DVB-RCS (Return Channel via Satellite) standard to support broadband services to mobile collective terminals in aeronautical, maritime, and railway land mobile scenarios ¹ [87][88]. The new standard has been recently finalized and is identified as DVB-RCS+M.

Although the DVB-RCS group activities have been mainly aimed at the standardization of the satellite return link, the new study mission was also addressing the satellite forward link design in order to provide a full broadband mobile satellite system toolbox. On the ground that the DVB-S2/RCS pair [89][90] is widely accepted for fixed broadband satellite communication systems, the DVB-RCS+M

¹The vehicular land mobile scenario is also addressed by the new standard but with a lower priority with respect to the railway.

adopts these standards as the starting baseline configuration for the mobile extension.

DVB-RCS+M is designed for operation in Ku (11-14 GHz) and Ka-band (20-30 GHz). Indeed, this design choice allows to exploit the existing DVB-RCS and DVB-S2 technologies and to use small antennas, thus reducing the deployment and operational costs. However, the drawback is that specific interference countermeasures are needed, because these bands are allocated to Mobile Satellite System (MSS) applications with a lower priority (on a secondary basis) with respect to fixed satellite systems (FSS), thus imposing stricter constraints on the admissible interference level caused to other primary systems and the power spectrum emission (namely, the off-axis power flux density) and a lower protection from the FSS generated interference. The solution devised by the DVB-RCS+M group for interference mitigation is the use of an optional direct sequence spread spectrum (DS-SS) mode for the DVB-S2 waveform, with spreading factors up to 4 for the forward link (FL) and up to 16 for the return link (RL) *single channel per carrier* (SCPC) option [91].

The adoption of DS-SS in the DVB-S2 waveform dictates the introduction of a code synchronization subsystem at the receiver side. In this chapter, the results of the design and performance assessment of the code synchronization subsystem are reported. Note that these results have been carried out in support of the adoption of DS-SS by the DVB-RCS+M ad-hoc group. The design described in this chapter refers in particular to the DVB-RCS+M FL and to the DVB-RCS+M RL SCPC mode in the most challenging railway scenario [88]. Code synchronization is accomplished jointly with frame acquisition in order to limit the impact on the receiver architecture. As in common practice, the code/frame epoch domain is discretized into a number of cells or hypotheses per chip, and acquisition is achieved through the detection of the spread DVB-S2 Start of Frame (SOF) [89] within the transmission flow.

The results presented in this chapter have been partially published in [9] and [10]. This work has been developed within the research group in collaboration with ETRI (Electronics and Telecommunications Research Institute) [23]. My contribution was in the performance evaluation and in the support to the DVB-RCS Guidelines preparation.

6.2 DS Spreading in the Forward Link of DVB-RCS+M

The DVB-RCS+M specifications foresee the adoption of the DVB-S2 waveform and frame structure for FL transmissions [89]. Accordingly, as depicted in Figure 6.1 the physical layer frame (PLFRAME) consists of L_F modulated symbols including the SOF of $L_{SOF}=26$ symbols, the physical layer signalling (PLS) field of 64 symbols, and the information payload interlaced every 1440 symbols with a pilot field of 16 symbols.

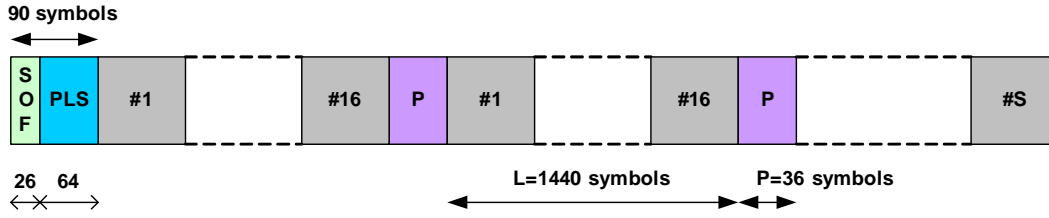


Figure 6.1: DVB-S2 Physical Layer Frame (PLFRAME) structure

The insertion of the SOF is required for frame synchronization purposes in the DVB-S2 receiver, while pilots are foreseen to ease the following estimation steps. Note that, while in the original DVB-S2 standard the pilot inclusion is optional, for mobile applications it becomes mandatory to enable efficient channel estimation in the very harsh scenarios at hand. This fact can be conveniently exploited by the code/frame acquisition subsystem.

In the DVB-RCS+M spread mode, DS-SS spreading is applied to the entire PLFRAME, including the header and the SOF in particular, so that code acquisition has to detect the presence of the spread SOF in the transmission flow. More in detail, DS spreading for DVB-RCS+M is accomplished through the exploitation of an Orthogonal Variable Spreading Factor (OVSF) sequence of length η (which corresponds to the spreading factor), with a following further scrambling phase to improve spectrum properties (Figure 6.2). The possible spreading sequences are shown in Table 6.1.

Both spreading and scrambling are reset at the beginning of each frame to ease synchronization at the receiver. The spread sequence $s[i]$ is therefore given by

$$s[i] = d[\lfloor \eta \rfloor] C[\lfloor i/\eta \rfloor] \quad i = 0, 1, \dots, (L_F \times \eta) - 1 \quad (6.1)$$

where $d[k]$ represents the complex modulated symbols of the PLFRAME, and $C[i]$ is the OVSF spreading sequence. After spreading, the scrambling sequence, $w[i]$ of

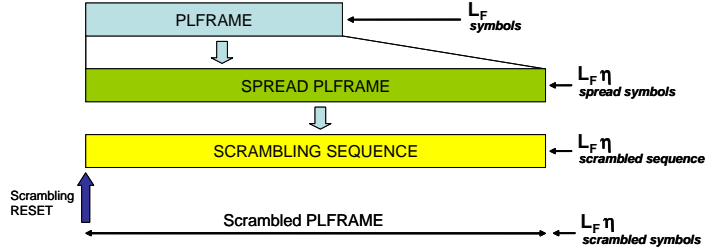


Figure 6.2: Forward link spectrum spreading

Spreading Factor	Chip Sequence
1	1
2	1, 1
2	1, -1
3	1, 1, 1
4	1, 1, 1, 1
4	1, 1, -1, -1
4	1, -1, 1, -1
4	1, -1, -1, 1

Table 6.1: Orthogonal Variable Spreading Factor (OVSF) sequences

length L_S , is applied yielding

$$z[k] = s[k]w[[k]_{L_S}] \quad k = 0, 1, \dots, (L_F \times \eta) - 1 \quad (6.2)$$

The complex sequence $z[i]$ is then filtered through a squared root raised cosine as mandated in [89].

In the FL a fixed chip rate of 27.5Mchip/s with roll-off equal to 0.35, thus yielding a total bandwidth of 36MHz, is considered. Interesting, having fixed the chip rate any variation in the spreading factor will result in a variation of the information bit rate. Finally, note that the frame length varies according to the adopted modulation, i.e. $PLFRAME = 33282 \cdot \eta$ in the case of QPSK, and $PLFRAME = 22230 \cdot \eta$ in the case of 8PSK.

6.3 Channel model

According to propagation measurements and the DVB-RCS+M framework analysis, aeronautical and maritime propagation condition can be safely modeled through the

classical AWGN channel [88]. For the railway scenario, rigorous modeling for the Line of Sight (LoS) propagation conditions calls for a Rice fading channel with a Rice factor of $K = 17.5$ dB, with superposition of a square wave 0 or 1 with duty cycle 1% that models the periodic obscuration events induced by the equally spaced electrical trellises (also referred to as power arches) used on the railway [88] to supply power to the electrical trains. According to this model, the channel is "on" with Rice propagation for 99% of the time, while it is "off" for the residual 1%, the transition from on to off occurring periodically.

In practice, in the "on" state, the large K factor experienced in LoS conditions makes actual acquisition performance very similar to the results in AWGN, which is thus addressed in the following.

A frequency offset Δf as large as 3 MHz and a Doppler rate of 1300 Hz/s are present, which take into account oscillator mismatch and terminal speeds. For completeness, the DVB-S2 phase noise mask reported in Table 6.2 and derived from [89] an [92] is considered, even if the non-coherent detection processing introduced to cope with the large frequency offset makes the acquisition subsystem resilient against it.

0.1 KHz	-45dBc/Hz
1 KHz	-65dBc/Hz
10 KHz	-80dBc/Hz
100 KHz	-95dBc/Hz
1000 KHz	-105dBc/Hz
> 10000 KHz	-115dBc/Hz

Table 6.2: Phase noise mask

6.4 Synchronization subsystem

In addition to frame synchronization, when DS spreading is introduced, code acquisition becomes a necessity to enable effective despreading at the receiver. This critical task is addressed jointly with frame acquisition, by detecting the spread SOF. Taking into account the presence of power arches that determines periodic deep fading events, the design of the code/frame acquisition subsystem needs to distinguish between five different operating modes, which correspond to the states of the associated Finite State Machine (FSM) described in Figure 6.3:

1. S^1 - *Cold start acquisition*, which is entered at terminal switch-on and after a failure of warm start acquisition; in this state, parameter uncertainty is highly challenging.
2. S^2 - *Verification mode*, which verifies the correctness of the frame acquisition decision.
3. S^3 - *Frame Tracking*, which is in charge of continuous verification and deep fade events detection [93]
4. S^4 - *Re-acquisition after short interruption*, which is the procedure put in place to recover the code alignment after a short interruption due, for example, to a deep fade induced by power arches, small bridges, etc; in this state, parameter uncertainty is limited, but acquisition must be fast in order to recover quickly from the interruption.
5. S^5 - *Warm start acquisition*, which takes place after long fading events or in time sliced operation. In this state, parameter uncertainty is larger than in the previous state.

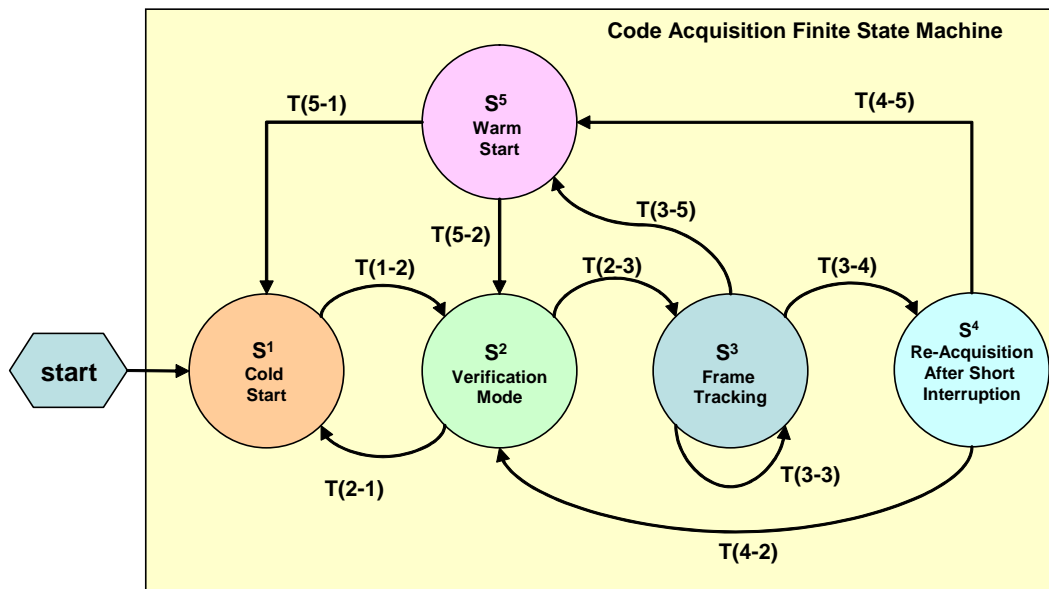


Figure 6.3: Code/frame acquisition finite state machine

Indicating with $T(m, n)$ the transition from state S^m to state S^n , it is possible to describe the FSM evolution through the following transitions:

- $T(1-2)$ occurs when the cold start frame synchronization procedure is terminated;
- $T(2-1)$ occurs when the verification mode reveals the incorrectness of the cold start frame acquisition decision, classifying the outcome of S^1 as a false alarm event;
- $T(2-3)$ occurs when verification is successfully completed, having verified the outcome of S^1 ;
- $T(3-3)$ is the loop transition on S^3 , which characterizes the normal operating state of frame synchronization;
- $T(3-4)$ occurs when the lock to the frame alignment is lost, e.g. in correspondence of a fade event;
- $T(3-5)$ occurs whenever it is known a-priori that the interruption cannot be recovered in state S^4 ;
- $T(4-2)$ occurs when re-acquisition after short interruption is successfully accomplished, recovering the frame alignment, and thus verification must be performed;
- $T(4-5)$ occurs when re-acquisition after short interruption is unsuccessful throughout a pre-defined time period during which the last synchronization lock is reliable;
- $T(5-2)$ occurs when the warm start acquisition produces a frame alignment hypothesis that must be verified by the verification procedure;
- $T(5-1)$ occurs when warm start acquisition fails to recover the frame alignment before time out.

In each state, the code/frame acquisition subsystem is composed by a code sequence detector, a decision criterion, and a controller that implements the control logic necessary to perform the acquisition procedure. The optimized design of all of these blocks has been the objective of this work. The results of the most interesting study cases for the problem at hand have been herein reported, i.e. cold start acquisition and re-acquisition after short interruptions, being the former the most critical for the impairments to be tackled, and the latter the most demanding in terms of performance requirements.

6.4.1 Cold start code acquisition

Code acquisition in cold start is very challenging due to the largest frequency error (3MHz at 27.5Mcps) and the vast uncertainty region for the unknown code epoch that spans over the entire spread frame length. Due to the low signal to noise ratio (SNR) before despreading, chip timing recovery is not feasible with satisfactory performance before code acquisition, thus at least $h = 2$ hypotheses per chip are tested in the synchronization subsystem, leading to an overall number $N = h\eta L_F$ of hypotheses to be tested by the synchronization subsystem.

To enhance the robustness against frequency offsets, a Post Detection Integration (PDI) approach has been used. The idea behind this approach consists in the adoption of a windowing technique, which limits coherent correlation over segments of length M of the transmitted sequence, performing the residual integration after non linear processing. In fact, the presence of a frequency offset $\nu = \Delta f T_c$, normalized to the chip time T_c , determines an energy degradation equal to $M \text{sinc}^2(M\nu)$ after coherent accumulation over M chips, which can be contained by appropriately selecting M , given the frequency offset. Thus, for all PDI-based detectors, correlation over the code sequence is split in two parts: coherent accumulation followed by PDI over the residual length $L = \eta L_{SOF}/M$. Different PDI approaches have been proposed in the literature, achieving different performance/complexity trade-offs: Non Coherent PDI (NCPDI), Differential PDI (DPDI), and Generalized PDI (GPDI) [94], which reveals to be the most robust against frequency uncertainty at the cost of increased complexity.

In the following, for cold start acquisition, the performance of GPDI are contrasted with a novel PDI solution, identified as Differential GPDI (D-GPDI), which pragmatically improves GPDI under very large frequency offsets by exploiting only its differential terms, the n -Span DPDI components. The block diagrams of D-GPDI, GPDI, NCPDI, and n -Span DPDI (which yields DPDI for $n = 1$) are reported in Figure 6.4. In the scenario at hand, due to the very large frequency error, D-GPDI with $M = 1$ and $L = \eta L_{SOF}$ is considered and compared with GPDI with $M = 2$ and $L = \eta L_{SOF}/M$.

To cope with the variable frame length foreseen by the DVB-S2 standard, a simple yet effective acquisition procedure is selected, i.e. a single dwell approach with serial scan of the uncertainty domain and application of the Threshold Crossing criterion [83]. This procedure can be modeled as a Markov chain, which can be characterized through the flow-graph depicted in Figure 6.5 in order to determine

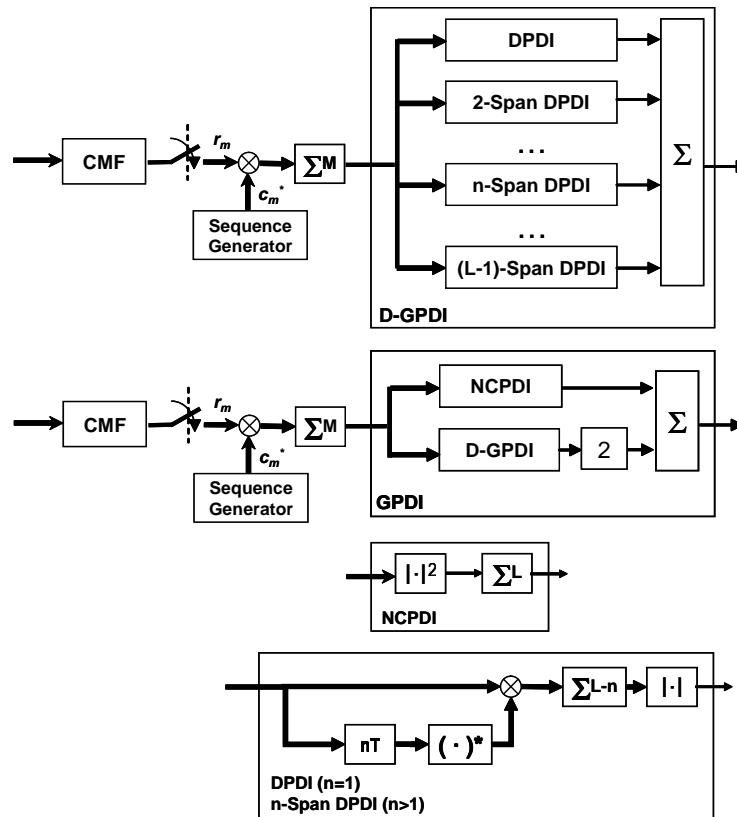


Figure 6.4: Detectors block diagrams for Non Coherent PDI (NCPDI), Differential PDI (DPDI), Generalized PDI (GPDI), and Differential GPDI (D-GPDI)

selected. Note that in this case a further verification performance improvement can be obtained by exploiting the full collection of pilots foreseen in the QPSK frame, which would lead, as a drawback, to the increase of the penalty time to the quantity $\eta 33282 T_c$.

To provide more conservative performance figures, the 99% acquisition time percentile is also assessed. To this aim, the probability density function (pdf) of the acquisition time is modeled using the one-sided central limit theorem yielding

$$P_{T_A}(T_A) = \frac{T_A^{a-1} e^{-T_A/b}}{b^a \Gamma a} \quad T_A \geq 0 \quad (6.4)$$

where

$$a = \frac{\hat{T}_A^2}{\text{Var}\{T_A\}} \quad b = \frac{\text{Var}\{T_A\}}{\hat{T}_A} \quad (6.5)$$

6.4.2 Acquisition after short interruptions

This operating mode represents the main peculiarity of the acquisition subsystem when mobile operation is considered. The most critical scenario in this sense is certainly represented by the railway applications. In fact, the periodic fading events caused by the presence of bridges and power arches impose to design an efficient re-acquisition strategy able to rapidly re-lock to the spread frame, after fading events that can be very long, up to 1s.

When the presence of the fading event is detected, all tracking circuits are promptly frozen in their last steady state condition, so that re-acquisition is only affected by a small residual frequency uncertainty due to clock instability and Doppler rate. This fact strongly relaxes the constraint of detector robustness against frequency offsets, and enables the adoption of an optimized detector that coherently accumulates over the entire spread SOF length, i.e. NCPDI with $M = \eta L_{SOF}$ and $L = 1$. However, for maximum hardware reuse, in practice the same robust detectors selected for cold start acquisition can still be exploited here, i.e. GPDI and D-GPDI, although they provide sub-optimum performance, as shown in the following section.

Similarly to cold start acquisition, also during re-acquisition after short interruptions, chip timing cannot be assumed to be ideally recovered, and acquisition must be done exploiting oversampling at the receiver, e.g. with $h = 2$.

During the blockage period caused by the fading event, the last code/frame lock becomes less reliable, due to the unavoidable clock drift, and the uncertainty region expands accordingly, spanning over U_r chips after the worst case fading duration.

Thus, when the constant modulation mode is selected, re-acquisition after short interruptions can be accomplished by applying a single dwell TC procedure to the serial inspection of only this limited uncertainty region, with considerable gain in terms of performance. In this case, the flow-graph of Figure 6.5 needs revisions to take into account that a reduced number of H_0 cells are present, and there exists a dwell time larger than $T_c/2$ and equal to $(N - hU_r)T_c/2$. A conservative characterization of the associated mean acquisition time can be derived by assuming to start the search phase in the worst case condition, i.e. from the first H_0 cell after the synchronous state, yielding

$$\begin{aligned} \bar{T}_A^C = \frac{1}{P_D} & \left\{ \frac{T_c}{2} [P_D + (U_r - 2)(2 - P_D)] \right. \\ & \left. + \frac{T_c}{2} (N - 2U_r)(1 - P_D) + T_p \frac{N-2}{2} P_{fa}(2 - P_D) \right\} \end{aligned} \quad (6.6)$$

A different approach must be followed if variable modulation is selected. Also in this case the a priori information related to the limited uncertainty region could be exploited to optimize the re-acquisition search phase, e.g. by tracing an expanding tree to explore small regions around the last lock, considering all possible frame lengths combinations. However, after a few steps, this strategy degenerates into searching over the entire longest frame length, and thus the achievable performance improvement may not justify the complexity increase. For this reason, for re-acquisition after shorty interruptions with variable modulation, exactly the same approach designed for cold start acquisition is still adopted, exploring directly the entire worst case region composed by N cells. Accordingly, the mean acquisition time is modeled by Equation (6.3).

6.5 Forward link performance results

6.5.1 Cold start code acquisition

For performance assessment, the worst SNR foreseen in DVB-S2 is considered, i.e. $E_s/N_0 = -2.35\text{dB}$ after despreading being E_s the average energy per symbol and N_0 the AWGN one-sided power spectral density. The corresponding SNR before despreading is dependent on the spreading factor according to $E_c/N_0 = 1/\eta E_s/N_0$, where E_c is the average energy per chip. A constant residual chip timing error $\delta T_c = T_c/4$ is considered, which corresponds to the worst case when oversampling $h = 2$ is used in the synchronization subsystem.

For cold start acquisition, the large frequency offset $\Delta f = 3\text{MHz}$ is considered, at the fixed chip rate of 27.5 Mcps. The reference case with no spreading is considered as a benchmark, and the achievable performance with $\eta = 2$ and $\eta = 4$ is compared, considering GPDI with $M = 2$ and $L = \eta L_{SOF}/2$ and D-GPDI with $M = 1$ and $L = \eta L_{SOF}$. The comparison in terms of Receiver Operating Characteristics (ROC), i.e. $P_{md} = 1 - P_d$ vs. P_{fa} , is provided in Figure 6.6, where it can be noticed that D-GPDI is slightly better than GPDI, providing a smaller P_{md} for a fixed P_{fa} , and there is only an almost imperceptible gain by increasing η for a fixed detector. Even if the gain with respect to the no-spreading case is not so

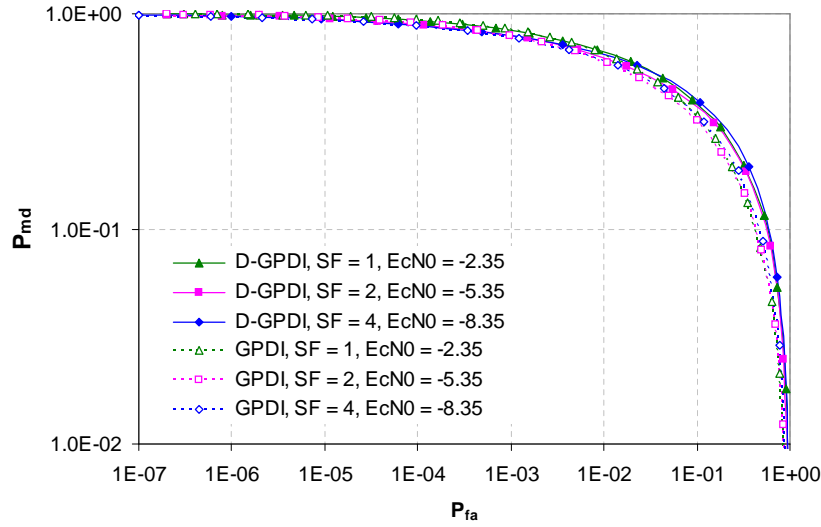


Figure 6.6: Cold start acquisition - Receiver Operating Characteristics

apparent by observing the ROC, completely different conclusions can be drawn by studying the mean acquisition time performance. Indeed, even very small differences in terms of P_{fa} and P_d can translate in significant gains for the associated mean acquisition time, due to their non-linear inter-relation described by Equation (6.3). This fact is confirmed by Figure 6.7, where the mean acquisition time is plotted versus the false alarm probability, considering $N = 2\eta 33282$ and $T_p = \eta 22230 T_c$, i.e. verification is achieved through pilot detection. Notably, each curve presents a minimum corresponding to the optimal operating point, which implements the best trade-off between missed detection and false alarm rates. For a fixed η , D-GPDI manages to outperform GPDI, revealing itself to be the most robust detector against such a penalizing frequency uncertainty. Interestingly, from the observation of Figure 6.7, it clearly appears that the price of spreading in the DVB-S2 air

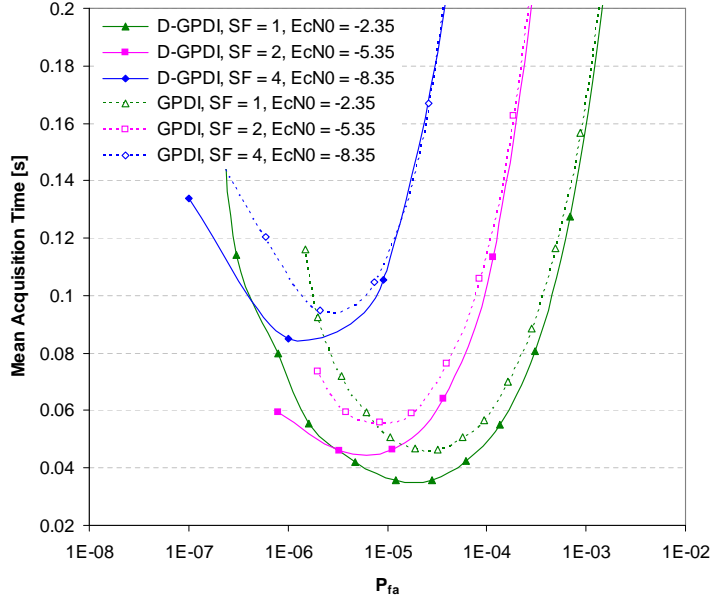


Figure 6.7: Cold start acquisition - Mean acquisition time vs. false alarm probability

η	Detector	P _{fa}	P _{md}	MAT [s]	Var Acq Time	99% T _A [s]
2	D-GPDI	3.30E-06	9.67E-1	0.067	0.005	0.314
2	GPDI	3.80E-06	9.73E-1	0.09	0.008	0.419
4	D-GPDI	1.00E-06	9.67E-1	0.111	0.013	0.518
4	GPDI	6.00E-07	9.78E-1	0.144	0.021	0.669

Table 6.3: Acquisition performance at the optimal operating point, i.e., minimum mean acquisition time, for D-GPDI and GPDI with different spreading factors, $\eta = 2$ and $\eta = 4$. Cold Start.

interface is paid in terms of acquisition time performance, which in fact degrades for increasing η , due to the largest number of single tests that has to be performed before acquiring. However, even in the worst case of $\eta = 4$, the acquisition subsystem is still able to provide $\bar{T}_A = 111\text{ms}$ with D-GPDI, which is largely satisfactory for practical applications.

In Table 6.3 the mean acquisition time and the 99th percentile are summarized for GPDI and D-GPDI.

6.5.2 Reacquisition after a short interruption

In the case of a re-acquisition after a short interruption, the maximum fade event duration is assumed equal to 1s for the railway scenario which corresponds to an interruption of 500 frames, when $\eta = 2$ and to 250 when $\eta = 4$. After this period, considering that all tracking circuits have been frozen in their last steady state operation, a clock instability of 5500Hz, and a Doppler rate of 200Hz, the frequency error can be assumed equal to 5700Hz. In addition, the clock drift introduces also a time uncertainty equal to ± 28 chips. Accordingly, the uncertainty region is equal to:

- 56 chips when the constant QPSK modulation mode is used;
- the entire largest frame length, i.e. $33282 \cdot \eta$ chips when the variable modulation mode is adopted;

Performance of re-acquisition after short interruptions for the constant modulation case is reported in Figure 6.8 where \bar{T}_A^C is plotted versus the false alarm probability, considering $U_r = 56$, $N = 2 \cdot \eta \cdot 33282$, and $T_p = 33282 \cdot \eta \cdot T_c$, i.e., verification with pilots within the QPSK frame. The same detectors as in cold start are still considered, with the addition of NCPDI. The reduced frequency error allows in fact to consider also the non-coherent approach that is unfeasible for the cold start mode. In this case D-GPDI is outperformed by GPDI, which integrates coherently over $M = 2$ chips and thus takes more advantage from the reduced carrier uncertainty. For the same reason, NCPDI outperforms both D-GPDI and GPDI.

Table 6.4 summarizes the optimal operating points for G-DPDI, GPDI and NCPDI. Although, NCPDI provides for the best performance, the mean acquisition time is largely acceptable also for the worst case, i.e., D-GPDI with $\eta = 4$, thus suggesting the possibility to adopt also for the re-acquisition after short interruption the D-GPDI approach which, as a matter of fact, must be used for the cold start case in order to deal with the large frequency uncertainty.

Similar conclusions can be drawn analyzing the mean acquisition time of re-acquisition with variable modulation, as depicted in Figure 6.9. In this case, the uncertainty region ranges over $N = 33282 \cdot \eta$ cells, and the penalty time is one frame. In the worst case, D-GPDI provides $\bar{T}_A = 31\text{ms}$, which is definitely acceptable for practical applications.

In Table 6.5 the mean acquisition time and the 99th percentile are summarized for GPDI, D-GPDI, and NCPDI. As for the constant modulation mode, although

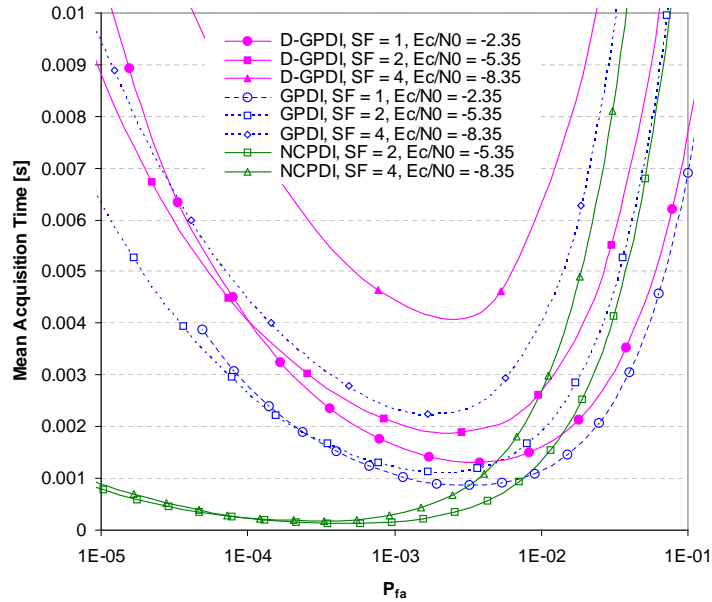


Figure 6.8: Re-acquisition after short interruptions with constant modulation - Mean acquisition time vs. false alarm probability

η	Detector	P _{fa}	P _{md}	Mean Acq Time [s]
2	D-GPDI	2.60E-06	9.28E-01	0.001897
2	GPDI	1.67E-03	4.90E-01	0.00113
2	NCPDI	3.52E-04	1.74E-01	0.000126
4	D-GPDI	7.68E-04	6.76E-01	0.00463
4	GPDI	1.70E-03	4.89E-01	0.002254
4	NCPDI	3.32E-04	1.30E-01	0.000176

Table 6.4: Acquisition performance at the optimal operating point, i.e., minimum mean acquisition time, for D-GPDI, GPDI, and NCPDI with different spreading factors, $\eta = 2$ and $\eta = 4$. Re-acquisition after a short interruption, constant QPKS modulation mode

NCPDI provides for the best performance, D-GPDI shall be preferred in order to reduce the acquisition subsystem complexity.

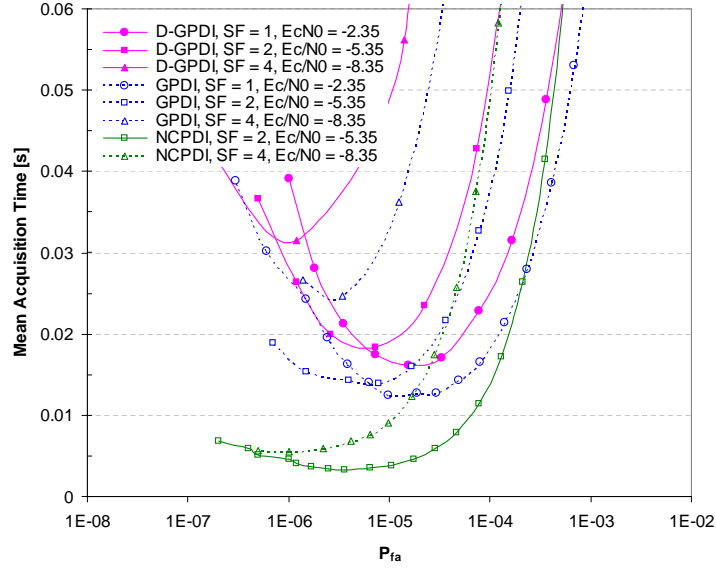


Figure 6.9: Re-acquisition after short interruptions with variable modulation - Mean acquisition time vs. false alarm probability

η	Detector	Pfa	Pmd	MAT [s]	Var Acq Time	99% T_A [s]
2	D-GPDI	2.60E-06	9.28E-1	0.0199	0.000402	0.093
2	GPDI	1.50E-06	9.15E-1	0.0154	0.000239	0.0705
2	NCPDI	1.04E-05	4.92E-1	0.0038	0.000014	0.018
4	D-GPDI	1.19E-06	9.11E-1	0.0315	0.002283	0.225
4	GPDI	3.40E-06	8.53E-1	0.0247	0.000628	0.1155
4	NCPDI	1.00E-06	5.67E-1	0.0055	0.000028	0.024

Table 6.5: Acquisition performance at the optimal operating point, i.e., minimum mean acquisition time, for D-GPDI, GPDI, and NCPDI with different spreading factors, $\eta = 2$ and $\eta = 4$. Re-acquisition after a short interruption, variable modulation mode

6.6 DS Spreading in the Return Link of DVB-RCS+M SCPC

The spreading scheme adopted for the SCPC mode is based on the forward link solution, but, in this case, only all-ones spreading sequences are used. Spreading factor up to 16 can be exploited, and the same modulation schemes to those used when Multi-Frequency Time Division Multiple Access (MF-TDMA) is employed ($\pi/2$ -BPSK and QPSK schemes), are considered. Note that, differently from the FL,

in the SCPC a fixed baud rate is considered (1Mbaud), and, consequently, variable chip rate dependant from the spreading factor η is foreseen. A shorter frame length with respect to the FL is provided, equal to $\eta 8370$ chips. The same propagation condition of the FL have been considered, i.e. LOS AWGN, but with a limited frequency uncertainty (3.0kHz due to oscillator mismatch and Doppler effect) since a preliminary frequency correction should be provided during the FL synchronization, and with two hypotheses per chip, leading to the worst case fractional timing delay of $0.25T_c$. Finally the same phase noise mask as for the FL scenario has been considered.

6.7 Return Link Performance results

Frame/code acquisition in the return link SCPC is the first operation to be performed, i.e. before carrier and timing estimation. In fact, in the presence of direct sequence spread spectrum it is difficult to perform parameter estimation with sufficient accuracy before code acquisition.

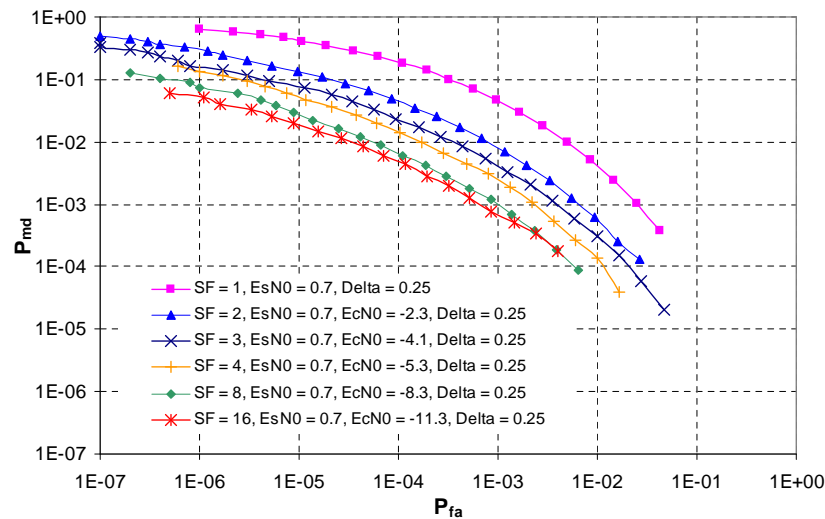


Figure 6.10: Simulated ROC performance at $E_s/N_0 = 0.7\text{dB}$, with non ideal sampling ($\delta = 0.25$) considering spreading factors $\eta = 1, 2, 3, 4, 8, 16$

In Figure 6.10, analytical and simulated ROCs are presented in AWGN with $E_s/N_0 = 0.7\text{dB}$ and chip time misalignment $\delta = 0.25$, in the exemplary scenarios with $\eta = 1, 2, 3, 4, 8, 16$. Notably, the analytical curves well validate the simulation results. By comparing the different spreading factors, it clearly emerges that in

the RL the introduction of DS spreading improves ROC performance because the interference introduced by the unknown information data (self-noise) during SoF search procedure is attenuated in this case. Similarly, the performance at $E_s/N_0 = -1\text{dB}$ are reported in Figure 6.11. Note that the results obtained are the complete opposite of the FL case, in which, being fixed the chip rate, the increase of the spreading factor implies an higher impact of the frequency error on the chips.

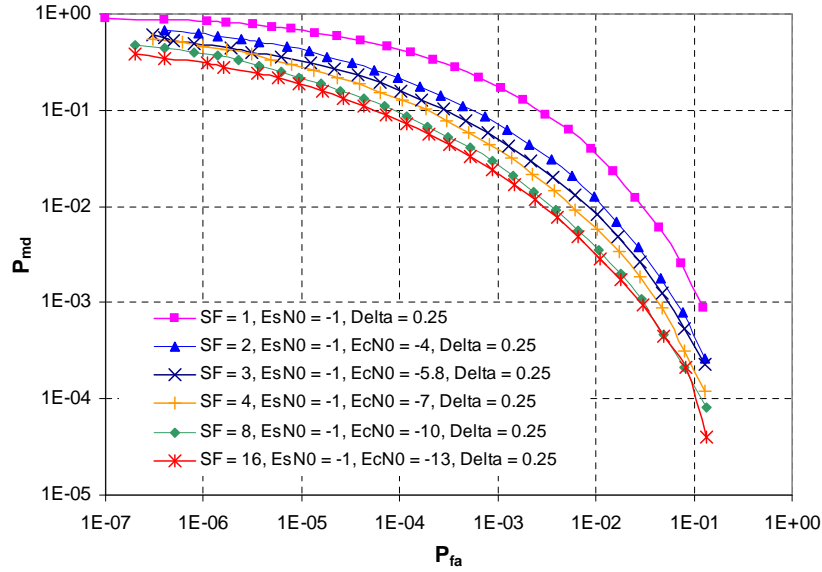


Figure 6.11: Simulated ROC performance at $E_s/N_0 = -1\text{dB}$, with non ideal sampling ($\delta = 0.25$) considering spreading factors $\eta = 1, 2, 3, 4, 8, 16$

In Figure 6.12 and Figure 6.13, the mean acquisition time (MAT) is reported vs. the false alarm probability, considering a single dwell serial search procedure [50], with two hypotheses per symbol to contrast the chip timing uncertainty. In particular, the worst case condition for the sampling error is assumed, considering a symbol/chip timing misalignment $\delta = 0.25$. The procedure terminates when the correct alignment has been detected. In case of false alarms, the procedure restarts after a penalty time $T_p = 2T_F$ (non absorbing false alarm), being T_F the frame duration.

The MAT performance confirms the results shown by ROC, i.e. performance improves by increasing the spreading factor. The best performance is achieved in correspondence of the minimum points of the MAT curves, which are summarized in Table 6.6. In any case, the worst case performance, which is 15ms for $\eta = 1$ and $E_s/N_0 = -1\text{dB}$ appears to be satisfactory.

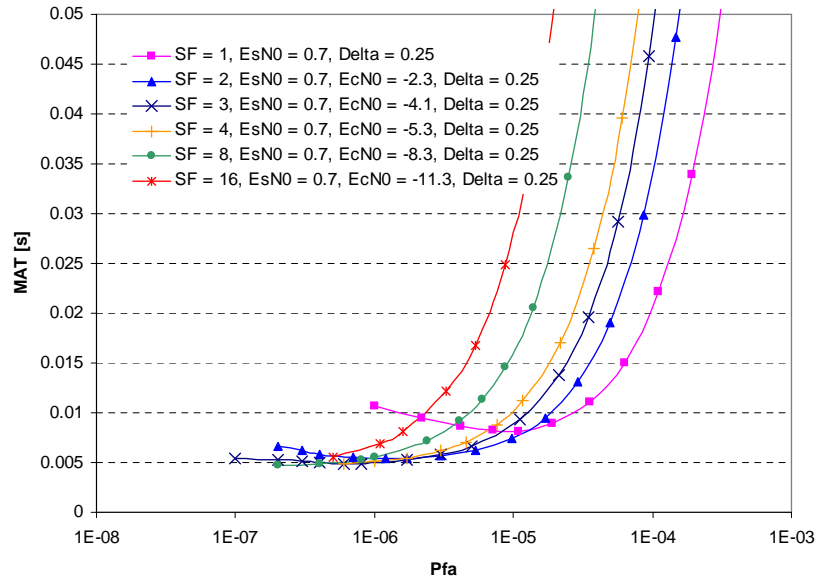


Figure 6.12: Mean Acquisition Time performance in AWGN at $E_s/N_0 = 0.7\text{dB}$, with non ideal sampling ($\delta = 0.25$) considering spreading factors $\eta = 1, 2, 3, 4, 8, 16$

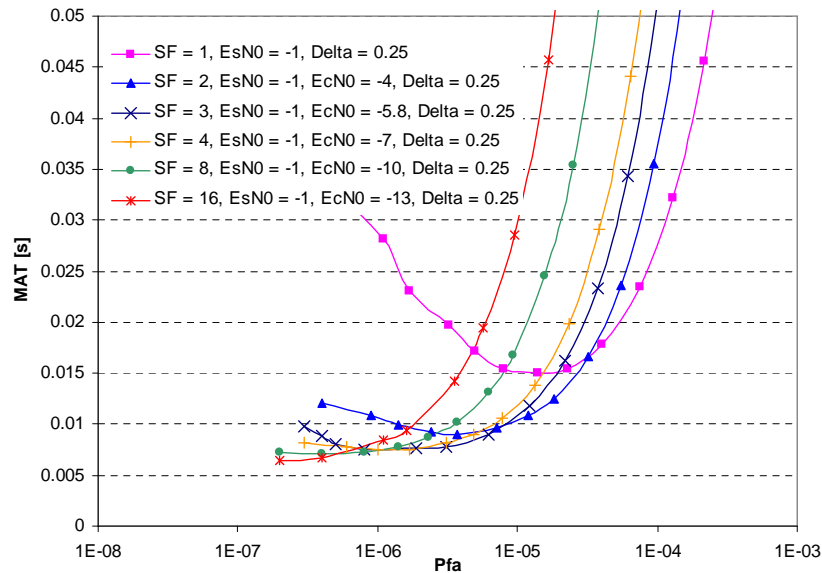


Figure 6.13: Mean Acquisition Time performance in AWGN at $E_s/N_0 = -1\text{dB}$, with non ideal sampling ($\delta = 0.25$) considering spreading factors $\eta = 1, 2, 3, 4, 8, 16$

6.8 Code acquisition in DVB-RCS+M Conclusions

The original design and performance assessment of code synchronization for the mobile option of DVB-RCS+M has been addressed in this chapter, showing that

E_s/N_0 [dB]	SF	E_c/N_0 [dB]	Pfa	Pmd	MAT [s]
0.7	1	0.7	1.1E-05	0.40	0.0079
	2	-2.3	1.7E-06	0.24	0.0052
	3	-4.1	8.0E-07	0.17	0.0048
	4	-5.3	6.0E-07	0.16	0.0048
	8	-8.3	2.0E-07	0.12	0.0045
	16	-11.3	5.0E-07	0.06	0.0053
-1	1	-1.0	1.4E-05	0.64	0.0145
	2	-4.0	3.7E-06	0.50	0.0087
	3	-5.8	8.0E-07	0.48	0.0073
	4	-7.0	1.0E-06	0.46	0.0073
	8	-10.0	4.0E-07	0.44	0.0069
	16	-13.0	2.0E-07	0.38	0.0062

Table 6.6: Minimum MAT in AWGN at $E_s/N_0 = 0.7$ and -1 dB, with non ideal sampling ($\delta = 0.25$) considering spreading factors $\eta = 1, 2, 3, 4, 8, 16$

the D-GPDI approach represents the most suitable scheme achieving excellent performance in every working conditions, especially in the Forward Link, where the frequency uncertainty is the main issue to cope with. On the other hand, in the Return Link the frequency uncertainty is limited, since a preliminary frequency correction during the Forward Link synchronization is foreseen. Thus, the classical NCPDI approach guarantees the best performance, anyway the mean acquisition time achievable with the D-GPDI is always limited to a few milliseconds, allowing fast acquisition in the highly challenging railway scenario as well.

7

Synchronization in Future OFDM Standards: LTE and WiMAX

Recent years have seen the consolidation of OFDM (Orthogonal Frequency Division Multiplex) [95] as the basic modulation for all the future broadcasting standards. Terrestrial systems like DVB-H (Digital Video Broadcasting - Handheld) or the incoming DVB-T2 [96] (Terrestrial second generation) and satellite systems like DVB-SH [97] (Satellite services to Handhelds) will exploit the advantages of OFDM, similarly to broadband WiMAX [98] (Worldwide Interoperability for Microwave Access) and LTE [99] (Long Term Evolution) or to the next generation standard DVB-NGH (Next Generation Handheld), which is currently on definition.

The advantages of OFDM lie in its inherent robustness against multipath and severe channel conditions, in its high spectral efficiency, and in its simpler channel equalization. On the other hand, the advantages of this flexible, low complexity and robust air interface translate in an optimized system capacity and a higher Quality of Service (QoS) only if an efficient synchronization strategy is applied. In fact, the most critical drawback of an OFDM system is its high sensitivity to synchronization non idealities. In particular, incorrect timing synchronization can effect inter-symbol

interference (ISI) and, if not perfectly compensated before the equalization process, can lead to heavy performance degradation. In addition, a carrier-frequency offset (CFO) can cause interference between adjacent subcarriers (ICI) and a consequent reduction of the useful signal power [100]. For these reasons, synchronization in OFDM, which has to take into account both time and frequency domain, is usually performed in several steps: Pre-FFT and Post-FFT synchronization. In the Pre-FFT phase, the estimation algorithms operate in the time domain and are in charge of performing the Coarse Timing Estimation (CTE) and Fractional Frequency Estimation (FFE), while in the Post-FFT phase, the algorithms operate in the frequency domain and have to accomplish the Integer Frequency Estimation (IFE), and the Fine Timing Estimation (FTE). The Pre-FFT algorithms are usually Guard Interval (GI) based [101][102], i.e. they exploit the correlation between the useful symbol part and the Cyclic Prefix (CP) of the received signal. The Post-FFT algorithms are usually based on a data aided estimation on the pilot tones. In the same time, another operation to be performed is the frame acquisition, which consists in the detection of the Start of Frame (SoF). This operation can be performed before the Pre-FFT Synchronization, i.e. in the time domain, or in the frequency domain after Pre-FFT Synchronization, i.e. when a coarse timing and frequency estimation has been already done in the time domain, according to the frame structure.

In this chapter, the analysis of frame synchronization in two novel OFDM standards, such as LTE and WiMAX, is provided [11]. These two standards can be both intended as 4G broadband standards. In fact, recent years have seen the rush towards the definition of Beyond 3G (B3G) evolution and 4G architectures, which will be intended to face with the following trends: flexible and reliable broadband air interfaces, with cognitive functions; improved coverage for ubiquitous connection; scalable and increased system capacity for mass-market services; dynamic spectrum management; new networking modes, i.e. multicast, broadcast, multi-hop, peer-to-peer, ad-hoc; evolved user terminals with multiple functionalities.

In this framework, three different evolutionary paths can be outlined, which are respectively identified as 3.5G, B3G, and 4G. In the following each one of these has been briefly explained. Note that, for the sake of simplicity, in the scientific research arena, all of these are intended as 4G evolutions.

- 3.5G: enhancements to 3G
 - Backward compatible with legacy radio networks
 - Objectives: capacity increase, better performance, lower cost

-
- Example: HSDPA enhancements
 - B3G: integration of diverse radio interfaces
 - Adding new air interfaces to the network
 - Objectives: new functionality, applications, content
 - Examples: WLAN/WiMAX, DVB-H, MediaFlo
 - 4G: new Air Interface in new Spectrum
 - Higher bit rates than 3G and full mobility
 - Higher spectral efficiency and lower cost per bit than 3G
 - Air interface optimized for IP traffic
 - Examples: 3GPP Long-Term Evolution (LTE) concepts

It is most probable that WiMAX and LTE will play central roles in the next years. For this reason, the problem of synchronization in these systems have raised interest in the field. Note that, in order to provide ubiquitous coverage to all the users, it is likely that a hybrid terrestrial-satellite infrastructure will be exploited from both the systems.

LTE is defined as a set of targets and requirements, provided by the 3GPP community in order to reply to ever more stringent user demand. Similarly, WiMAX represents the latest technology that has promised to offer broadband wireless access over long distance. Although the two competing standards perform rather equal since they both exploit the same state-of-the-art techniques [103], and, considering all the possible way to be implemented, they can differ only on the air interface, the preamble has been differently designed in the two cases, leading to different approach and different performance. In the next sections, the following acquisition strategies have been analyzed:

- LTE Frame Acquisition in Frequency Domain (after Pre-FFT Synchronization)
- WiMAX Frame Acquisition in Time Domain (before and after Pre-FFT Synchronization)

Note that this work has been carried out in the European project 4G framework [21], and my contribution has been focused on the detectors design and on the synchronization performance evaluation.

7.1 System Model

An OFDM system using an Inverse Fast Fourier Transform (IFFT) of size N_{FFT} is considered. Each OFDM symbol, in the frequency domain, is composed of $N_a < N_{FFT}$ data symbols $a_{k,l}$, where l represents the OFDM symbol time index and k represents the subcarrier frequency index. Then, data symbols are shaped by a rectangular pulse of length T_u and modulated onto subcarriers with baseband frequency $f_k = k/T_u$. At the output of the IFFT, in the time domain, the OFDM symbol is formed by N_{FFT} baseband samples $s(i)$, where i represents the time domain index. For each OFDM symbol a guard interval of length T_g is inserted to avoid ISI. During the guard interval the periodic repetition (CP) of the last N_g samples of the current OFDM symbol is transmitted so as to avoid intercarrier interference. The resulting symbol has duration $T_g + T_u$, or equivalently, $N_g + N_u$ samples [104].

Note that both the systems are analyzed assuming 5MHz bandwidth, and the classic characteristics of the Forward Link (FL) Broadcasting Scenario. In this framework, LTE is characterized by a fixed sub-carrier spacing of 15kHz, and a fixed FFT length $N_{FFT} = 2048$, and the bandwidth is calculated according to the N_a effective active carriers (i.e. $N_a = 300$ for the 5MHz bandwidth). In WiMAX the sub-carrier spacing depends on the selected N_{FFT} (i.e. $N_{FFT} = 512$ for the 5MHz bandwidth leads to 10.94kHz spacing, with $N_a = 420$ active carriers). The characteristics of the two systems are summarized in the following Table.

7.2 Frame Acquisition in LTE

The LTE frame is characterized by the constant duration of 10ms, and it is partitioned into sub-frames of 1ms Transmit Time Interval (TTI) duration. In addition, a LTE frame is composed by 20 slots. An entire preamble dedicated to the synchronization is not foreseen, but two different Unique Words (UWs) of 72 symbols are inserted at the end of the 1st and of the 11th slot of each frame, identified respectively PSCH and SSCH, as shown in Figure 7.1. Two different sequences are used, Zadoff-Chu [105] for the primary preamble, and an interleaved concatenation of two binary sequences of length 31 for the secondary preamble. The acquisition process can be performed in two different ways. One possible solution can be to divide the entire process into two acquisitions in cascade, in which the former is performed by a serial search of the first UW, which provides the acquisition of the ID cell group,

PHY-FL Broadcasting Scenario		
	LTE	WiMAX
Channel Bandwidth	5 MHz	5 MHz
N_{FFT}	2048	512
Subcarrier Spacing	15 kHz	10.94 kHz
Active Sub-carriers N_a	300	420
Number of data OFDM symbols per TTI	12	12
TTI Duration	1 ms	1.49 ms
OFDM Symbol Duration T_u	83.33 μ s	114.29 μ s
Sampling Time T_s	32.55 ns	179 ns
CP Length	16.67 μ s [1/4]	22.85 μ s [1/4]

Table 7.1: Parameters of LTE and WiMAX Air Interfaces

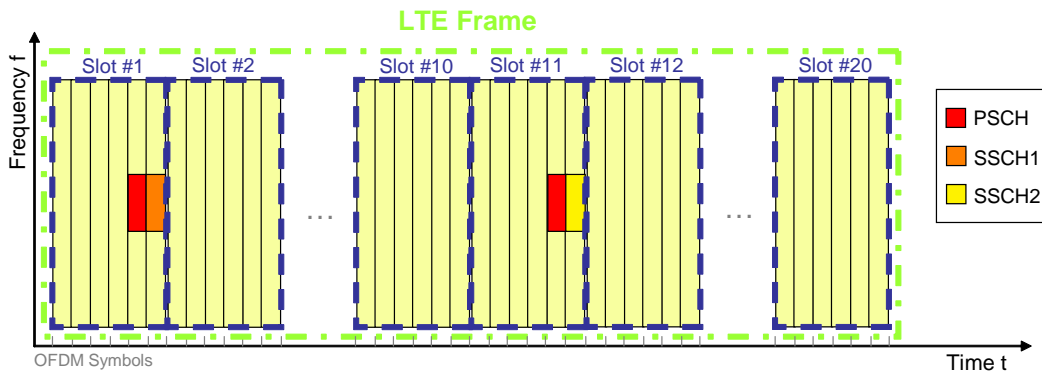


Figure 7.1: LTE Frame Structure

and the latter on the second one, which is in charge of estimate the Cell Number. Note that, in this case, the second acquisition starts only when the alignment with the first UW has been reached. A complete acquisition is declared if both the acquisition processes have been completed. Another solution consists in considering the two UWs as a single UW and performing acquisition over the entire 144-length known preamble, but in the following this approach has been not investigated, since requires a complexity increase, without ensuring any significant performance gain.

Since in the time domain it is not possible to extract only the UW without counteracting the interference from the data, in the following only the frame acquisition in the frequency domain has been analyzed. The general block diagram of a receiver

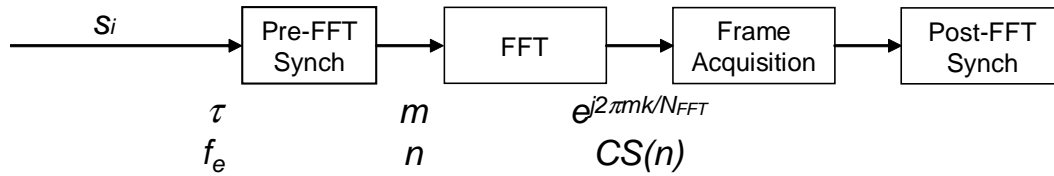


Figure 7.2: Receiver Block Diagram

is shown in Figure 7.2. Note that the frame acquisition is performed in the frequency domain after the Pre-FFT Synchronization, thus, after the CTE and the FFE that exploit the presence of CP to perform the first estimate. In the figure, the different residual unknown quantities and their effects have been highlighted: the timing and the frequency offsets τ and f_e are partially compensated by the Pre-FFT estimation block, leaving the residual timing error m , and the integer frequency offset n ; the FFT block transforms a timing error in time domain directly in a frequency offset in the frequency domain and viceversa, thus, after the FFT, a phase rotation $e^{j2\pi mk/N_{FFT}}$, and a circular shift $CS(n)$ affect the samples.

Assuming that the timing offset is assumed to be uniform distributed between

$$\left[-m_{max} \frac{T_u}{N_{FFT}}, m_{max} \frac{T_u}{N_{FFT}} \right] \quad (7.1)$$

and that a realistic value of m_{max} is in the range of $[20, 30]$ as detailed in [104], a Post Detection Integration (PDI) approach should be considered, and in particular the classical Non Coherent PDI (NCPDI), which guarantee a good performance/complexity trade-off (Figure 7.3).

In order to cope with this frequency rotation, a PDI length L_{PDI} equal to 2 is sufficient. Figure 7.4 shows the performance in terms of ROCs of the described

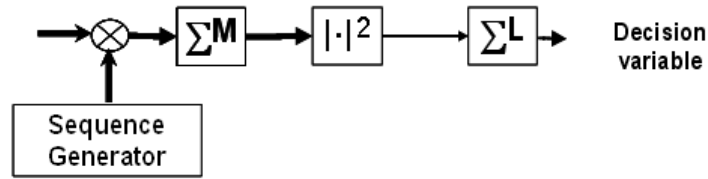


Figure 7.3: Non Coherent Post Detection Integration (NCPDI)

approach. This figure refers to an AWGN scenario with E_s/N_0 equal to $0dB$, where E_s represents the energy per OFDM sample, while N_0 is the two-sided power spectral density of the gaussian noise. Note that the PDI length equal to 2 represent the best solution since the full coherent correlation (PDI length equal to 1) brings to non satisfactory performance.

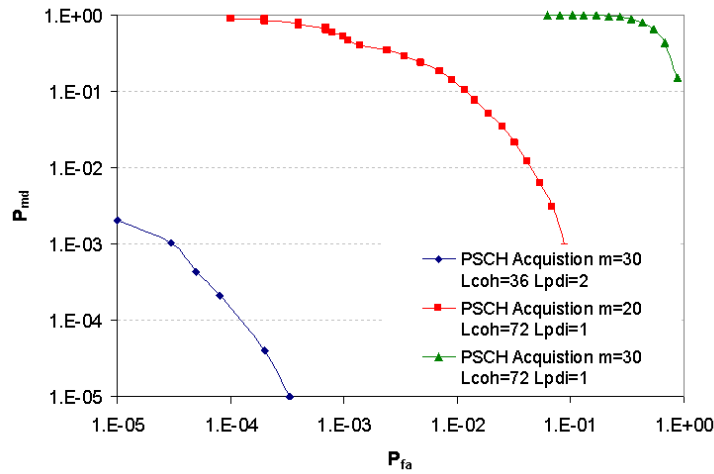
Figure 7.4: Performance of the LTE PSCH Acquisition: AWGN $E_s/N_0 = 0dB$

Figure 7.5 shows the performance in a Rice fading channel. Performance has been considered for a signal to noise ratio of $E_s/N_0 = 0dB$ and Rice factor of $7dB$. Note that acquisition performance with a PDI strategy ($L_{PDI} = 2$) still guarantees good performance.

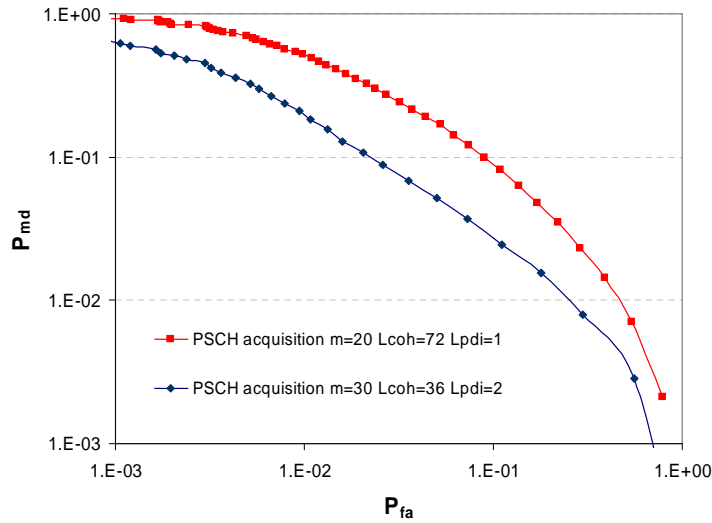


Figure 7.5: Performance of the LTE PSCH Acquisition in a Rice fading channel: $E_s/N_0 = 0\text{dB}$ and Rice factor of 7dB

7.3 Frame Acquisition in WiMAX

Differently from LTE, in WiMAX the preamble is inserted in the first symbol of the frame, as shown in Figure 7.6. The preamble is a BPSK modulated Pseudo Noise (PN) code, mapped on the carriers accordingly to some parameters like ID_{cell} and others. The number of the active tones depends on the N_{FFT} according to the

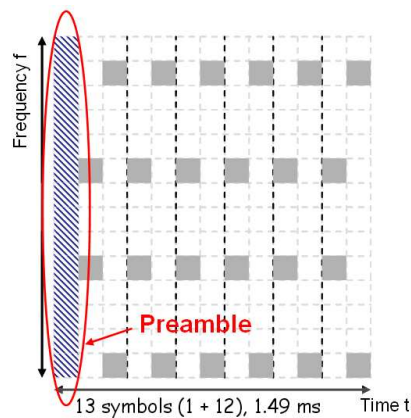


Figure 7.6: WiMAX Frame Structure

following table:

Since the first symbol is dedicated entirely to the transmission of the preamble,

NFFT	Active Carriers
2048	568
1024	284
512	144
128	36

Table 7.2: Number of the Active Carriers on the WiMAX Preamble

acquisition can be performed both in the frequency and in the time domain without any filtering. Anyway, in the frequency domain the sequence mapped into the tones is selected inside a set of 114 possible sequences, depending on the segment used and ID_{cell} parameter [98]. Thus, in order to find the SoF, if acquisition on the frequency domain is pursued, all the possible sequences should be tested, leading to a significant complexity increase. On the other hand, the preamble tones are distributed with a certain pattern on the carriers, in particular, as detailed in Figure 7.7, separated by two free carriers, and thus translating in a nearly equal repetition of about $\frac{T_u}{3}$ in the time domain, i.e. $S1$, $S2$, and $S3$ as shown in Figure 7.8.



Figure 7.7: Structure of the active carriers in the WiMAX preamble

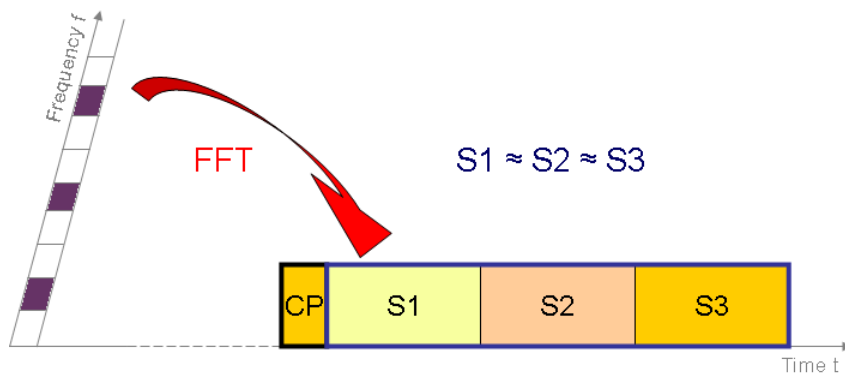


Figure 7.8: Structure of the WiMAX preamble in the time domain

Thus, this peculiar position of preamble tones permits acquisition in the time

domain without knowing the effective transmitted sequence, but exploiting only a sliding windowing approach. For this reason, in the following, only this simple acquisition scheme in the time domain has been analyzed.

The block diagram of the detector is reported in Figure 7.9, and in Figure 7.10 the principle of the sliding window correlation is explained. This simple and efficient technique, proposed in [106], computes the correlation between the received samples and the complex conjugate of the received time domain signal delayed by τ samples, resulting in

$$F(m) = \left| \sum_{i=m}^{m+N-1} r^*(i-\tau) \cdot r(i) \right| \quad (7.2)$$

where N represents the correlation length.

This strategy, usually adopted to exploit the correlation properties of the CP in the GI based estimation algorithms, can be extended in this case for a longer sequence, due to the peculiar shape of the preamble.

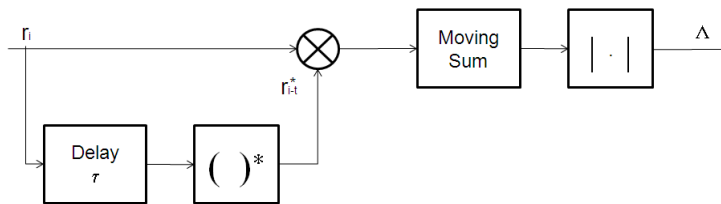


Figure 7.9: Sliding Window Correlation Scheme

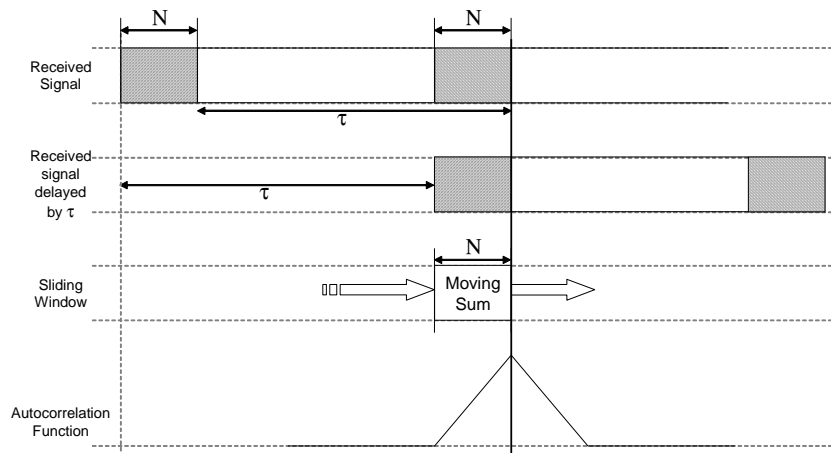


Figure 7.10: Moving Sum: a practical example

In particular, correlation with the conjugated version of the signal itself in the

time domain with a delay $\tau = T_u/3$ should be foreseen in this case, and the correlation length can be chosen between two possibilities: taking into account also the CP, i.e. $N = 2/3T_u + T_g$, or only the repetitions inside the preamble, i.e. $N = 2/3T_u$, as shown in Figure 7.11.



Figure 7.11: Sliding Window approach for WiMAX Preamble Detection

Note that the correlation function resulting from this choice is different in the two cases (Figure 7.12). In particular, considering also the CP into the sliding window, i.e. a $2/3T_u + T_g$ correlation length, outperforms the correlation of length $2/3T_u$ only, thus in the following only the former is exploited.

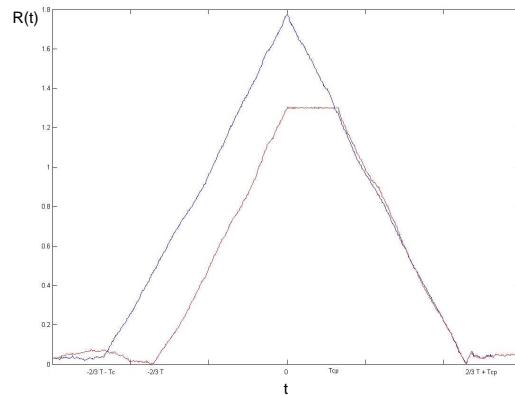


Figure 7.12: WiMAX Frame: Autocorrelation Function

Note that the frame acquisition in time domain can be performed as the first operation by the receiver, even before the GI based Pre-FFT estimation. If it is assumed to be the first operation to be performed, no preliminary hypothesis on the timing uncertainty is foreseen. On the contrary, if the GI based Pre-FFT estimation is pursued, a limited timing uncertainty should be considered, i.e. the timing error to

consider is uniform distributed inside the variance of the Pre-FFT estimate. In the following a discretization of 4 hypotheses (cells) per T_u is considered, so transforming the uncertainty region into a region of $4 * 12 = 48$ cells, and each cell has a length of $T_u/4$. As expected, acquisition before the cyclic prefix is linked to a timing uncertainty of the entire cell length (about T_u), while acquisition after the CTE has a residual timing uncertainty of about $30T_s$. Performance of frame acquisition has been evaluated in terms of ROCs.

Figure 7.13 confirms this hypothesis, considering an AWGN scenario with two different signal to noise ratios, $E_s/N_0 = -5\text{dB}$ and $E_s/N_0 = 0\text{dB}$, where E_s refers to the energy per OFDM sample. If a preliminary estimation on the timing uncertainty is provided before the frame acquisition, more robust performance can be obtained, very close to the ideal one. On the other hand, if frame acquisition is the first operation to be performed, performance can be poor and acquisition can result challenging. In this case a finer discretization should be considered, and a joint frame acquisition / frequency estimation can be exploited since, as detailed in the next chapter, the longer correlation of the preamble with respect to the CP can lead to better performance.

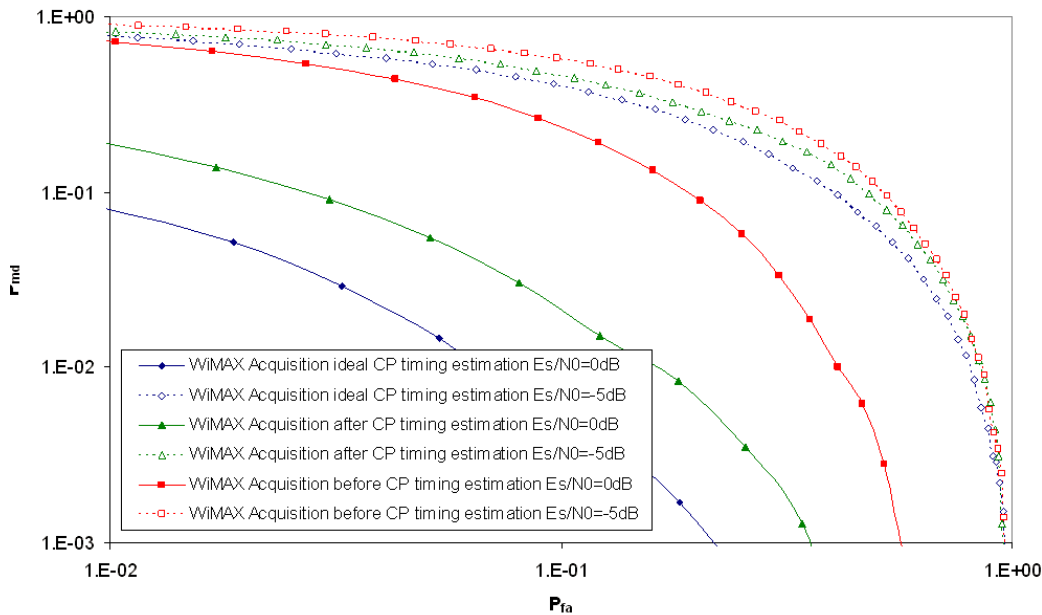


Figure 7.13: Performance of WiMAX Preamble Detection

7.4 Synchronization in LTE and WiMAX: Conclusions

In this chapter the frame synchronization in LTE and WiMAX systems has been investigated. Although the two 4G systems are very similar in terms of air interfaces, and, consequently, in terms of performance, the approaches to be used are completely different. LTE does not foresee any preamble devoted to synchronization aspects, but reserves some carriers to the transmission of a synchronization code. Thus the frame acquisition is seen as a secondary operation to be performed in the frequency domain subject to the primary synchronization provided by the Guard Interval-based algorithms. On the other hand, WiMAX standard supplies a preamble which should be used for the frame synchronization in the time domain, and can be also exploited for the fractional frequency estimation (FFE). Of course, the presence of the preamble and its exploitation in time guarantees robust performance and it can be seen as a reliable alternative to the Pre-FFT estimation algorithms. The frame synchronization in the frequency domain can be seen as a secondary operation, whose performance depends on the Pre-FFT estimation algorithms, and it can be seen as a robust alternative to the Post-FFT estimation algorithms. The following chapter highlights the advantages of the insertion of a preamble in a future satellite-terrestrial OFDM broadcasting standard.

8

Preamble Insertion in Future Satellite-Terrestrial OFDM Broadcasting Standards

As detailed in the previous chapter, the main advantages of OFDM lie in its inherent robustness against multipath and in its high spectral efficiency. This chapter addresses another key aspect: since multipath reflections with a delay spread less than the guard interval cause no inter-symbol interference, OFDM can be exploited to enable Single Frequency Network (SFN) coverage. SFN is a broadcast system consisting of transmitters with overlapping coverage areas that send the same frequency and time synchronized signal. Hence, the same signal can arrive at the receiver antenna from different transmitters and be correctly received with a significant power gain even if each transmitted signal has with its own delay as long as all the echoes arrive with a delay shorter than the guard interval. Moreover, since high reliability and ubiquitous coverage is demanded of future systems, hybrid satellite-terrestrial architecture have been widely investigated in recent years. These architectures can exploit the SFN paradigm, by adopting OFDM and designing the guard interval accordingly. In this kind of framework, synchronization becomes even more chal-

lenging, and the use of a preamble can be instrumental to guarantee an efficient joint synchronization and frequency estimation.

Note that some standards, like DVB-T2 or WiMAX, provide a preamble at the beginning of each frame, whose detection is performed in the time domain, and that can also be used for a more precise Fractional Frequency Estimation (FFE); other standards, like DVB-H and DVB-SH [97], have been designed without any preamble, but with some signalling bits, called TPS (Transmission Parameter Signalling), that are in charge of informing the receiver about frame position, code rate, used modulation, and other parameters necessary to locate the received signal in both time and frequency and to start the demodulation and the decoding operations. This chapter focuses on the problem of the preamble insertion in those systems, for example the DVB-SH, which have been designed without it, focusing on the performance in terms of Frame Acquisition probability, CTE and FFE Mean Square error.

The results presented in this chapter have been partially published in [12]. The proposal of the adoption of a terrestrial standard like preamble for a future satellite communication system and its performance analysis, is my main contribution on this topic.

8.1 System model

In the following, we consider an OFDM signal with N total subcarriers and N_a active subcarriers, with $N_a < N$. The l -th OFDM symbol $s_l = (s_{0,l}, \dots, s_{N-1,l})$, is obtained as the N points Inverse Discrete Fourier Transform (IDFT) of the vector of complex symbols $x_l = (x_{0,l}, \dots, x_{N-1,l})$, as:

$$s_{i,l} = \frac{1}{\sqrt{N}} \sum_{k=0}^{N-1} x_{k,l} e^{j2\pi ki/N} \quad i = 0, \dots, N-1 \quad (8.1)$$

In general, the complex symbols $x_{k,l}$ carry either data information or pilot (scattered and continual) reference symbols, used for synchronization and channel estimation. In order to avoid intersymbol interference and maintain subcarrier orthogonality even in multipath, a cyclic prefix of length N_g samples is inserted at the beginning of each OFDM symbol. This is followed by digital to analogue conversion at sampling time T , so that the time continuous signal can be written as:

$$s(t) = \frac{1}{T_u} \sum_{l \rightarrow -\infty}^{+\infty} \text{rect} \left(\frac{t}{T_L} - \frac{1}{2} - l \right) \cdot \sum_{k=0}^{N-1} x_{k,l} e^{j2\pi \frac{1}{T_u} k(t-T_g)} \quad (8.2)$$

where $T_u = NT$ represents the OFDM useful symbol duration, $T_g = N_g T$ represents the duration of the guard interval associated to the cyclic prefix, therefore $T_L = T_u + T_g$ is the total OFDM symbol duration, and $f_u = \frac{1}{T_u}$ is the subcarrier spacing. The OFDM signal is transmitted over a time-varying frequency selective fading channel, under the assumption that the channel coherence time exceeds T_L . The baseband equivalent channel impulse response is modeled as a tapped delay line:

$$h(t) = \sum_j h_j(t) \delta(t - \tau_j(t)) \quad (8.3)$$

where $h_j(t)$ and $\tau_j(t)$ are respectively the gain and delay of the j -th path, at time t . In Rayleigh fading conditions, $H_{k,l}$ can be modeled as a complex Gaussian random variable with zero mean and variance σ_H^2 per branch. The total channel energy is normalized, i.e. $\sum_j E[h_j^2] = 1$, and the maximum delay is assumed to be smaller than the guard interval duration:

$$\tau_{MAX} = \max_j(\tau_j) \leq T_g \quad (8.4)$$

The received signal can be written as

$$r(t) = h(t) * s(t) + n(t) \quad (8.5)$$

where $n(t)$ represents Complex Additive White Gaussian Noise (AWGN) random process filtered on the receiver bandwidth. Under the hypothesis that $\tau_j(t)$ remains constant and considering timing and frequency offset at the receiver, sampling the received signal every T seconds yields:

$$r(ut) = e^{j2\pi\Delta f T u} \sum_j h_j(ut) s(ut - \tau_i - \Delta t) + n(ut) \quad (8.6)$$

where $E[n(t)^2] = N_0$ is the mono-lateral noise power spectral density, while, Δt and Δf represent respectively timing and frequency offset. The latter can be modelled as the sum of two contributions: an integer multiple of f_u , and a fractional part

$$\frac{\Delta f}{f_u} = n + \xi \quad (8.7)$$

where $n \in Z$ and $\xi \in [-0.5; 0.5[$. Having removed the guard interval and re-arranged the vector at the input of the FFT, the samples belonging to the l -th OFDM symbols are the elements of the \mathbf{r}_l vector.

$$r_{i,l} = r((l(N + N_g) + N_g + u')T) \quad (8.8)$$

$$i = |u'|_N \quad l = \lfloor u'/N \rfloor \quad (8.9)$$

Assuming that $h_j(t)$ remains constant over a OFDM symbol duration, at the output of the FFT, in the frequency domain, the OFDM symbol is:

$$y_{k,l} = \frac{1}{\sqrt{N}} \sum_{i=0}^{N-1} r_{i,l} e^{-j2\pi ki/N} \quad (8.10)$$

$$= x_{k-n,l} H_{k-n,l} e^{j\frac{2\pi k \Delta t}{T_u}} + n_{k,l} \quad (8.11)$$

where according with DFT normalization factor $\frac{1}{N}$ has been taken into account, $n_{k,l}$ is the complex AWGN sample in the frequency domain, and $H_{k,l}$ is the Channel Transfer Function (CTF) at the subcarrier k , in the l -th symbol:

$$H_{h,l} = \frac{1}{\sqrt{N}} \sum_{j=0}^{N-1} h_{j,l} e^{-j2\pi kr_j/T_u} \quad (8.12)$$

8.2 Hybrid channel Description

Satellite-Terrestrial SFN networks have the intrinsic advantage of providing seamless coverage between urban and rural/open areas, relying on the transmission of the same signal both on the satellite and on the terrestrial component. The most peculiar situation is when the user terminal is located at the edge of the terrestrial coverage, where the power received from the satellite is comparable to the power received from the terrestrial component. Large relative delays are experienced in the received signal, since it is not possible to synchronize the reception of satellite and terrestrial signals in the entire coverage region. We consider the relative delay Δ between satellite and terrestrial component. For mobile terminals, since the relative speed with respect to the satellite and to the terrestrial repeater is different, different Doppler shifts are present on the LoS components of the different signal replicas. A channel model that takes into account these aspects is introduced, and named *Hybrid Channel* model, that assumes that the satellite path is modeled through a Ricean fading, while the terrestrial propagation is modeled by TU6, as detailed in Table 8.1.

8.3 Preamble Description

In the following the preamble taken from the DVB-T2 [96] standard has been considered as the benchmark for the analysis. Note that introduction of a preamble in other standards needs an entirely different optimization in order to minimize the

	Fading	Relative Delays (μ s)	Relative Losses (dB)
1	Rice $K = 7$	0	-3
2	Rayleigh	$0.0 + \Delta$	-7.2
3	Rayleigh	$0.2 + \Delta$	-4.2
4	Rayleigh	$0.5 + \Delta$	-6.2
5	Rayleigh	$1.6 + \Delta$	-10.2
6	Rayleigh	$2.3 + \Delta$	-12.2
7	Rayleigh	$5.0 + \Delta$	-14.2

Table 8.1: Hybrid Channel power delay profile

overhead and to be able to transmit all the necessary parameters with a sufficient protection. This analysis is focused only on the possibility of estimate jointly timing and frequency, leaving to further works these considerations. The main advantage of the use of a preamble is to allow the receiver to locate the received signal in both time and frequency.

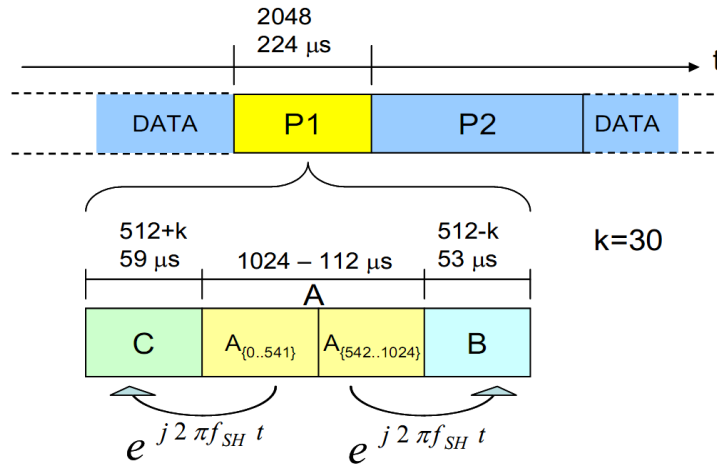


Figure 8.1: P1 Structure in time domain

The DVB-T2 preamble, called $P1$, is composed by an OFDM symbol, called A , as shown in Figure 8.1, of length 1024 samples, with two guard interval portions added at both sides. The length in samples of the $P1$ is fixed, regardless of the FFT mode and guard-interval configuration. Differently from the cyclic prefix used in all the normal OFDM symbols, a frequency shifted version of the symbol is used with a fixed frequency shift f_{SH} equal to $1/1024T$. Let C be the left guard interval, which is the frequency shifted version of the first $542T$ of A , while let B be the right guard

interval of the symbol conveying the frequency shifted version of the last $482T$ of A . The total symbol lasts $224\mu\text{s}$ in 8MHz configuration, comprising $T_A = 112\mu\text{s}$, the duration of the part A of the symbol plus the two modified guard interval sections C and B of $T_C = 59\mu\text{s}$ ($N/2 + k = 542$ samples long, with $k = 30$) and $T_B = 53\mu\text{s}$ ($N/2 - k = 482$ samples long, with $k = 30$). The main part A of the symbol foresees the transmission of two signalling fields, exploiting only $N_a = 384$ active carriers of the $1k$ OFDM symbol. The used carriers occupy roughly 6.83MHz band from the middle of the nominal 7.61MHz signal bandwidth, while the active carriers are DBPSK modulated.

The time-domain baseband waveform of the $P1$ preamble can be defined as:

$$P1(t) = \begin{cases} P1^A(t)e^{j2\pi f_{SH}t} & 0 \leq t \leq 542T \\ P1^A(t - 542T) & 542T \leq t \leq 1566T \\ P1^A(t - 1024T)e^{j2\pi f_{SH}t} & 1566T \leq t \leq 2048T \\ 0 & \text{otherwise} \end{cases} \quad (8.13)$$

Preamble symbol $P1$ has three main purposes. First it is used during the initial signal scan for fast recognition of the T2 signal, for which just the detection of the $P1$ is sufficient. The second task is to signal basic TX parameters that are needed to decode the rest of the preamble which can help during the initialization process. The third purpose of $P1$ is to enable the receiver to detect and correct frequency and timing synchronization. In the next Section a joint Frame Detection / Frequency Estimation scheme based on the $P1$ structure is described.

8.4 Joint Frame Detection / Frequency Estimation scheme

In the following the principles of a novel detector are shown. The idea is to jointly perform the frame detection and the frequency estimation, exploiting in the time domain the presence of the preamble shown in the previous section. In [107] a detector has been proposed for the frame acquisition, while in this paper a different optimization is used in order to obtain a finer timing estimation and to allow the frequency estimation to work with a limited timing misalignment. More details are shown in the following.

8.4.1 Frame Detection

The most intuitive strategy to perform detection of the DVB-T2-like preamble described in the previous section implies two correlations running in parallel, each one searching for maximum similarity with its respective part of the repetition, and on identifying the peak, obtained through the multiplication of the two outputs [107]. Indeed, when the correlation windows are aligned, the detector gives its maximum peak and the $P1$ is normally detected even in noisy conditions. The block diagram showed in Figure 8.2 implements the correlation for both parts of the $P1$ symbol, minimizing the number of complex multipliers.

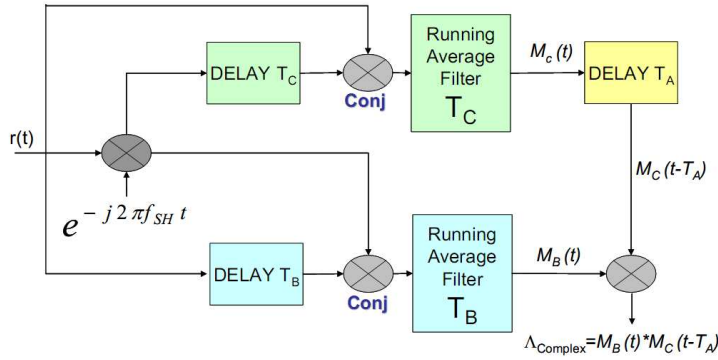


Figure 8.2: Detector block diagram optimized for P1 preamble (Adaptive Correlator Scheme)

The delay elements T_C and T_B , together with an associated multiplier and running-average filter, are the core of a scheme that detects each frequency-shifted repetition of the signal, C and B respectively. The delay element T_A makes the outputs of these two correlators line up in time. Differently from [107], in this paper the sliding window size of the running average filter has been set different for the two branches (Adaptive Correlator Scheme), i.e. T_C samples long for the leg C and T_B for the leg B , resulting in a overall correlation function with a triangular shape, as the one shown in Figure 8.3.

In Figure 8.3, the autocorrelation function (ACF) and relative argument values are reported both for the two branches and the final output of Adaptive Correlator Scheme, considering AWGN (Additive White Gaussian Noise) and Signal to Noise Ratio E_s/N_0 equal to 20dB. Let $r(t)$ be the received signal, it is possible to define

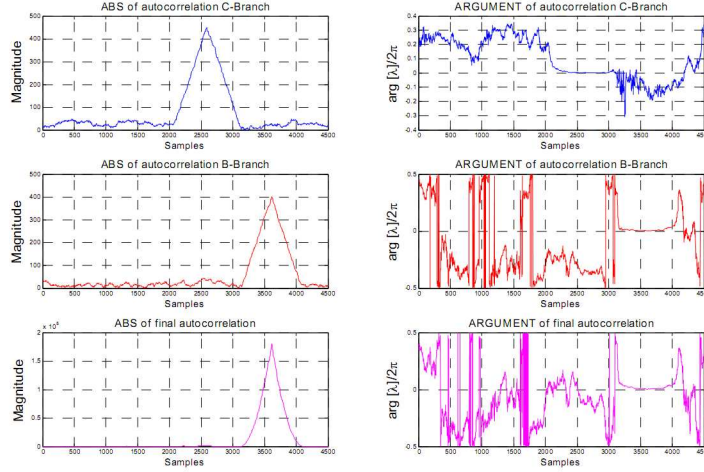


Figure 8.3: Autocorrelation function and argument with the Adaptive Correlation Scheme considering AWGN with $E_s/N_0 = 20\text{dB}$

the metric M for each branch as:

$$M_C(t) = \sum_{i=t-T_B+1}^t r^*(i)r(i-T_C)e^{-j2\pi f_{SH}(i-T_C)} \quad (8.14)$$

$$M_B(t) = \sum_{i=t-T_B+1}^t r^*(i)r(i-T_B)e^{-j2\pi f_{SH}(i-T_B)} \quad (8.15)$$

and the accumulated variable at the output as:

$$\Lambda(t) = M_B(t) * M_C(t - T_A) \quad (8.16)$$

The presence of a peak at the output may be detected by applying a suitable threshold (ξ) and may be taken to indicate the presence of the specific preamble. In the following, in order to provide an average performance of this scheme, detection probability has been evaluated, considering the dimension of the region of correct alignment cell (H1 cell) of length 340 samples and no a priori information. Thus, the search of the peak has to take into account a random timing error inside the H1 cell.

We have analyzed two cases: AWGN channel and Hybrid channel with $\Delta = 47.3\mu\text{s}$ and different mobile terminal speeds. In Table 8.2 and Table 8.3 the results in terms of Detection Probability (P_d) are reported with a fixed False Alarm Probability (P_{fa}) of 0.001 and 0.01 respectively. Note that the P1 seems to be very robust even in very harsh conditions like mobile hybrid channel.

Table 8.2: P1 Detection Probability - Pfa = 0.001

Pfa=0.001	-12dB	-10dB	-5dB	0dB
AWGN	$\xi = 6 * 10^5$ $P_d = 0.15$	$\xi = 2 * 10^5$ $P_d = 0.40$	$\xi = 3 * 10^4$ $P_d = 1$	$\xi = 7 * 10^3$ $P_d = 1$
HYB 170km/h	$\xi = 6 * 10^5$ $P_d = 0.12$	$\xi = 6 * 10^5$ $P_d = 0.32$	$\xi = 9 * 10^4$ $P_d = 0.45$	$\xi = 1 * 10^4$ $P_d = 0.69$

Table 8.3: P1 Detection Probability - Pfa = 0.001

Pfa=0.01	-12dB	-10dB	-5dB	0dB
AWGN	$\xi = 3.5 * 10^5$ $P_d = 0.34$	$\xi = 1.4 * 10^5$ $P_d = 0.60$	$\xi = 2 * 10^4$ $P_d = 1$	$\xi = 5187$ $P_d = 1$
HYB 170km/h	$\xi = 3 * 10^5$ $P_d = 0.31$	$\xi = 2 * 10^5$ $P_d = 0.5$	$\xi = 3 * 10^4$ $P_d = 0.61$	$\xi = 1 * 10^4$ $P_d = 0.81$

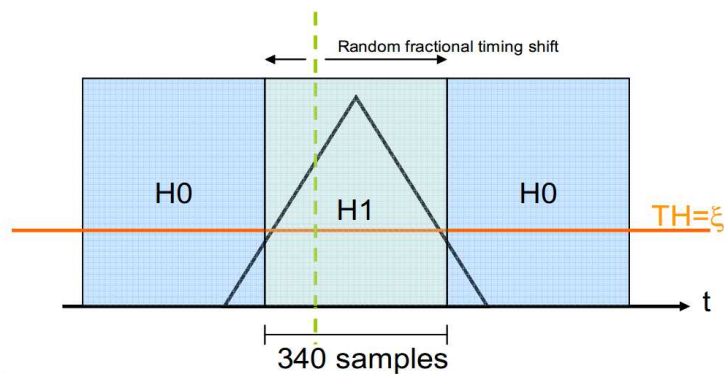


Figure 8.4: Detection in the presence of fractional timing error

Note that to effectively exploit the threshold optimization a Signal to Noise Ratio estimator (SNoRE) [108][109] is required as shown Figure 8.5.

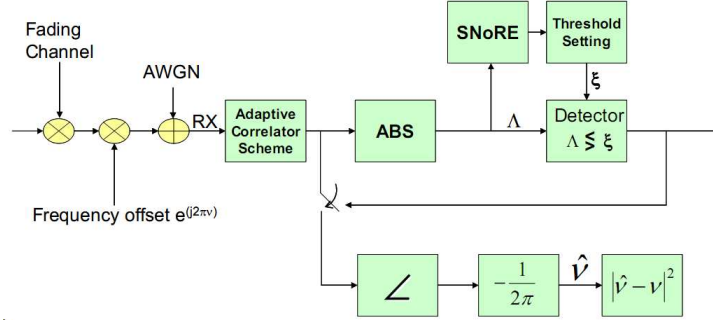


Figure 8.5: Simulation scheme for P1 performance evaluation

8.4.2 Frequency Estimation

In order to preserve the mutual orthogonality amongst subcarriers, it is necessary to estimate the fractional part of the normalized carrier frequency offset exploiting the P1 preamble [100]. In branch B, under the hypothesis of correct alignment, it is possible to observe the carrier frequency offset exploiting the correlation between the received part B and the corresponding portion of received part A, which are identical except for a phase offset equal to $2\pi\Delta f_n N_B/N$ due to the carrier frequency offset. In the same manner, in the branch C, it is possible to exploit the correlation between the received part C and the corresponding portion of received part A considering the offset equal to $2\pi\Delta f_n N_C/N$. The phase of the Complex Accumulated Variable Λ is given by:

$$\angle(\Lambda) = \angle(M_B) + \angle(M_C) = 2\pi\Delta f_n + \angle(n'(t)) \quad (8.17)$$

where \angle represents the angle operator. Therefore it is possible to estimate the carrier frequency simply observing the phase of the metric:

$$\hat{\Delta f}_n = \hat{\nu} = -\left(\frac{1}{2\pi}\angle(\Lambda)\right) \quad (8.18)$$

From Equation 8.18 it is worthwhile to note that Δf_n can be estimated without any ambiguity within a normalized range of $[-0.5 : 0.5]$ that is exactly the domain of the fractional part of the carrier frequency offset normalized to the sub-carrier frequency spacing. As shown in Figure 8.3, this method is robust against timing misalignment.

8.5 Numerical Results

To evaluate the frequency estimation performance on the P1 preamble, the simulation chain shown in Figure 8.5 has been considered. Note that the frequency estimation is performed jointly with the frame detection. Thus, when a detection event is declared, the corresponding fractional frequency offset is extracted.

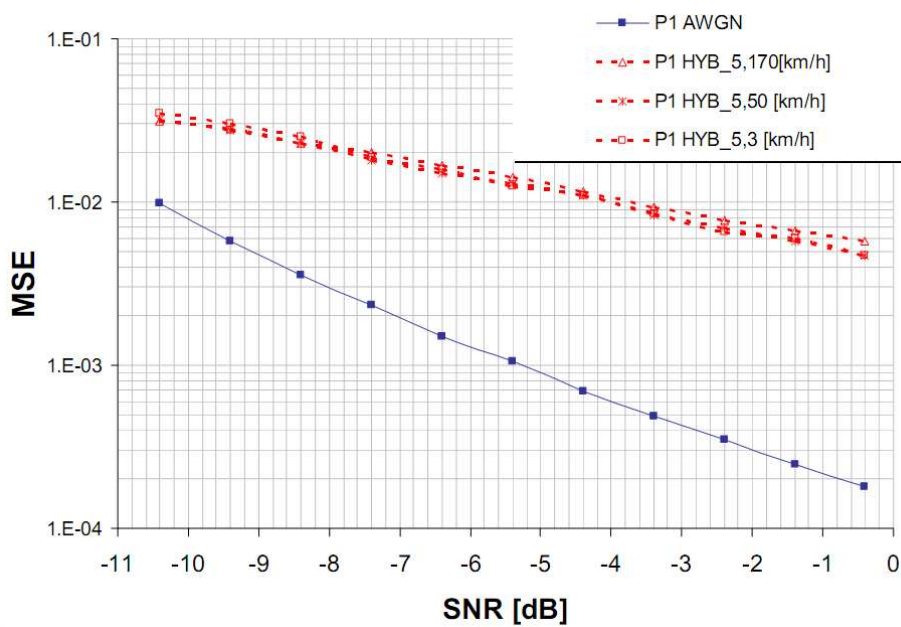


Figure 8.6: Fractional frequency estimation (MSE) in AWGN and HYB channel at 3 km/h

The results reported in Figure 8.6 and Figure 8.7 show MSE (Mean Square Error) performance in the two scenarios for different SNR.

The reported results show good performance even for low SNR values. A comparison with classical Cyclic Prefix OFDM approach (GI Based) [101][102] has been carried out taking into account that the Cyclic Prefix is 1/8 of the frame length equal to 256 samples.

8.6 Preamble Insertion in Future OFDM Broadcasting Standards: Conclusions

In this chapter, the introduction of a DVB-T2-like preamble in future satellite-terrestrial broadcasting OFDM standards has been evaluated. A novel joint scheme

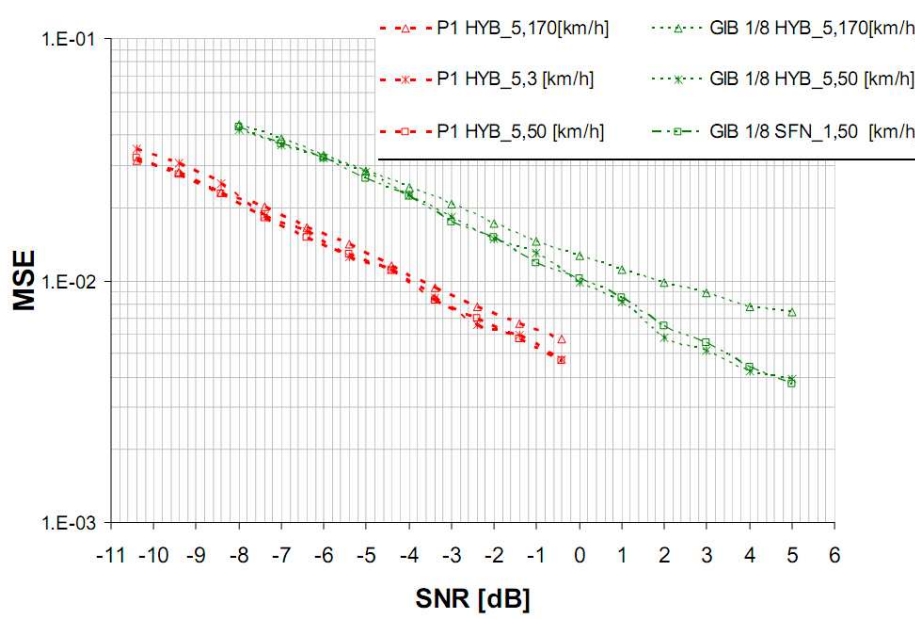
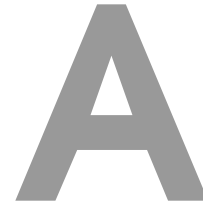


Figure 8.7: Comparison between P1 and Guard Interval Based (1/8) approaches (MSE) in AWGN and HYB channel at 3 km/h

to estimate the start of frame and the frequency has been proposed and its performance has been evaluated in a very challenging scenario such as the hybrid satellite terrestrial mobile channel. Simulations show that the proposed approach can overcome the classical Guard Interval Based techniques, even for very low SNRs.



Single Frequency Satellite Networks

A.1 Introduction

Satellite communications are experiencing very significant technical evolutions, which will be key in defining the role of satellites in future networks as a means to provide *broadband* access to the Internet over vast coverages. These changes have been enabled by new techniques and technologies: adaptive coding and modulation for the exploitation of EHF bands, where several GHz of band are available; on board processing for in-space routing; large reflectors for multi-beam antennas with hundreds of spot beams; exploitation of digital beam forming network concept; as well as significant improvements in on-board power amplification. All of this goes in the direction of maximizing system capacity and flexibility, and in general its effectiveness.

On the other hand, satellite *broadcasting* systems are naturally still focused on the objective of ensuring good coverage over vast areas and, consequently, have hardly exploited the new techniques potential. In fact, the classic Direct-To-Home (DTH) TV broadcasting satellite network provides service with a single beam typically operated in K_u band, where hundreds of Standard Definition or High Definition TV (SDTV, HDTV) channels can be carried over the entire service area. This is a

successful paradigm with seemingly little room for innovation. More recent developments are in the area of Mobile Broadcasting to hand-held terminals, which require a lower frequency band with a more benign propagation environment, such as the S-band. Since spectrum availability is here much scarcer (a maximum of 30 MHz), it is necessary to use more efficiently the radio resource by exploiting frequency reuse. Considering European coverage, the satellite antenna pattern is typically organized into country-specific linguistic beams, which are grouped in clusters and assigned different frequency sub-bands, which can be reused in non-adjacent beams. Interference is caused by antenna sidelobes, which must be carefully kept under control. Unfortunately, the amount of reuse that can be achieved is small, and essentially determined by geographic configuration.

In this chapter a radical increase in the fragmentation of the service area is proposed, both for fixed and for mobile applications, through the only exploitation of signal processing techniques over multi-beam antennas with hundreds of beams, also for broadcasting systems. Wherever content is identical in different beams (over a region, a country, or the entire service area) the same frequency band is used to realize a Single Frequency Satellite Network (SFSN), reminiscent of the Single Frequency Network (SFN) concept of terrestrial broadcasting systems, without resorting to any complexity increase in the antenna beamforming or any impact on the receiver. This architecture allows to have unprecedented flexibility in satellite broadcasting systems, as will be discussed shortly.

The reason why this idea has never been considered, or it has been rejected altogether, is that the signals carried by multiple beams in a SFSN mutually interfere in overlapping regions, inducing null-capacity zones wherever interference is destructive. If no countermeasures are taken, it proves impossible to provide uniform quality of service (QoS) throughout the service area. The innovative idea is to use Orthogonal Frequency Division Multiplexing (OFDM) [95] jointly with a new form of Multi Beam Cyclic Delay Diversity (MBCDD) which creates synthetic multipath through the assignment of beam specific power delay profiles. In this way, frequency selectivity is introduced which results in sufficient diversity to avoid destructive interference, guaranteeing correct signal reception in the entire coverage area.

Let's dwell briefly over the advantages and disadvantages of this approach. As for the main positive aspects, it is considered the possibility to: use the same antenna pattern to provide broadcasting and broadband access, for triple play services; de-

liver efficiently local content and reuse that part of the spectrum extensively; shape precisely and adaptively the contour of beams by grouping spots; use power control selectively over those narrow beams where atmospheric conditions are bad; use a large number of small High Power Amplifiers (HPAs) instead of a few powerful HPAs for the same total power. On the down side, the use of OFDM and MBCDD is not as power efficient as conventional single-carrier techniques, and requires the use of channel equalizers in the receivers. However, this is not a relevant problem, since the equalization is performed in the frequency domain and even a single carrier receivers shall provide an AGC (Automatic Gain Control) device in order to have channel equalization.

The results presented in this chapter have been partially published in [13] and [14]. Note that my contribution to this topic lies on the design of the synthetic multipath profile and of the on-board antenna, and on the parameters optimization.

A.2 OFDM and Cyclic Delay Diversity

This section briefly describes the concept of Cyclic Delay Diversity (CDD) for OFDM systems. As well known, OFDM is a multicarrier transmission technique, which splits the available spectrum into several narrowband parallel channels, corresponding to multiple sub-carriers modulated at a low symbol rate. The OFDM signal can be expressed as

$$s(t) = \sum_{k=0}^{N_{FFT}-1} x_k \cdot e^{j2\pi k \frac{t}{T}}, \quad -T_g \leq t < T \quad (\text{A.1})$$

where x_k are the complex-valued modulated data symbols, N_{FFT} is the total number of sub-carriers, T is the useful OFDM symbol time, T_g is the guard interval duration. The guard interval is filled with a cyclic prefix to maintain orthogonality in multipath. Note that, in order to avoid adjacent channel interference, only N_a active carriers are typically used.

Besides using the bandwidth very efficiently, OFDM guarantees high robustness against multipath delay spread, by allowing extremely simple equalization in the frequency domain. So much so that it is possible to increase artificially the channel delay spread by inserting TX-antenna specific cyclic delays. CDD [110], [111] is a MIMO (Multiple Input Multiple Output) scheme which allows to enhance frequency selectivity by inserting additional multiple paths that wouldn't naturally occur. Figure A.1 illustrates the block diagram of an OFDM transmitter applying CDD on its

N_{TX} antennas. As shown, the same OFDM modulated signal is transmitted over

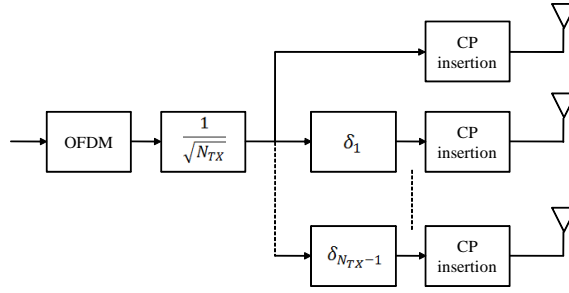


Figure A.1: CDD OFDM transmitter

N_{TX} antennas with an antenna specific cyclic shift. These shifts are indicated in the time domain by δ_i , $i = 1, \dots, N_{TX} - 1$, $\delta \in \mathbb{Z}$ and correspond to a multiplication by a phase factor $\psi_i = e^{-j2\pi f \frac{\delta_i}{N_{FFT}}}$. The latter, together with the normalization term used to split equally the transmission power among the antennas, can be interpreted as due to the channel, leading to an equivalent overall channel transfer function reported in Equation (A.2) [110]:

$$H_{eq}(f) = \frac{1}{\sqrt{N_{TX}}} \sum_{i=0}^{N_{TX}-1} \psi_i \cdot H_i(f) \quad (\text{A.2})$$

where $H_i(f, t)$ denotes the channel transfer function from the i -th transmitter antenna to the receiver antenna. Equation (A.2) applies to the MISO (Multiple Input Single Output) case, and can obviously be extended to MIMO. Compared to the original propagation channel, the composite channel using CDD shows a much richer multi-path profile, i.e. an increased frequency diversity of the received signal thanks to the contribution of the CDD transmission scheme. This is especially useful on poor multi-path scenarios in combination with a powerful coding scheme.

A.3 SFN over satellite networks

Since the general aim of a broadcast service is to deliver the same signal to a very large audience dislocated over a wide area, one of the most effective solutions is to establish a satellite network. As clearly explained in the Introduction of this chapter, the main novelty consists in providing broadcasting services through a multi-spot antenna synthesizing local beams, whereby several spots may be sending identical signals, to realize a SFSN. On board multi-beam antennas can be realized through the adoption of a Cassegrain reflector (which includes a parabolic primary

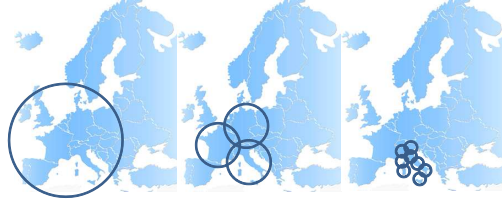


Figure A.2: Broadcasting over Europe: single beam, linguistic beams, local beams

mirror and a hyperbolic secondary mirror) and multi-feed horns; a similar structure to those utilized in Earth station antennas. More precisely, instead of having a single focal point where the feed must be located, the multi-beam antenna has a focal surface on which various feeds can be placed. Such an antenna system has a very compact structure and an adequate flexibility. The design of the reflectors position and feeders configuration realizes the desired beam geometry, in particular the beam overlapping areas on ground and the antenna sidelobes which are the main interference sources. Let's see how a SFSN can be designed exploiting such a multi-beam antenna, through the combined use of OFDM and MBCDD, performing signal processing at the gateway and assuming a transparent satellite transponder with beamforming.

A.3.1 Multi-beam coverage for SFSN

As mentioned before, combining signals coming from two or more overlapping beams generates null-capacity zones wherever they interfere destructively, causing deep fade events. If fading is frequency non-selective, this means that in certain points of the Earth surface no useful energy can be received. Obviously, this situation would be unacceptable for a broadcasting service since it is impossible to provide a uniform QoS throughout the coverage area. The proposed strategy, relying on the adoption of OFDM on the satellite link, is to apply MBCDD to each beam by imposing a specific delay profile that guarantees frequency selectivity over the signal bandwidth, generating a new source of diversity. This frequency selectivity is beneficial since it can be exploited through coded OFDM and leads to an overall transfer function without any null zone in the entire bandwidth.

Consider the k -th beam. Let $H^k(f, \alpha, \phi)$ be the channel transfer function corresponding to this beam as seen by a point on Earth reached through a link with amplitude gain α and overall phase rotation ϕ . Clearly, α accounts for the path loss, while ϕ includes the initial phase imposed by the gateway transmitter, the phase

rotation due to satellite beamforming and that due to propagation delay. Both α and ϕ are assumed to be constant over the entire signal bandwidth.

Let $H_n^k = H^k(n\Delta f, \alpha_k, \phi_k)$ be the transfer function coefficient pertaining to the n -th OFDM subcarrier, where the constants α_k and ϕ_k are implicit for notation simplicity. Assume MBCDD is applied by creating N_k synthetic signal replicas at the gateway, each delayed by $\delta_{i,k}$ and scaled by an amplitude coefficient $A_{i,k}$, for $i = 1, \dots, N_k$. Thus, the n -th transfer function coefficient can be described as:

$$H_n^k(\alpha_k, \phi_k) = \alpha_k e^{j\phi_k} \sum_{i=1}^{N_k} A_{i,k} e^{-j2\pi n \frac{\text{mod}(\delta_{i,k}, N_{FFT})}{N_{FFT}}} \quad (\text{A.3})$$

where $\text{mod}(a, b)$ indicates a module b . The $2N_k + 1$ parameters characterizing the power delay profile synthesized for the generic k -th beam give great flexibility, with plenty of degrees of freedom in selecting delays and amplitudes. These parameters can be optimized in the transmitter without any consequences at the receiver. The only constraint is that non selective fading per subcarrier should be guaranteed at all locations, in order to allow simple equalization; besides, channel estimation could become too challenging if the number of paths increases excessively.

Note that the application of CDD is not realized with different antennas as in its original form, but through digital processing at the gateway. In this way the system results to be more flexible, since no limitation in the number of delays is introduced, independently of the number of antenna elements.

A.3.2 Spot Beam Radiation Diagram

In order to describe the radiation pattern of each beam, the model described in [112] and [113] has been used. The generic tapered-aperture antenna radiation pattern is reported in the following equation:

$$G(u_k) = G_{M,k} \left(\frac{(p+1)(1-T)}{(p+1)(1-T)+T} \right)^2 \cdot \left(\frac{2J_1(u_k)}{u_k} + 2^{p+1} p! \frac{T}{1-T} \frac{J_{p+1}(u_k)}{u_k^{p+1}} \right)^2 \quad (\text{A.4})$$

where $G_{M,k}$ is the maximum gain for the k -th beam, p is a design parameter, T is the aperture edge taper, $J_p(u)$ is the Bessel function of the first kind and order p , $u_k = \frac{\pi d_{a,k}}{\lambda} \sin \theta_k$, $d_{a,k}$ is the effective antenna aperture for the k -th beam, and λ is the wavelength. Note that in the following, the mask corresponding to $G(u_k)$ with $T = 20\text{dB}$ and $p = 2$, depicted in Figure A.3, has been used. For simplicity, a

flat model of the Earth surface has been assumed, which is sufficiently accurate for beams which are not too large and not far from the sub-satellite point.

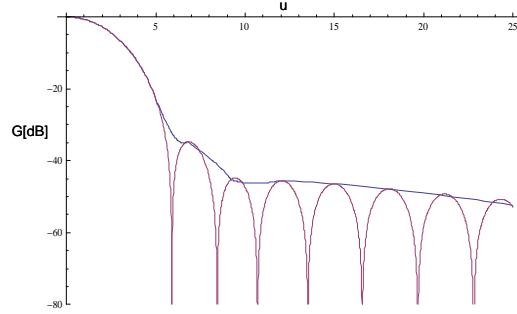


Figure A.3: Spot beam radiation and mask for $T = 20\text{dB}$ and $p = 2$

A.3.3 MBCDD Approximated Transfer Function

The aim of this section is to evaluate the overall effect of beam superposition. Let N_B be the number of overlapping beams insisting on a specific location with the same transmitted power, and H_n be the overall transfer function coefficient corresponding to the n -th subcarrier. Note that, at any location all α_k coefficients are identical for any k ; therefore, only ϕ_k needs to be explicit. It holds

$$H_n = H_n(\phi_1, \dots, \phi_{N_B}) = \sum_{k=1}^{N_B} \sqrt{G(u_k)} H_n^k(\phi_k) \quad (\text{A.5})$$

The collection of N_{FFT} channel coefficient forms the overall transfer function over the signal bandwidth. Figure A.7 shows a snapshot of this overall transfer function obtained with three overlapping beams at the same power level for $N_{FFT} = 2048$. Note that, as desired, frequency selectivity is obtained, which enables our SFSN architecture, at the price of the introduction of channel coding and equalization.

Since the OFDM signal experiences a frequency selective channel, a figure that can represent the effective performance obtained over the entire band is introduced: the *approximated transfer function*, \bar{H} , defined as the average of the absolute values of the channel transfer coefficients:

$$\bar{H} = \frac{1}{N_{FFT}} \sum_{n=0}^{N_{FFT}-1} |H_n| \quad (\text{A.6})$$

Note that this function is an approximation of the figure of merit shown in the following, which is representative of system performance. Figure A.5 shows the

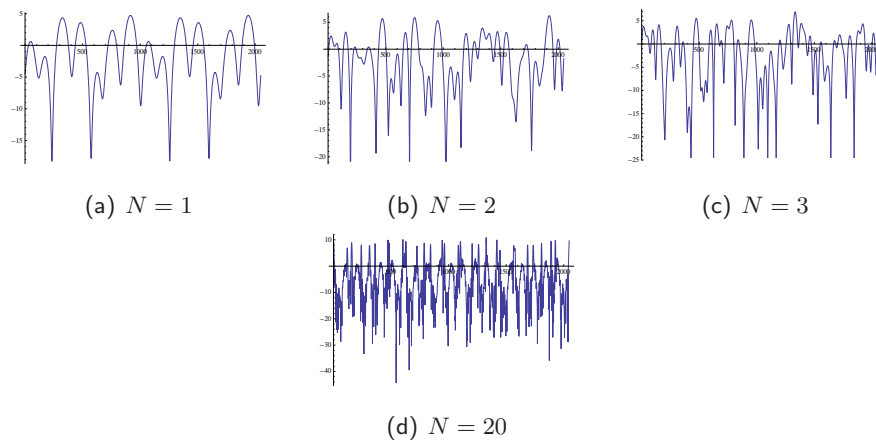


Figure A.4: Overall transfer function for three beams and $N = 1, 2, 3, 20$ paths each beam as a function carrier index

effective transfer function for $N_B = 3$, a fixed value for ϕ_3 , and variable ϕ_1 and ϕ_2 . The overlapping beams are assumed to be at the same power level, without MBCDD. Note that for certain combinations of phases the transfer function of the

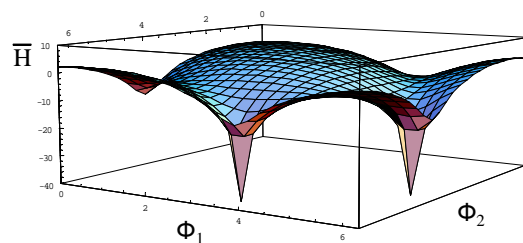


Figure A.5: Effective transfer function without MBCDD. Three overlapping beams.

channel without MBCDD presents deep fades of the effective transfer function, which correspond to a null-capacity zone.

A.4 SFSN Capacity

In this section the SFSN capacity in information theoretic terms is introduced. Let P/N be the signal-to-noise ratio over a sub-carrier that would be experienced by a receiver in the absence of self-interference generated by CDD and with an isotropic antenna. Thus, in any specific location the capacity can be obtained as [114]:

$$C = \sum_{n=1}^{N_a} \log \left(1 + \frac{F_n P}{N} \right) \quad (\text{A.7})$$

where $F_n = |H_n|^2$ for MBCDD, while in the case of a single beam F_n only accounts for the antenna gain at the specific location. Now the SFSN capacity shown in Equation (A.7) is used to provide an initial comparison between the single and multiple beam cases. A fair comparison is difficult because the geometry of single-beam/multi-beam coverage areas and the system requirements are quite different. Anyway, in order to have a preliminary evaluation, the capacity can be estimated assuming to have the same EIRP (Effective Isotropic Radiated Power) in the two cases. This is reasonable because with multiple beams the antenna gain increases but the beam power decreases. Anyway, since the systems are different, OFDM for multi-beams and single carrier for single beam, a complete link budget analysis should be considered in order to provide a comparison fair as much as possible, as shown in the next section. In the meantime, let us make a simple assumption which favors completely the single beam case, by placing the user at the subsatellite point for the single beam case and in the middle point of beam-overlapping regions for the multi-beam case. The capacity obtained in these conditions is shown in Figure A.6. Even in this extreme case, it can be seen that the MBCDD capacity is

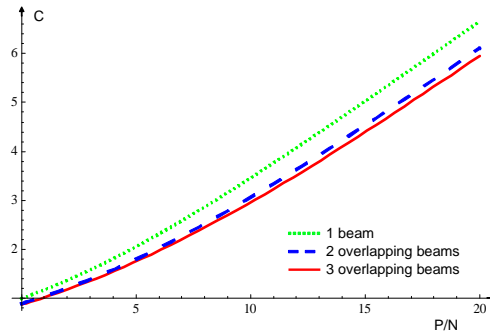


Figure A.6: Capacity comparison in the three scenarios: single beam, two overlapping beams, three overlapping beams.

not far from the best case of single beam capacity, which is a good and somewhat unexpected result. The analysis has been carried out for 3 overlapping beams, due to the geometrical properties of a cluster size of 3. For more overlapping beams the result do not show a significant variation, due to the high directivity of satellite beams.

In any case, it is necessary to optimize the on-board antenna radiation diagram (beam apertures and centers) in order to maximize the flatness and fairness of the received power in the entire region.

A.4.1 Parameter Optimization

A proper choice of the MBCDD parameters is fundamental in order to ensure that signal nulls are canceled and the capacity does not significantly fluctuate. In the following analysis only the scenario with three overlapping beams has been considered, but the same conclusions can be extended in the other scenarios. The experience on satellite beams interference shows that the worst case in a three beam cluster structure is given in the point which is equidistant from all the center beams, receiving the same power from all the interfering beams. Furthermore, the impact of the second tier of interferers can be neglected, due to their lower strength.

To reduce the number of degrees of freedom, it is possible to assume for all the MBCDD delay profiles, uniform amplitudes, $A_{i,k} = A \forall i, k$, and equally spaced paths, i.e. $\delta_{i,k} = i \cdot \delta_{0,k}$, under the fundamental requirement $\delta_{0,1} \neq \delta_{0,2} \neq \delta_{0,3}$.

The approach chosen in optimizing the remaining parameters was the minimization of the maximum fluctuation of the capacity, and the best results are obtained when the following three quantities

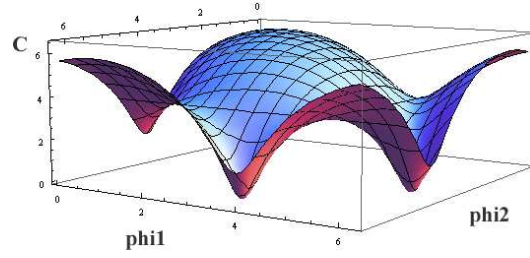
$$\text{mod}(\delta_{0,1}, N_{FFT}), \text{mod}(\delta_{0,2}, N_{FFT}), \text{mod}(\delta_{0,3}, N_{FFT})$$

are incommensurable. Figure A.7 shows different capacity, considering a fixed value for the phase ϕ_3 , and variable ϕ_1 and ϕ_2 : the first one represents the capacity obtained without MBCDD, which presents nulls when the phases ϕ_k combine in a destructive way, exactly in the same way as for the approximated transfer function; the second one shows the capacity with MBCDD but with non-optimized parameters; the third shows a flat capacity obtained with incommensurable delays.

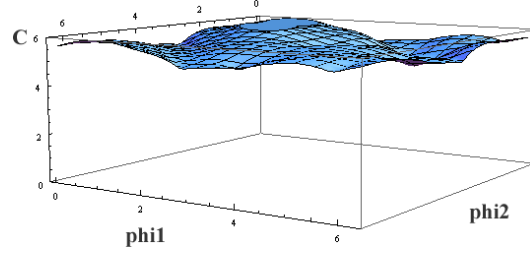
A.5 Preliminary Proof of Concept

The design of the on-board antenna should be aimed at producing a uniform QoS across the entire service area. Numerical results obtained in different beam geometry scenarios are obtained. The following assumptions have been used:

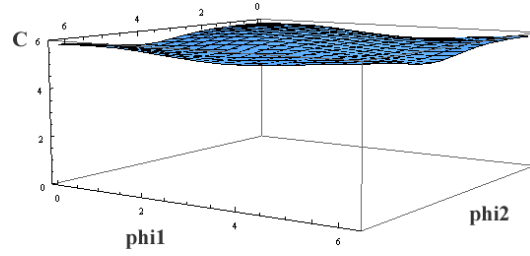
- $N_{FFT} = 2048$
- Uniform spaced delays, $\delta_i = i \cdot \delta_0$
- Number of multiple paths on each beam N_i equal to 2
- Uniform amplitude delay profile $A_i = A$ within the same beam



(a) Capacity without MBCDD: Three overlapping beams



(b) Capacity with MBCDD. Three overlapping beams. Non-optimized parameters



(c) Capacity with MBCDD. Three overlapping beams. Optimized parameters

Figure A.7: Parameter optimization

- Same amplitude delay profile among different beams, $A_1 = A_2 = A_3$
- Incommensurable delays
- Effective antenna aperture d_a equal to 1.4 m for each beam
- Fixed $\frac{P}{N}$ equal to 7dB
- Service area covered with 6 beams

The analysis has been carried out by discretizing the service area into 51×51 hexagonal cells and evaluating the capacity in their centers. Moreover, since the capacity behavior is insensitive with respect to the phases ϕ_k , as shown in Section A.4.1 for

incommensurable delays, a set of random ϕ_k has been chosen for the sake of simplicity. As desired, Figure A.8 shows that a constant capacity can be achieved in

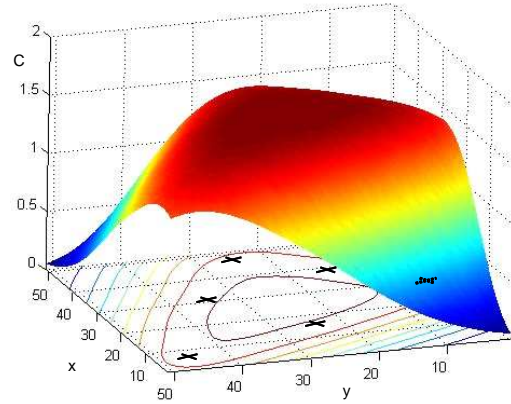


Figure A.8: Capacity obtained in an area covered with six beams.

the interested area, inside the projected internal circle, where the contributions of the six beams allow an extremely uniform QoS; besides, out of the service region the capacity obviously decreases since there are no beams covering this area. This capacity shaping is clearly detailed also in Figure A.9. The proposed strategy is easily scalable to a wider service area with several beams which provide a very flat capacity all over it.

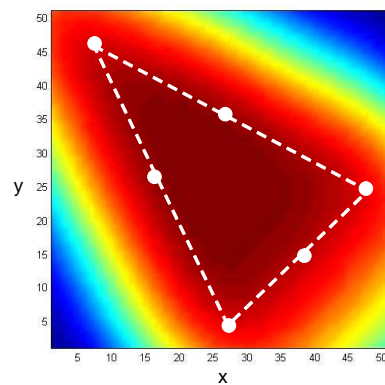


Figure A.9: Snapshot of capacity

A.6 Link Budget Analysis

In the following a more detailed analysis is conducted: a link budget analysis is shown for the SFSN concept considering, for comparison, also the single beam case with a single carrier transmission and the single beam with OFDM. Note that the analysis has been conducted for a service in Ku band (carrier frequency equal to 12GHz), but the same evaluation can be carried out for other bands. Moreover, a GEO satellite is assumed.

	Single Beam	OFDM	SFSN
Satellite T_{sys}	723K	723K	723K
Satellite Antenna Efficiency	0.65	0.65	0.65
Satellite Antenna Diameter	1m	1m	16m
Satellite Antenna Gain	40.11dBi	40.11dBi	64.20dBi
Satellite OBO	1dB	4dB	4dB
Satellite Input Loss	2dB	2dB	2dB
Satellite G/T	11.37dB/K	11.37dB/K	35.45dB/K
Receiver T_{sys}	150K	150K	150K
Receiver Antenna Efficiency	0.65	0.65	0.65
Receiver Antenna Diameter	0.9m	0.9m	0.9m
Receiver Antenna Gain	39.20dB	39.20dB	39.20dB
Receiver G/T	17.44dB/K	17.44dB/K	17.44dB/K
Clear Air Atmospheric Loss	3dB	3dB	3dB
Frequency	12GHz	12GHz	12GHz
Bandwidth	500MHz	500MHz	500MHz
Path Loss	205.10dB	205.10dB	205.10dB
Number of Beams	1	1	400
Transmit Power per Beam	19.54dB	19.54dB	-6.48dB
Total Transmit Power	19.54dBW	19.54dBW	19.54dBW
EIRP	53.66dB	50.66dB	48.72dB
P/N	7.60dB	4.60dB	2.67dB

Table A.1: Link budget for Single Beam and SFSN systems

All the systems have been dimensioned taking into account the best achievable coverage for an area of 650.000 squared km with the same total transmit power. In

particular, for the single beam case, the effective antenna diameter of the satellite has been set to obtain the 3dB edge loss on the boarder of the coverage area. On the other hand, the effective antenna diameter of each beam in the SFSN has been choose according to the considered beam geometry. In any case, in both the systems, all the parameters in A.6 have been set in order to have the best trade-off between coverage and link budget requirements. Results in A.6 show that different signal to noise ratios (P/N) are experienced by a receiver using the three systems. In particular, the use of OFDM both in the SFSN concept and in the single beam requires a larger Output Back-Off (OBO) with respect of the single carrier approach. On the other hand, the combining of the signals coming from different beams, foreseen by the SFSN concept, can compensate the losses in the link budget. In the following section, a more complete comparison of the two systems is conducted, using the signal to noise ratios obtained in this analysis.

A.7 Numerical Evaluation

Now the capacity obtained with the single beam scheme and with the SFSN approach is calculated. A vast service area of about 650.000 squared km has been considered. Note that this value approximately corresponds to a linguistic beam coverage region. The following assumptions have been used for the SFSN system:

- Service area covered with 400 beams organized in a uniform grid (20×20)
- $N_{FFT} = 2048$
- Uniform spaced delays, $\delta_i = i \cdot \delta_0$
- Number of multiple paths on each beam N_i equal to 3
- Uniform amplitude delay profile $A_i = A$ within the same beam
- Same amplitude delay profile among different beams, $A_1 = A_2 = \dots = A_i = \dots = A(400)$
- Incommensurable delays

Note that the analysis has been carried out considering the outputs of A.6, thus $\frac{P}{N}$ equal to 7.60dB in the single beam single carrier case, 4.60dB in the single beam with OFDM, and 2.67dB in the SFSN. Moreover, the service area has been discretized into 90×90 hexagonal cells and the capacity has been evaluated in their centers. Finally,

since the capacity behavior is insensitive with respect to the phases ϕ_k , as shown in Section A.4.1 for incommensurable delays, a set of random ϕ_k has been chosen for the sake of simplicity. Figure A.10 shows the capacity comparison between the systems

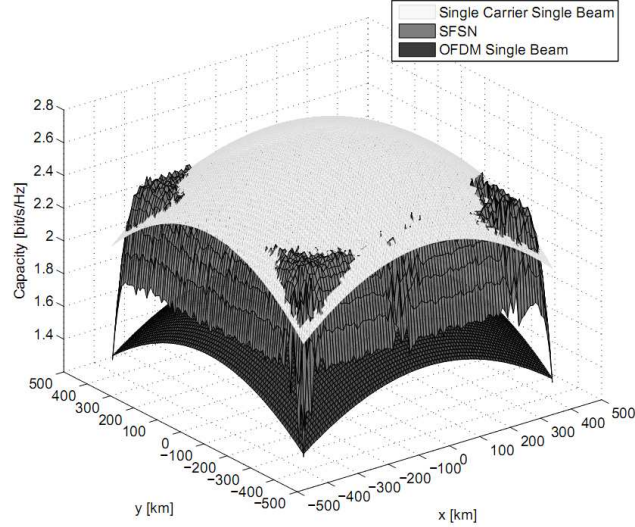


Figure A.10: Capacity comparison: SFSN vs. Single Beam Single Carrier

according to the link budget shown in A.6. As expected, a quasi-constant capacity can be achieved in the interested area, where the contributions of the beams allow an uniform QoS; besides, out of the service region the capacity obviously decreases since there are no beams covering this area. On the other hand, the single beam single carrier approach outperforms SFSN in the zone closer to the center of the coverage area, but results in poorer performance in the zone around the boarder, while the single beam OFDM scheme presents the worst behavior. Note that the proposed strategy is easily scalable also to a smaller or a wider service area, just taking into account the beams position and MBCDD parameters.

A.8 Single Frequency Networks over Satellite: Conclusions

This chapter contains a novel approach for multi-spot broadcasting systems via satellite. Relying on the SFN concept and OFDM principles, uniform coverage and QoS can be guaranteed by applying the CDD technique on each beam to eliminate the null-capacity zones by introducing frequency selectivity. A link budget analysis is proposed in order to perform a fair comparison between SFSN and a classical single beam single carrier system. As expected, differently from the single beam,

the SFSN system is able to guarantee a flat capacity over the entire service area, at the cost of a correct design of beams position and CDD parameters. However, this design is computed once for all, and involves only the gateway for signal processing and the satellite for beam shaping. No further complexity is required at the receiver. An operator adopting the concept of SFSN will enjoy unprecedented broadcasting flexibility and ease of convergence with broadband services.

Conclusions and Future Developments

This thesis has addressed the problem of synchronization both in recent GNSS and communication systems. In particular new issues due to the adoption of novel modulations, as Binary Offset Carrier (BOC) in navigation, and Orthogonal Frequency Division Multiplexing (OFDM) in communication have been tackled.

The first part of the dissertation has dealt with the problem of code acquisition and code tracking of BOC modulated signals. In Chapter 2, novel acquisition techniques have been proposed in order to mitigate the effects of the timing misalignment for low complexity receivers. In Chapter 3 Different Post Detection Integration (PDI) techniques, which are already known in the communication framework, have been adapted for GNSS in order to cope with harsh scenarios, like indoor or urban canyons, with the aim of improving the sensitivity of GNSS receivers without limiting receivers dynamics. Moreover, in Chapter 4 code synchronization for high-order BOC modulated signals has been investigated in the presence of signal distortion and multipath. A theoretical framework for the two dimensional correlation of BOC modulated signals in the presence of signal distortion has been assessed. Finally, in Chapter 5 a possible extension of the classical concept of an Assisted GNSS system has been investigated where the assistance network can estimate both the presence and the parameters of possible interferers and broadcast this information to the users. An analytical evaluation of the improvements in terms of Mean Acquisition Time (MAT) has been conducted, under the hypothesis that low complexity mitigation filters are adopted by the users.

The second part of this thesis investigates the problem of synchronization in several communication standards. In Chapter 6 the design of a frame synchronization subsystem for the future satellite broadband standard, the DVB-RCS+M, has been conducted. This standard allows to support the broadband services of collective mobile terminals in aeronautical, maritime, and railway mobile scenarios, and requires limited mean acquisition time in particular during the re-acquisition

after fading events operational mode. In Chapter 7 performance of frame synchronization in the future OFDM standards, like WiMAX and LTE, has been assessed. Chapter 8 is devoted to the investigation of the possible insertion of a preamble in future hybrid satellite terrestrial broadcasting standards which will exploit the OFDM modulation, in order to permit a joint frame detection / frequency estimation scheme. Finally, Appendix A has been dedicated to the definition and evaluation of a novel concept, identified as Single Frequency Satellite Network, whose intention is to exploit the multi-beam capabilities of the state-of-the art satellites also for broadcasting systems, where only digital baseband processing has been applied instead of beamforming, allowing potential for flexibility and reconfigurability.

Even if in this thesis some effort has been put forth in order to fill the gap between navigation and communication, the possibility to establish a common link should be considered as the next important challenge. Navigation systems, in fact, at the time of this thesis, can be considered like trivial Code Division Multiple Access (CDMA) radio communication links characterized by very limited bit rates, since the focus has always been only on their ranging properties. In the future, new services will require higher bit rates, more stringent communication capabilities, and different application scenarios. Moreover, the introduction of hybrid terrestrial satellite positioning approaches will require a much deeper exploitation of communication concepts in navigation, like the possible adoption of a common modulation. For example, the idea of using multicarrier signals also for future navigation signals, is already under discussion [115]. As detailed in this thesis, the main advantage of a multicarrier signal design is its intrinsic robustness against multipath and severe channel conditions. Thus, since one of the principal error sources of the GNSS error budget is represented by multipath, the adoption of this kind of modulation is raising a lot of interest. Therefore, in this framework, synchronization will become once again the fundamental function of every communication and navigation receiver.

Personal Publications

- [1] M. Villanti, C. Palestini, R. Pedone, and G.E. Corazza, “Robust Code Acquisition in the Presence of BOC Modulation for Future Galileo Receivers,” *IEEE International Conference on Communications (ICC '07)*, pp. 5801–5806, 24-28 June 2007.
- [2] G.E. Corazza, C. Palestini, R. Pedone, and M. Villanti, “Robust Detectors for Code Acquisition with BOC Modulation for GNSS receivers,” *International Workshop on Satellite and Space Communications, 2007. IWSSC '07*, pp. 299–303, Sept. 2007.
- [3] G.E. Corazza, C. Palestini, R. Pedone, and M. Villanti, “Soft Combining for Improved Sensitivity GNSS Code Acquisition,” *Proceedings of 3rd ESA Workshop on Satellite Navigation User Equipment Technologies Navitec*, December 2006.
- [4] G.E. Corazza, C. Palestini, R. Pedone, and M. Villanti, “Primary Code Acquisition Based on Multi-hypothesis Secondary Code Ambiguity Elimination,” *Proceedings of ION GNSS*, September 2007.
- [5] C. Palestini, R. Pedone, M. Villanti, and G.E. Corazza, “Integrated NAV-COM Systems: Assisted Code Acquisition and Interference Mitigation,” *IEEE Systems Journal on Recent Advances in Global Navigation and Communication Satellite Systems*, vol. 2, no. 1, pp. 48–61, March 2008.
- [6] G.E. Corazza, C. Palestini, R. Pedone, and M. Villanti, “Code Acquisition with Interference Mitigation for Galileo Receivers,” *Proceedings of ION GNSS*, September 2007.
- [7] F. Bastia, C. Palestini, R. Pedone, M. Villanti, and G.E. Corazza, “Staggered Time and Frequency Search to Aid Frame Synchronization,” *Proceedings*

of International Symposium on Spread Spectrum Techniques and Applications ISSSTA, pp. 1871–1875, August 2008.

- [8] C. Palestini, F. Bastia, G.E. Corazza, A. Vanelli-Coralli, M. Villanti, and R. Pedone, “Time and Frequency Staggered Search for BOC Modulated Ranging Signals,” *Proceedings of 4th ESA Workshop on Satellite Navigation User Equipment Technologies Navitec*, December 2008.
- [9] A. Vanelli-Coralli, G.E. Corazza, C. Palestini, R. Pedone, M. Villanti, H. Lee, and P.S. Kim, “Code Acquisition for Next Generation Mobile Broadband Satellite Services,” *IEEE International Conference on Communications, 2008. ICC '08*, pp. 1871–1875, May 2008.
- [10] P. Kim, A. Vanelli-Coralli, M. Villanti, R. Pedone, S. Cioni, M. Neri, C. Palestini, M. Papaleo, H. Lee, and G.E. Corazza, “Direct Sequence Spectrum Spreading Techniques for Next Generation Mobile Broadband Satellite Services,” *Wiley International Journal of Satellite Communications and Networking*, Oct 2009.
- [11] C. Bastia, Bersani, E.A. Candreva, S. Cioni, M. Corazza, G.E. Neri, C. Palestini, M. Papaleo, S. Rosati, and A. Vanelli-Coralli, “LTE Air Interface over Broadband Satellite Networks,” *Eurasip Journal on Wireless Communications and Networking*, November 2009.
- [12] F. Bastia, C. Palestini, S. Rosati, M. Neri, and G.E. Corazza, “Preamble Insertion in Future Satellite-Terrestrial OFDM Mobile Broadcasting Standards,” *International Communications Satellite Systems Conference (ICSSC) 2009*, June 2009.
- [13] G.E. Corazza, C. Bersani, C. Palestini, and A. Vanelli-Coralli, “Single Frequency Satellite Networks: a Novel Approach for Multi-Spot Broadcasting,” *International Communications Satellite Systems Conference (ICSSC) 2009*, June 2009.
- [14] G.E. Corazza, C. Palestini, E.A. Candreva, and A. Vanelli-Coralli, “The Single Frequency Satellite Network Concept: Multiple Beams for Unified Coverage,” *IEEE Globecom 2009*, November 2009.

-
- [15] C. Palestini, L. Deambrogio, F. Bastia, and G.E. Corazza, “An Insider View on the Tracking Loops: a Novel Ultra-Tight GNSS/INS Hybridization Approach,” *Proceedings of the IEEE/ION PLANS 2010*, May 2010.
- [16] F. Bastia, L. Deambrogio, C. Palestini, M. Villanti, R. Pedone, and G.E. Corazza, “Hierarchical Code Acquisition for Dual Band GNSS Receivers,” *Proceedings of the IEEE/ION PLANS 2010*, May 2010.

Bibliography

- [17] F.M. Gardner and W.C. Lindsey, “Guest Editorial, Introduction to the Special Issue on Synchronization,” *IEEE Trans. on Comm.*, vol. 28, no. 8, pp. 1105–1106, Aug. 1980.
- [18] EC FP6 GALILEO Research and Development Activities (Second Call Area 1B), *Management of Galileo Interferences and Counter-measures*, web site: <http://uranium.stu-dif.com/sensors-processing>.
- [19] EC FP6 GALILEO Research and Development Activities (Second Call Area 1B), *Assisted Galileo/GPS/EGNOS Mass Market Receiver*, web site: <http://www.galileoju.com/>.
- [20] EC FP6 IST-2003-507052 SatNEx Satellite communications Network of Excellence, web site: <http://www.satnex.org/>.
- [21] ESA Project, *Study of Satellite Role in 4G Mobile Networks*.
- [22] ESA Project, *OFDM - Study of Enhanced OFDM Techniques*.
- [23] ETRI Korea-ARCES, *Collaborative Research on Enhanced Broadband Mobile Satellite Communications based on DVB-S2*, 2005 - 2009 .
- [24] ESA Project, *Peer-To-Peer Positioning*.
- [25] R. Pagny, J.-C. Dardelet, and Chenebault J., “From EGNOS to Galileo: A European Vision of Satellite-Based Radio Navigation,” *Annals of telecommunications*, vol. 60, no. 3-4, Intelligent transportation systems, March-April 2004.
- [26] J.G. McNeff, “The Global Positioning System,” *IEEE Trans. on Microwave Theory and Techniques, Invited paper*, vol. 50, no. 3, pp. 645–652, March 2002.
- [27] J.K. Holmes, *Coherent Spread Spectrum Systems*, Krieger, 1990.

- [28] E.D. Kaplan, *Understanding GPS: Principles and Applications*, Artech House, 1996.
- [29] “GALILEO Signal in Space Interface Control Document, Issue 8.0,” Tech. Rep. GAL-ICD-GLI-SYST-A/0258, Galileo Joint Undertaking, Oct. 2004.
- [30] J.W. Betz, “Binary Offset Carrier Modulations for Radionavigation,” *Journal of The Institute of Navigation*, vol. 48, no. 4, pp. 227–246, Winter 2001-2002.
- [31] J.-A. Avila-Rodriguez, S. Wallner, G.W. Hein, E. Rebeyrol, O. Julien, C. Macabiau, L. Ries, A. De Latour, L. Lestarquit, and J. Issler, “CBOC - An Implementation of MBOC,” *Proceedings of First CNES Workshop on Galileo Signals and Signal Processing*, October 2006.
- [32] G.W. Hein, J.-A. Avila-Rodriguez, L. Ries, L. Lestarquit, J. Issler, J. Godet, and T. Pratt, “A Candidate for the Galileo L1 OS Optimized Signal,” *Proceedings of the International Technical Meeting of the Institute Of Navigation ION GNSS 2005*, September 2005.
- [33] M. Fantino, P. Mulassano, F. Dovis, and L. Lo Presti, “Performance of the Proposed Galileo CBOC Modulation in Heavy Multipath Environment,” *Springer Wireless Personal Communications*, vol. 44, no. 3, pp. 323–339, February 2008.
- [34] “GIOVE-A + B Navigation Signal in Space Interface,” Tech. Rep. ESA-DTEN-NG-ICD/02837, European Space Agency, 2006.
- [35] “Galileo Open Service Signal in Space Interface Control Document,” Tech. Rep. GAL OS SIS ICD/D.1, European Space Agency / Galileo Joint Undertaking, February 2008.
- [36] G.W. Hein, J.-A. Avila-Rodriguez, S. Wallner, A.R. Pratt, J. Owen, J. Issler, J.W. Betz, C.J. Hegarty, S. Lenahan, J.J. Rushanan, A.L. Kraay, and T.A. Stansell, “MBOC: the New Optimized Spreading Modulation Recommended for GALILEO L1 OS and GPS L1C,” *Proceedings of the IEEE ION Position, Location, and Navigation Symposium PLANS*, pp. 883–892, April 2006.
- [37] J.-A. Avila-Rodriguez, G.W. Hein, S. Wallner, J. Issler, L. Ries, L. Lestarquit, A. De Latour, J. Godet, F. Bastide, T. Pratt, and J. Owen, “The MBOC Modulation: The Final Touch to the Galileo Frequency and Signal Plan,” *Proceedings of the International Technical Meeting of the Institute Of Navigation ION GNSS 2007*, September 2007.

- [38] J.-A. Avila-Rodriguez, G.W. Hein, S. Wallner, J. Issler, L. Ries, L. Lestarquit, A. De Latour, J. Godet, F. Bastide, T. Pratt, and J. Owen, "The MBOC Modulation: The Final Touch to the Galileo Frequency and Signal Plan," *Journal of the Institute of Navigation*, vol. 55, no. 1, pp. 15–28, 2008.
- [39] J.-A. Avila-Rodriguez, *On Generalized Signal Waveforms for Satellite Navigation*, PhD Thesis.
- [40] O. Julien, C. Macabiau, G. Lachapelle, M.E. Cannon, and C. Mongredien, "A New Unambiguous BOC(n,n) Signal Tracking Technique," *Proceedings of the European Navigation Conference GNSS 2004*, May 2004.
- [41] O. Julien, C. Macabiau, M.E. Cannon, and G. Lachapelle, "ASPeCT : Unambiguous Sine-BOC(n,n) Acquisition/Tracking Technique for Navigation Applications," *IEEE Transactions on Aerospace and Electronic Systems*, vol. 43, no. 1, pp. 150–162, 2007.
- [42] K. Borre, D.M. Akos, N. Bertelsen, P. Rinder, and S.H. Jensen, *A Software-Defined GPS and Galileo Receiver: A Single-Frequency Approach*, Springer, 2007.
- [43] A.J. Viterbi, *CDMA, Principles of Spread Spectrum Communications*, Addison-Wesley Wireless Communications Series. Addison-Wesley Publishing Company, Apr. 1995.
- [44] P. Villanti, M. Salmi and G.E. Corazza, "Differential Post Detection Integration Techniques for Robust Code Acquisition," *IEEE Trans. on Comm.*, vol. 55, no. 11, pp. 2172–2184, November 2007.
- [45] G.E. Corazza and R. Pedone, "Generalized and Average Likelihood Ratio Testing for Post Detection Integration," *IEEE Trans. on Comm.*, vol. 55, no. 11, pp. 2159–2171, November 2007.
- [46] J.G. Proakis, *Digital Communications*, McGraw-Hill, 1995.
- [47] G.E. Corazza, P. Salmi, A. Vanelli-Coralli, and M. Villanti, "Differential and Non-Coherent Post Detection Integration Techniques for the Return Link of Satellite W-CDMA Systems," *Personal, Indoor and Mobile Radio Communications (PIMRC 2002)*, Sep. 2002.

- [48] G.E. Corazza and R. Pedone, "Generalized and Average Post Detection Integration Methods for Code Acquisition," *Int. Symposium of Spread Spectrum Systems and Applications (ISSSTA2004)*, Aug. 2004.
- [49] M. K. Simon, *Probability Distributions Involving Gaussian Random Variables: A Handbook for Engineers and Scientists*, Kluwer Academic Publishers - Springer, May 2002.
- [50] G. E. Corazza, R. Pedone, and M. Villanti, "Frame Acquisition for Continuous and Discontinuous Transmission in the Forward Link of Satellite Systems," *International Journal of Satellite Communications and Networking*, vol. 24, no. 2, pp. 185–201, 2006.
- [51] M. Villanti, R. Pedone, A. Vanelli-Coralli, and Corazza G.E., "Return Link RACH Code Acquisition Based on Combining Techniques for Future S-DMB Systems," *2nd International Symposium on Wireless Communication Systems*, pp. 807 – 811, September 2005.
- [52] M. Villanti, R. Pedone, A. Vanelli-Coralli, and Corazza G.E., "Soft Combining Technique for Return Link RACH Code Acquisition in Rice Fading Channels," *Advanced Satellite Mobile Systems (ASMS) conference*, May 2006.
- [53] G.E. Corazza, *Digital Satellite Communications*, Springer-Verlag, Inc., New York, 2007.
- [54] E.-S. Lohan, A. Lakhzouri, and M. Renfors, "Selection of the Multiple-Dwell Hybrid-Search Strategy for the Acquisition of Galileo Signals in Fading Channels," *15th IEEE Int. Symp. on Personal, Indoor and Mobile Radio Communications (PIMRC 2004)*, vol. 4, pp. 2352–2356, Sept. 2004.
- [55] M.L. Psiaki, "Block Acquisition of Weak GPS Signals in a Software Receiver," *ION GPS 2001*, Sep. 2001.
- [56] Y. T. Su, "Rapid Code Acquisition Algorithms Employing PN Matched Filters," *IEEE Trans. on Comm.*, vol. 36, no. 6, pp. 724–733, June 1988.
- [57] C. Palestini, "Acquisition and Tracking of Galileo E1-A in the Presence of Signal Distortion," *ESA Report*, July 2009.

- [58] M.S. Hodgart, P.D. Blunt, and M. Unwin, "The Optimal Dual Estimate Solution for Robust Tracking of Binary Offset Carrier (BOC) Modulation," *Proceeding of ION GNSS*, September 2007.
- [59] N. Blanco-Delgado, G. Lopez-Risueno, G. Seco-Granados, A. Garcia-Rodriguez, and D. Jimenez-Banos, "Indoor Acquisition and Tracking Performance of Galileo L1 OS Signals," *3rd Workshop on Satellite Navigation User Equipment Technology Navitec*, December 2006.
- [60] G.E. Corazza, "On the MAX/TC Criterion for Code Acquisition and Its Application to DS-SSMA Systems," *Communications, IEEE Transactions on*, vol. 44, no. 9, pp. 1173–1182, Sep 1996.
- [61] P.M. Fishman and J.W. Betz, "Predicting Performance of Direct Acquisition for the M-Code Signal," *Proceeding of ION National Technical Meeting*, January 2000.
- [62] M. Villanti, R. Pedone, M. Iubatti, and G.E. Corazza, "On the Design of a Common Avenue for Frequency Estimation and Frame Synchronization," *WCNC Wireless Communications and Networking Conference*, April 2006.
- [63] U. Mengali and A.N. D'Andrea, *Synchronization Techniques for Digital Receivers*, Plenum Publishing Corporation, New York, 1997.
- [64] A.J. Van Dierendonck, P. Fenton, and T. Ford, "Theory and Performance of Narrow Correlator Spacing in a GPS Receiver," *Journal of the Institute of Navigation*, vol. 39, no. 3, January 1992.
- [65] P. Fine and W. Wilson, "Tracking Algorithm for GPS Offset Carrier Signals," *Proceeding of ION GNSS*, September 1999.
- [66] L.B. Milstein, "Interference Suppression to Aid Acquisition in Direct-Sequence Spread-Spectrum Communications," *IEEE Trans. on Comm.*, vol. 36, no. 11, pp. 1200–1206, Nov. 1988.
- [67] Proakis J.G. Ketchum J.W., "Adaptive Algorithms for Estimating and Suppressing Narrow-Band Interference in PN Spread-Spectrum Systems," *IEEE Trans. on Comm.*, vol. 30, no. 5, pp. 913–924, May 1982.
- [68] J.W. Betz, "Effect of Narrowband Interference on GPS Code Tracking," *Proceedings of ION 2000 National Technical Meeting*, January 2000.

- [69] L.B. Milstein, "Interference Rejection Techniques in Spread Spectrum Communications," *Proc. of the IEEE*, vol. 76, no. 6, pp. 657–671, June 1988.
- [70] L.A. Rusch and H.V. Poor, "Narrowband Interference Suppression in CDMA Spread Spectrum Communications," *IEEE Trans. on Comm.*, vol. 42, no. 2/3/4, pp. 1969–1979, February/March/April 1994.
- [71] P.T. Capozza, B.J. Holland, T.M. Hopkinson, and R.L. Landrau, "A Single-Chip Narrow-Band Frequency-Domain Excisor for a Global Positioning System (GPS) Receiver," *IEEE Journal of Solid-State Circuits*, vol. 35, no. 3, pp. 401–411, March 2000.
- [72] M.V. Tazebay and A.N. Akansu, "Adaptive Subband Transforms in Time-Frequency Excisors for DSSS Communications Systems," *IEEE Trans. on Sig. Process.*, vol. 43, no. 11, pp. 2776–2782, November 1995.
- [73] M.G. Amin, "Interference Mitigation in Spread Spectrum Communication Systems Using Time-Frequency Distributions," *IEEE Trans. on Signal Processing*, vol. 45, no. 1, January 1997.
- [74] R.L. Fante and J.J. Vaccaro, "Wideband Cancellation of Interference in a GPS Receive Array," *IEEE Journal of Solid-State Circuits*, vol. 36, no. 2, pp. 549–564, April 2000.
- [75] M. G. Amin and W. Sun, "A Novel Interference Suppression Scheme for Global Navigation Satellite Systems Using Antenna Array," *IEEE Journal on Selected Areas in Comm.*, vol. 23, no. 5, pp. 999–1012, May 2005.
- [76] M. G. Amin, L. Zhao, and A. R. Lindsey, "Subspace Array Processing for the Suppression of FM Jamming in GPS Receivers," *IEEE Trans. on Aerospace and Electronic Systems*, vol. 40, no. 1, Jan. 2004.
- [77] G. Seco-Granados, J.A. Fernandez-Rubio, and C. Fernandez-Prades, "ML Estimator and Hybrid Beamformer for Multipath and Interference Mitigation in GNSS Receivers," *IEEE Transactions on Signal Processing*, vol. 53, no. 3, pp. 1194–1208, Mar. 2005.
- [78] M. Villanti, R. Pedone, G.E. Corazza, and R. Crescimbeni, "Joint Time-Frequency Domain Interference Mitigation for Galileo L1 Band Receivers," *Int. Symposium of Spread Spectrum Systems and Applications (ISSSTA2006)*, Aug. 2006.

- [79] F. Hlawatsch and G.F. Boudreaux-Bartels, "Linear and Quadratic Time-Frequency Signal Representations," *IEEE Signal Processing Magazine*, pp. 21–67, Apr. 1992.
- [80] J.W. Betz, "Effect of Partial-Band Interference on Receiver Estimation of C/N0: Theory," *Proceedings of ION 2001 National Technical Meeting*, January 2001.
- [81] D. Borio, L. Camoriano, and L. Lo Presti, "Two-Pole and Multi-Pole Notch Filters: a Computationally Effective Solution for Interference Detection and Mitigation," *Telecommunications, 2007. ITST '07. 7th International Conference on ITS*, pp. 1–6, 6-8 June 2007.
- [82] M. Casadei, G.E. Corazza, M. Iubatti, A. Vanelli-Coralli, and M. Villanti, "Robust Code Acquisition with Parallel Frequency Testing for Indoor GNSS," *3rd ESA Workshop on Satellite Navigation User Equipment Technologies Navitec*, Dec. 2006.
- [83] A. Polydoros and C.L. Weber, "A Unified Approach to Serial Serach Spread-Spectrum Code Acquisition-Part I: General Theory," *IEEE Trans. on Comm.*, vol. COM-32, n.5, pp. 542–549, May 1984.
- [84] A. Vanelli-Coralli, G.E. Corazza, G.K. Karagiannidis, P.T. Mathiopoulos, D.S. Michalopoulos, C. Mosquera, S. Papaharalabos, and S. Scalise, "Satellite Communications: Research Trends and Open Issues," *Satellite and Space Communications, 2007. IWSSC '07. International Workshop on*, pp. 71–75, Sept. 2007.
- [85] S. Cioni, G.E. Corazza, and A. Vanelli-Coralli, "Antenna Diversity for DVB-S2 Mobile Services in Railway Environments," *International Journal of Satellite Communications and Networking*, vol. 25, no. 5, pp. 443–458, 2007.
- [86] H. L. Van Trees, *Detection, Estimation, and Modulation Theory. Part I: Detection, Estimation, and Linear Modulation Theory*, John Wiley and Sons, Inc., New York, 1968.
- [87] TM-RCS0626, Mobile Applications of DVB-RCS Study Mission Report, March 2006.

- [88] S. Cioni, C. Párraga Niebla, G. Seco Granados, S. Scalise, Vanelli-Coralli A., and Vázquez Castro M.A., “Advanced Fade Countermeasures for DVB-S2 Systems in Railway Scenarios,” *EURASIP Journal on Wireless Communications and Networking Special Issue on Satellite Communications*, 2007.
- [89] ETSI EN 302 307 V1.1.1 (2004-01), Digital Video Broadcasting (DVB) - Second generation framing structure, channel coding and modulation systems for Broadcasting, Interactive Services, News Gathering and other broadband satellite applications, 2004.
- [90] v. 1.4.1 ETSI EN 301 790, Digital Video Broadcasting (DVB): Interaction channel for satellite distribution systems, Sep. 2005.
- [91] H. Skinnemoen, “DVB-RCS: Revitalizing the Open Standard for Mobile Applications,” *13th Ka and Broadband Communications Conference*, Sep. 2007.
- [92] E. Casini, R. De Gaudenzi, and A. Ginesi, “DVB-S2 Modem Algorithms Design and Performance over Typical Satellite Channels,” *International Journal of Satellite Communications and Networking*, vol. 22, no. 3, pp. 281–318, 2004.
- [93] R. De Gaudenzi, M. Luise, and R. Viola, “A Digital Chip Timing Recovery Loop for Band-Limited Direct-Sequence Spread-Spectrum Signals,” *Communications, IEEE Transactions on*, vol. 41, no. 11, pp. 1760–1769, Nov 1993.
- [94] R. Pedone, M. Villanti, G.E. Corazza, and Mathiopolous T., “Robust Frame Synchronization Design in the Presence of Frequency Errors,” *11th Ka Broadband Communication Conference 2005*, Sep. 2005.
- [95] S.B. Weinstein and Ebert P.M., “Data Transmission by Frequency-Division Multiplexing Using the Discrete Fourier Transform,” *IEEE Transactions on Communication Technology*, vol. 19, no. 5, pp. 628–634, October 1971.
- [96] DVB TM-T2 0083, Pilots, Channel sounding and Equalisation - BBC Research, 2006.
- [97] ETSI EN 302 583, Framing Structure, channel coding and modulation for Satellite Services to Handheld devices (SH) below 3 GHz, 2008.
- [98] IEEE Standard for Local and metropolitan area networks, Part 16: Air Interface for Fixed Broadband Wireless Access Systems, 2004.

- [99] 3GPP TS 36.211, Evolved Universal Terrestrial Radio Access (E-UTRA): Physical Channels and Modulation (Release 8).
- [100] M. Speth, S. A. Fechetl, G. Fock, and H. Meyr, "Optimum receiver design for wireless Broad-Band system using OFDM part I," *IEEE Trans. on Communications*, vol. 47, no. 11, pp. 1668–1677, November 1999.
- [101] M. Speth, S. A. Fechetl, G. Fock, and H. Meyr, "Optimum receiver design for wireless Broad-Band system using OFDM part II," *IEEE Trans. on Communications*, vol. 49, no. 4, pp. 571–578, April 2001.
- [102] J. Van de Beek, M. Sandell, and P.O. Borjesson, "ML estimation of timing and frequency offset in OFDM systems," *IEEE Trans. on Signal Processing*, vol. 45, no. 7, pp. 1800–1805, July 1999.
- [103] C. Ball, T. Hindelang, I. Kambourov, and S. Eder, "Spectral Efficiency Assessment and Radio Performance Comparison between LTE and WiMAX," *IEEE 19th International Symposium on Personal, Indoor and Mobile Radio Communications, 2008. PIMRC 2008*, Sept. 2008.
- [104] S. Rosati, S. Cioni, M. Neri, A. Vanelli-Coralli, and G.E. Corazza, "Joint Symbol Timing and Carrier Frequency Recovery for DVB-SH System," *Satellite and Space Communications, 2007. IWSSC '07. International Workshop on*, pp. 79–83, Sept. 2007.
- [105] D. Chu, "Polyphase Codes with Good Periodic Correlation Properties," *Information Theory, IEEE Transactions on*, vol. 18, no. 4, pp. 531–532, Jul 1972.
- [106] T. Keller and L. Hanzo, "Orthogonal Frequency Division Multiplexing Synchronization Techniques for Wireless Local Area Networks," *Proceedings of 7th IEEE International Symposium on Personal, Indoor and Mobile Radio Communications (PIMRC '96)*, pp. 963–967, Oct. 1996.
- [107] ETSI TR 102 831, Implementation guidelines for a second generation digital terrestrial television broadcasting system (DVB-T2), 2006.
- [108] R. Lopez-Valcarce and C. Mosquera, "Maximum Likelihood SNR Estimation for Asynchronously Oversampled OFDM Signals," *Signal Processing Advances in Wireless Communications, 2008. SPAWC 2008. IEEE 9th Workshop on*, pp. 26–30, July 2008.

- [109] S. Cioni, G.E. Corazza, and M. Bousquet, "An Analytical Characterization of Maximum Likelihood Signal-to-Noise Ratio Estimation," *Wireless Communication Systems, 2005. 2nd International Symposium on*, pp. 827–830, September 2005.
- [110] A. Dammann and S. Kaiser, "Transmit/Receive Antenna Diversity Techniques for OFDM Systems," *European Transaction on Telecommunications*, vol. 13, no. 5, pp. 531–538, September–October 2002.
- [111] A. Dammann, S. Plass, and S. Kaiser, "Cyclic Delay Diversity-A Simple, Flexible and Effective Multi-Antenna Technology for OFDM," *Proceedings of International Symposium on Spread Spectrum Techniques and Applications (ISSSTA2008)*, August 2008.
- [112] F. Vatalaro, G.E. Corazza, and C. Caini, "Analysis of LEO, MEO, and GEO Global Mobile Satellite Systems in the Presence of Interference and Fading," *IEEE Journal on Selected Areas in Communications*, vol. 13, no. 2, pp. 291–300, February 1995.
- [113] C. Caini, G.E. Corazza, G. Falciasecca, M. Ruggieri, and F. Vatalaro, "A Spectrum- and Power-Efficient EHF Mobile Satellite System to be Integrated with Terrestrial Cellular System," *IEEE Journal on Selected Areas in Communications*, vol. 10, no. 8, pp. 1315–1325, October 1992.
- [114] G. Bauch, "Capacity Optimization of Cyclic Delay Diversity," *Proceedings of Vehicular Technology Conference VTC2004-Fall*, pp. 1820–1824, September 2004.
- [115] F. Zanier and M. Luise, "Fundamental Issues in Time-Delay Estimation of Multicarrier Signals with Applications to Next-Generation GNSS," *10th International Workshop on Signal Processing for Space Communications (SPSC)*, October 2008.

Acknowledgments

The present work has been developed during the years spent in the Digicomm research group of the University of Bologna, and there are special people I want to acknowledge because they have been extremely important to me during the course of my thesis.

I would like to express my deepest and most sincere gratitude to my supervisor, Professor Giovanni E. Corazza for his excellent guidance and inspiring support during the course of my studies. He has been essential for instilling in me the interest for the research, and for unveiling all the secret of creativity. Thanks to his precious suggestions, and for his continuous enthusiasm working together has been a great experience.

I owe my thanks to all my colleagues at the Digicomm group, for their technical support and for their friendship. In particular I would like to thank: Raffaella Pedone and Marco Villanti, for their precious guidance that has been of incomparable value for me; Alessandro Vanelli Coralli, for the many technical discussions from which I have so much profited; my PhD fellows Marco Papaleo, Enzo Alberto Candreva, and Stefano Rosati, for their priceless support and the inspiring discussions; Stefano Cioni, Massimo Neri, Rosario Firrincieli, for their precious suggestions; the new guys and girl of the navigation team, Lina Deambrogio, Francesco Bastia, and Giulio Gabelli (one day, guys, this will all be yours); my past colleagues, Cecilia Bersani and Matteo Peverati, and the newcomers, Valentina Pullano, Ilaria Thibault, Alessandro Guidotti, Riccardo Baroni, and Valeria Petrini, for making the work place a fun place to be.

My research activity has gained a considerable added value thanks to my stay at ESTEC, European Space Agency (ESA). I am sincerely indebted to Dr. Riccardo De Gaudenzi and Jean-Luc Gerner for giving me the opportunity of working within the Radio Navigation working group at ESTEC and for their valuable guidance. In particular I want to thank Dr. Gustavo López Risueño for his outstanding super-

vision and patience, and all the colleagues at ESTEC that have welcomed me and made my stay a great experience.

I would like to acknowledge also my international reviewers, Prof. Carlos Mosquera, and Dr. Jose Angel Avila Rodriguez, for their precious and greatly appreciated comments and suggestions.

My most heartfelt gratitude goes to my family, my Mum Marisa, my Dad Sandro, and my brother Fabio. I would have not reached this point in life without their support. Finally, I would like to special thank Valentina for her support, love and understanding, which have been necessary to get things done.